Title
The Role of Fluxionality in the Deactivation Processes of Supported Cluster Catalyst

Author
Poths, Patricia

Publication Date
2023

Peer reviewed|Thesis/dissertation

UNIVERSITY OF CALIFORNIA
Los Angeles

The Role of Fluxionality in the Deactivation Processes of Supported Cluster Catalysts

A dissertation submitted in partial satisfaction
of the requirements for the degree
Doctor of Philosophy in Chemistry

by

Patricia Poths

2023

ABSTRACT OF THE DISSERTATION

The Role of Fluxionality in the Deactivation Processes of Supported Cluster Catalysts

by

Patricia Poths
Doctor of Philosophy in Chemistry
University of California, Los Angeles, 2023
Professor Anastassia N. Alexandrova, Chair

Realistic modelling of catalysis requires the incorporation of complexity in the form of fluxionality. This means the inclusion of multiple thermally accessible isomers in the starting ensemble, and along potential reaction pathways. Furthermore, the role of fluxionality on fundamental physical behavior of the system must also be accounted for. This work focuses on extending this fluxionality paradigm both along reaction mechanisms to capture the full complexity of experiment, as well as part of the fundamental physical processes of cluster catalyst deactivation such as sintering or poisoning. Fluxionality is incorporated into DFT calculations via global optimization of cluster catalyst structures and relevant reaction intermediates. It essential to account for isomeric diversity for improved interpretation of experimental results, which enables the identification of novel size-dependent sintering behavior that has subsequently been confirmed experimentally. Furthermore, this allows us to go beyond simple interpretation of experimental results to more complex predictions of changes in the structure and composition of the system. For example, this enabled the prediction of self-limiting coke formation in Pt_4Ge systems, and aided in understanding why Pt_4 in contrast rapidly continues to coke.

The dissertation of Patricia Poths is approved.

Yu Huang

Benjamin J. Schwartz

Philippe Sautet

Anastassia N. Alexandrova, Committee Chair

University of California, Los Angeles

2023

To everyone who believed in me before I believed in myself.

TABLE OF CONTENTS

LIST OF FIGURES

LIST OF TABLES

ACKNOWLEDGMENTS

While I have enjoyed science since high school, it was only in my third year at Imperial that I realized that computational chemistry was what I ultimately wanted to pursue. Professors Alexei Kornyshev, Fernando Bresme, and John Seddon at Imperial College London are the ones who ultimately put me on this path, for which I am eternally grateful.

I would like to thank my advisor, Professor Anastassia Alexandrova for her unwavering support during my PhD, her constant belief in my abilities, and for letting me take ideas and run with them in whatever direction I wanted. I would also like to thank my other committee members, Professors Philippe Sautet, Benjamin Schwartz, and Yu Huang for their valuable advice on this work.

No scientific work has been performed alone, so I would like to additionally thank all the group members past and present (and friends!) who directly supported me with my work; Ashley, Harry, Tom, Edison, Borna, Zisheng, and Santiago - as well as other group members and friends, TJ, Zerina, Claire, Will, Winston, Rob, Nathaniel, Cecilia, Jack, David, Matthew, and Kirill, for being such a lively bunch and making the PhD experience worth it. I will miss all of you.

Finally, I would like to thank my parents for fostering a love for science and an inquisitive nature throughout my life. This, along with their support during my PhD, has helped me become the scientist I am today.

This research has been supported by funding from AFOSR Grant FA9550-16-1-0141, DOE-BES grant DE-SC0019152, the Chemistry and Biochemistry Summer Mentored Research Fellowship, and the UCLA Dissertation Year Fellowship. CPU resources at the DoD (Department of Defense) High Performance Computing Modernization Program, including the U.S. Air Force Research Laboratory DoD Supercomputing Resource Center (AFRL DSRC), the U.S. Army Engineer Research and Development Center (ERDC), the Navy Supercomputing Resource Center (Navy DSRC), the Extreme Science and Engineering Discovery Environment's (XSEDE) and NERSC were used to conduct the computational part of this

work.

Chapter 2 is adapted with permission from Liu, G.‡; **Poths, P.‡**; Zhang, X.; Zu, Z.; Marshall, M.; Alexandrova, A. N*.; Bowen, K. H.* CO_2 Hydrogenation to Formate and Formic Acid by Bimetallic Palladium-Copper Hydride Clusters. 2020, J. Am. Chem. Soc., 142, 7930-7936, DOI: 10.1021/jacs.0c01855. Copyright 2020 American Chemical Society.

Chapter 3 is adapted with permission from Zandkarimi, B.‡; **Poths, P.‡**; Alexandrova, A. N.* When Fluxionality Beats Size Selection: Acceleration of Ostwald Ripening of Sub-Nano Clusters. 2021, Angew. Chem. Int. Ed., 60, 11973-11982, DOI: 10.1002/ange.202100107. Copyright 2021 Wiley-VCH GmbH.

Chapter 4 is adapted with permission from **Poths, P.‡**; Hong, Z.‡; Li, G.; Anderson, S. L.*; Alexandrova, A. N.* "Magic" sinter-resistant cluster sizes of Pt_n Supported on Alumina. J. Phys. Chem. Lett., 2022, 13, 47, 11044–11050, DOI: 10.1021/acs.jpclett.2c03114. Copyright 2022 American Chemical Society.

Chapter 5 is adapted with permission from **Poths, P.**; Sun, G.; Sautet, P.*; Alexandrova, A. N.* Interpreting operando XANES of supported Cu and CuPd clusters in conditions of oxidative dehydrogenation of propane: dynamic changes in composition and size. 2022, J. Phys. Chem. C, 126, 1972–1981, DOI: 10.1021/acs.jpcc.1c10356. Copyright 2022 American Chemical Society.

Chapter 6 is adapted with permission from **Poths, P.**; Li, G.; Morgan, H. W. T.; Masubuchi, T.; Alexandrova, A. N.; Anderson, S. L. Got Coke? Self-Limiting Poisoning Makes an Ultra Stable and Selective Sub-nano Cluster Catalyst. ACS Catalysis 2023, 13, 2, 1533–1544, DOI: 10.1021/acscatal.2c05634. Copyright 2023 American Chemical Society.

Chapter 7 is adapted from **Poths, P.***; Morgan, H. W. T.; Li, G.; Fuchs, A.; Anderson, S. L.; Alexandrova, A. N.* Promoter-Poison Partnership Protects Platinum Performance in Coked Cluster Catalysts. 20223, J. Phys. Chem. C., accepted.

VITA

2014–2018 MSci in Chemistry with Molecular Physics, Imperial College London, UK

PUBLICATIONS

Poths, P.; Morgan, H. W. T.; Li, G.; Fuchs, A.; Anderson, S. L.; Alexandrova, A. N.* Promoter-Poison Partnership Protects Platinum Performance in Coked Cluster Catalysts. 2023, J. Phys. Chem. C., accepted

Poths, P.; Zandkarimi, B.; Alexandrova, A. N.; Jiminez-Izal, E. Pt:Ge ratio as a lever of activity and selectivity control of supported PtGe clusters in thermal dehydrogenation. 2023, ChemCatChem, e202201533.

Poths, P.; Li, G.; Morgan, H. W. T.; Masubuchi, T.; Alexandrova, A. N.; Anderson, S. L. Got Coke? Self-Limiting Poisoning Makes an Ultra Stable and Selective Sub-nano Cluster Catalyst. ACS Catalysis 2023, 13, 2, 1533–1544.

Poths, P.* ‡; Hong, Z.‡; Li, G.; Anderson, S. L.*; Alexandrova, A. N.* "Magic" sinter-resistant cluster sizes of Ptn Supported on Alumina. J. Phys. Chem. Lett., 2022, 13, 47, 11044–11050

Lavroff, R. H.; Morgan, H. W. T.; Zhang, Z.; Poths, P.; Alexandrova, A. N.* Ensemble representation of catalytic interfaces: soloists, orchestras, and everything in-between. Chem. Sci., 2022, 13, 8003-8016.

Poths, P.; Alexandrova, A. N.* Theoretical perspective on operando spectroscopy of fluxional nano-catalysts. 2022, J. Phys. Chem. Lett., 13, 4321-4334.

Guo, H.; Poths, P.; Sautet, P.*; Alexandrova, A. N.* Oxidation Dynamics of Supported Catalytic Cu Clusters: Coupling to Fluxionality. 2022, ACS Catalysis, 12, 818-827.

Poths, P.; Sun, G.; Sautet, P.*; Alexandrova, A. N.* Interpreting operando XANES of supported Cu and CuPd clusters in conditions of oxidative dehydrogenation of propane: dynamic changes in composition and size. 2022, J. Phys. Chem. C, 126, 1972–1981.

Shumilov, K. D.; Mehmedovic, Z.; Yin, H.; Poths, P.; Nuryyeva, S.; Liepuoniute, I.; Jang, C.; Alexandrova, A. N.* Understanding hardness of doped WB4.2. 2021, J. Phys. Chem. C, 125, 9486-9496.

Zandkarimi, B.‡; Poths, P.‡; Alexandrova, A. N.* When Fluxionality Beats Size Selection: Acceleration of Ostwald Ripening of Sub-Nano Clusters. 2021, Angew. Chem. Int. Ed., 60, 11973-11982.

Liu, G.‡; Poths, P.‡; Zhang, X.; Zu, Z.; Marshall, M.; Alexandrova, A. N*.; Bowen, K. H.* CO2 Hydrogenation to Formate and Formic Acid by Bimetallic Palladium-Copper Hydride Clusters. 2020, J. Am. Chem. Soc., 142, 7930-7936.

Poths, P.; Chinea-Cano, E.; Dzigal, N.; Darby, IG; Osan, J.; Padilla-Alvarez, R.* Experimental assessment of effectively probed volume in confocal XRF spectrometry using microparticles. X-Ray Spectrometry. 2019; 48: 553– 560.

CHAPTER 1

Introduction

Attempts to understand the fundamental underpinnings of catalysis drives significant computational investigation of model systems. Matching these models to reality, however, remains a challenge. [1] Significant work has been performed modelling ideal, pristine surfaces, and possible mechanisms on these surfaces, based on past UHV surface science experiments. However, recent progress in *operando* imaging of catalysts under realistic reaction conditions has revealved that catalysts restructure when exposed to reactants, and are generally quite dynamic under reaction conditions. [2] This especially applies to so-called cluster catalysts, which consist of only a handful of metal atoms on some support. The Alexandrova group has in recent years shown the importance of including so-called "fluxionality" when modelling these subnanoclusters; specifically in including multiple isomers, as they have been shown to be thermally and kinetically accessible under the high temperatures typical for thermal catalysis. Understanding how these ensembles impact subsequent catalyst activity has been an area of active research in the group. [3–8] It has been shown that higher-energy metastable isomers are often what drives catalyst activity of these clusters; this is demonstrated in Chapter 2 for the gas-phase $PdCuH_4^-$ cluster, where the active metastable isomer readily activates CO_2 into formate and formic acid, while the ground state cluster overbinds formate, preventing its release. This work was performed in collaboration with Kit Bowen's group at Johns Hopkins.

Another crucial aspect of fluxionality relates to understanding how catalyst deactivation can be limited via doping of subnanoclusters. [9–14] While subnanocluster catalysts have many advantages, such as atom utility, better performance than bulk [15], and the ability

to break past scaling relations,[3] they are uniquely susceptible to deactivation, either via sintering [16–18] or catalyst poisoning. [19] Sintering, the process by which small clusters agglomerate to form larger clusters is the deactivation pathway felt most keenly, as the atoms in the clusters are dramatically undercoordinated compared to larger, more bulk-like NPs. [16–18, 20–22] For oxide-supported metal clusters and NPs, this is widely accepted to proceed via Ostwald ripening, or the migration of single atoms from smaller clusters to larger clusters. [16, 23, 24] Systems consisting of a single NP size have been shown to sinter more slowly than those with a variety of cluster sizes. [25] This is attributed to a lack of differences in surface energy between the NPs. While this works for larger NPs, for subnanoclusters with an ensemble of accessible isomers would not experience the same effect. This is demonstrated in Chapters 3 and 4, which address the sintering of $Pt_{1\text{-}8}$ clusters supported on TiO_2 and Al_2O_3. In Chapter 3, for TiO_2-supported Pt clusters, it is shown that including isomeric diversity generally results in more Oswald ripening, using a purely theoretical approach. Additionally, some cluster sizes (Pt_3/TiO_2 and Pt_7/TiO_2) exhibit unique stability against sintering. The existence of "magic" sinter-resistant cluster sizes is verified on a different support with a combination of theory and experiment in Chapter 4, for α-Al_2O_3 supported Pt clusters. Not only was it predicted that Al_2O_3-supported Pt_4 and Pt_7 clusters are particularly sinter-resistant, but this was then verified with experiment by our collaborator Scott Anderson at the University of Utah.

Beyond understanding how fluxionality accelerates sintering, a vital part of understanding subnanocluster behavior is the ability to track whether clusters sinter or not. This is addressed in Chapter 5 by fitting the *operando* XANES of Cu_3PdO_x and Cu_4O_x obtained during conditions of oxidative dehydrogenation of propane to both cluster and bulk standards. The bulk fraction of the XANES fits is shown to increase irreversibly with temperature, while the cluster fraction decreases, suggesting that the clusters sinter. Thus it is proposed that fitting the *operando* XANES of cluster catalysts with both computed cluster and experimental bulk standards can serve as a method to track extent of sintering of subnanoclusters. It

is important to use both, since it has been shown that the XANES of clusters cannot be fit with bulk standards alone, as changes in local environment of the more amorphous clusters results in XANES feature that do not trend with oxidation state in the same way bulk does.

Catalyst poisoning is another major method of deactivation. As mentioned above, dopants have been widely explored in efforts to reduce deactivation via both sintering and poisoning. [9–14] Dopants previously investigated for this include B, [9] Si, [26] and Sn. [12, 27, 28] Chapters 6 and 7 explore the effect of Ge doping, which was previously predicted computationally in the group, [13] on catalyst deactivation via coke formation, under conditions for ethane dehydrogenation, using ethane as a model for the dehydrogenation of longer-chain alkanes. In collaboration with Scott Anderson's group at the University of Utah, it is explored how Ge prevents deactivation via self-limiting coking, where a small amount of C is incorporated into the Pt_4Ge clusters, increasing their stability and selectivity without compromising activity.

Accessing this self-limiting coking state is only possible from a metastable isomer, which is initially only present in small amounts, but becomes stabilized along the reaction coordinate. This once again emphasizes that often the active species for catalysis are higher-energy states. This effect is contrasted with the incorporation of the same amount of carbon into Pt_4 clusters in Chapter 7. Pt_4 does not show a signature of self-limiting coking with retained activity towards ethane dehydrogenation upon incorporation of C_2. Ge is thus determined to limit further coke buildup while retaining catalyst activity via electronic effects, rather than structural effects, as C_2 incorporation into Pt_4 vs. Pt_4Ge results in similar restructuring of the underlying core structure. Ultimately, this provides a new outlook on how dopants improve catalyst activity and selectivity not simply by preventing buildup of coke, but via electronic interaction between the dopant and the poison. Furthermore, the activity of Pt_4GeC_2 compared to Pt_4C_2 is determined to be due to differences in kinetic accessibility of the entire ensemble, suggesting that a thorough analysis of the kinetics of cluster transformations in (de)activation processes could be essential in understanding catalyst behavior.

Overall, this work explores the role that fluxionality plays in catalyst deactivation processes, ranging from sintering to catalyst poisoning. Fluxionality is inextricably linked with physical behavior of catalysts; in order to realistically model catalysts, it is essential to consider it at every point along the reaction coordinate, and while assessing potential deactivation pathways.

CHAPTER 2

CO_2 Hydrogenation to Formate and Formic Acid by Bimetallic Palladium-Copper Hydride Clusters

2.1 Introduction

Transforming CO_2 into reduced, value-added molecules is of great interest for environmental and economic reasons. For catalytic CO_2 functionalization, bimetallic catalysts have shown improved activity and selectivity over single-component ones, as lattice engineering can be utilized to tailor the surface and electronic structures of bimetallic catalysts and thus to regulate their performance.[29–32] The rational design of high-efficiency bimetallic catalysts demands mechanistic understanding of how the catalytic CO_2 transformation processes on the active sites. While it is well-established that the formation of metal hydrides and the insertion of CO_2 into the metal-hydrogen bond are the critical steps in CO_2 hydrogenation, comprehensive knowledge about them remains limited due to a lack of direct experimental characterization on these key reaction intermediates.[31, 33–36] In particular, it is less clear how the interplay between different metals can alter catalyst properties, including hydrogen and CO_2 binding sites, electronic structures, charge transfer property, and release of products, all of which influence catalytic performance.

Synergy between the experimental characterization of reaction intermediates and state-of-the-art quantum chemistry calculations enables the gas-phase studies of CO_2 reduction and hydrogenation to provide mechanistic insight into CO_2 functionalization at the molecular level. [37–45] While single metal hydrides (e.g. Cp_2TiH^+,[41] PtH_3^-,[42] FeH^-,[43]

and $Cu_{1,2}H_2^-$[41, 44]) can convert CO_2 into formate and formate complexes, we are not aware of utilizing bimetallic hydrides for CO_2 hydrogenation. The present work focuses on the hydrogenation of CO_2 via reaction with the anionic bimetallic palladium-copper tetrahydride cluster, $PdCuH_4^-$. We selected the palladium-copper hydride because its reaction with CO_2 is an ideal model for understanding the hydrogenation process over bimetallic palladium-copper catalysts, which have shown superior CO_2 hydrogenation activity compared to single-component palladium or copper catalysts. [46–50] We show that a metastable $PdCuH_4^-$ isomer catalytically converts CO_2 to formic acid, in-line with recent theoretical predictions reporting catalysis on fluxional clusters can be driven by less stable but more active cluster isomers accessible in reaction conditions. [51–57]

2.2 Result and Discussion

$PdCuH_4^-$ was prepared in a pulsed arc cluster ionization source (PACIS), which has been applied to generate various metal hydrides.[58, 59] Briefly, a 30 μs duration, ultra-high voltage and current discharge was used to vaporize Pd and Cu powders. Almost simultaneously, high-pressure hydrogen gas was injected into the discharge region. The resulting mixture of atoms, ions, and electrons reacted to form $PdCuH_4^-$. $PdCuH_4^-$ clusters were then collisionally cooled and carried downstream by the supersonically-expanding hydrogen gas to interact with CO_2 in a reaction cell,[42, 60, 61] where additional energy as high as 1 eV can be provided to the reaction via the multi-collisions with the fastest H_2 molecules in the Maxwell-Boltzmann distribution. The resultant anionic products were identified by time-of-flight mass spectrometry. Figure 2.1 presents mass spectra with or without CO_2. With no CO_2 in the reaction cell, we observed the mass series of $PdCuH_4^-$ (Figure 2.1A), and its match with the simulated isotopic pattern confirms $PdCuH_4^-$ as the only palladium-copper hydride formed under our experimental conditions (Figure 2.1B). When CO_2 was added to the reaction cell, prominent mass series appeared at masses both higher and lower than

$PdCuH_4^-$ (Figure 2.1C). The higher-mass series is the reaction intermediate $PdCuCO_2H_4^-$, which were identified by comparing the experimental and simulated isotopic patterns (Figure 1D). The lower-mass peaks are formate- and formic acid-containing anionic clusters. The tagging of formic acid to anionic formate made possible observation of this neutral molecule by mass spectrometry. The high summed intensity of formate and formic acid products indicates that $PdCuH_4^-$ hydrogenates CO_2 efficiently. Note that the observation of formic acid suggests the reaction

$$PdCuH_4^- + CO_2 \rightarrow PdCuH_2^- + HCOOH(\text{formic acid})$$

yet $PdCuH_2^-$ or other palladium-copper hydrides were absent after $PdCuH_4^-$ reacted with CO_2. This implies regeneration of $PdCuH_4^-$ via H_2 absorption to $PdCuH_2^-$. Therefore, we proposed that the catalytic reaction

$$H_2 + CO_2 \xrightarrow{[PdCuH4^-]}]HCOOH$$

had occurred under our experimental conditions.

We then applied anion photoelectron spectroscopy to characterize $PdCuH_4^-$ and $PdCuCO_2H_4^-$ (Figure 2.2. For $PdCuH_4^-$, two electron binding energy (EBE) peaks at 3.36 and 3.83 eV are assigned as the vertical detachment energies (VDE). The VDE is defined as the photodetachment transition energy at which the Franck-Condon overlap is at its maximum between the anion's vibrational wave function and that of its neutral counterpart with both in their ground electronic states. For $PdCuCO_2H_4^-$, its VDE values are 2.49, 3.93, and 4.40 eV.

Figure 2.3 shows the calculated structures that are confirmed to account for the experimentally measured PES. Structure A and B are two low energy $PdCuH_4^-$ isomers, the latter 0.46 eV higher in energy. These two structures differ only in location of one H atom – both have the same low spin state (multiplicity 1). Based on the similar charges on the metal

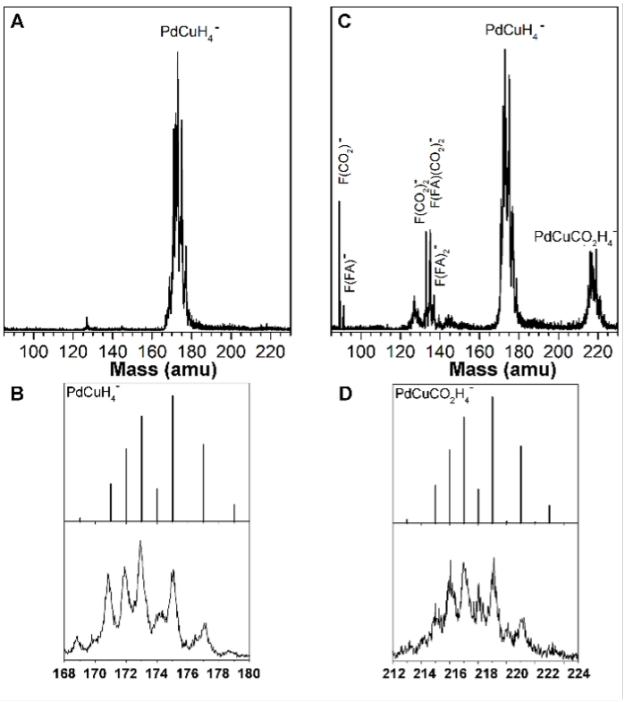

Figure 2.1: (A) The mass spectrum of $PdCuH_4^-$ cluster anions. (B) Simulated and experimental mass spectra of $PdCuH_4^-$. (C) Mass spectrum of $PdCuH_4^-$ reacting with CO_2. (D) Simulated and experimental mass spectra of $PdCuCO_2H_4^-$. F indicates formate. FA indicates formic acid.

centers across both structures, it does not appear that there is a significant change in the formal oxidation state of each metal between A and B. Structures C, D, and E are isomers of $PdCuCO_2H_4^-$ derived from CO_2 reacting with A and B. In structure C, CO_2 is inserted into the Cu-H bond of structure A. Structure D, on the other hand, is obtained by CO_2 association with the Pd and H atoms in structure B. Both structure C and D have a formate moiety, the latter 0.92 eV higher in energy. For structure D, the H atom that bridges Pd and Cu atoms can further transfer to the formate moiety, forming structure E with a formic acid moiety. The dissociation of structure E into formic acid and $PdCuH_2^-$, which is structure F, may explain the observation of formic acid in the experiment. All structures are in their respective low-spin states. Based on the atomic charges of all of the structures, it appears that both Pd and Cu are in their 0 oxidation state throughout. The H ligands instead experience the most significant changes in charge. The verification of these calculated structures

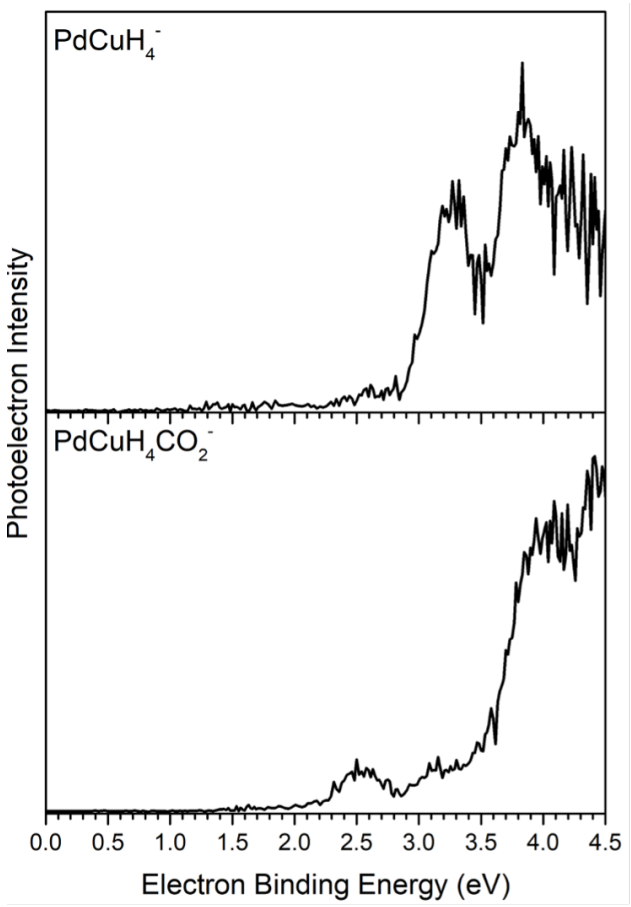

Figure 2.2: Photoelectron spectra of $PdCuH_4^-$ (A) and $PdCuCO_2H_4^-$ (B) measured with 266 nm (4.66 eV) photons.

was accomplished by calculating their VDEs at the CCSD//UPBEPBE/aug-cc-pvtz+pp level of theory and comparing with the experimental values (Table 2.1). For $PdCuH_4^-$, structure A and B respectively match the higher and the lower EBE feature in the experimental photoelectron spectrum. For the $PdCuCO_2H_4^-$ spectrum, the feature at 4.40 eV is attributable to structure C, and the feature at 3.93 eV is due to photodetachment of structure E. The feature at 2.49 eV does not match the calculated VDE of any $PdCuCO_2H_4^-$ structure. Instead, it agrees with the calculated VDE of structure F. This suggests that during photodetachment, $PdCuCO_2H_4^-$ was also photodissociated into $PdCuH_2^-$ (structure F) and formic acid. The dissociation product $PdCuH_2^-$ was subsequently photodetached,

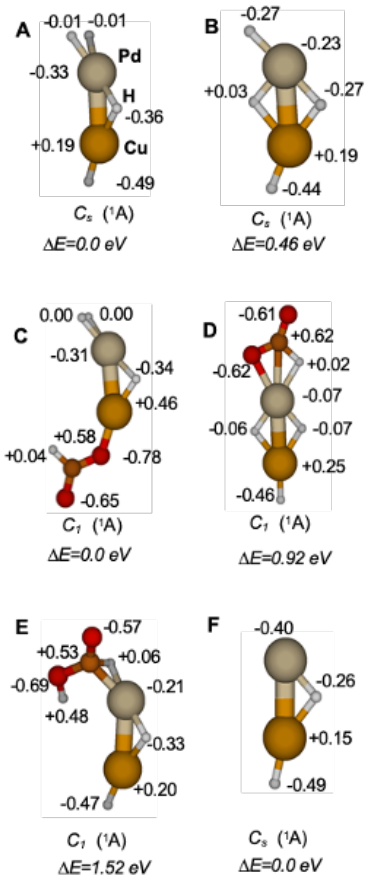

Figure 2.3: The calculated relevant lowest energy structures of $PdCuH_4^-$ (A and B), $PdCuCO_2H_4^-$ (C, D, and E), and $PdCuH_2^-$ (F). Symmetry, spectroscopic label, and energy relative to the global minimum structure of the same stoichiometry are shown below each structure. The charge on each atom is also shown.

contributing the 2.49 eV feature in the $PdCuCO_2H_4^-$ spectrum. To support this statement, we took the $PdCuCO_2H_4^-$ spectra with different laser power while keeping other collection conditions unchanged. The photoelectron intensity of the feature at 2.49 eV, I, shows a non-linear dependence on the laser power, P, which can be represented by $I \propto P^{1.67}$ (Figure A1). This suggests that it is the two-photon process that primarily contributes to this feature. This photodissociation/photodetachment phenomenon has been observed in our previous photodetachment experiment on anionic metal-hydride-CO_2 adducts.[42]Structure D should be present despite having a calculated VDE beyond the range of the photodetachment laser,

	$PdCuH_4^-$			$PdCuCO_2H_4^-$		$PdCuH_2^-$
Structure	A	B	C	D	E	F
Expt. VDE	3.83	3.36	4.40	N/A[a]	3.93	2.49
Calc. VDE	3.71	3.51	4.36	5.44	3.79	2.25

Table 2.1: Computed VDEs for each structure from Figure 2.3 and their corresponding experimental values. All VDE values are given in eV. [a] This structure's EBE is higher than the photon energy of the photodetachment laser.

as structure E is derived from it. Therefore, the two $PdCuH_4^-$ and three $PdCuCO_2H_4^-$ isomers were all observed experimentally. The high-energy environment in PACIS enables the formation of $PdCuH_4^-$ clusters with different energies,[62] which were subsequently cooled to their ground electronic states before interacting with CO_2.

The observation of two isomers of $PdCuH_4^-$ and their respective CO_2 insertion complexes suggests two reaction mechanisms beginning from structures A and B. Figure 2.4 presents the two calculated reaction pathways. The pathway in red is initiated by structure A, while the pathway in blue starts with structure B. When structure A interacts with CO_2, CO_2 inserts into its Cu-H bond without a barrier, forming structure C. This insertion step is exothermic by 1.32 eV. Structure C, however, is a very stable adduct, as seen by the high energy required for it to release formate as the product. The high dissociation energy of 2.38 eV according to calculations, is unlikely to occur under the multi-collision conditions in the reaction cell. Therefore, it is unlikely that the formate observed in the experiment formed via this mechanism. The reaction starting from structure B, on the other hand, proceeds on a smoother potential energy surface. Upon interaction, CO_2 is associated with the Pd and H atoms to form structure D. The transition from structure B to D is also barrierless. An H atom that bridges the Pd and Cu atoms in structure D subsequently transfers to the formate moiety, forming structure E, with an activation barrier 0.95 eV above structure D or 0.09 eV above the entrance channel. The dissociation of structure E into $PdCuH_2^-$ and formic acid is endothermic by 0.80 eV. Therefore, all steps on the structure B initiated pathway are within 0.5 eV of the entrance channel energy, making them accessible under the experimental conditions where excess energy is provided via multi-collisions with the fast-moving

H_2 molecules.[38, 63]When electrons are present in the reaction environment, the released formic acid can deprotonate to yield formate via the dissociate electron attachment, a common acid-electron interaction in the gas phase. As mentioned earlier, the reaction does not stop at the $PdCuH_2^-$ ion; there is no evidence of it in the mass spectrum, suggesting that in the presence of abundant H_2 in the reaction cell, the following reaction takes place:

$$H_2 + PdCuH_2^- \rightarrow PdCuH_4^-$$

This reaction is 0.87 eV exothermic if forming structure A, or 0.41 eV exothermic if leading to structure B. Thus, the H2 environment readily regenerates the $PdCuH_4^-$ clusters, completing the catalytic cycle.

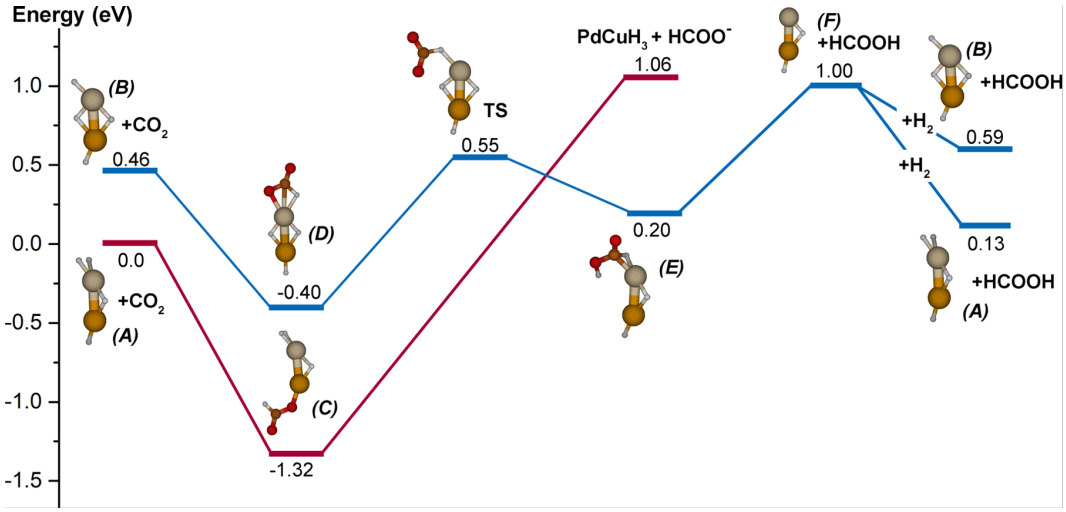

Figure 2.4: Profile for the reaction of CO_2 with $PdCuH_4^-$. Zero-point energy corrected energies are given in eV. The letters in the parentheses correspond to their labels in Figure 2.3. The potential energy surface is referenced to the total energy of structure A and an isolated CO_2.

Compared to Cu, Pd is stronger in binding H but weaker in binding O.[33]Therefore, the structure with more H binding to Pd is more stable. Since structure A has one H atom that binds exclusively to Pd rather than both Pd and Cu, it is lower in energy than structure B. For structure A, however, the binding of more H exclusively to Pd inhibits the binding

of CO_2 on Pd.[64]Instead, CO_2 inserts into the Cu-H bond, forming the strong Cu-O bond (structure C). The high dissociation energy of the Cu-O bond prevents the release of formate product, ending this pathway in a "catalytic deadlock". In structure B, Pd is more exposed while Cu is more coordinated, which facilitates the initial CO_2 binding to the Pd atom. Since Pd has weak O binding, the formic acid moiety associates with Pd via Pd-C and Pd-H interactions, as shown in structure E. Dissociation of the formic acid product is thus much less endothermic with this reaction pathway. Also importantly, the Pd site becomes exposed after releasing the formic acid, and can readily absorb an H_2 molecule to complete the catalytic cycle. This result echoes recent reports emphasizing the metastable structures as the actual active sites in cluster catalysis.[55]

The charge analysis can further rationalize the different reactivity of the two $PdCuH_4^-$ clusters (Figure 2.3). The calculated atomic charges show a difference in the charge distributions in CO_2 bound to structures A and B. When CO_2 is bound to Cu, as in structure C, the charge difference between Cu and the formate fragment is more significant than the analogous charge difference between Pd and the formate fragment. Furthermore, Cu is positively charged, while Pd is negatively charged, so the formate moiety interacts more strongly with Cu.

2.3 Conclusions

To summarize, we have demonstrated that the bimetallic $PdCuH_4^-$ clusters can convert CO_2 into formate and formic acid. Mass spectrometric analysis of the reaction products between $PdCuH_4^-$ and CO_2 reveals the reaction intermediate $PdCuCO_2H_4^-$, the reaction products formate and formic acid, and the regeneration of $PdCuH_4^-$, completing the catalytic cycle. Different isomers of $PdCuH_4^-$ and $PdCuCO_2H_4^-$ are identified by anion photoelectron spectroscopy and electronic structure calculations. Mechanistic study confirms that metastable structures as the catalytic driving force. This work represents the first example

of CO_2 hydrogenation by bimetallic hydride clusters, providing insight into understanding the catalytic properties of bimetallic catalysts.

2.4 Methods

2.4.1 Experimental Methods

The experimental technique, anion photoelectron spectroscopy, is conducted by crossing a mass-selected beam of negative ions with a fixed-energy photon beam and energy analyzing the resulting photodetached electrons. This technique is governed by the energy-conservation relationship, $h\nu$ = EBE + EKE, where $h\nu$, EBE, and EKE are the photon energy, electron binding (transition) energy, and the electron kinetic energy, respectively. Our photoelectron spectrometer, which has been described previously,[65] consists of one of several ion sources, a linear time-of-flight (TOF) mass spectrometer, a mass gate, a momentum decelerator, a neodymium-doped yttrium aluminum garnet (Nd:YAG) laser for photodetachment, and a magnetic bottle electron energy analyzer. Photoelectron spectra were calibrated against the well-known photoelectron spectrum of Cu^-. The $PdCuH_4^-$ anions were generated using a pulsed-arc (discharge) cluster ionization source (PACIS), which has been described in detail elsewhere.[66]This cluster anion source has been used to generate a variety of transition metal hydride cluster anions.[59, 67–69]It provided us with a broad range of cluster sizes and compositions. During PACIS operation, a 30 μs long, 4000 volt electrical pulse applied across the anode and the mixed Pd/Cu pressed-powder cathode in the discharge chamber vaporizes the Pd and Cu atoms. Almost simultaneously with the discharge, 180 psi of ultrahigh purity hydrogen gas was injected into the discharge region, where it was dissociated into hydrogen atoms. The resulting mixture of atoms, ions, and electrons then reacted and cooled as it expanded through the PACIS housing. After a small gap, this flow then continued through a 15 cm long collision/reactor cell before exiting into high vacuum. To initiate the reaction between CO_2 and $PdCuH_4^-$, pure CO_2 was injected into the collision cell using a second

pulsed valve. The resultant anions then drifted through a skimmer, through a differentially pumped region, and into the TOF region, where they were perpendicularly extracted and mass-selected prior to photodetachment. Due to palladium's and copper's isotope patterns and the presence of multiple hydrogen atoms, photoelectron spectra were taken at all observed mass peaks.

2.4.2 Computational Methods

The calculated structures presented in this work were computed using density functional theory (DFT), using the PBEPBE[70] functional in Gaussian16.[71] The initial structure search was performed using the LANL2DZ[72–74] basis set, after which the lowest energy structures were further optimized using the aug-cc-pvtz+pp[75] basis set. After geometry optimization, the energies of the anionic and neutral clusters were calculated at the CCSD[76–79]//UPBE level to determine the vertical detachment energies (VDE) for each structure for comparison with experimental PES results. CASSCF (m,n)[80–88] up to (14,14) was run to verify the accuracy of the single reference method. CCSD//UPBE was used rather than TD-DFT for VDE calculations due to the unreliability of the result as the functional was changed, and CCSD(T) was not used as perturbation theory failed for some structures. Only the first VDE was calculated for each structure- if there are VDE^{2+} peaks present in the spectrum they are not accounted for, but all peaks present in the experimental spectrum have corresponding computed VDEs. Charges on each atom were calculated using natural population analysis.[89]

CHAPTER 3

When Fluxionality Beats Size Selection: Acceleration of Ostwald Ripening of Sub-Nano Clusters

3.1 Introduction

Subnanometer metal clusters are, in general, thermodynamically less stable than larger clusters, since they have numerous low-coordination sites, large surface area to volume ratio, and fewer metal-metal bonds that can stabilize the cluster. As a result, they tend to sinter more rapidly than larger nanoparticles.[90–93] Sintering, the process in which smaller clusters are consumed by and grow into larger clusters is driven by increasing stability of clusters as they grow, and is one of the primary deactivation pathways of nanoparticle catalysts.[94, 95] Metal nanoparticles sinter via either particle migration and coalescence, or Ostwald ripening. [90, 96, 97] Weak cluster–support interaction promotes Brownian-type motion of particles on the support, favoring the particle migration and coalescence mechanism. In contrast, during Ostwald ripening, atoms detach from clusters, diffuse along the surface, and join other clusters. Since smaller clusters generally dissociate more easily, while larger clusters are better at retaining the arrived monomers, larger clusters tend to grow to the expense of the smaller ones. This mechanism is more prevalent in clusters that are bound strongly to the support and are therefore less likely to move around the surface. Sintering of supported metal catalysts has been studied extensively by several groups. [98–102] For instance, Campbell et al. showed accurate size dependence of particle energies (using direct measurement) is crucial in order to be used in kinetic models and one cannot use the Gibbs-Thompson relation, [103]

which relates the chemical potential of a metal atom in a particle of radius R to the one in the bulk, to estimate the dependence of particle energy.[100] There are other multiple models of Ostwald Ripening that explicitly incorporate kinetics in their derivations, many of which treat the metallic nanoparticles as spherical structures with varying degrees of wetting on the surface support, depending on surface-support interactions. [103–105] Our work differs in our approach compared to these works, as we focus on sub-nano clusters, and therefore do not consider the clusters as "wetting" the support to varying degrees, dependent on the interfacial surface energies of the cluster/air, support/air, and cluster/support. Instead, we consider the full electronic energy of the entire Pt_n cluster, n = 1–8, in order to incorporate in isomeric diversity explicitly. Using these electronic energies, we model the sintering process as the result of the thermodynamic driving force of the different chemical potentials of the clusters and evaluate differences in these driving forces as a result of isomeric diversity.

Supported small clusters can be extraordinary catalysts, particularly at nano- and sub-nanometer sizes, which are then desirable to preserve. Also, nearly every atom in small clusters is surface-exposed and can participate in catalysis, thus reducing the amount of precious metal needed. For these reasons, there have been many efforts to prevent cluster catalyst sintering. Some of these efforts include doping or alloying with other elements to tune clusters' electronic structure, [10, 106–109] size selection of deposited clusters,[25] and introduction of capping agents to metal nanoparticles.[110] Among these approaches, size-selection has been shown to effectively suppress Ostwald ripening, because of the elimination of the main driving force for ripening: different surface energies of different cluster sizes. [25] Specifically, this was shown for Pt_n ($n > 21$) on several different supports including Si_3N_4 and SiO_2.[25]

However, we showed on a number of examples that, in sub-nanometer regime, for a specific cluster size, under typical reaction conditions (e.g. temperature of 700 K), several metastable cluster isomers in addition to the global minimum (GM) structure are present, interconvert, and affect all catalyst properties. [51, 52, 111, 112] We argue here that sinter-

ing must be impacted by this dynamic fluxionality. We show that, although size selection is an effective method to prevent sintering for large and relatively rigid clusters, smaller size-selected clusters sinter rapidly because of their access to multiple isomers, all having different surface energies, and thus preserving a driving force for sintering. Our model of Ostwald ripening of Pt clusters on the TiO_2(110) surface shows that the presence of metastable structures increases the driving force for the sintering of subnanometer Pt clusters. Additionally, the extent of the effect is in fact size-dependent

Note that our approach will hold for all catalytic systems regardless of the complexity of the surface (with step edges, vacancies, and other defects), and it is useful when the system is prone to dynamism in reaction conditions and thus to exhibiting isomeric diversity. However, this work focuses on one surface as an example, and it is purposefully chosen to be simpler, in order to deconvolute the effect of isomeric diversity from support-induced complications, including support restructuring. On the other hand, cluster-support interaction can also affect the sintering rate of clusters. For weaker cluster-support interaction our revised theory for Ostwald ripening would still hold, but would have to be appended with particle migration and coalescence, and we hypothesize that the particle mobility would also be size- and isomer-dependent.

Finally, note that this study is largely based on thermodynamics, whereas the kinetics of all elementary steps in principle could be important for sintering. However, the main driving force of particles leaving smaller clusters and joining larger ones is a thermodynamic one, stemming from the difference between chemical potentials of clusters with different size (a 'thermoactivated' process).[113] In this work, the kinetics for the monomer migration is taken into account explicitly, while the dissociation kinetics is approximated from the BEP relations, which we test and find holding true for the problem at hand.

3.2 Computational Methods

3.2.1 Global Optimization

Global optimization of $Pt_n/TiO_2(110)$ (n = 1–8) was performed using plane wave density functional theory (PW-DFT) implemented in the Vienna Ab initio Simulation Package (VASP) [114–117] and projector augmented wave (PAW) potentials [118] and the PBE[70] functional. The kinetic energy cutoff of 400.0 eV was chosen for the plane waves. A convergence parameter of $10^{-}6$ eV for the electronic relaxation was used. Geometric relaxations were performed until forces on all atoms are less than 0.01 eV/Å. Gaussian smearing with the sigma value of 0.1 eV was used. The $TiO_2(110)$ surface was previously optimized,[119] and modeled as a (2×4) unit cell with four trilayers along the z-direction. A vacuum gap of 13 Åwas used to avoid interactions between repeated images. During the geometric optimization the lower half of the slab was kept fixed. Only Γ-point sampling was used to obtain the energy due to a fairly large size of the super cell. For $Pt_1/TiO_2(110)$ PES sampling, the unit cell was divided into an 11×11 grid, and the relaxation was done on the z coordinate of Pt while its x and y coordinates were fixed (Figures 3.1 and B.1).

In order to produce the initial geometries for sampling of Pt_n, a parallel global optimization and pathway toolkit (PGOPT) was used. [120] PGOPT generates structures based on the bond length distribution algorithm (BLDA), restricting the distance of each atom to its first and second nearest neighboring atoms to follow a normal distribution. This results in creating initial structures which are more chemically relevant, and thus easier to converge. We generated 25, 35, 50, 60, 80, 120, and 180 different initial structures for sampling of Pt_2/TiO_2, Pt_3/TiO_2, Pt_4/TiO_2, Pt_5/TiO_2, Pt_6/TiO_2, Pt_7/TiO_2, and Pt_8/TiO_2 respectively. In order to reach local minima on the PES, every structure was then fully optimized using DFT until forces on all atoms are less than 0.01 eV/Å. Obtained structures were compared to each other in order to filter out the duplicates. Note that the equilibrium populations

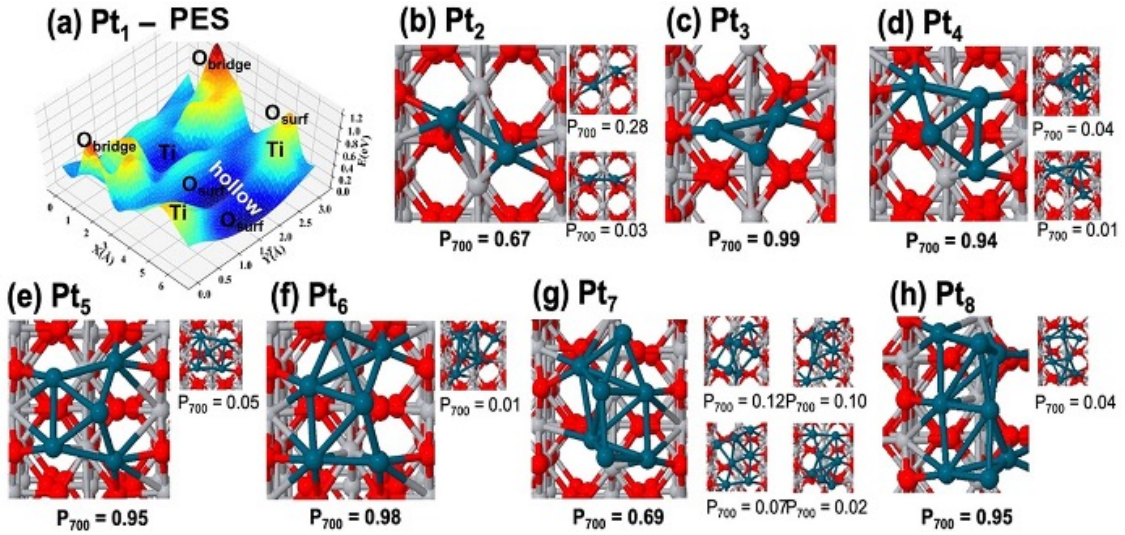

Figure 3.1: (a) The PES for the Pt monomer on TiO_2 (see SI Figure B.1 for full PES along with the surface model). (b-h) GMs and accessible low-energy isomers of Pt_n (n = 2–8) on TiO_2(110); P_{700} signifies the Boltzmann probability of population at 700 K. Cyan – Pt, red – O, grey – Ti.

were calculated based on Boltzmann populations [10, 120]

$$P_i = \frac{Z_{elec,i} Z_{trans,i} Z_v ib, i}{Z} {}_{rot,i}\sum_i Z_i \approx \frac{g_i e^{-\beta E_i}}{\sum_i g_i e^{-\beta E_i}}$$

Where $Z_{elec,i}$, $Z_{trans,i}$,$Z_{vib,i}$, and $Z_{rot,i}$ are electronic, translational, vibrational, and rotational partition functions respectively. Here, we only consider the electronic contribution and ignore other degrees of freedom. In order to select the thermodynamically accessible isomers at relevant temperatures a cut-off energy of 0.4 eV was used. The GM structures for each sampled cluster size (Pt_2–Pt_7) and several local minima with appreciable populations at 700K are shown in Figure 3.1 (b-h). Finally, the charge analysis was done using the Bader scheme. [121–124]

3.2.2 Monte Carlo Simulations

The 2D Ostwald ripening model was based on pre-computed cluster structures and energies. Every Pt_n/TiO_2 (n = 1–7) structure was obtained from global optimization and projected onto the 2D model of the support. Note that Pt_8 was not used as a starting size for sintering, in order to always have a possibility of the n+1 clusters to form with the isomeric diversity (Pt_9 and larger clusters were considered without isomeric diversity; see below). The size of the support was 158 Å× 72 Å, or (24 × 24) unit cells of TiO_2(110). The total number of clusters in the starting configuration was 100, for all systems. Note that most obtained local minima occupy the same hollow site on the slab. In our sintering model, we disregard the site and make all sites on the 2D model equally likely for deposition. However, all the energies of the cluster isomers corresponded to their true preferred locations and were weight by the Boltzmann probabilities. Each cluster shape was approximated by the smallest circle containing all atoms in the cluster. During each step of sintering, an atom from a randomly chosen cluster (which can be a monomer) was moved using the Markov chain Metropolis Monte Carlo algorithm. The temperature of the simulation was 700 K, which corresponds to the high end of the dehydrogenation of ethylene on supported Pt clusters, measured by temperature programmed desorption (TPD). [56, 125] Every attempted cluster dissociation was associated with the precomputed thermodynamic penalty, and subjected to the Metropolis acceptance criterion. If a move brought a migrating monomer to an association with a stationary cluster, the probability of association was 100%. Atomic Pt evaporation and redeposition were ignored, as those were found to be minimal by theory and experiment. [56, 126] The sampling of the Pt_n/TiO_2 (n = 1–8) PES showed that, for every cluster size, several structural isomers should be thermally-accessible at 700 K (Figure 3.1). Thus, a cluster randomly selected to undergo a dissociation or association with a monomer can be any of its thermally-accessible minima, with a probability dictated by the Boltzmann populations of the given minimum. If two neighboring clusters grew enough to fuse, they were considered a single cluster, with the corresponding larger size, isomeric diversity, and

energetics.

For clusters larger than Pt_8, cluster diversity was ignored in the model, and only a single structure and energy were considered. Figure B.2 shows the binding energy of Pt clusters per atom as a function of the number of atoms in the cluster. This was used to estimate the energy for the larger clusters. The model for the radial growth of the larger clusters was based on Wulff constructs. First, it was determined that the Pt (100) facet of the bulk Pt was the preferred for the $Pt/TiO_2(110)$ contact. From there, Wulff constructs based on Winterbottom constructs, therefore taking into account the cluster/support interfacial energy, were prepared using Wulffpack[127] (see Figure B.3 for details).

The simulations were started both from the monodisperse cluster size distributions, and from the polydisperse systems with mixtures of cluster sizes (Figure 3.2). The monodisperse systems, thus far posited to withstand sintering better than polydisperse11 systems, are the main focus of this study. Three different types of simulations were performed. In the first type, only GMs of the starting clusters were included, and in the process of sintering only GM structures of larger clusters could form. Note that the simulations starting from the monomers are specific, because the energy depends solely on the monomer location on the surface, and in this case, we do not enforce the GM-only starting configuration, to treat these systems on equal footing with others in terms of the random initial cluster placement on the support. In the second type of simulations, we start from the more realistic system characterized by temperature-dependent isomeric diversity for each cluster size, and the sintering proceeds with an access to higher-energy isomers of the forming clusters, all being based on their relative Boltzmann weights. Finally, in order to further account for the possible poorly-understood kinetic effects during cluster synthesis, we also probed the sintering of the systems that initially had fully random isomeric distributions (i.e. not obeying the Boltzmann distribution, and instead definitely exceeding the thermodynamically dictated number of higher energy isomers), but that sinter to larger clusters in accordance with the Boltzmann statistics for the forming cluster sizes. We call these three types of simulations

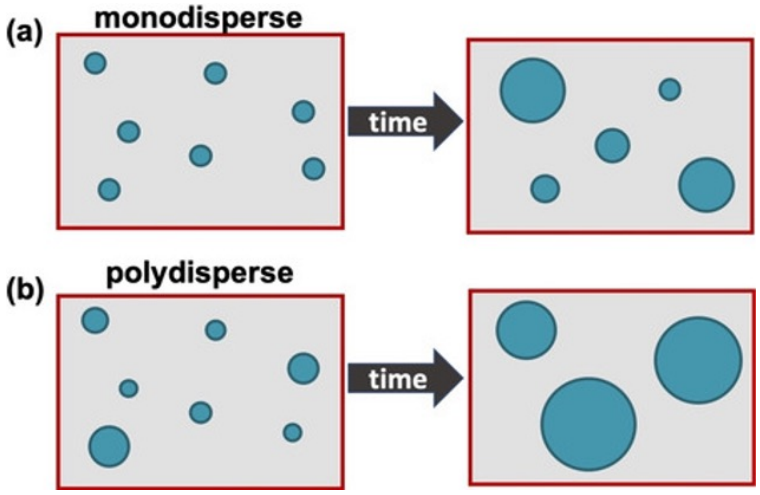

Figure 3.2: Schemas of the monodisperse and polydisperse setups for sintering simulations. Note that the actual unit cell and the number of deposited clusters used in the simulations are significantly larger (see text).

the GM, Boltzmann, and isomer runs.

To ensure the rigorous averaging, for each isomer simulation, 5 different initial configurations were prepared with isomeric diversity. The coordinates and cluster sizes of each initial state with isomeric diversity were used for the Boltzmann/GM runs, simply replacing some/all of the higher-energy isomers with the GM cluster. Each of these initial states were then sintered 5 times, for 100,000 MC steps, to ensure randomization via MC. Note that the end of the simulation is somewhat arbitrary; the eventual result of sintering is rather uninteresting (one large particle), and we are interested in the sintering rate rather than the end result.

For the polydisperse systems, the procedure was identical: multiple cluster sizes were randomly placed on the surface, and the system was allowed to sinter, either accessing the isomeric diversity or not. We probed two ranges of cluster sizes at the start of sintering: Pt_2-Pt_7, and Pt_1-Pt_5, as well as three initial proportion of the monomers (10%, 25%, and 50%).

Note that, in order to obtain a more quantitative picture of sintering, the actual barriers of all involved elementary steps should be calculated, [105] and a model such as kinetic Monte

Carlo [128–130] would have to be used. The barriers involved in the monomer migration on the surface are explicitly taken into account in our simulations, but the step of atom dissociation from a cluster is not. Given the number of isomers and clusters sizes, as well as the choices for dissociating atoms and end products, the estimated number of pathways would be 103, i.e. impracticable. However, by BEP relationships,[131, 132] barriers and energies of reaction steps should be related. In order to test the validity of the BEP relations for our fluxional clusters, we performed the explicit reaction pathway calculations for the dissociation of the GM and LM2 of supported Pt_4 (Figure B.4). These clusters were chosen due to significant difference in the deposition sites and energies, and the fact that their dissociation produces different isomers of Pt_3 (and the GM of Pt_1). Despite the significantly different chemistries, and large differences in the dissociation barriers, the calculated the ratios between the dissociation barriers and the reaction energies are nearly identical for GM and LM2 (see Figure B.4). While this test is by no means exhaustive, and exhaustive tests are out of reach, we infer that the established BEP relations qualitatively hold true, and the simulations produce a qualitatively reliable picture from thermodynamics alone, as indeed suggested by the Ostwald's theory.

We should also note that there are several approaches to model sintering using kinetic Monte Carlo (kMC) or MD simulations. [133–135] However, as already mentioned, the computational cost of kMC, with thousands of reaction pathways in our case, would be unsurmountable. On the other hand, in order to obtain a reliable result from MD simulations, a very long MD simulation in required, in order to visit enough local minima, and that is, again, computationally impractical. In addition, MD would not be able to involve more than just a few structures (usually only 2), due to the computational expense. Using accurate sampling of PES and MC simulations, we cover a huge size- and isomeric diversity, and, relying on BEP relations, cover a massive number of chemical events leading to sintering. While still containing approximations, we believe our method has a significant advantage and brings new insight.

3.3 Results and Discussion

The relative sintering rates were monitored as the decay in the number of clusters with the number of MC steps, the evolution of the average and maximum cluster sizes at every stage of sintering, and the cumulative relative populations of cluster sizes.

3.3.1 Monodisperse Systems

We find that the sintering rates of the clusters of all sizes are substantially impacted the isomeric diversity, when it is included in the simulations (Figure 3.3). Broadly, systems with greater isomeric diversity sinter faster than the systems represented by just the GM. Note that, while the GM-only simulations do not represent a physical reality, they serve as a contrast, and demonstration of an important phenomenon: small clusters are exempt from sintering suppression by size-selection. Interestingly, there is also a strong size-dependence to the sintering behavior. Three different categories of systems can be identified, based on the decay in the number of clusters with MC time steps, and its sensitivity to the isomeric diversity. Category 1 includes Pt_3, Pt_6, and Pt_7. These systems show the strongest difference between the sintering rates of the GM, Boltzmann, and isomer configurations (Figure 3.3a). Clusters of the Category 2, which includes $Pt_2$and Pt_5, have intermediate differences (Figure 3.3b). Clusters of Category 3, Pt_1, and Pt_4, have small to negligible difference between the GM, Boltzmann, and isomer runs (Figure 3.3c).

The difference between the categories is further illustrated by the standard deviation over the 25 MC simulations, shown in Figure 3.3 (d-f) for cluster sizes representative of each category: Pt_3, Pt_2, and Pt_4. The same plots for all other sizes are given in the SI Figure B.5. The total standard deviation, s, was computed by treating the standard deviation of each of the 5 different runs as separate data sets, and combining them according to equation 1, where n_i is the number of data in set i, s_i is the standard deviation of set i, y_i is the mean

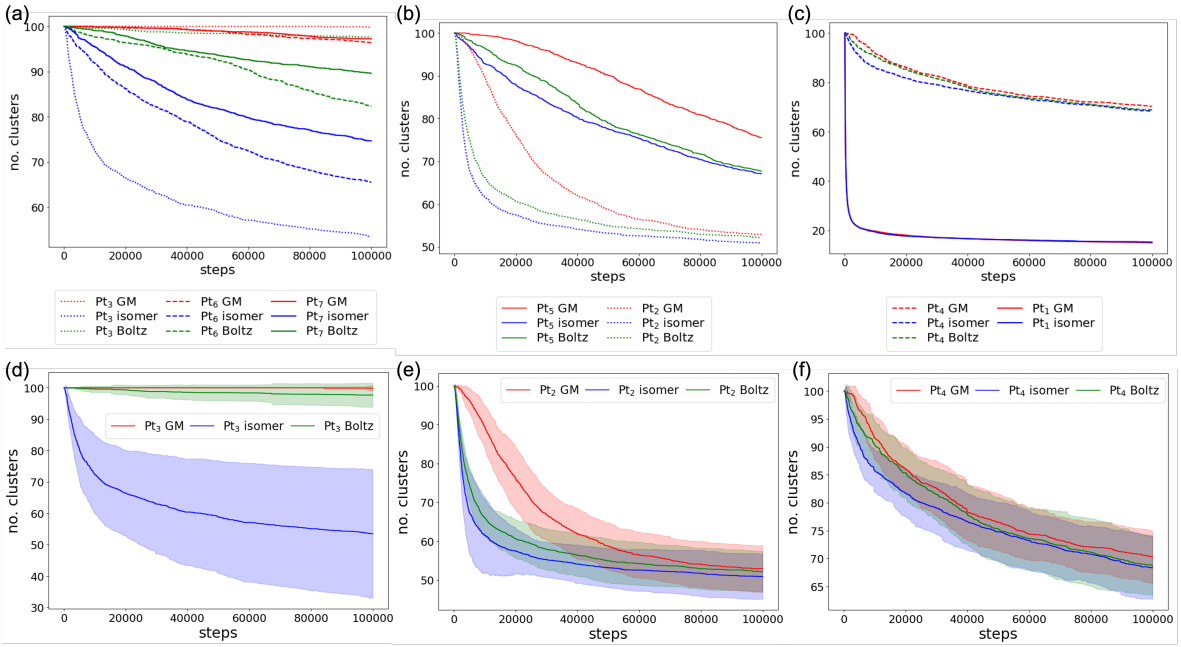

Figure 3.3: Sintering of monodisperse systems monitored via the total number of clusters present as a function of the MC step: Red - the GM-only sintering regime, green – sintering regime with the Boltzmann-weighted isomeric diversity, blue - sintering regime that starts from fully random isomer distributions and accesses isomeric diversity during sintering with the Boltzmann-weighted probabilities. (d), (e), and (f) show the standard deviations across the 25 MC simulations for Pt_3, Pt_2, and Pt_4, respectively.

of set i, and y is the mean of the combined sets.

$$s = (\sum_{i}^{5} \frac{n_i s_i^2 + n_i(\bar{y}_i - \bar{y})^2}{n_i})^1/2$$

There is a strong variation in the standard deviation between the simulations that start from different cluster sizes. For example, it reaches its extreme for the sintering of Pt_6 and Pt_7, regardless of the starting conditions. In contrast, for Pt_3, the standard deviation for the GM and Boltzmann simulations are significantly smaller than for the isomer simulations, suggesting that the higher-energy isomers of Pt_3, if formed, can promote sintering quite dramatically.

The practically important result is the relative sintering resistance (or the lack of) of the size-selected clusters in the presence of the isomeric diversity (green and blue curves in Figure 3.3). The resistance can be read from the relative steepness of the green (most realistic) and blue curves as a function of MC steps, and the number of clusters remaining on the surface at the end of the run. By this measure, Pt_3 and Pt_7 are the more stable against sintering among the considered cluster sizes, and could be called "magic number" clusters. Notice also that estimating sintering rate on the basis of just the GM can be misleading. For example, Pt_2 would be estimated to be more sinter-resistant than it really is (red versus green plots in Figure 3.3e). And yet, the GM-only estimation of sintering rate would not be too far off for, e.g., $Pt_{3,4}$ (Figures 3.3d,f). In other words, the role of isomeric diversity in sintering is cluster-size dependent and non-trivial, and the most dramatic example are clusters of Category 1, Pt_3 and Pt_7.

The simplest, "step one" explanation for the observed size-dependence of the sintering acceleration via isomeric diversity can be derived from the first sintering step: $Pt_n + Pt_n \rightarrow Pt_{n-1} + Pt_{n+1}$ (Table 3.1). The energetics of the "step one" processes suggests that clusters of certain sizes need to overcome a large energy penalty before clusters of different sizes can start to populate the system and shift away from monodispersity. Once the shift occurs, the

more rapid sintering is promoted, as the energy differences between the clusters increase and progressively favor the growth of large clusters out of smaller ones.

Monodisperse Sintering Step	ΔE (eV)
Pt_2+Pt_2 $\rightarrow$ Pt_1 + Pt_3	–0.84
Pt_3+ Pt_3 $\rightarrow$ Pt_2 + Pt_4	0.51
Pt_4+ Pt_4 $\rightarrow$ Pt_3 + Pt_5	–0.05
Pt_5+ Pt_5 $\rightarrow$ Pt_4 + Pt_6	0.12
Pt_6+ Pt_6 $\rightarrow$ Pt_5 + Pt_7	–0.31
Pt_7+ Pt_7 $\rightarrow$ Pt_6 + Pt_8	0.23

Table 3.1: The computed energetics of "step one" for sintering in fully monodisperse systems. Energetics derived from the GM energies of all cluster sizes.

While the "step one" explanation appears to be enough to rationalize the sintering stability of Pt_3 and Pt_7, it is insufficient for some other cluster sizes. For example, the "step one" of sintering of Pt_6 is, in fact, energetically favorable, in contrast to Pt_3 and Pt_7, and this would suggest that Pt_6would behave entirely differently; yet it does not (Figure 3.3a). Therefore, there must be additional fundamental reasons that dictate the total nature of sintering for monodisperse systems.

In order to explain the sintering behaviors across cluster sizes, we propose a "competing pathways" concept. After the "step one" of a monodisperse system sintering, other cluster sizes start to build up. Their subsequent sintering is subject to the energetics associated with the monomer exchange with clusters of other cluster sizes, the majority of which at the beginning are still of the initial size (e.g. Pt_6). The balance between favorability and unfavourability for Pt_n undergoing sintering (monomer moving from small clusters to large clusters) and reverse sintering (monomer moving from large to small clusters) with all other cluster sizes and their isomers present in the ensemble at 700 K are shown in Figure 3.4.

For example, Figure 3.4a,b shows the favorability of the forward and reverse sintering, respectively, of Pt_6 in the presence of Pt_n: Pt_6 + Pt_n $\rightarrow$ Pt_7 + Pt_{n-1}, and Pt_6 + Pt_n $\rightarrow$ Pt_5 + Pt_{n+1}. The magnitudes of the GM contributions to both forward and reverse pro-

cesses are also highlighted (dark red and dark green portions of the plots). Hence the figure indicates whether the GM pathway is favorable or unfavorable, and the proportion relative to higher-energy pathways for the same process that contain higher energy isomers can be seen. This aids our understanding of how probable non-GM pathways are. As is clear by the proportion of green on the graphs for Pt_6, that the forward and reverse sintering are both similarly favorable, and the GM contributes to a large fraction of the favorable pathways in both directions. However, as the forward and reverse favorabilities are fairly well-balanced, especially in the GM-only scenario, they should effectively cancel out, and hinder sintering. Once higher energy isomers can contribute, the probability of reverse sintering is lessened slightly compared to the probability of forward sintering, by the presence of higher-energy isomers of both Pt_6 and the clusters of other sizes. This isomer-induced imbalance pushes the sintering process forward, yielding the differences in sintering rates between the GM, the Boltzmann, and particularly the isomer simulations (Figure 3.3a).

The sintering of Pt_5 (cluster of the Category 2) is a contrast to Pt_6. For Pt_5, the first step of sintering is energetically unfavorable. Despite this, the GM-only Pt_5 clusters sinter significantly faster than GM-only Pt_6 (Figure 3.3a,b), for which the first step is energetically favorable. While this appears as a paradox, it in fact emphasizes that "competing pathways" of sintering with other cluster sizes that build up in the early stages of sintering is an essential ingredient in the theory of sintering. The competing pathways for Pt_5 (Figure 3.4c,d) highlight the differences in the energetic balance of the forward and reverse sintering for Pt_5, versus those for Pt_6, for example. While the energetics of Pt_5 does not favor sintering at "step one", as soon as Pt_6 forms from Pt_5, further sintering of the system is energetically favorable. The reverse sintering of Pt_4 and Pt_6 with Pt_5 is favorable. However, cluster sizes further away from Pt_5, i.e. Pt_3, Pt_7, and Pt_8 do not tend to undergo reverse sintering with Pt_5, indicating that the overall balance is tipped in favor of sintering as a greater diversity of cluster sizes begins to build up. The inclusion of higher energy isomers, both for the initial, and all forming cluster sizes, tips the balance further in favor of sintering forward, hence

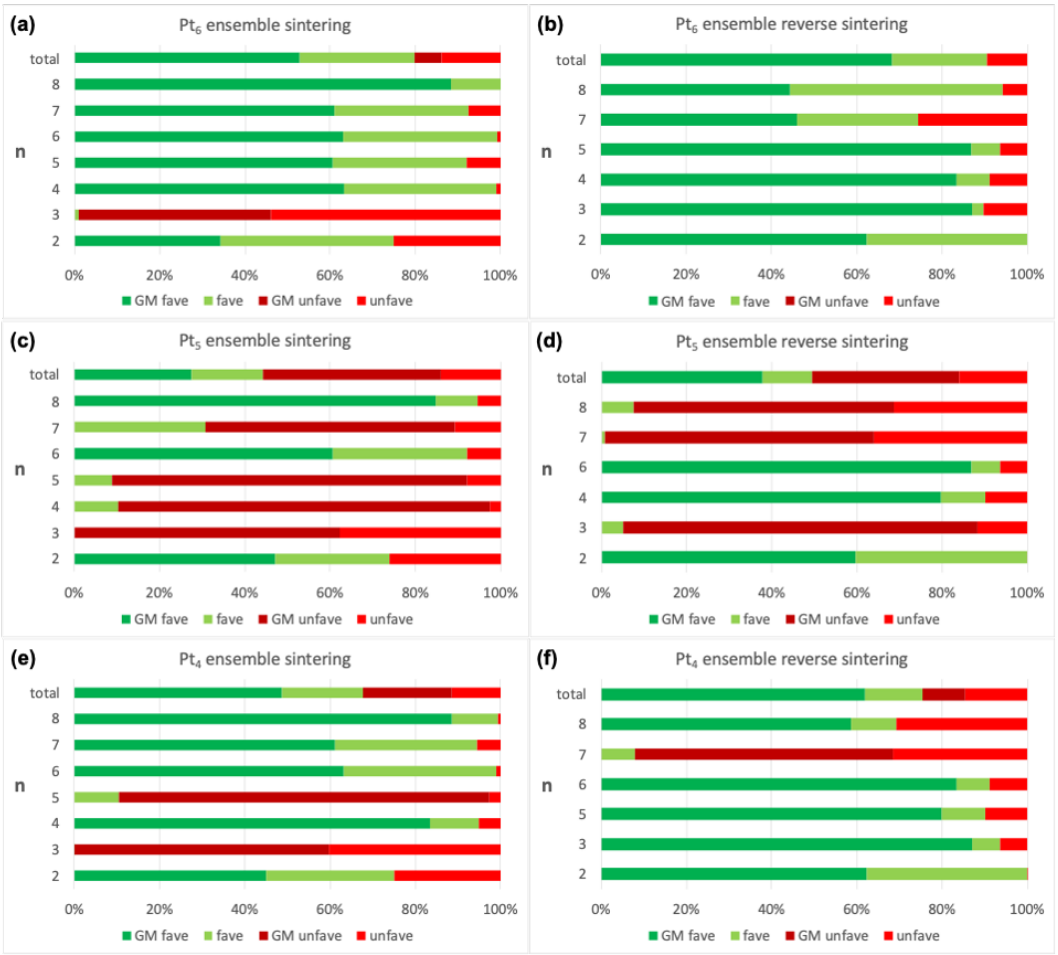

Figure 3.4: Favorability (in %) of (a) sintering and (b) reverse sintering of Pt_6 ((c) and (d) for Pt_5, and (e) and (f) for Pt_4) in the presence of Pt_n (n = 2–8) cluster (bottom to top row in each panel). Green and red indicate the proportion of thermodynamically favorable and unfavorable pathways respectively. The amount each possible pathway contributes to either case is scaled by the Boltzmann probability of the combination of isomers in the sintering process occurring together. The dark green or dark red indicates the GM contribution to favorable or unfavorable sintering, respectively. The data is based directly on the computed energetics of all possible sintering and reverse sintering pathways.

why the isomer and Boltzmann sintering proceed faster than GM-only sintering, and also why the monodisperse GM-only Pt_5 may sinter faster than the equivalent of Pt_6.

Finally, Pt_4 is a representative of Category 3, and is a case where there is a small difference between the GM and isomeric runs, and the overall process of sintering proceeds with an intermediate rate. In this case, the "step one" and the "competing pathways" justifications are both necessary to rationalize the sintering behavior. The Pt_4 sintering "step one" is energetically favorable for the GMs (Table 3.1), which on its own would suggest facile sintering for systems both with and without isomeric diversity. However, from the competing pathways (Figure 3.4e,f), one can see that sintering of Pt_4 with Pt_3 and Pt_5 (which would form during "step one") is unfavorable in the GM case. This results in a bottleneck in the sintering process; however, once either Pt_6 or Pt_2 forms in the system, Pt_4 sintering can proceed apace. When including higher energy isomers, however, this bottleneck is somewhat alleviated, as the sintering of some combinations of higher energy isomers is energetically favorable. Hence sintering with isomeric diversity proceeds at a slightly faster pace than without it, in this case (Figure 3.4e).

The cumulative size distributions in the ensembles of cluster states formed by the end of the sintering simulations are plotted in Figure 3.5. In general, the increase in isomeric diversity leads to the greater populations of larger, Pt_{8+}, clusters, and longer tails in the histograms toward larger nanoparticles. There is also a pronounced size-dependence. For example, for Pt_3, the most extreme case of Category 1, the final distribution for the GM-only simulations is dominated by a single peak at Pt_3, indicating an utter lack of sintering (red in Figure 3.5a). The Boltzmann-based sintering simulations, which are still overwhelmed by the GM of Pt_3, are very similar and produce only small, though non-negligible populations of larger clusters (green in Figure 3.5a). The isomer runs, which were isomer-diversified on purpose at the start of the simulation, in contrast, produce much more spread-out distributions, and a significant access to larger clusters (blue in Figure 3.5a). While the isomeric diversity introduced at the start in the isomer runs is can be considered artificial, it sug-

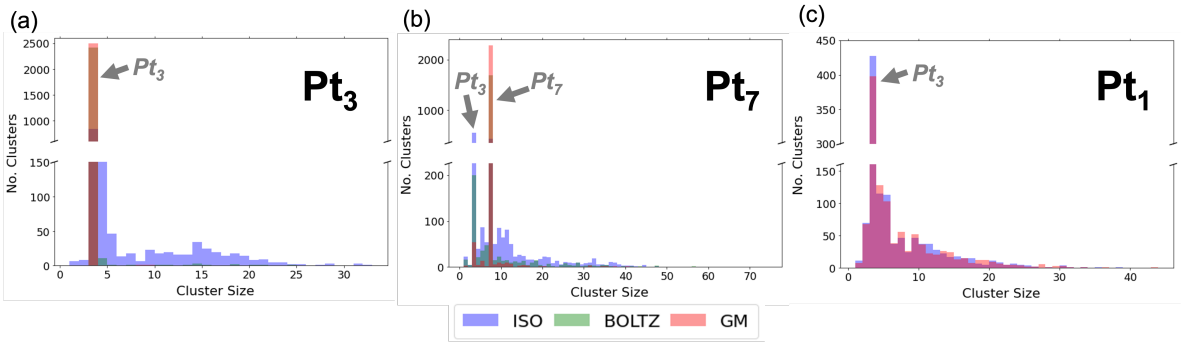

Figure 3.5: Cluster size distribution in the final MC step of the simulation of GM-only, Boltzmann, and isomer simulations for monodisperse $Pt_n/TiO_2(110)$ (n = 1, 3, 7).

gests that kinetic effects in cluster formation may further accelerate sintering to some extent. Overall, we see further evidence that Pt_3 is a "magic number" cluster, in its stability against sintering. This can be seen also from the energetics of sintering and reverse sintering (Figure B.7), and throughout Figure 3.4, where all the bars for sintering with Pt_3 are red. Generally, Pt_3 will not grow or be consumed, even by larger clusters.

Pt_7 is a more moderate case of Category 1, (Figure 3.5b), and interestingly, its sintering produces a double peak in the cluster size distribution, at Pt_3, and at Pt_7, as a testament to the stability of both cluster sizes. The relative heights of the peaks change with increasing isomeric diversity: while GM-only simulations result primarily in the intact Pt_7, isomeric diversity allows for the population of other cluster sizes, and in particular, produces a considerable amount of Pt_3. This is attributed to the stability of the GM of Pt_7 against sintering, and a much-reduced sintering stability of its higher-energy isomers. Notice that only 69% of the Pt_7/TiO_2 population is in the GM at 700 K (Figure 3.1). Some of the populated higher-energy isomers are significantly different in shape: they are quasi-single layer, i.e. flatter on the support. Notably, Pt_7 is the cluster size where all sorts of catalytic activities have been seen, from CO oxidation to ethylene dehydrogenation,[56, 136, 137] the latter being attributed mainly to the flatter higher-energy isomers. Also, accessible isomeric diversity leads to the population of diverse active sites, and may indeed be the origin of catalytic activity of supported Pt_7in a variety of reactions.

Finally, for the sintering of monodisperse Pt_1, there is virtually no impact from the inclusion of higher-energy isomers (Figure 3.5c). The behavior is also very similar for other clusters in Category 3: Pt_2, Pt_4, and Pt_5, (Figure B.6). As another measure of sintering rates, and confirming all the conclusions already made, the maximum and average cluster sizes as sintering progresses are plotted in Figure B.8.

The computed charges on all thermally accessible isomers of Pt_n (n = 1–8) clusters provide an electronic structure insight into the diverse sintering stabilities (Figure B.10). First, all clusters donate electrons to the support, larger clusters generally donate more as a whole (though the trend is non-linear), but less on the per-atom basis, and local minima generally donate less than their corresponding GMs (most of the times). In other words, as temperature increases, and local minima are introduced in the population, the ensemble-average positive cluster charge decreases. A differentiating effect is an intra-cluster charge separation, which is found only in Pt_3, Pt_7, and also in Pt_8 (Table B.1). Such a separation was previously proposed to be the cause of the experimentally seen sintering resistance of Pt_4Sn_3/SiO_2, [11] For Ptn/TiO_2, a possible reason for the "magic number" stability of Pt_3 and Pt_7 can therefore be proposed: A homolytic dissociation creating a neutral Pt atom on the support requires an electronic structure reorganization within the cluster, likely associated with a concurrent shape change, and thus, being energetically costly. Dissociating a Pt atom heterolytically from a polarized cluster (though not the possibility that we explicitly consider here) would obviously create a charged Pt monomer whose migration on the ionic support would be hindered. Hence, an electronic structure argument can be made in the in-line with our observations (Figures 3a, 5b).

3.3.2 Polydisperse systems

To elucidate the effect of the cluster isomeric diversity on the sintering of polydisperse systems, sintering simulations were performed for sample systems with clusters, $Pt_{1–5}$ (Figure 3.6) and $Pt_{2–7}$ (Figure B.9), and with the monomer composition of 10%, 25%, and 50%. Here

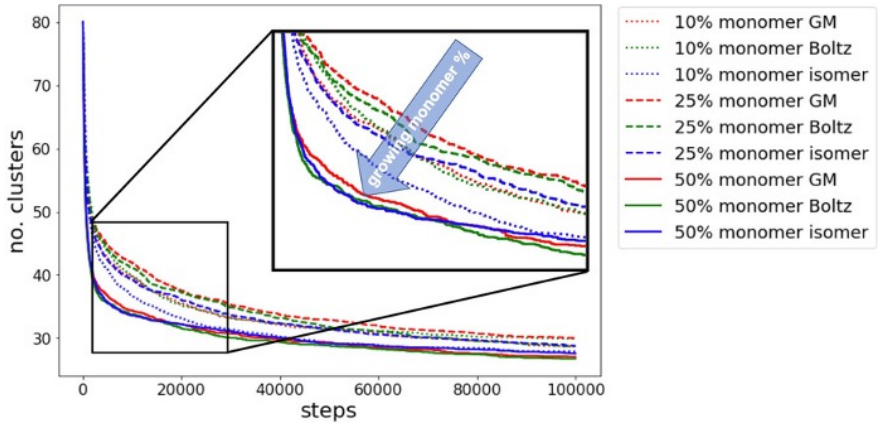

Figure 3.6: Sintering of polydisperse $Pt_{1–5}$ cluster systems, with varying amounts of included monomers: 10%, 25%, and 50%. GM, Boltzmann, and isomer setups are shown in red, green and blue, respectively. The inset highlights that the increasing concentration of the monomers accelerates sintering and in fact overwhelms the effect of the isomeric diversity in the ensemble of larger clusters.

again, an influence of the higher-energy isomers on the sintering rate is apparent (Figure 3.6), however, it is much smaller than for the monodisperse systems, and it is essentially erased at the highest monomer content of 50%. This is expected: since sintering is driven by the differences in surface energies, polydisperse systems are not immune to sintering from the start. Additionally, as the mobile Pt_1 is the natural driver of Ostwald ripening, and itself sinters rapidly (Figure 3.3b), its purposeful introduction produces but the expected result.

3.4 Conclusions

We showed that in the sub-nano regime, thermal Ostwald ripening of supported Pt clusters cannot be efficiently suppressed by size-selection. This is in stark contrast with larger size-selected nanoparticles. The effect is due to cluster structural fluxionality, which enables the thermal access to higher-energy cluster isomers, which have diverse surface energies. Different cluster sizes have specific isomeric distributions, with relatively more (or even significantly more) stable GMs, or instead a greater spread of the population toward the metastable minima. In addition, the GMs and metastable minima may or may not differ

significantly in their stability against dissociation, in order to produce monomers for Ostwald ripening. These effects create profound differences in how the isomeric diversity impacts cluster sintering for different cluster sizes. For example, we find that Pt_3 is a "magic number" cluster, which does not sinter quickly even with the assistance of its higher-energy isomers (because those are poorly-accessible). Pt_7 is next most stable cluster, though in this case the isomerization to metastable states is relatively easy, and to some degree facilitates the formation of Pt_3 again, and some other minority cluster sizes. $Pt_{2,4}$ sinter rapidly, etc. The sintering stabilities of specific species are linked to their electronic structure, and it appears that greater cluster-support charge transfer and intra-cluster charge separation are the stabilizing factors. The sintering acceleration role of cluster fluxionality and metastable isomers becomes less pronounced but still apparent in polydisperse systems. However, the large concentration of monomers (50% or more) can overwhelm the isomeric effect. Thus, the full thermal ensembles of metastable cluster states accessible to the system at catalytic temperatures (e.g. 700 K) has to be considered when assessing cluster sintering stability, or designing cluster catalysts that would be sintering-resistant.

The complexity of the sintering process for fluxional sub-nano clusters is encompassed in the proposed theory of "competing pathways", which accounts for the full spectrum of forward and reverse sintering steps, starting from a given cluster size, and all the accessible isomers at the start and along the process of sintering. This statistical atomistic model of the sintering process explains the apparent disparities in the sintering behaviors and strong cluster size-sensitivities.

CHAPTER 4

"Magic" Sinter-Resistant Cluster Sizes of Pt_n Supported on Alumina

4.1 Introduction

Sintering of subnano cluster catalysts is a serious limitation for their practical use. [17, 18, 20, 21] While subnano cluster catalysts exhibit unique size-dependent activity and selectivity, [19, 138, 139] along with superior atom efficiency, along with their ability to break past scaling relations, [3] their lack of stability with respect to sintering means that typically they rapidly deactivate compared to larger nanoparticles (NPs).[17, 18, 20, 140] As a result, they are unlikely to persist long enough under realistic reaction conditions to make use of their unique properties. The sintering of oxide-supported subnanoclusters is generally accepted to proceed via Ostwald ripening [23, 24, 140], where atoms detach from clusters, diffuse on the surface, and join other clusters. Because larger clusters tend to be more stable than small clusters due to higher metal-metal coordination, ripening leads to growth of larger clusters at the expense of small clusters. This is in contrast to the Smoluchowski ripening, which occurs by surface migration and coalescence of entire clusters. The thermodynamic driving force in both cases is the size dependence of surface energy, which decreases with increasing size. [141–143] Furthermore, it has been shown experimentally that for small NPs consisting of 68+ atoms, sintering is slower for a more monodisperse NP size distribution, compared to NPs with a broader size distribution. [25] because monodispersity minimizes difference in surface energy of the different NPs.

When considering subnanoclusters, with only a handful atoms, the situation is more complex because clusters can be fluxional, i.e., have multiple, interconverting, thermally accessible isomers witgh different energies. [4, 5, 144, 145] This means that even for a perfectly monodisperse cluster size distribution (e.g. only clusters of Pt_7), isomeric differences in the stability with respect to dissociation may still exist, providing the thermodynamic driving force for sintering. Thus sintering may not be suppressed by size-selection of fluxional clusters. The role of isomeric diversity in accelerating Ostwald ripening of monodisperse Pt_n/TiO_2 has previously been shown using a purely theoretical approach. [146] Interestingly, while isomeric diversity did broadly tend to accelerate sintering, size-dependent sintering behavior also became apparent. Some size effects arose due to particular stability of a cluster size, such as Pt_3/TiO_2, while others were due to the balance of forward vs. reverse sintering events (e.g., Pt_6/TiO_2). Ultimately, we predicted that certain "magic sinter-resistant" cluster sizes can arise, which should persist longer than other cluster sizes at catalytic temperatures. [146] The work, thus, suggests that the general trend of faster trend of faster sintering for smaller NPs is over-simplified when applied to subnano clusters. . In order to further explore this behavior, we adapted our approach to investigate Pt_n/Al_2O_3, both with experiment and theory. Size-selected clusters of $Pt_{1\text{-}7}$ were deposited alumina, and investigated with Ion Scattering Spectroscopy (ISS) before and after heating, to see if size-dependent sintering could be observed. We then assessed the size-dependent sintering behavior using our Metropolis Monte Carlo method. [146]

4.2 Experimental Methods

Size-selected Pt_n/alumina samples were preared using a cluster deposition instrument and protocols described previously. [19] Pt_n^+ were created by laster vaporization, guided through 5 stages of differential pumping, then mass-selected to produce beams of atomically size-selected clusters (Pt_n , n=1-7), which were guided into an ultrahigh vacuum system,

where they were deposited on alumina support. The alumina supports were ~ 5 nm thick films grown on Ta(110), using growth conditions previously shown to give films with hexagonal symmetry. [147, 148] We previously studied the effects of the alumina film thickness for Pt_n/alumina/Ta(11), finding that for films thicker than ~ 3 nm, the Pt and alumina core valence electronic structures, ISS intensities, and activity for a probe reaction (CO oxidation) were thickness-independent. [149] The total amount of Pt deposited on each sample was constant at 1.5 $\times 10^{14}$ Pt atoms/cm^2, corresp[onding to] 0.1 of a close-packed Pt monolayer. The only difference between the Pt_n/alumina samples was, thus, the size of cluster deposited. Low-energy He^+ ion scattering spectroscopy (ISS) was performed on the as-deposited samples, and after the sample had been flashed to 750 K. Each ISS experiment comprise a series of ISS spectra, allowing the intensities associated with scattering from Pt, Al, and O atoms in the surface layer to be monitored vs. exposure to the He^+ beam, which slowly sputters the surface. The Pt ISS intensities plotted below correspond to the average of the peak intensties in the first three spectra measured for each sample. To avoid complications from He^+ damage to the samples, the as-deposited and post-heating measurements were done on separate, freshly prepared samples.

4.3 Computational Methods

4.3.1 Global optimization

Global optimization for Al_2O_3-supported Pt_2-Pt_8 clusters was performed using our in-house code parallel global optimization and pathway toolkit (PGOPT), with a bond length distribution algorithm (BLDA) to accelerate sampling through the generation of chemically reasonable starting geometries. The calculations were performed with projected augmented wave density functional theory (PAW-DFT) with the Vienna Ab-initio Simulation Package (VASP) version 5.4.4. A plane-wave KE cutoff of 400 eV, a convergence parameter of 10^{-6} eV, and Gaussian smearing with a sigma value of 0.1 eV were used for the relaxation. The

geometry relaxation would proceed until the forces on all atoms are below 0.01 eVÅ^{-1}. We ensured a thorough sampling by starting with 200 structures, for each cluster size and optimizing more if there was fewer than 20% duplicates in the computed ensemble. The potential energy surface (PES) for Pt_1 on alumina was obtained by calculating the energy of a single Pt atom at each point on a fine 11×11 grid partitioning the unit cell. **The α-Al_2O_3 (0001) surface was modeled as previously, [19] as a (3×3) unit cell with four trilayers in the z-direction, and a 15 Å vacuum gap. The lower half of the slab was fixed to the bulk positions.** Since the latice is hexagonal, the shape of the unit cell is rhombic, with side of 4.840 Åand an angle of 120 degree. Hence, the shape of the mesh was also rhombic. Due to the large size of the supercell, only Γ k-point sampling was used. Once each cluster size was considered suitably sampled, the isomers within a 0.4 eV cutoff from the global minimum (GM) DFT energy were selected as the thermodynamically-accessible ensemble. The energies of these isomers were used in the metropolis Monte Carlo simulations of sintering. See the Figure 4.2 for the ensembles of $Pt_{2\text{-}8}$ isomers and their Boltzmann populations at 750K. Bonding analysis was performed using LOBSTER, using the PBEVaspFit basis set, with a projection basis of $5p5d6s$ for Pt, $3s3p$ for Al, and $2s2p$ for O. [150–152] Absolute charge spilling was under 1.1% for all calculations.

4.3.2 Monte Carlo Simulations

The 2-D Monte Carlo (MC) simulations were based on DFT-calculated cluster structures and energies. For Pt_2 to Pt_8, the energies of the clusters within 0.4 eV of the lowest energy structure were included, and the clusters were approximately represented as circles. The radii were set as the smallest circles in the xy plane encompassing the given cluster isomer, allowing for not only cluster sizes, but also the isomers to be distinguished. Note that Pt_8 was not chosen as a starting cluster size for the sintering simulations, to ensure that, for each starting cluster size, Pt_n, there exists an explicitly computed isomeric diversity of the size, $Pt_{n\pm1}$. For Pt_{9+} clusters, the energies and shapes were extrapolated based on the linear

function (Equation (1) and (2) as detailed in the SI). Monomer motion during the simulation was modeled during each MC step by choosing three cluster step sizes for three possible directions along hexagonal grids within a distribution of reasonable lengths for the monomer to hop. Each step size was on along the grid, so the monomer will only move randomly on the grid. If this location corresponded to the surface, the energy of the monomer was taken from the PES, and the energy change due to the monomer motion was computed as $Pt_n \rightarrow Pt_{n-1} + Pt_1$(PES). If the monomer landed on a cluster, the energy was calculated based on $Pt_n + Pt_m \rightarrow Pt_{n-1} + Pt_{m+1}$. In order to only explore the size-dependent sintering effects, as opposed to coverage effects, we controlled the cluster-cluster distance to be 5 Å for all sizes. 100 clusters were initially randomly deposited on the support in each case. As a result, the size of the Al_2O_3 supercell was varied with starting cluster size. It was chosen to be 18×18 primitive cells for Pt_1, 22×22 primitive cells for Pt_2, 24×24 primitive cells for Pt_3, 26×26 primitive cells for for Pt_4, 28×28 primitive cells for Pt_5, and 30×30 primitive cells of $\alpha-Al_2O_3$ for both for Pt_6, and for Pt_7.

The temperature of the simulations was 750 K, i.e., the maximum of the temperature ramp used in the experiment. Two types of MC simulations were run: "monodisperse", where all starting clusters had the same size, and "polydisperse", where the initial cluster size was allowed to vary. For the monodisperse case, the number of the Metropolis steps was chosen to be $n \times 100,000$, where n is the starting cluster size. This was done to give all cluster sizes an equal chance to be consumed during the simulations, as a minimum of n steps are required to consume one Pt_n cluster via Ostwald ripening. Thus, we can assume that the systems have been computationally sintered to similar levels of equilibration, and any differences in the sintering outcomes are due to fundamental differences in cluster stabilities. The monodisperse simulations were also performed with and without isomeric diversity, to assess the effect of the existence of metastable structures on sintering. [146] For brevity, we label these two types of simulations are labelled in this study as "Global Minimum (GM) only", and "Boltzmann Population (BP)", respectively. While particle migration and

coalescence are not simulated, we did account for cluster coalescence that occurred when clusters grew enough to overlap, without changing center of mass. Further details of the simulations are provided in Appendix C Algorithm 1 and Algorithm 2.

4.4 Results and discussion

4.4.1 Experimental detection of cluster sintering

Because of a combination of shadowing, blocking, and low ion survival probability, [153, 154] peaks observed in low-energy He^+ scattering (ISS) primarily result from the scattering of He^+ from single atoms in the top-most sample layer. [155] Scattering from subsurface atoms primarily contributes to a broad background signal,as do multiple scattering events. Thus, for samples of Pt_n clusters deposited on alumina, all of which containing the same total number of Pt atoms, the intensities of the Pt ISS peaks reflect the fraction of Pt atoms exposed in the surface layer. For cluster isomers with a single layer on the support, the Pt ISS intensities should be high, but if multi-layer isomers or structures are present, the intensity would be reduced, as only the topmost layer is efficiently detected. [156]

Figure 4.1 plots the Pt ISS intensities for samples of $Pt_{1\text{-}7}$/alumina before and after ramping the temperature to 750 K at 3 K/sec to drive sintering. The intensities are the Pt peak intensities, normalized to the sum of the Pt, Al, and O peak intensities, compensating for any small day-to-day variations in ISS detection sensitivity. As noted, separately prepared samples were used for the "before" and "after" samples, to avoid the effects of He^+ beam damage on the "after" data.

The spectra measured before heating (never heated above room temperature) it can be seen that the Pt intensities increase from Pt_1 to Pt_3, are constant within the ~ $\pm 5\%$ uncertainty from Pt_3 to Pt_6, then decrease for Pt_7. For clusters of just a few atoms, we expect that all the Pt atoms should contribute to the ISS signals, unless the Pt is in clusters large enough that some fraction of the atoms are in a second layer, reducing the detection

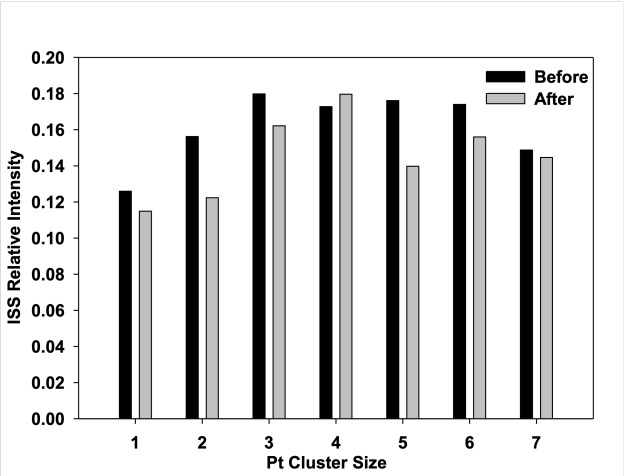

Figure 4.1: Initial ISS intensity before (black) and after (grey) heating to 750K with cluster size.

sensitivity for underlying atoms. Thus, we interpret the constant ISS signal for $Pt_{3\text{-}6}$ as indicating that these clusters have single-layer structures in which all the Pt atoms are exposed in the surface layer. The decrease at Pt_7 is attributed to the beginning of the transition to multi-layer cluster geometries, expected for larger clusters. [156] Note that supported clusters in this size range can have multiple isomers, and ISS averages over the isomer population. The significantly lower Pt ISS intensities for Pt_1 and Pt_2 suggest that significant formation of multi-layer structures occurs even before heating. For Pt atoms, this clearly indicates that diffusion and agglomeration must have occurred prior to heating, and it is not surprising that supported atoms might sinter easily because diffusion requires breaking no Pt-Pt bonds and fewer Pt-support bonds, than in larger clusters. Indeed, we typically observe that deposited atoms sinter readily, resulting in significantly lower ISS intensities, compared to samples prepared with clusters. The observation that the Pt ISS intensity for the as-prepared Pt_2/alumina sample is also somewhat lower than for the $Pt_{3\text{-}6}$/alumina samples suggest that some sintering occurred for dimers as well.

After heating to 750 K, the intensities for Pt_1 and Pt_2 decreased, more so for Pt_2, such that the two samples had similar intensities, indicating that multilayered clusters formed in both cases. This shows that 750 K heating led to further sintering, which was more

apparent for Pt_2, presumably because the Pt_1 sample was already substantially sintered prior to heating. Pt_3 showed a ~ 8% decrease in Pt intensity, indicating either a small amount of sintering, or thermal isomerization took place, resulting in Pt atoms with low ISS detection sensitivity. For Pt_4, 750 K heating led to a ~ 2% increase in Pt intensity, well within the uncertainty, but for Pt_5 the intensity dropped by ~ 20% - well outside the uncertainty. Pt_6 also showed a small heating-induced decrease, consistent with either a small degree of thermal sintering or thermal isomerization to more compact isomers. Finally, for Pt_7, which had some multi-layer isomers present before heating, there was no significant change. These data clearly show size-dependent sintering behaviour, and varying stabilities, which will be addressed below.

4.4.2 Magic Sinter-Resistant Cluster Sizes

To assess the size-dependent sintering behavior of $Pt_{1\text{-}8}/Al_2O_3$, we prepared 8 different simulations as described in the Computational Methods section. The GMs and thermally-accessible structures of the clusters at 750 K are shown in Fig. 4.2. Since our sintering code is based on Metropolis Monte Carlo, instead of kinetic Monte Carlo, we cannot directly access timescales from our simulations. However, we can analyze the final distribution of cluster sizes after some duration of the simulation, to see whether any cluster sizes persist, indicating particular thermodynamic stability. Select final cluster size distribution histograms for different initial sizes are shown in Fig. 4.3, and the rest can be found in the Fig. C.3. For initial cluster sizes Pt_2 (Fig. 4.3a), or Pt_4 (Fig. 4.3b), the final cluster size distribution is dominated by Pt_4. This suggests that Pt_4 is a particularly stable cluster size; Pt_2 sinters to form primarily Pt_4, and Pt_4 exhibits little sintering. This result is consistent with the experiment ISS results, which show that Pt_2 sinters significantly, whereas Pt_4 is essentially unaffected by 750 K heating. The final size distribution for Pt_7 initial size (Fig. C.3) is dominated by Pt_7; Pt_7, like Pt_4, is particularly resistant to thermal sintering. The exceptional stability of Pt_4 and Pt_7 can also be seen by examining the final size distributions for

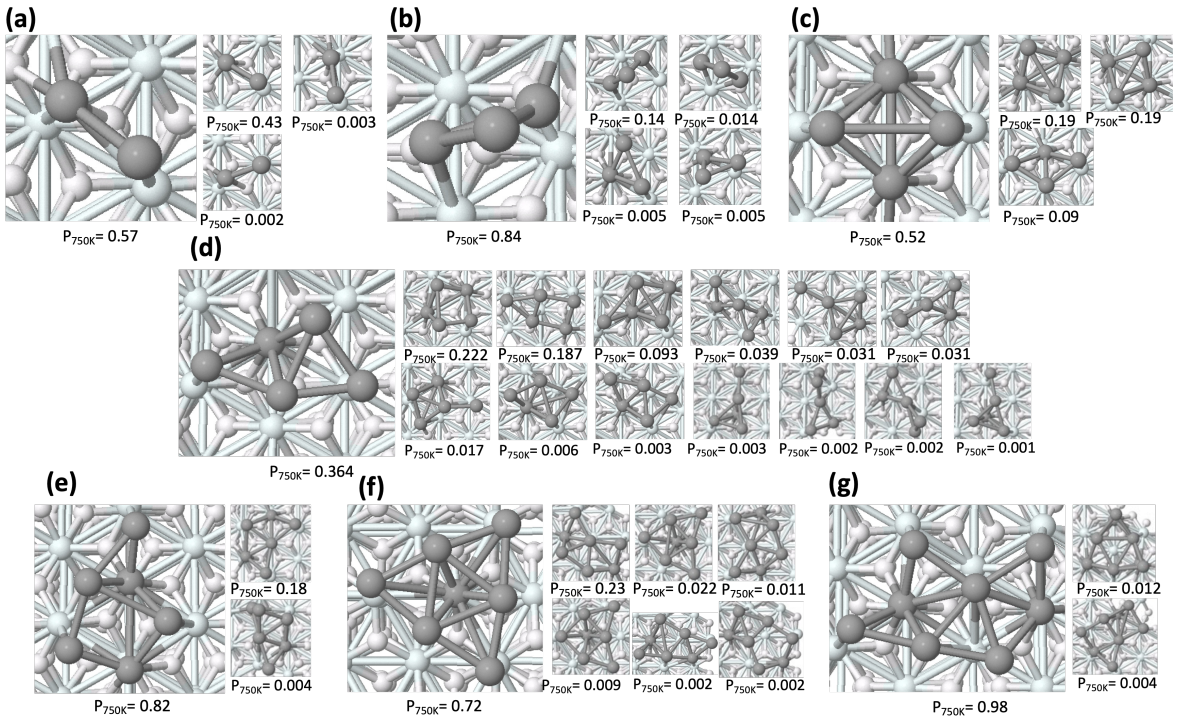

Figure 4.2: Ensembles of Pt_2-Pt_8 isomers and their Boltzmann populations at 750K.

simulations starting with Pt_5 (Fig. 4.3c) or with a distribution of initial cluster sizes (Fig. 4.3d). In both cases, a variety of final sizes formed, however the distributions are dominated by Pt_4 and Pt_7. Clearly, when either are present, either as the initial size or formed by sintering, they tend to persist. This persistence regardless of the starting point of the sintering simulation indicates that these two cluster sizes exhibit particular stability in the Ptn/Al_2O_3 system. In contrast, for TiO_2-supported Pt clusters, Pt_3 and Pt_7 were identified to be sinter-resistant, using the approach previously termed "competing pathways", which we now apply to this system. [146]

4.4.3 Competing Pathways of Sintering

The "competing pathways" formalism is based on the thermodynamics of all relevant steps involved in sintering of a particular cluster size. The energetics of the monomer move-

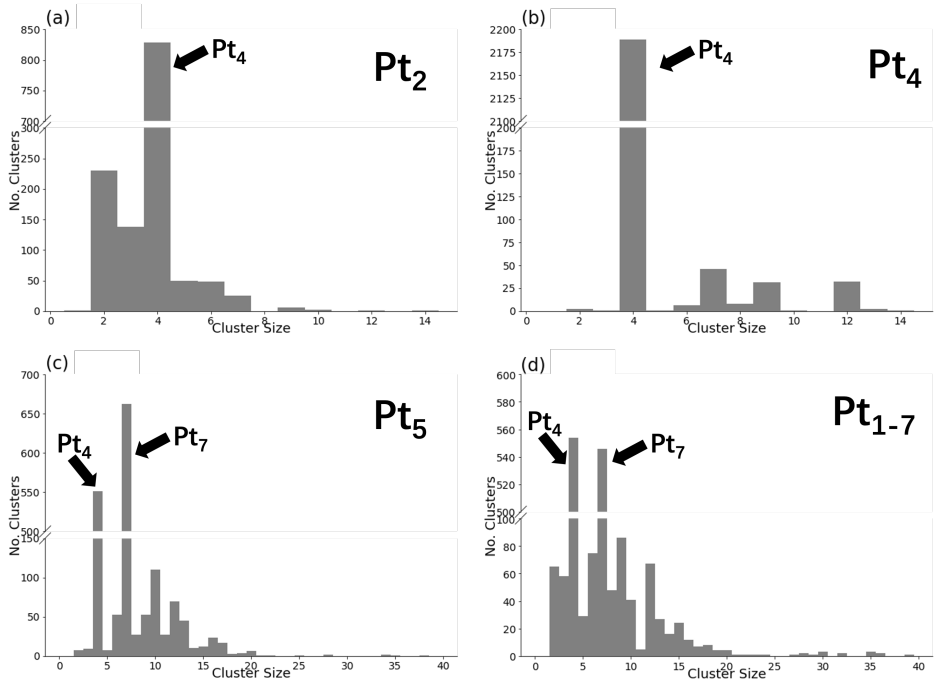

Figure 4.3: Final cluster size distributions resulted from the sintering simulations that started from the (a) Pt_2, (b) Pt_4, (c) Pt_5, and (d) random cluster size distributions. Note that major peaks for Pt_4 and Pt_7 form regardless of starting point, indicating the remarkable stability of these cluster sizes.

ment between different cluster sizes and all their accessible isomers are calculated to assess thermodynamic (un)favorability of such Ostwald ripening steps. It is essential to consider the energetics of monomer migration between all cluster sizes, as they build up and participate in sintering, rather than simply considering said energetics only between the initial, size-selected clusters. The persistence of a given cluster size throughout the sintering process is determined by the energetic relationship between the isomers of a given cluster size and those of all other cluster sizes.

Figure 4.4 a, b shows the ensemble energetic driving force for forward and reverse sintering steps, respectively. Forward sintering refers to the movement of monomers from small to large clusters, while reverse sintering refers to the movement of monomers from large to small clusters. For each cluster size in Figure 4.4, we consider the energetics of monomer transfer between the isomers of said cluster size, and all isomers of all other cluster sizes. We then

calculate the energy difference, and weight it by the probability of the given combination of isomers occuring, based on their Boltzmann populations, which is then normalized by the number of Pt atoms in the cluster. This is represented by the magnitude of the bar in Figure 4.4, split into unfavorable (red, positive, preventing sintering), and favorable (green, negative,driving sintering) contributions. For a breakdown of each cluster size combination, and how we obtained the ensemble-averaged energy values, see Supplementary Note Analytic Methods.

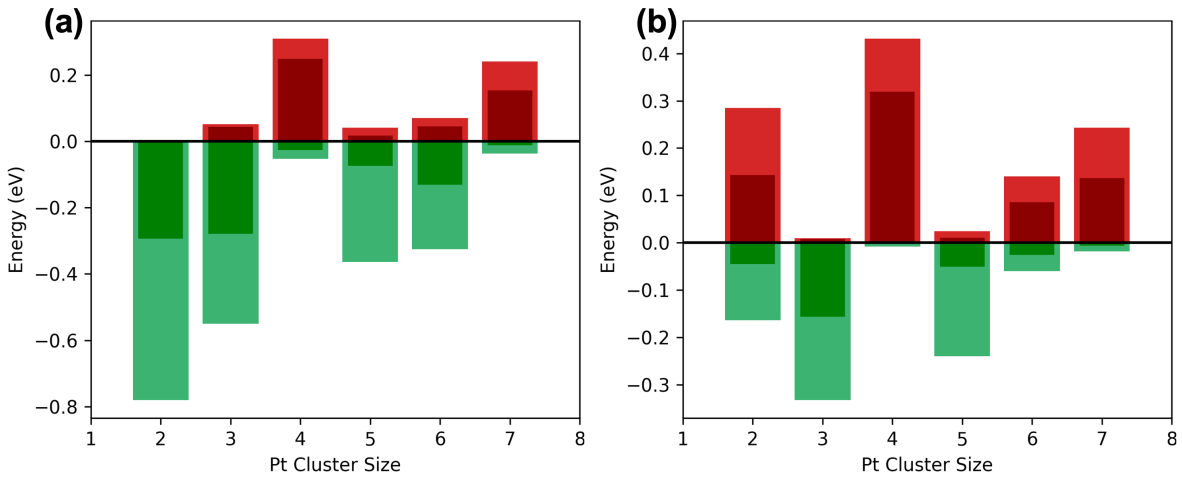

Figure 4.4: Sintering energetics for (a) forward and (b) reverse sintering as a function of Pt cluster size. The red and green bars represent the ensemble-averaged energetics of unfavorable and favorable cluster combinations undergoing monomer transfer, respectively. The dark green and dark red indicates the fraction contributed by only GM combinations of isomers.

Figure 4.4a shows that for all Pt_n, except for Pt_4 and Pt_7, forward sintering (forming larger clusters) is favorable, while Figure 4.4b shows that reverse sintering (forming smaller clusters) is generally less favorable, but again is particularly unfavorable for Pt_4 and Pt_7. The energetics predict that these two cluster sizes should be particularly stable with respect to both shrinking and growth. This explains the prevalence of Pt_4 and/or Pt_7 peaks in Figure 4.3, and is consistent with the experimental finding that neither Pt_4 and/or Pt_7 show significant changes in the Pt ISS intensity when heated, whereas all the other sizes show

change, consistent with net cluster growth. Since monomer motion between Pt_4 and Pt_7 and most of the other cluster sizes and isomers is energetically unfavorable, both cluster sizes build up regardless of the cluster size composition of the starting point of the Monte Carlo simulations. Hence, in the absence of adsorbates, these two cluster sizes are "magic" in the sense of resistance to thermal sintering. Note that in the experiments, the lowest final ISS intensities were for Pt_1 and Pt_2, suggesting that they sintered to particularly large multilayer structures, whereas larger clusters such as Pt_5 or Pt_6 also sintered, but with a larger fraction of the Pt atoms remaining in the top-most layer, i.e., forming fewer or smaller multilayer clusters. This propensity of the smallest Pt_n to sinter to larger final cluster reflects the relative instability of atoms (and dimers) with respect to diffusion on the surface. Note that monomer motion on the support was explicitly accounted for in our MC simulations, however motion of larger cluster sizes was not.

Beyond the "magic" sinter-resistant cluster sizes, we can use the competing pathways formalism to understand different types of sintering patterns. Figure 4.4 suggests that Pt_2 and Pt_6 should have the same patterns of sintering; monomer movement from smaller to larger clusters involving Pt_2 and Pt_6 is very favorable, while the reverse is not. Thus, they can easily be consumed in the sintering process, and would not contribute to any suppression of overall sintering due favorability of the reverse sintering processes. Pt_3 and Pt_5 also share a similarity: both forward and reverse sintering are favorable, though forward sintering is more so. Thus, these clusters would tend to have a lower apparent driving force for sintering compared to Pt_2 and Pt_6, as they both grow and shrink, passing through Pt_5 along the way, on average keeping the starting size of Pt_5 for longer. More details of Favoribility (in percent) of reverse sintering and ensemble sintering for each cluster size are in Fig. C.2.

4.4.4 Bonding Analysis

The fundamental origin of the Pt_4 and Pt_7 thermodynamic stability is rooted in their physical and electronic structure. From a simple visual inspection of Pt_4 and Pt_7 isomers in

Figure 4.2, we see that the GM structures for these two cluster sizes are much more crystalline than the other cluster sizes. Furthermore, there appear to be more under-coordinated Pt atoms in Pt_5 and Pt_6 compared to Pt_4 and Pt_7. For a quantitative investigation of the Pt-Pt and Pt-support bonding, we used the LOBSTER program [150] to obtain the ICOHP [151] values for relevant atom pairs. The ICOHP values are then used to classify Pt-Pt and Pt-support bonds as strong and weak, and to count them (Figure C.4). What we find is that Pt_4 and Pt_7 GM structures have more bonds per Pt atom than any other cluster size and isomer, meaning that in gaining or losing an atom, the total number of bonding interactions would decrease. Interestingly this comes from different contributions; for Pt_4, many of these bonds come from interactions with Al and O atoms of the support, while for Pt_7 it is mostly with other Pt atoms. We can also see the interplay between Pt-Pt and Pt-support interactions in the structures- more planar structures that interact more with the support have more negative ICOHP values for Pt-support interactions (Figure C.5). Thus, the unique stability of Pt_4 and Pt_7 arises from the regular, crystalline nature of their GM structures, which is reflected both in the number of Pt-Pt bonds and strong bonding with the support. We note that in our previous study [146] of size-specific sintering of Pt cluster on rutile TiO_2, Pt_3 and Pt_7 were predicted to to feature particular sintering resistance. We attribute the difference to the interaction with the support oxygen atoms, which favor the backing of the cluster structures most resembling the bulk at the different cluster sizes for these two supports.

The spatial information about the sintering processes features a contrast between different cluster sizes. We evaluate this at the end of sintering simulations. Examples for Pt_2-Pt_7 are shown in C.6. For Pt_2 and Pt_3, a greater diversity of cluster sizes has accumulated, and there are many gaps between clusters as some have been entirely consumed. While Pt_4 and Pt_7 dominate the sintered size distributions, there is a wide range of cluster sizes present, indicating that sintering has taken place without spatial preference. In contrast, when starting from the particularly stable cluster sizes, Pt_4 and Pt_7, most clusters remain

unchanged, with what sintering took place remaining highly localized, forming a few larger and smaller clusters, but leaving most of the system intact. In other words, there were a few very localized regions with high sintering activity, reflecting nucleation-like behavior. For Pt_5 and Pt_6, where the starting cluster sizes are between two particularly stable cluster sizes, we see a different sintering regime. Here, sintering starts everywhere on the surface, but as Pt_4 and Pt_7 clusters form in the process, they hinder further sintering. This could be considered "reverse nucleation", where eventually sintering is restricted to some areas with a greater range of cluster sizes, not because that was where sintering initially began, but because that is where enough cluster size diversity remains to drive sintering. This gives us potential signatures to look for experimental systems of size-selected clusters or nanoparticles, when attempting to identify if a cluster size is stable or not; a stable cluster size would show overall little change, aside from some locations where much larger nanoparticles formed, while less stable cluster sizes would exhibit a much broader cluster size distribution throughout the sintering process.

4.5 Conclusion

In conclusion, we have presented experimental and theoretic evidence for the existence of sinter-resistant cluster sizes for $Pt_{1\text{-}8}/Al_2O_3$. Pt_4 and Pt_7 were predicted to not only be particularly stable against sintering from a monodisperse cluster size starting distribution, but were also shown to persist even when (a) not initially present in the monodisperse cluster size distributions and (b) when sintering starts form a mix of initial cluster sizes. This was validated experimentally using ISS before and after heating to 750 K. The stability of these clusters is attributed to the ensemble energetics of forward vs. reverse sintering. For both Pt_4 and Pt_7, the energetics of monomer movement to and from other cluster sizes is generally energetically unfavorable. Therefore, even in a system with multiple cluster sizes, which should therefore generally have a strong driving force for sintering, we see Pt_4 and

Pt_7 persist in our simulations. This stability is furthermore attributable to the particular geometric and electronic structure of the global minimum Pt_4 and Pt_7 isomers, which are much more crystalline than clusters of other sizes, with a greater number of bonds per Pt atom than all other cluster sizes and isomers.

While these sinter-resistant sizes are specific to the Pt_n/Al_2O_3 system, the general conclusions that (i) sintering of subnano cluster is a size-dependent phenomenon, (ii) there are "magic numbers" of sintering stability, (iii) sintering is driven by the entire ensemble of thermally-accessible isomers, with metastable states driving sintering and (iv) several spatial regimes of sintering (global, nucleation-like, mixed) exist which can be used as signatures of cluster sintering stability in experiment. These key findings should remain valid for many systems, as we have already shown the existence of sinter-resistance size dependence for a different support. [146] Identifying cluster sizes that may persist under reactions conditions is essential, as it can be used to target them as potential active sites, either through direct synthesis, or by their formation during reaction. While systems under catalytic conditions will have bound adsorbates, we expect these general findings to hold, and will address the role of adsorbates on sintering in future work.

CHAPTER 5

Interpreting *operando* XANES of Supported Cu and CuPd Clusters in Conditions of Oxidative Dehydrogenation of Propane: Dynamic Changes in Composition and Size

5.1 Introduction

Operando XANES is a powerful technique for tracking compositional changes of supported subnano-clusters since it is sensitive enough to track changes during the actual reaction process without disturbing the reactivity of the system. [157–159] Furthermore, since XANES is sensitive to the local environment of the atoms being probed, it can be used to investigate very small clusters dispersed on a substrate with a high degree of accuracy and low signal to noise ratio.[160, 161] XANES is sensitive to the oxidation state of the system, and can therefore provide detailed chemical information even at a low loading of the active species.[161] Specifically, as the species becomes oxidized, the XANES rising edge energy shifts to higher energies due to the reduced shielding and greater electron-nuclear attraction, providing valuable information about the state of the system in situ. Additionally, with approaches such as Linear Combination Fitting/Analysis (LCF/LCA) and Principal Component analysis (PCA), the changes in the spectra can be translated into the changes of the fraction of different components in the system as well as the presence of active sites, as a function of, e.g., reaction time, or reaction conditions.[162, 163]

Operando XANES has been used for quite some time now, for example, for determining active species[158] and subtle changes due to catalyst irradiation[164] in electrochemistry, [162] and for tracking nanoparticle agglomeration. [165, 166] More recently, analysis types such as LCA and PCA began to be used to extract composition information from a basis set of single-component XANES standards, for example, the approach has been used to evaluate average oxidation state of the metal in metal clusters in reaction conditions.[167, 168] Furthermore, using machine learning (ML) techniques, specific structural information can be extracted from experimental XANES and EXAFS spectra,[166, 169, 170] though EXAFS is less useful for subnano clusters, due to their low loading on flat supports and thus poor signal to noise ratio.

Previously, we have shown that more precise fits of *operando* XANES spectra of supported subnano clusters can be realized using computed cluster standards, rather than the traditional bulk standards.[171] Small clusters are both disordered, and dynamic, in terms of their structure and composition,[51, 52, 111] and may thermally populate multiple isomers in reaction conditions,[51–57, 111] which can substantially contribute to the *operando* XANES signal. In view of this complexity, the small size effects, and the interactions with the support, the bulk standards represent a limited basis for these clusters. We previously showed that while bulk copper oxides have higher rising edge energies with increasing oxidization, the same trend does not hold for the global minima of surface-supported clusters computed with DFT; in fact the rising edge can vary significantly between isomers of the same cluster composition, highlighting the crucial role the specific local environment of the cluster plays in determining the XANES spectrum of subnano clusters.[171] Based on these results, we proposed that a better way to interpret the *operando* XANES of small, fluxional nanoclusters would be to do a global optimization of the cluster in question with varied oxygen contents, and then use these cluster standards to fit the experimental spectra.

We apply these techniques to supported Cu_4 and Cu_3Pd clusters, which are potential candidates for the catalytic hydrogenation of CO_2 to alcohols,[172] oxidative dehydrogenation

of hydrocarbons,[173]and electroreduction of CO_2.[174] Our study addresses these clusters in conditions of oxidative dehydrogenation of propane[175] using O_2 as an oxidant, with the O atom adsorbates coming from O_2 dissociation, and hydroxyl groups coming from water dissociation (water is a product from the oxidative dehydrogenation of propane). The *operando* XANES used in this study were collected during the corresponding temperature programmed reaction (TPRx).[171, 175] We test the various ways in which the experimental *operando* XANES could be fitted and propose to use both bulk and cluster standards to get a more realistic interpretation of the evolution of the clusters in reaction conditions. In contrast with how agglomeration has previously been monitored via application of machine learning,[166] where the agglomeration was tracked via differences in predicted NP size via interatomic distances and coordination numbers extracted from XANES with a neural net approach, and experimental GISAXS, or through analysis of EXAFS, [165] here we show that, through fitting of the experimental spectra with both bulk and cluster standards, we can track the growth of the bulk fraction as well as the changes in composition/oxidation state as the temperature changes.

5.2 Methods

Cu_3PdO_x (x=2-5) and $Cu_3PdO_y(OH)_2$ (y=1,2) cluster structures were obtained via global optimization using the in-house PGOPT code.[120] This code uses the Vienna Ab Initio Simulation Package[114, 115, 176] to perform the DFT local optimizations, using a plane-wave basis set, the projector-augmented wave method[118] and the PBE functional.[70] The geometry optimization was performed with a plane-wave kinetic energy cutoff of 400 eV, and a convergence criteria of 10e-5 (10e-6) eV for the ionic (electronic) steps. Gaussian smearing with a width of sigma=0.1 eV was used. In order to better model copper, we used DFT+U,[177] with the U value of 7 eV, as benchmarked in a previous paper.[178] The surface used was a partially hydroxylated amorphous Al_2O_3 that was optimized during a

previous study.[179]

XANES spectra of the relevant structures were calculated using the finite difference method (FDM) and the Hedin-Lundqvist exchange-correlation potential implemented in the FDM Near Edge Structure (FDMNES) ab initio package.[180, 181] FDMNES works in real space, and builds a cluster of a specified radius (we used 6Å) around the absorbing atoms of interest, after which the absorption spectra in the specified energy range are calculated for each non-equivalent absorbing atom and then combined. The XANES spectra of the bulk standards were computed using the structures from the materials project (structures shown in Fig. D.1).[182] The computed XANES spectra were normalized and used as standards for LCF of the experimental spectra at different temperatures, using the Athena software.[183] The experimental spectra referenced have been previously published.[175] LCF was performed for energies between -20 and 20 eV around the white line peak.

The quality of each LCF, denoted R-factor, was determined using the following equation:

$$R = \frac{\Sigma(\text{data - fit})^2}{\Sigma(\text{data})^2}$$

Where the sum is over all the fit and data points within the specified energy range for the fit. Note that this is absolute deviance over the entire energy range, agnostic of the regions of the deviation. Thus, fits with similar R-factors might show deviations in different parts of the spectra. Furthermore, as LCF is done with least squares minimization in Athena it is important to note that the solution is not necessarily unique, and can/will depend on the basis set of standards

5.3 Results and Discussion

5.3.1 *Operando* XANES in conditions of oxidative dehydrogenation of propane

The *operando* XANES for the Cu K-edge of Cu_3Pd/Al_2O_3 were collected under reaction conditions for the oxidative dehydrogenation (ODH) of propane, during TPRx (Figure 5.1). The spectra were collected during heating from 25 °C to 550 °C (solid lines), and then cooling down to 25 °C (dashed lines). A distinct change throughout heating and cooling can be seen, where the initial XANES at 25 °C has a small pre-edge peak, and has very little shoulder, with a fairly sharp white line peak. As the system is heated to 550 °C, however, a shoulder in the rising edge develops. This shoulder does not go away after subsequent cooling, suggesting that some irreversible change has happened relative to the initial spectrum. The spectra for

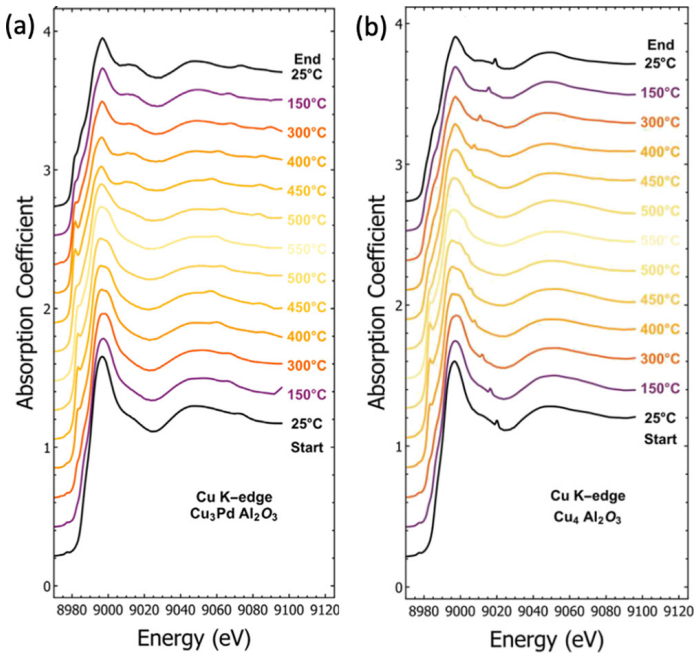

Figure 5.1: The normalized *operando* XANES for (a) Cu_3PdO_x/Al_2O_3 and (b) Cu_4O_x/Al_2O_3 (reproduced with permission from [175]) obtained by experiment during a heating and cooling cycle showing the changes in the spectrum as a function of temperature (in °C). The intensity of each spectrum after 25 °C is offset for clarity

the Cu_3Pd/Al_2O_3 and Cu_4/Al_2O_3 clusters have been published previously,[171, 175] and are

reproduced with permission in Figure 5.1b. Our approach towards interpreting these spectra differs from that of Ref [175], whose principle component analysis approach for determining the primary components of the experimental spectra involves no inherent chemical meaning. Ours on the other hand is based on the chemical species that could reasonably be considered present. Therefore the conclusions that we draw are informed by chemical reality.

5.3.2 The choice of standards for interpreting *operando* XANES

In order to interpret the spectra in Figure 5.1, we performed global optimization of Cu_3PdO_x and $Cu_3PdO_y(OH)_2$, supported on alumina, with varying the oxygen content for non-hydrated clusters between 2 and 5 atoms per cluster, as was the range determined previously.[171, 178] Water produced by the reaction has a small partial pressure at low conversion considered here, but can nevertheless thermodynamically result in adsorption of one H_2O molecule, leading to the $Cu_3PdO_y(OH)_2$ structure with y=1 or y=2. The resulting global minimum (GM) structures for each composition are shown in Figure 5.2. We used these structures to compute the XANES spectra. Using them as the computed cluster standards, we fit the experimental spectra from Figure 5.1, and the results are shown in Appendix D (Figure D.2). Note that using the GM structures (as opposed to averaged XANES of all of thermally-accessible isomers) as the standards is sufficient because the GMs completely dominate the averages, since their Boltzmann populations are 94 - 99.9%. The one exception to this is $Cu_3PdO_2(OH)_2$, where the GM represents 60.6% of the ensemble at 500 °C, the first local minimum (LM1) is 36.3%, and LM2 is 2.3% (structures shown in Figure D.3). However, we still only used the GM structure in the fits because (a) the GM and LM1 spectra are not as significantly different, and (b) the spectrum Boltzmann-averaged over GM, LM1, and LM2 is minimally different to the GM-only spectrum. We also did the full spectrum fit using the Boltzmann-averaged spectrum and found only minute differences (SI figure D.4), especially because the presence of the $Cu_3PdO_2(OH)_2$ composition in the fit is minute at all temperatures, regardless of whether or not we used the Boltzmann-averaged standard.

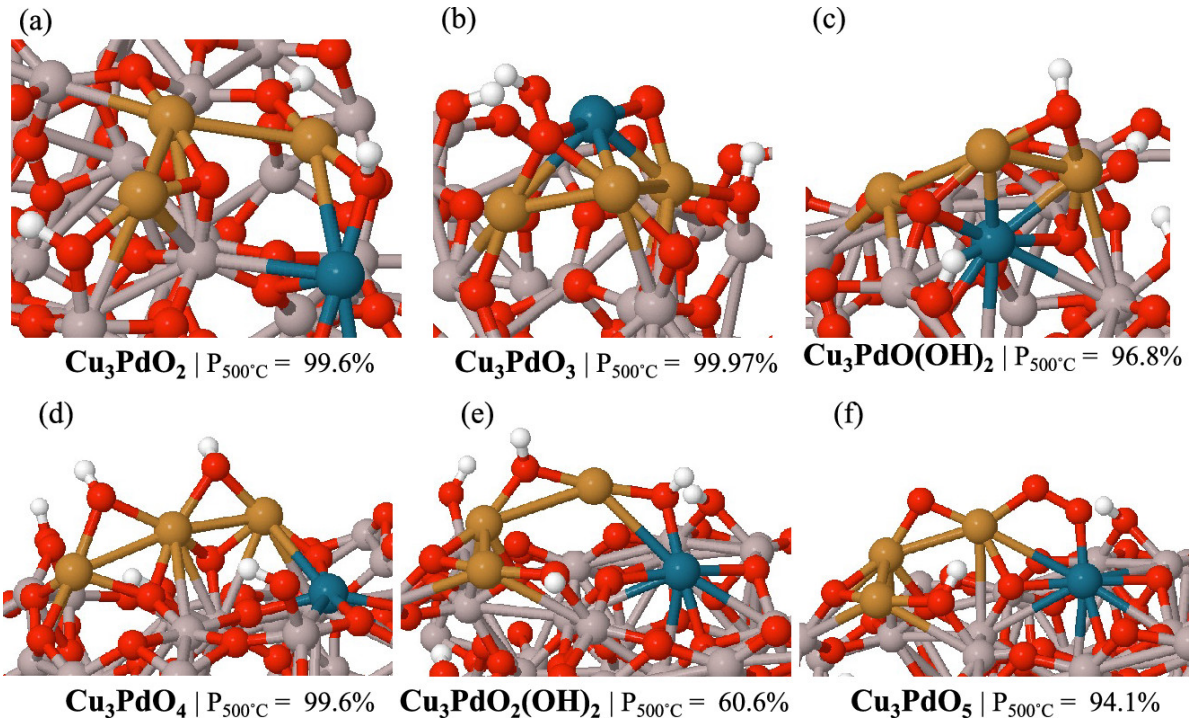

Figure 5.2: The GM structures of (a) Cu_3PdO_2, (b) Cu_3PdO_3, (c) $Cu_3PdO(OH)_2$, (d) Cu_3PdO_4, (e) $Cu_3PdO_2(OH)_2$, (f) Cu_3PdO_5. Note that these compositions correspond to the cluster added to the support and sampled, whereas the actual oxygen content/oxidation state of the Cu can deviate due to the interactions with the hydroxylated alumina oxide support, with possible proton migration from the support to the cluster, as seen for example in d. Cu shown in brown, Pd in dark blue, H in white, Al in grey, and O in red.

The computed XANES of the clusters from Figure 5.2 are shown in Figure 5.3a. The XANES for the Cu4Ox structures of our previous publications[171, 178] (structures shown in Figure D.5), and of the computed bulk relative to experimental bulk where available[184] are shown in Figure 5.3b,c. Notice the very good performance of the computational methodology for the bulk XANES compared to experiment (Figure 5.3c) There have been a number of studies where the experimental XANES of Cu and other complexes have been well-replicated by theory, indicating the power of the approach.[185–189] For the most part, experimental spectra can be well-reproduced with FDMNES, especially when using the FDM for smaller complexes lacking significant second-shell contributions and higher symmetry, which describes our Cu_3PdO_x and Cu_4Ox clusters quite well. [185, 187] There are some limitations

to the computational spectra, including slightly off relative intensities of peaks and overestimation of sharpness[186, 190] however we do not consider these significant compared to the error introduced by fitting a spectrum with inappropriate spectra. The computed spectra in Figure 5.3 constitute the basis set of standards that we use in LCF of the experimental spectra in Figure 5.1. A file with all of the spectra in Figure 5.3 is provided as part of the SI, including both the computed standards, and comparison to experimental spectra. Initially, we considered only computed XANES spectra of supported clusters for the standards (see Appendix D for all of the fits), however we found that, upon adding the bulk standards, the fits were highly improved. Notice also that using only the cluster standards produces considerably worse fits (Table D.1 vs Table D.2 in Appendix D).

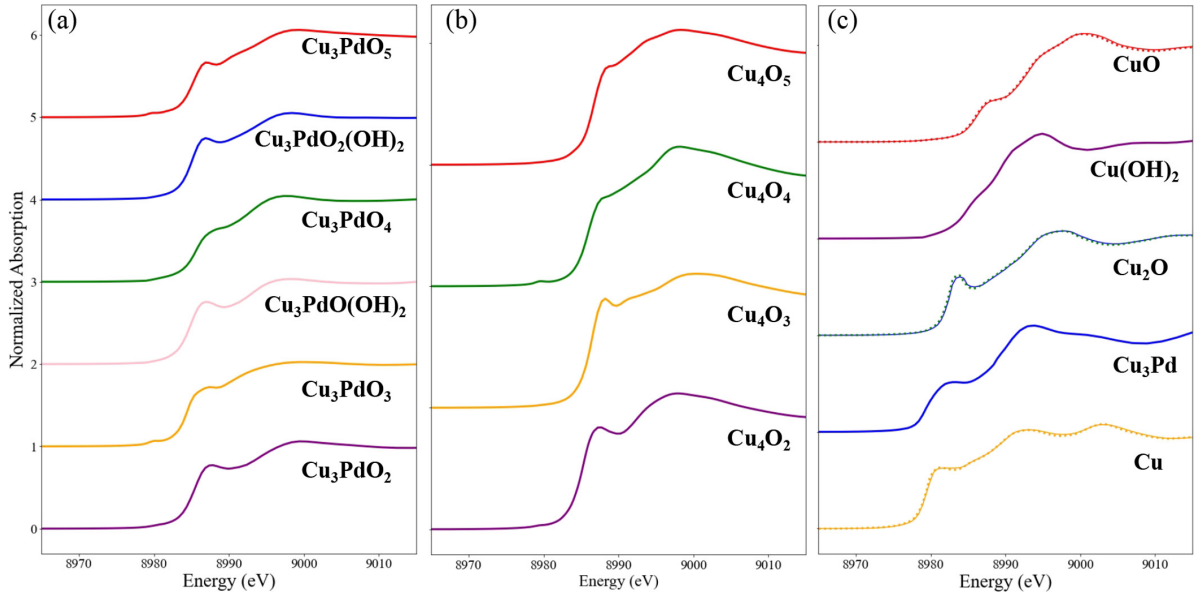

Figure 5.3: The computed XANES spectra to be used as the basis sets for LCFs, of (a) GMs of the Cu_3PdO_x clusters, (b) GMs of the Cu_4O_x clusters, and (c) bulk standards with the corresponding experimental spectra (where available) shown in dashed lines. used in the linear combination fitting of the experimental XANES.

5.3.3 Dynamic evolution of compostion with temperature

Some of the best achieved fits of the experimental spectra are shown in Figure 5.4a,b, and in Figure 5.4c-f the contributions of different cluster and bulk components of the fits are shown individually. The fits clearly indicate several compositional and size changes as a function of temperature. Focusing first on the compositional changes and the cluster contributions to the fits, we see changes in oxygen content with temperature. Initially, at the lower temperatures, the clusters are quite deeply oxidized, with the dominant composition being Cu_3PdO_4, and Cu_3PdO_5 as a close second (Figure 5.4e,f). The clusters with smaller oxygen contents, if present, are only in very small amounts. As the system is heated, we see a gradual decrease in the Cu_3PdO_4 and Cu_3PdO_5 content, as well as in the general cluster content, which decreases as the bulk fraction grows (see below). We only see a small contribution of reduced clusters (as Cu_3PdO_3) at high temperature, and Cu_3PdO_4 remains the dominant cluster composition. Cu_3PdO_5 almost vanishes at temperatures above 400 °C but we see it rebound as the system cools down. Hence, the cluster fraction of the system shows reduction and reoxidation, at increasing and decreasing temperatures, respectively, but the effect is somewhat limited in amplitude.

Finally, we observe a significant change in the total bulk contribution relative to the total cluster contribution with temperature; As the temperature increases, there is a clear increase in the bulk fraction of the fit, which then plateaus and remains relatively constant (within the bounds of experimental error, uncertainties with the computed spectra, and the method of fitting) as the system is cooled (Figure 5.4c,d). We would caution against a literal interpretation of the bulk fractions. For example, the already relatively high bulk fraction of the as-deposited clusters at 25 °C suggests that bulk standards stand for some cluster forms (examples of such substitution are Cu_3PdO_4 and CuO, or Cu_4O_2 and Cu/Cu_2O, the latter is discussed in more detail below). Instead of the absolute fraction of the bulk in the fits, the trend in the growing bulk fraction with increasing temperature is a relative and thus more reliable metric. We see a 40% increase in the bulk fraction while heating to 550C

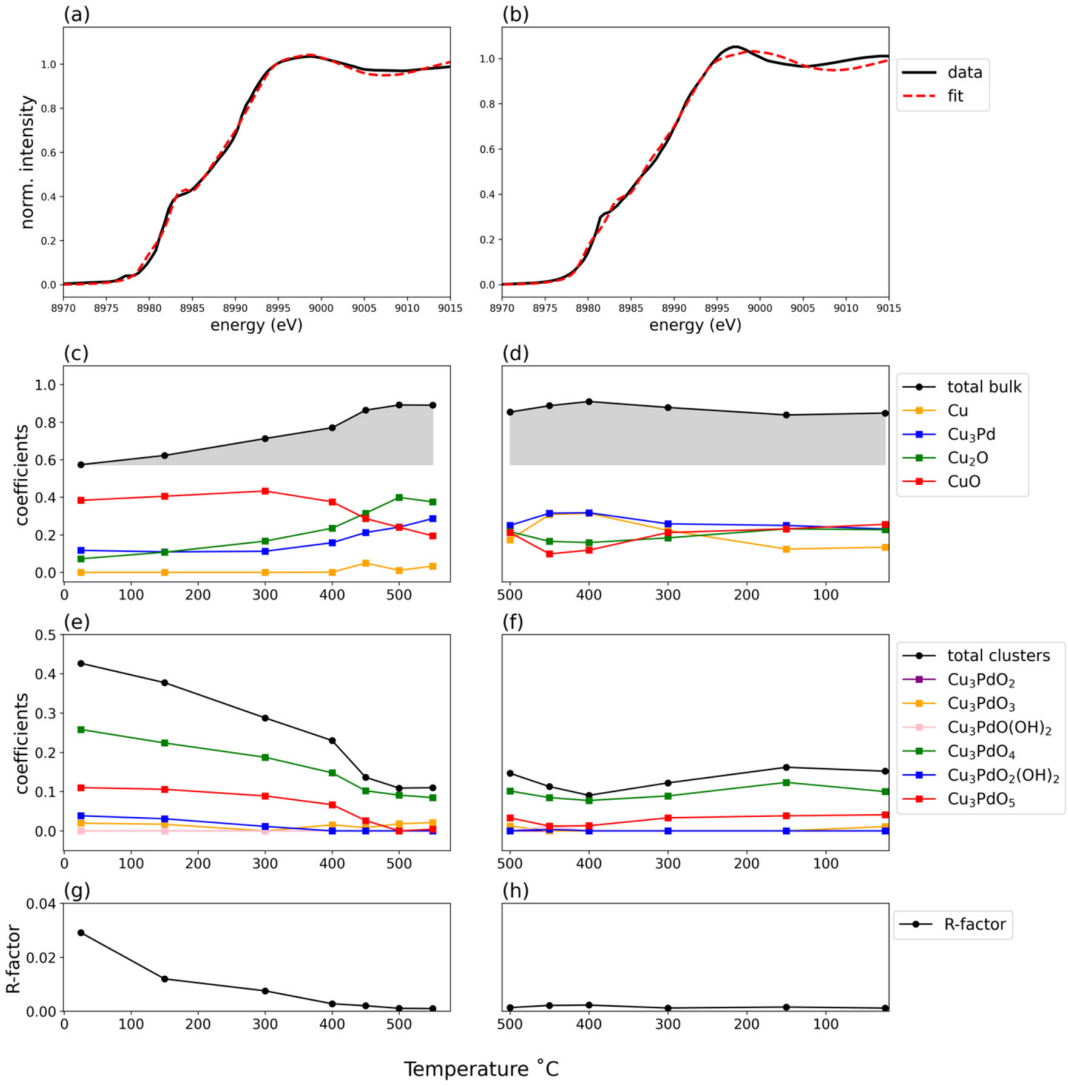

Figure 5.4: The evolution of the standards' coefficients with temperature of the *operando* XANES of Cu_3Pd, fit with both bulk and cluster standards. (a) and (b) show some of the best fits after heating (at 550 °C) and cooling (150 °C) respectively. (c) and (d) show the evolution of the bulk coefficients during heating and cooling respectively, while (e) and (f) show the evolution of the cluster coefficients during heating and cooling respectively. (g) and (h) show the evolution of the R-factor with temperature while heating and cooling respectively. We can clearly see via the shaded region of (a) that the total bulk fraction of the LCF increases as temperature increases, and in the (b) we see the total bulk fraction of the LCF remains essentially constant during cooling.

(gray areas in Figure 5.4c,d). This suggests that heating induces the process of sintering of the deposited Cu3Pd clusters, which then slows down and stops as the system is cooled. Because the adsorbate binding free energy is sensitive to temperature, whereas sintering is not reversed by cooling, we conclude that the sintering process is likely standard and driven by minimization of the surface energy of the particles, rather than by the reversible adsorption/desorption of reagents.

The updated fits using the mixed cluster and bulk standards for the *operando* XANES of Cu_4 clusters on alumina are shown in Figure 5.5. Each individual fit is shown in Figure D.6. Among clusters, Cu_4O_4 and Cu_4O_5 compositions dominate at lower temperatures, whether or not bulk is included in the LCFs. Their fraction decreases as temperature increases, again regardless of the standards used. A comparison of the fits without (a) and with (b) bulk included in the fit for three temperatures (formatted to be similar to the previous paper[171]) is given in Figure 5.6. One notable change once bulk is included, is the differences in population of the Cu_4O_2 and Cu_4O_3 cluster components of LCF. In the absence of bulk, Cu_4O_2 starts off as a small fraction, but grows dramatically as temperature is increased. When bulk is included in LCF, however, the fraction of bulk Cu_2O and Cu grows, instead of the Cu_4O_2 cluster content. In contrast, in the absence of bulk, Cu_4O_3 is not present in the fit, however once bulk is included, Cu_4O_3 is the third most dominant cluster composition. The overall conclusion of partial reduction of the system with increasing temperature, followed by partial reoxidation during cooling, holds for Cu_4O_x as it does for Cu_3PdO_x clusters.

However, we see that by not including bulk, we may get an inaccurate idea of the composition of the system, and overestimate the amount of Cu_4O_2 present. For example, with a less complete cluster-only basis set for LCF, Cu_4O_2 will serve as a stand-in for bulk Cu_2O and Cu. We see this because when we include the bulk in LCF, the R-factor value improves. We also see this effect when considering the inclusion of $Cu(OH)_2$ bulk, as will be discussed also later in the text. This mimicking to some extent is inevitable since our

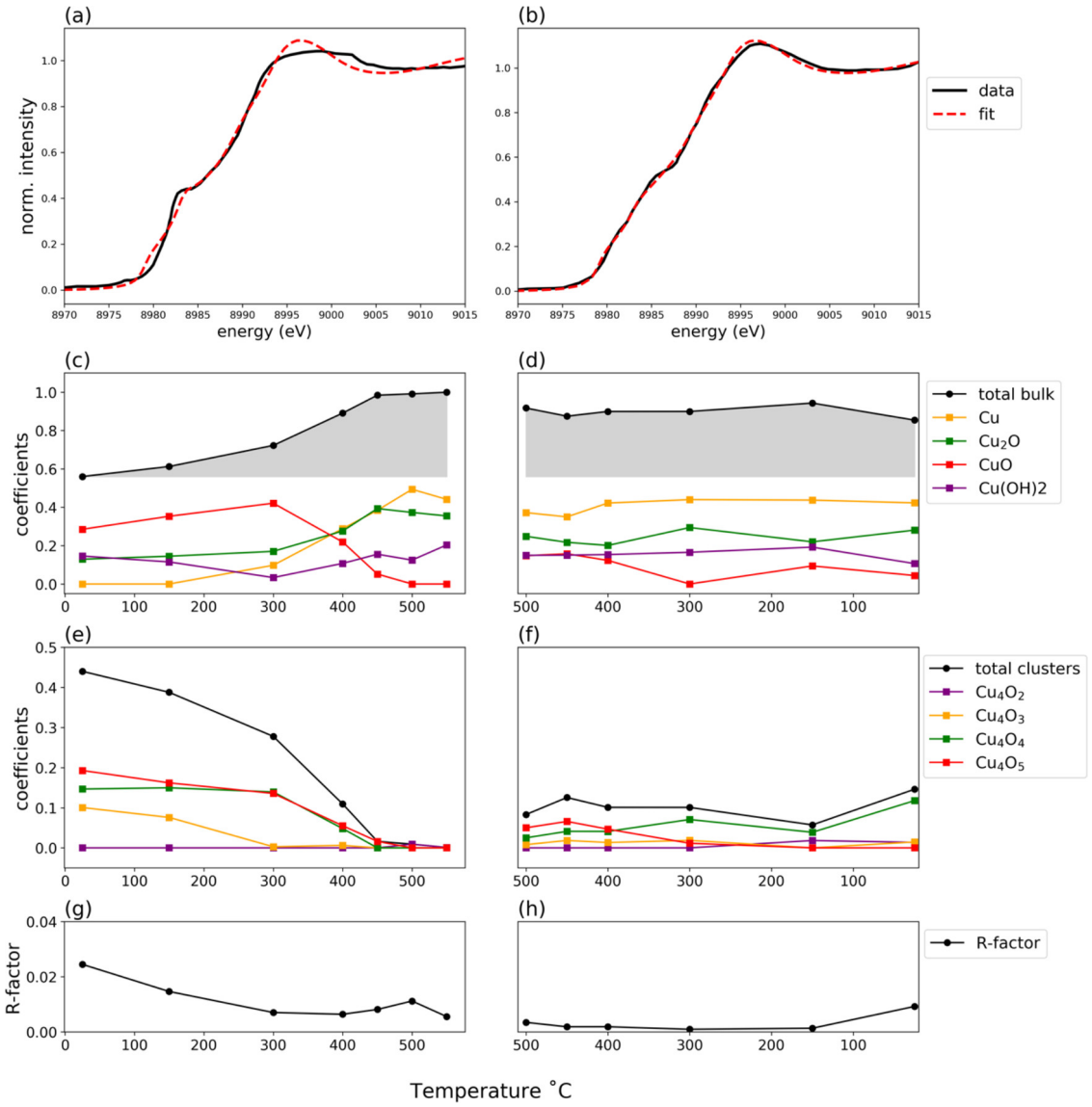

Figure 5.5: The evolution of coefficients with heating and cooling for the Cu_4O_x system. (a) and (b) are example quality fits to the data for 550 °C upon heating and 150 °C during cooling respectively. (c) and (d) show the evolution of the bulk coefficients during heating and cooling respectively, while (e) and (f) show the evolution of the cluster coefficients during heating and cooling respectively. (g) and (h) show the evolution of the R-factor with temperature while heating and cooling respectively. We can clearly see via the shaded region of (a) that the total bulk fraction of the LCF increases as temperature increases, and in the (b) we see the shaded region remains essentially constant during cooling.

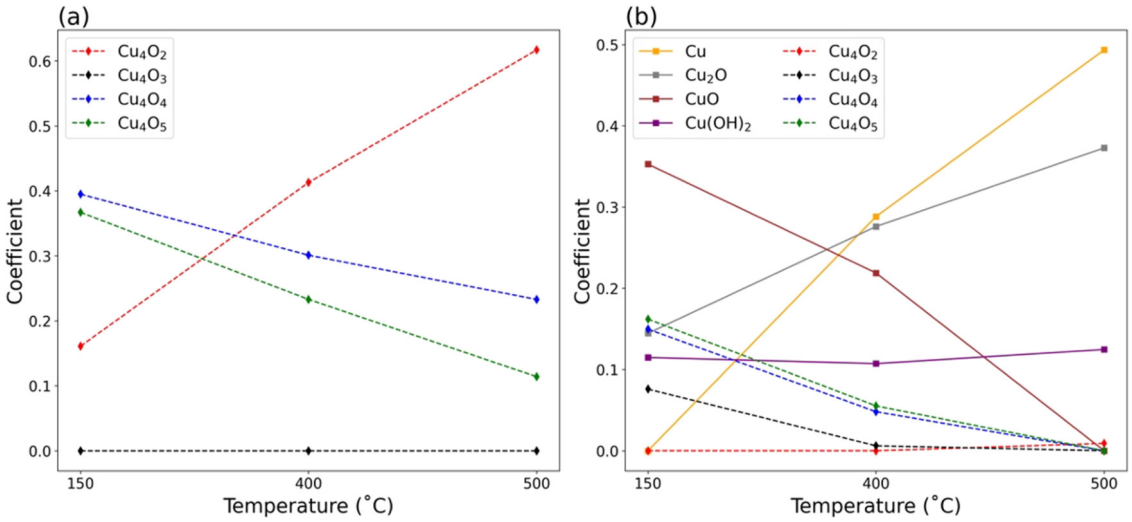

Figure 5.6: Comparison between the (a) cluster-only and (b) cluster and bulk fits of the Cu_4 clusters, highlighting the differences resulting from including bulk in the fits. Note that in the cluster-only fits, the Cu_4O_2 content grows sharply as the system is heated, while the inclusion of bulk instead shows Cu and Cu_2O bulk fractions growing instead of Cu_4O_2.

basis set of standards is non-orthogonal, and the standards share similarities, especially when considering chemically related systems.

We also see for the bulk fractions (Figure 5.5 c, d) a similar behavior to the Cu_3Pd clusters, where the increase in fraction of bulk metallic Cu with heating is not reversed upon cooling, and it remains the dominant bulk component. Again, we see that the system does not return to the same state as at the initial temperature of 25 °C, but instead is dominated by Cu, though it contains similar amount of Cu_2O and $Cu(OH)_2$. The CuO fraction also recovers somewhat from the peak temperature, however it remains the minority bulk component, indicating only partial reoxidation. The cluster compositions (Figure 5.5 e, f) after cooling are slightly different to pre-heating, where Cu_4O_4 is still dominant, but the fraction of Cu_4O_5 has decreased from being similarly dominant to Cu_4O_4 to zero.

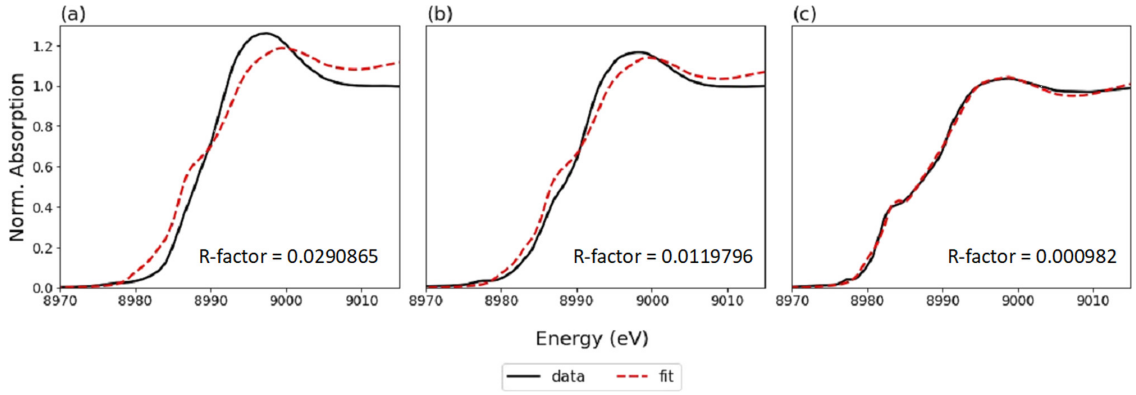

Figure 5.7: The XANES fit for Cu_3Pd clusters at (a) 25 °C as-deposited, (b) heated at 150 °C, and (c) when heated at its maximum of 550 °C, showing the visual improvement of the fit that corresponds to the improvement of the R-factor with temperature as seen in Figure 5.4.

5.3.4 Discussion on the ambiguity and under-determined nature of the problem

The LCFs for each temperature for the Cu_3Pd and Cu_4 XANES show a definite change in the quality as the temperature increases from the 25 °C to 550 °C (Figure 5.7).

At lower temperatures the fits have a higher R-factor (Figure 5.4g,h and Figure 5.5g,h), which then falls as the temperature increases and then stays nearly constant and low during cooling. We tentatively attribute this to the fact that the as-deposited clusters did not have a chance to fully equilibrate at such low temperatures, and thus retain some gas phase structural characteristics. In other words, the poorer fits can be attributed to kinetic trapping of metastable isomers of the Cu_3Pd/Cu_4 deposited clusters as they land on the surface. Since our basis set consists of the DFT GM Cu_3Pd and Cu_4 clusters with varying oxygen content, which are more representative of the thermally equilibrated ensemble, and the ideal bulk structures, the resultant LCFs have worse R-factors. As the system is subsequently heated, the clusters have time and energy to overcome this kinetic trapping and reach their thermally-equilibrated ensembles of structures, resulting in a better R-factor with the equilibrated standards. Several other schemes for fitting were tried (see discussion in the next section), to see if any lead to systematic improvement of the R-factor, and none were successful. This

too supports the thermal equilibration hypothesis, as our existing basis set would not be able to capture features characteristic of metastable states, only thermally equilibrated ones.

Close examination of LCFs as a function of temperature reveals some features present in the fit that are not in the actual data. The most prominent example of this is the sharpness of the white line peak of the fit while compared to the data (see the full fits for Cu_3Pd and Cu_4 in the SI- it's most obvious in the Cu_4 fits, in Figure D.8), especially at the initial low temperatures. A very notable feature of the bulk XANES, particularly of the metallic Cu and Cu_3Pd, is a much sharper white line peak than any of the cluster standards (Figure 5.2), something that has also been noted in literature.[161, 169] This mismatch of the peak sharpness between the fit and the data is not constant throughout the entire heating/cooling cycle. In fact, once the system has been heated to 550°C, and is beginning to cool, the data adopts the sharper shape of the white line peak that the fit readily replicates (Figure 5.7 (a) vs (c)). We believe that this is further evidence for (a) sintering, and (b) the over-estimation of the bulk fraction at lower temperatures during heating (which occurs because that is the only way within our basis set to approximate the changes in the rising edge energy – see Appendix D.2 for cluster-only fits). Furthermore, the basis set only includes the extremes of the system sizes: the as-deposited tetraatomic clusters, and the (quasi-infinite) bulk, whereas particles of intermediate sizes and different oxygen contents, or fractal-like aggregates previously suggested[166] are not represented. Therefore, cluster aggregation is not followed by LCF in full detail, as the experimental XANES might contain features intermediate between clusters and bulk that are not represented in our standards.

It is possible to occasionally obtain fits of comparable quality (judged by the R-factor) but corresponding to quite different system compositions. One example of this is the inclusion of $Cu(OH)_2$ bulk in the basis set, which, for both Cu_3Pd and Cu_4, does not change the R-factor significantly (e.g. for Cu_4 0.0244925 versus 0.02159 at 25 °C before heating, or 0.0070381 versus 0.0075387 at 300 °C while heating, with and without $Cu(OH)_2$ respectively, see Table D.3 for more detail). While this creates an impression that the fraction of $Cu(OH)_2$ in the fit

should be small, it ends up comprising up to 20% when included. For more detail see Figure D.8 and D.9. We have performed a large number of LCFs, using different approaches, such as expanding/contracting the basis set with varying strategies, decomposing the standards into XANES of typical specific atoms of the clusters, etc. (see more details in the SI). We find that multiple approaches can yield similar results. However, it stands true that fitting the XANES of subnano clusters using bulk-only standards is problematic,[171] largely because there is no simple correlation between the rising edge energy and the degree of oxidation of the metal in the cluster, in contrast to bulk copper oxides, due to size and shape effects, and interactions with the oxide support (See Figure D.10 for more detail). The fits that include bulk and cluster standards are improved, over both cluster-only, and bulk-only fits. Furthermore, we performed a stability analysis of the fits for three different fits, and have determined that their stability is sufficient for the conclusions we draw from their trends (Figure D.11). We also note, that despite the fact that some of our cluster standards appear quite similar, the R-factors computed between them indicate that our fits are suitably accurate. When accounting for the most similar spectra, we see that there is no significant change in the conclusions we might draw from the fits (D.12). Therefore, the qualitative conclusions regarding partially reversible reduction of the clusters, and partial and irreversible sintering during the temperature ramp are valid despite the complications.

5.4 Conclusion

Operando XANES have been measured as a function of a reversible temperature ramp, between 25 °C and 550 °C for Cu_4 and Cu_3Pd clusters supported on alumina and exposed to the oxidizing atmosphere in conditions of propane ODH. The XANES spectra show size and compositional changes upon heating, only some of which are reversible upon cooling. We demonstrate that, by using both bulk and cluster standards during LCF of *operando* XANES, more accurate fits can be obtained than using only bulk (as is the standard practice), or only

clusters standards (as we proposed previously). Mixed standards not only yield higher quality fits, but also allow tracking cluster sintering, in addition to the evolution of oxygen content. We find that the clusters reduce and partially reoxidize, as the temperature is increased and decreased, respectively. This is consistent with all previous reports. However, we also find evidence that the fraction of the bulk irreversibly grows, regardless of the subtleties of the fitting algorithm, which allows us to account for the irreversible change in the spectra as a result of the TPRx cycle. This suggests that cluster sintering occurs and can be detected in *operando* XANES, if the fits include both the cluster and the bulk standards. The larger sintered particles show a smaller trend to be oxidized/reduced than the small clusters in reaction conditions. Secondly, our results suggest that low-temperature XANES at the onset of the heating ramp corresponds to likely metastable, trapped states of the cluster coming from the gas phase. The XANES at these temperatures cannot be satisfactorily fit to any combination of bulk and supported cluster standards, in contrast to the XANES at all other, higher temperatures. We wish to emphasize that the coefficients of each standard in the fit need to be interpreted qualitatively rather than quantitatively. However, the evolution of the coefficients with temperature should be taken as representative as the overall trend. Our approach of combined standards opens perspectives for a detailed understanding of XANES spectra and therefore of the nature and structure of cluster catalysts in reaction conditions.

CHAPTER 6

Got Coke? Self-Limiting Poisoning Makes an Ultra Stable and Selective Sub-Nano Cluster Catalyst

6.1 Introduction

There is a great drive to go sub-nano in precious metal catalysis, because in sub-nano clusters, nearly all the expensive metal atoms are exposed to reactants, increasing cost-effectiveness. Clusters can also have better catalytic activity than the bulk metal,[15] provide a parameter for catalyst tuning (size), and can break scaling relations that can limit the activity of larger catalytic centers.[3] Pt-based catalysts are widely used in refining, transforming chemicals, and converting environmentally harmful products, [191–195] and the challenge to the use of sub-nano Pt catalysts in such applications relates to stability. Because the metal-metal coordination is low, few-atom clusters are significantly more susceptible than larger nanoparticles to both thermal sintering and poisoning. For example, in alkane dehydrogenation for alkene production, the high operating temperatures can lead to sintering, and reactive sites are easily poisoned by carbon deposition ("coking") if the catalyst selectivity is not high enough. Past research showed that sintering and coking can be inhibited by growing porous overcoatings on nanometer catalyst particles,[196] but this approach partially blocks the catalytic sites, lim-iting efficiency.[191, 197] For sub-nano Pt clusters deposited on SiO_2 supports, we showed that even a single cycle of alumina atomic layer deposition overcoating completely blocked all Pt sites, rendering the clusters inert.[198] Coked catalysts are often regenerated by oxidizing away carbon deposits at high temperatures, however, that would

tend to deactivate sub-nano clusters by sintering. [199, 200] Alloying sub-nano clusters to modify the chemical and thermal properties is another approach; for example, alloying oxide-supported Pt cluster catalysts with tin or boron prevents carbon deposition and inhibits sintering, [10–12, 108] however, these elements are not ideal because they also block a substantial fraction of the catalytically active Pt sites.

Germanium was recently suggested by Jimenez-Izal et al.[13] as a dopant for small Pt clusters to inhibit coking and sintering under conditions of alkane dehydrogenation. Supported Pt_2Ge clusters were predicted to be more sinter-resistant than Pt_3, Pt_2Sn, and Pt_2Si clusters, and to be highly active for ethane dehydrogenation to ethylene, while being highly selective against deeper dehydrogenation that tends to lead to coking. Although density functional theory (DFT) simulations were promising, previous experimental work on Ge-containing catalysts was not always successful. For example, several studies found that activity for dehydrogenation of cyclohexane was substantially lower for PtGe catalysts than for analogous Pt catalysts. [201, 202] Note, however, that these studies focused on catalysts with particle sizes much larger than the sub-nano clusters examined here. Here we report a novel approach to improving cluster catalyst stability, in which self-limiting coking converts alumina-supported Pt_nGe_x catalyst clusters to a $Pt_nGe_xC_y$ form that is catalytically active and thermally and chemically stable. The effect is illustrated here using Pt_4Ge and Pt_4GeC_2 catalyst clusters, focusing on two critical factors in the overall process of ethane-to-ethylene dehydrogenation – high selectivity toward desorption of intact ethylene (avoiding deeper dehydrogenation/coking), and maintaining a large number of strong ethylene binding sites, required to promote ethane-to-ethylene conversion. The actual ethane-to-ethylene step is assessed by DFT only, because ethane sticks too weakly to study by our UHV surface science methods.

6.2 Results and Discussion

6.2.0.1 Pt_4Ge/alumina characterization

As described in the Methods section, Pt_4Ge/alumina samples were prepared by soft-landing mass-selected Pt_4 clusters on thin-film alumina supports, followed by Ge addition by exposure to $GeCl_4$ and H_2. The Pt_4 cluster coverage was 3.8 x 10^{13} clusters/cm^2, equivalent to 10% of a close-packed Pt monolayer (ML). S/TEM imaging on both carbon and alumina-coated aluminum grids is described in the supplementary information (Fig. E.1). Individual atoms were not resolved, but from the cluster spot densities, sizes, and stability under the e-beam, we conclude that small Pt_n are stable at room temperature on both carbon and alumina. One question is whether the Pt clusters remain adsorbed at their landing sites, or if they might diffuse and bind at defects in the alumina film. Evidence bearing on this question is discussed in the supplementary information, leading to the conclusion that the Pt clusters do not diffuse to, and bind at defects, apart from a small fraction that probably landed on or close to such sites.

X-ray photoelectron spectra (XPS) were used to measure the Ge : Pt stoichiometry,

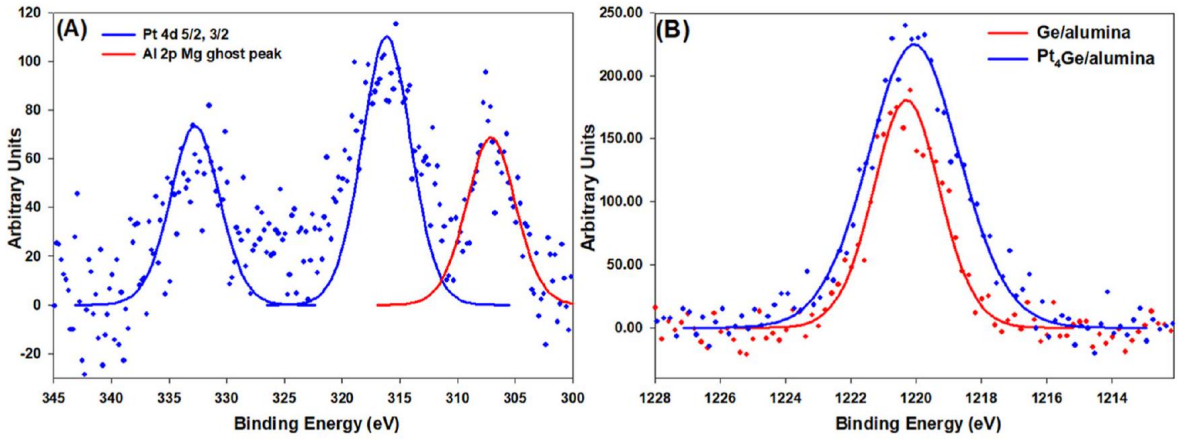

Figure 6.1: XPS showing selective binding of Ge to Pt clusters. (A) XPS of Pt 4d 2/5 and 3/2 of Pt_4Ge/alumina, red colored peak is from Mg contamination in the Al source. (B) Ge 2p 3/2 peak for Ge/alumina in red and Pt_4Ge/alumina in blue.

using an approach discussed in the supporting information. The resulting Ge : Pt ratio was found to be 1.07 : 4, i.e., one Ge atom was deposited per Pt_4 cluster. In addition, there was some non-specific Ge deposition on the alumina support, but as shown below and in the supporting information, this alumina-bound Ge is not catalytically active itself and has little effect on the catalytic properties of Pt_n clusters deposited on a Ge-treated alumina support. Note that the XP spectra shown Figure 6.1 were taken for as-prepared samples (after the H_2 exposure that re-move most, but not all the Cl atoms from the $GeCl_4$ precursor). These Cl atoms complicate interpretation of the Pt and Ge binding energies.

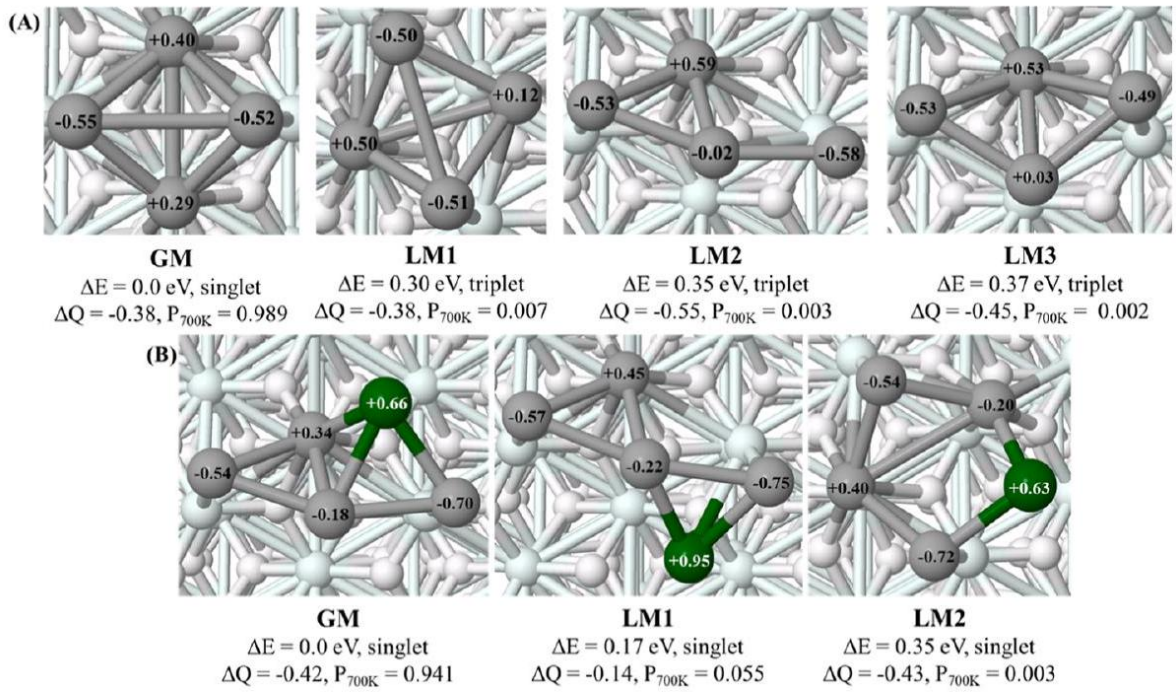

Figure 6.2: Thermally accessible structures, which are within 0.4 eV of the lowest energy structure. (A) Computed thermally accessible structures of Pt_4/alumina. (B) Computed thermally accessible structures of Pt_4Ge /alumina. The spin state, net support-to-cluster electron transfer (ΔQ), Bader charges on each cluster atom, and the thermal population at $700K$ (P_{700K}) are shown. GM = global minimum. For each LM, the energy above the GM (ΔE) is given. Images showing the entire supercell are in the Supporting Information. Pt is shown in grey, Ge in green, Al in pale blue, and O in pale pink.

6.2.0.2 Cluster structures from DFT

Figure 6.2 shows the thermally accessible isomers for Pt_4/α-Al_2O_3 (Fig. 6.2A) and Pt_4Ge/α-Al_2O_3 (Fig. 6.2B), calculated using global optimization at the DFT level, as described in the methods section. The predicted isomer populations at 700 K, near the upper end of the experimental temperature range, are given as P_{700K}. For Pt_4/alumina, the global minimum structure (GM) is a spin-singlet, but all other thermally-accessible local minima (LM) are spin-triplets. The structures have Pt atoms with both positive and negative charges, but in all cases, there is net support-to-cluster electron transfer (ΔQ). For Pt_4Ge/alumina, the GM and all thermally accessible LMs are singlets, with substantial Ge-to-Pt_4 electron transfer, and also net support-to-cluster electron transfer.

6.2.0.3 Ethylene TPD analysis

For selective alkane dehydrogenation, it is critical that the nascent alkene product desorbs from the catalyst, rather undergoing further dehydrogenation of decomposition that tends to deposit carbon. In addition, the catalyst clusters must provide large numbers of strong alkene binding sites to enhance the alkane-to-alkene conversion. To probe the branching between alkene desorption vs. unwanted dehydrogenation/coking, we have adopted the strategy of adsorbing ethylene on the catalyst at low temperature, then measuring, using temperature-programmed desorption (TPD), the branching between intact ethylene desorption vs. hydrogen desorption, which signals dehydrogenation and carbon deposition. In addition, C 1s XPS after multiple ethylene ad-sorption/desorption cycles was used to directly measure the tendency toward carbon deposition.

Figure 6.3 shows TPD data collected for Pt_4/alumina and Pt_4Ge/alumina samples, both with identical, 0.1 ML-equivalent of Pt deposited asPt_4 clusters. The data shown are from experiments in which 21 sequential TPD runs were done for each sample. For each run, the

sample was first exposed to a saturation dose of C_2D_4 (10 L) at 150 K, and then heated at 3 K/sec to 750 K while mass-spectrometrically monitoring desorption of C_2D_4 and D_2. No signal was observed for desorption of acetylene or other hydrocarbon species, and no additional D_2 desorbed in test experiments in which the samples were ramped to higher temperatures, indicating that ethylene either desorbed intact, or dehydrogenated to 2 $C_{(ads)}$ + 2 $D_{2(gas)}$. For comparison, the figure also shows the desorption signals observed from the alumina and Ge-treated alumina (Ge/alumina) supports with no clusters present. For both supports, C_2D_4 corresponding to a few percent of a monolayer adsorbed during the 150 K dose, desorbing below 250 K when heated. This support-bound C_2D_4 is attributed to binding at defects in the alumina film. No D_2 desorption was observed, showing that neither the alumina nor Ge/alumina supports were active for ethylene dehydrogenation, and as might be expected, the desorption signals in repeated runs were unchanged.

During the 1st TPD from the Pt_4/alumina sample, there was substantial C_2D_4 desorption in the 250 – 450 K range, corresponding to ethylene binding to the Pt_4 clusters, in addition to a lower temperature feature attributed primarily to weak binding to the alumina support. D_2 desorbed in a broad feature extending from 250 K to 750 K, implying that many of the C_2D_4 molecules dehydrogenated, liberating D_2 and depositing carbon. During the 2nd run there was substantially less C_2D_4 desorption above 250 K and a general shift to desorption at lower temperatures, implying fewer and weaker C_2D_4 binding sites. The amount of D_2 desorption also decreased, suggesting that dehydrogenation occurs primarily for strongly bound C_2D_4, but that the number of such sites was much smaller in the 2nd TPD cycle due to coking and/or sintering. As additional cycles were carried out, the decrease in C_2D_4 desorption at high temperatures, and the reduction in D_2 desorption continued, with the rate of change slowing as the clusters were mostly deactivated.

The 21 TPD run experiments took >20 hours each, making repetition impractical and raising the possibility that surface contamination might have influenced the results in later cycles. Therefore, we also carried out repeated experiments studying the effects of the first

six TPD runs, which were responsible for most of the change in catalyst properties. Quantitative analysis of the desorption is based on these six-TPD experiments. As described elsewhere[12] it is possible to calibrate the absolute sensitivity of the TPD system, and Table E.1 gives the numbers of C_2D_4 and D_2 molecules desorbing per Pt_4 cluster in each of the 6 TPD runs, averaged over the four available data sets. Because there was no evidence of adsorbed hydrogen remaining at 750 K, the number of C atoms deposited should be equal to the number of D_2 molecules desorbing, and the total number C_2D_4 molecules adsorbed during each 150 K dose can be estimated as the number C_2D_4 desorbing + half the number of D_2 desorbing. During the 1st TPD, an average of $\sim$2.9 C_2D_4/Pt_4 were adsorbed, of which $\sim$56% desorbed intact, with the remainder dehydrogenating to liberate D_2 and deposited an average of $\sim$2.5 C atoms/cluster. Because of the cluster isomer distribution, some cluster-to-cluster variation is expected, but we interpret the 1st TPD desorption numbers as indicating that three C_2D_4 molecules typically adsorbed per cluster at 150 K, of which two typically desorbed intact upon heating, the other decomposing to liberate 2 D_2(gas) and deposit 2 C per cluster. By the 6th TPD cycle, the number of C_2D_4 adsorbed perPt_4 had dropped $\sim$58% to just $\sim$1.23, of which $\sim$82% desorbed intact, with the remainder decomposing to deposit C and liberate D_2. For the Pt_4/alumina sample, the total D_2 desorption during the 6 TPD runs corresponded to the deposition of $\sim$5.75 C atoms per depositedPt_4 cluster.

Pt_4Ge/alumina presents a striking contrast. As described in the Methods, the final step in Pt_4Ge/alumina preparation involved 750 K heating to desorb residual Cl and hydrogen (as HCl and H_2 – Fig. E.2), and to em-phasize the point that the Pt_4Ge/alumina samples had already been heated once prior to the initial C_2D_4 TPD runs, the TPD cycles in Fig. 6.3D and E are numbered starting with "2nd TPD". The C_2D_4 desorption observed in this 2nd TPD forPt_4Ge/alumina was quite similar in both intensity and structure to that in the 1st run onPt_4/alumina, with a low-temperature component at least partly due to desorption from the Ge/alumina sub-strate, and a high-temperature component attributed to sites on thePt_4Ge clusters. In contrast, D_2 desorp-tion (i.e., carbon deposition) was much weaker

forPt_4Ge than in either the 1st or 2nd TPD runs for Pt_4/alumina, and had a bi-modal temperature dependence, suggesting that what little D_2 desorbed, was produced by two processes with different activation energies. The D_2 desorption features can, in principle, be fit to extract E_a values, requiring some assumption about the kinetic order of the rate-limiting steps. We previously examined D_2 TPD from small Ptn/alumina exposed to D_2 under conditions similar to those used here for C2D4,[19] observing recombinative desorption starting at ∼230 K, peaking just below 300 K, and terminating at ∼450 K. The fact that the desorption features for D_2 generated by C_2D_4 decomposition do not match the recombinative feature observed in D_2 TPD suggests that some other step in the D_2 production pathway is rate-limiting. For simplicity, we assume that this step follows 1st order kinetics[203] and further assume a prefactor of 10^{15} sec^{-1}. This crude approximation gives effective (i.e., averaged over all accessible pathways and cluster isomers) E_a values of ∼1.1 V for the 350 K feature, and ∼2.5 eV for the 500 K feature, in the range observed for C-H activation in the DFT calculations. During subsequent TPD cycles, there continued to be a small and diminishing amount of D_2 production, and the C_2D_4 desorption behavior evolved, but note that when a steady state had been reached after ∼15 runs, the C_2D_4 desorption, particularly at higher temperatures, was substantially higher forPt_4Ge than forPt_4.

Again, quantitative desorption analysis was done for the first 6 TPD runs. The total number of C_2D_4 molecules adsorbed per Pt_4Ge cluster in the 2nd TPD was ∼1.71, of which ∼86% desorbed intact, with the balance decomposing to liberate D_2 and deposit ∼0.5 C/cluster on average (Table E.2). Given that C atoms deposit in pairs (no desorption of C_1 or $C_{>2}$ species is observed), we interpret this to mean that the Pt_4Ge clusters initially had one or two C_2D_4 molecules adsorbed, and that on ∼25% of the clusters, one ethylene decomposed to deposit two C atoms. Thus, the probability of carbon deposition during this 1st TPD run was ∼one-fourth that for the Pt_4/alumina samples. By the 6th TPD cycle, the number of adsorbing C_2D_4 molecules was still ∼1.46/cluster, of which 91% desorbed intact, with the balance decomposing to liberate D_2 and deposit just ∼0.28 C/Pt_4Ge cluster. Thus,

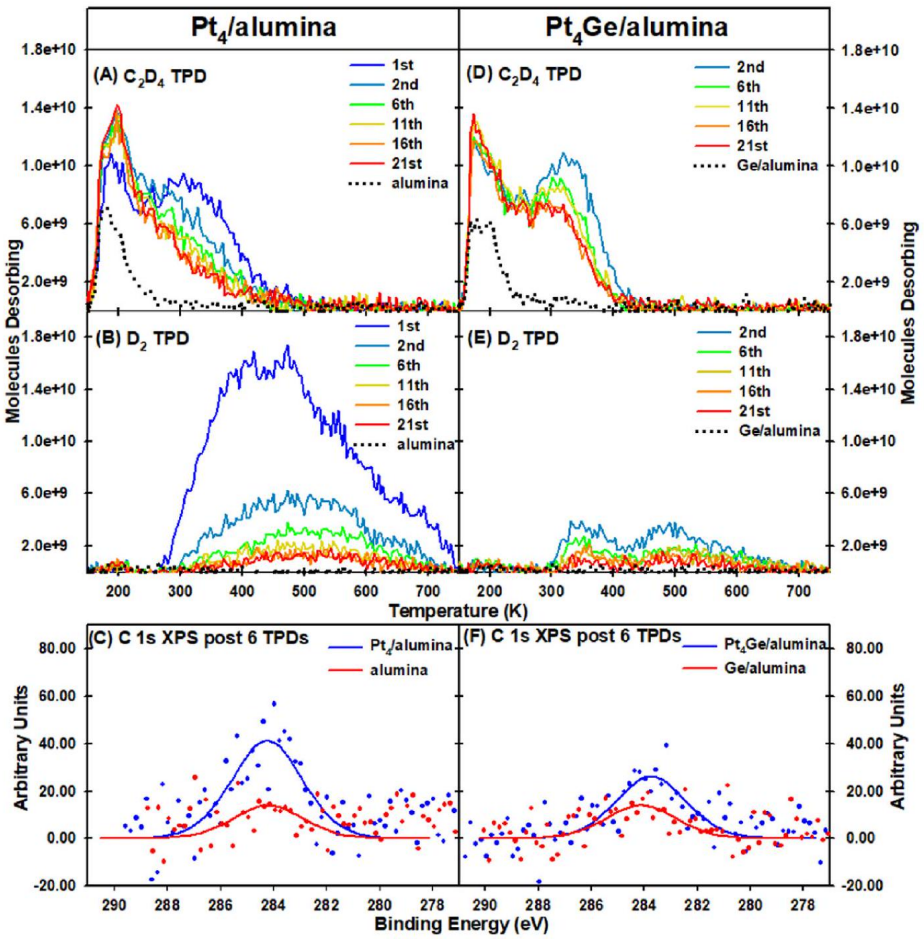

Figure 6.3: Temperature-programmed desorption (TPD) results showing C_2D_4 and D_2 desorption, with XPS scans of the C 1s region. Left column: Pt_4 /alumina. Right column: Pt_4Ge /alumina. (A,D) show desorption of intact C_2D_4. (B,E) show desorption of D_2. (C,F) show carbon 1 s XPS from Pt_4 /alumina and Pt_4Ge /alumina after six TPD cycles; control samples (alumina and Ge/alumina) were also probed post the six TPDs.

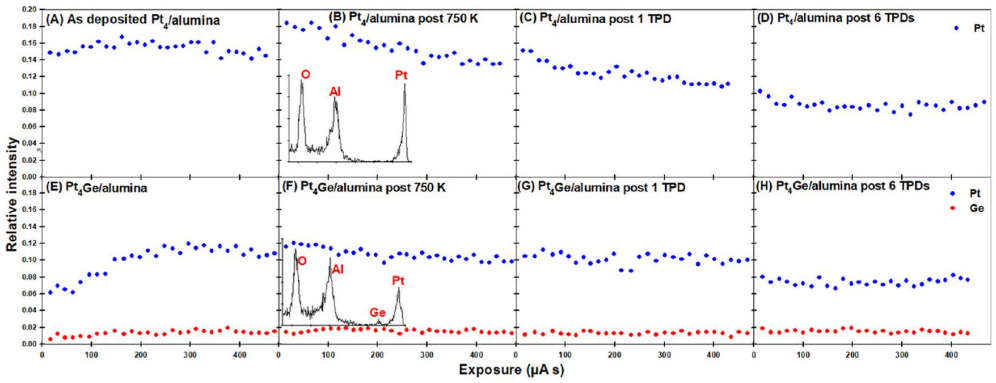

Figure 6.4: Low-energy He^+ ISS showing relative intensities of Pt and Ge. (A) As-deposited Pt_4/alumina, (B) Pt_4/alumina post 750 K heat, inset shows the raw ISS at $\sim$ 30 μAs exposure. (C) Pt_4/alumina post one C_2D_4 TPD, (D) Pt_4/alumina post six C_2D_4 TPDs, (E) As-prepared Pt_4Ge / alumina, (F) Pt_4Ge /alumina post 750 K heat, inset shows the raw ISS at $\sim$ 30 μ As exposure. (G) Pt_4Ge/alumina post one C_2D_4 TPD, and (H) Pt_4Ge /alumina post six C_2D_4 TPDs.

during the 2nd TPD for Pt_4Ge/alumina, the number of ethylene adsorbing per cluster was ∼41% lower than in the 1st TPD for Pt_4/alumina, but by the 6th TPD, the number was ∼20% higher for Pt_4Ge. We interpret this to imply that addition of a Ge atom reduced the initial number of ethylene binding sites, but the binding sites, and particularly the catalytically important strong/high temperature binding sites, survived much better under reaction conditions for Pt_4Ge than for Pt_4.

From the total D_2 desorption during the 6 TPD runs, we estimate that the total carbon deposition on Pt_4Ge/alumina amounts to ∼1.8 C atoms per deposited Pt_4Ge cluster, which is less than a third the total estimated for Pt_4/alumina (5.75 C/cluster). It should be noted that due to uncertainties in the intensity calibration process, the absolute desorption numbers given here and in Tables E.1 and E.2 are uncertain by ∼50%, how-ever, the relative uncertainties for comparing TPD data in different experiments are smaller – on the order of ±10%. Thus, the TPD data indicate that Pt_4/alumina cokes more than a factor of three faster than Pt_4Ge/alumina.

6.2.0.4 Carbon deposition analysis

Carbon deposition was also probed directly by C 1s XPS after the 6 TPDs, as summarized in Figs. 6.3C and 6.3F. XP spectra are shown for the Pt_4/alumina and Pt_4Ge/alumina samples, and for Pt-free alumina and Ge/alumina samples after 6 C_2D_4 TPDs. The signals are weak because the coverage of clusters, responsible for most carbon deposition, was small, as is the C 1s photoemission cross section. Nonetheless, it is clear that the C 1s signal for Pt_4/alumina is substantially larger than the signal for the alumina support, and after subtracting the support contribution, the net carbon deposition corresponds to ∼8 ± 5 C atoms/cluster. The C/Pt ratio was calculated assuming both C and Pt are in the surface layer, in which case,

$$C/\mathrm{Pt} = (I_C \cdot \sigma_{\mathrm{Pt}}) \,/\, (I_{\mathrm{Pt}} \cdot \sigma_C)\,,$$

where I_C and $I_P t$ are the integrated intensities for the C 1s and Pt 4d peaks, and σC and σPt are the sublevel photoemission cross sections.[204] The C 1s signal for the Pt_4Ge/alumina sample is smaller, and after subtracting the support contribution, the carbon deposition is estimated to be 3 ± 3 C atoms/Pt_4Ge cluster. Thus, both the absolute number of deposited C atoms/cluster, and the ∼3:1 ratio of C deposition on Pt_4 compared to Pt_4Ge, are consistent with the values derived from analysis of D_2 TPD.

To provide additional insight into the carbon/Pt morphology, the samples were also probed by low energy He^+ ion scattering before and after 6 TPDs (Fig. 6.4). Example ISS spectra shown as insets have peaks due to He+ scattering from individual Pt, Ge, Al, and O atoms in the top-most sample layer, superimposed on a smooth background from multiple or sub-surface scattering processes. The background rises sharply at lower energies, preventing direct observation of surface carbon. The main plots in Fig. 6.4 show how the background-subtracted Pt and Ge peak intensities vary as a function of exposure to the ∼0.35 μA He^+ beam, which slowly sputters materials from the surface. To compensate for any He^+ intensity variations, the Pt and Ge intensities are normalized to the total (Pt+Ge+Al+O) intensity, which is nearly invariant under He^+ exposure.

For as-deposited Pt_4/alumina (Fig. 6.4A), the Pt ISS intensity initially increased slightly, then slowly declined at long exposures as Pt atoms were slowly sputtered from the surface. The slight increase was attributed to exposure of additional Pt due to sputter removal of a small coverage of adventitious adsorbates, e.g. H_2 or CO, which have partial pressures ≤ ∼5 × 10^{11} Torr in the UHV system. If an as-deposited Pt_4/alumina sample is briefly heated to 750 K to remove the adsorbates prior to ISS analysis (Fig. 6.4B), the Pt intensity is higher than in the unheated sample, and simply decreases with exposure time as Pt is sputtered.

Note that if the Pt_4 clusters had sintered at 750K to form larger, multilayer clusters on the surface, this would have substantially decreased the Pt ISS intensity, thus such extensive sintering is ruled out by the result in Fig. 6.4B, consistent with the conclusions from the S/TEM data. The initial Pt ISS intensity for Pt_4/alumina after a single C_2D_4 TPD experiment (Fig. 6.4C) was ∼18% smaller than that for the 750 K heated Pt_4/alumina sample in Fig. 6.4B, suggesting that the Pt signal was attenuated by deposited carbon, and the attenuation increased after 6 TPDs (Fig. 6.4D), as expected.

The as-prepared Pt_4Ge/alumina sample was probed both before (Fig. 6.4E) and after (Fig. 6.4F) the 750 K heating used to remove residual H and Cl from clusters. For the unheated clusters, the initial Pt and Ge intensities were small, increasing as the adsorbed H and Cl were sputtered, exposing underlying Pt and Ge atoms. Both Pt and Ge signals decreased slightly at long exposures as Pt and Ge were lost to sputtering. For the sample probed after 750 K heating (Fig. 6.4F), the initial Pt and Ge intensities were similar to the maximum intensities seen for the unheated sample, i.e., removing the adsorbates by heating vs. He+ sputtering had similar effects. The initial Pt ISS signal for the heated Pt_4Ge/alumina sample was ∼37% smaller than the signal observed for heated Pt_4/alumina, presumably reflecting some shadowing or blocking of He^+ scattering from Pt by the Ge atom. The 37% lower Pt ISS intensity was quite similar to the 41% lower total adsorbed C2D4 measured in the initial Pt_4Ge/alumina TPD (Tables E.1 and E.2). For Pt_4Ge/alumina samples that were heated to 750 K then subjected to either 1 or 6 TPD runs (Fig. 6.4G and H), the Pt intensities were attenuated compared to the heated sample, as expected from the fact that some carbon deposition occurred.

The post-6-TPD initial Pt ISS intensity for the Pt_4/alumina sample (Fig. 6.4D) was ∼44% attenuated compared to the initial intensity of the 750 K heated Pt_4/alumina sample. It is not surprising that there was attenuation, given the carbon deposition observed by TPD and XPS (∼6 C/cluster from TPD, ∼8 C/cluster from XPS). Indeed, the surprise is that the attenuation was not much larger. For example, 5- and 20-fold attenuations of

the Pt ISS signals were found to result from adsorption of just a single layer of H or O atoms, respectively, on sub-nano Pt_n/SiO_2. [205]Thus, the much smaller Pt ISS attenuation indicates that the C atoms must primarily be bound in sites where they have little effect on He^+ scattering from Pt, such as sites around the cluster periphery or buried in the cluster core. Nonetheless, the TPD results show that these C atoms strongly attenuate strong ethylene binding, suggesting that carbon has a substantial electronic effect.

For the Pt_4Ge/alumina sample after 6 TPDs (Fig. 6.4H), the initial Pt signal was ∼31% attenuated, relative to the heated Pt_4Ge/alumina (Fig. 6.4F), which can be compared to the amount of C deposition seen from TPD (∼1.8/cluster) and XPS (∼3/cluster). For both Pt_4 and Pt_4Ge samples, ISS indicates that a significant fraction of the Pt atoms remained accessible to He+ scattering after 6 TPD runs.

To summarize the experiments, adding a single Ge atom reduced carbon deposition by a factor of ∼three, but there was still significant carbon deposition for Pt_4Ge, amounting to ∼2 C atoms/cluster after 6 TPD runs. Nonetheless, the Pt_4Ge clusters retained most of their strong/high temperature ethylene binding sites, even after 21 TPD runs, while these high temperature sites were almost entirely suppressed for Pt_4/alumina. Questions we seek to address are: Why is carbon deposition only partly suppressed for Pt_4Ge/alumina? What is the nature of the strong (high temperature) ethylene binding sites retained for Pt_4Ge, but lost for Pt_4/alumina? And why, despite retaining strong C_2D_4 binding sites, does Pt_4Ge nearly stop producing D_2?

DFT was used to address these questions and to examine the activity of the model catalysts for the ethane-to-ethylene dehydrogenation reaction, which cannot be studied under surface science conditions.

6.2.0.5 DFT of ethane, ethylene, and acetylene C-H activation barriers

Pt_4Ge/alumina clusters are found to strongly bind and activate ethane on all thermally accessible isomers (Fig. 6.2B), and there are well over 50 configurations for C_2H_6-

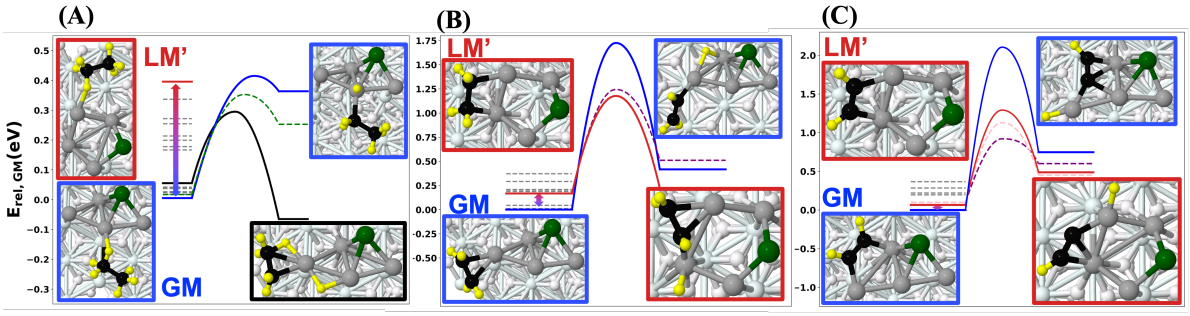

Figure 6.5: Representative ethane, ethylene, and acetylene C-H activation barriers for Pt_4Ge. C-H activation barriers on Pt_4Ge / alumina thermal ensemble of states for (A) ethane, (B) ethylene, and (C) acetylene. Pt is shown in grey, Ge in green, C in black, H in yellow, Al in pale blue, and O in pale pink.

Pt_4Ge/alumina with energies below 0.4 eV, i.e., with non-zero thermal populations at 700 K. All of the low-lying configurations appear to activate ethane, as shown by C-H bond elongations ranging from 1.140 Å to 1.158 Å, compared to the un-activated C-H bond length of 1.09 Å. Figure 6.5A illustrates two reactant configurations and gives energies (horizontal lines) for a dozen more. The two illustrated are built on the GM and on the second local minimum (LM2) for the bare Pt_4Ge cluster. The LM2-based structures are singled out for reasons that will be made clear shortly. Once adsorbates bind to LM2, the structures are labeled LM', because their thermal accessibility is changed by the binding of adsorb-ates. For all the lowest-energy configurations, the activation barriers for breaking the first C-H bond are found to be $\leq$ 0.4 eV, well below the energy for desorption of ethane from the clusters ($\leq$ 0.6 eV, see Fig. E.4 and text). Thus, DFT shows that ethane should bind to all isomers of Pt_4Ge/alumina, and dehydrogenate in preference to desorbing. Another factor that tends to promote dehydrogenation is that the H atom products readily recom-bine and desorb as H_2 at moderate temperatures, as shown in Fig. 6.3E. To verify that Pt_4Ge clusters are not poisoned by ethyl, we computed the activation barrier activating the second C-H bond, for the initial low-barrier pathway. This second C-H activation barrier is practically negligible (0.02 eV), and the resulting structure for ethylene + 2H bound to Pt_4Ge was $\sim$0.74 eV lower in energy than the ethyl-bound intermediate (Fig. E.6), which was already $\sim$ 0.1 eV below

intact ethane bound to the cluster. Therefore, we conclude that Pt_4Ge should be highly active for ethane dehydrogenation to ethylene + 2H.

To examine the pathways that must ultimately lead to carbon deposition, we next performed DFT calculations for ethylene and acetylene binding and dehydrogenation on the thermally-accessible isomers of the Pt_4Ge clusters (Figs. 6.5B and C). Note that adsorbates can bind with different energies on different cluster isomers, which can significantly change isomer populations, with important effects on the mechanism. We found that ethylene predominantly binds to the Pt_4Ge clusters (including the most abundant GM) in the π-mode, i.e., with the ethylene π bond coordinated to a single Pt atom, retaining the C sp^2-hybridization (Fig. E.7). The barriers for the GM π-mode-bound ethylene to undergo C-H dissociation are higher than the desorption energies, and thus π-mode-bound ethylene is predicted to mostly desorb intact, rather than undergoing further dehydrogenation, consistent with the small D_2 desorption branching observed for the Pt_4Ge/alumina catalyst. Importantly, however, one of the thermally-accessible isomers of ethylene-Pt_4Ge, LM' (corresponding to LM2 of the bare cluster), binds ethylene in a di-σ mode (Fig. 6.5B), and in this configuration the barrier to C-H dissociation is significantly lower than in any of the π-mode-bound configurations. Furthermore, the LM' isomer binds ethylene much more strongly than the GM isomer, with an adsorption energy of -1.96 eV (Fig. E.7, E.8). LM2 for the bare cluster has P_{700K} of only 0.3% – far too small to account for the amount of D_2 desorption observed during TPD. However, the ethylene di-σ bond in LM' is strong, stabilizing LM' and increasing its P_{700K} to $\sim$3%.

We propose that dehydrogenation on an isomer with small, but significant population, accounts for carbon deposition being only partly suppressed for Pt_4Ge/alumina. Specifically, during each TPD cycle, most of the Pt_4Ge would desorb C2D4 intact, but the small fraction in LM' configurations would dehydrogenate C_2D_4, giving rise to the observed small D_2 signals. Isomerization between the thermally accessible isomers within the ensemble ensures that LM' is re-populated each TPD cycle, thus LM' acts as a "gateway" isomer that

keeps dehydrogenating ethylene on a fraction of the cluster population during repeated TPD cycling. We expect that all of the clusters eventually pass through this gateway during repeated TPD cycling, becoming coked. The calculated population of the C_2D_4-LM' isomer ($\sim$3%) is smaller than the population ($\sim$25%) suggested by D_2 TPD signal, however, we note that isomer populations depend exponentially on their relative energies, thus amplifying the effects of small DFT errors.

For coke to form, dehydrogenation must proceed further, beyond acetylene. With acetylene bound to Pt_4Ge (Fig. 6.5C, S9), the isomer populations adjust again: the LM' isomer drops even further in energy relative to the GM, such that its P_{700K} increases to $\sim$10% of the total population. The population dehydrogenates acetylene with a high propensity, rather than desorbing it, as suggested by the fact that in a number of the low-lying isomers of C_2H_2 Pt_4Ge/alumina, acetylene dehydrogenates spontaneously (Fig. E.9). For the thermally accessible isomers in which C_2H_2 remains intact, the computed first C-H dissociation barriers are well below the desorption energies for intact acetylene, which exceed 2 eV from all isomers (Fig. 6.5C, E.10). Notably, LM'-based isomers continue to dehydrogenate more aggressively than GM-based isomers, judging by the computed barri-ers, and new Pt_4Ge core isomers are stabilized due to the strong binding of acetylene, provide lower-barrier routes for dehydrogenation (Fig. 6.5C, dashed lines, Fig. E.10 for structures). Hence, theory predicts that once acetylene forms on the Pt_4Ge cluster, regardless of the isomer, it will always dehydrogenate, though higher-energy isomers will dehydrogenate at lower temperatures, some with dehydrogenation barriers less than 1 eV. This prediction is consistent with the observation that no intact acetylene desorption is ever seen for Pt_4Ge/alumina in the experiments (Fig. E.11). Thus, in ethylene TPD (and in the ethane-to-ethylene reaction), we predict that Ge addition largely, but not completely, suppresses carbon deposition, such that in repeated TPD cycles (or long reaction times) the clusters will slowly all become coked by at least a pair of carbon atoms, with the LM' isomer serving as a gateway to coking.

To assess the favorability of dehydrogenation versus C-C bond breaking (cracking), we

computed the energetics (and barriers) of cracking compared to C-H activation. For the Pt_4Ge cluster, we found no cracking pathways that could compete with C-H activation either thermodynamically or kinetically. The single struc-ture, the result of cracking ethylene, that might compete is shown in Fig. E.19, however it is both thermody-namically more uphill than any C-H breaking endpoints and has a higher barrier (1.42 eV) than any of the LM' ethylene dehydrogenation barriers.

The next question posed by the experiments is how Pt_4Ge/alumina retains its high-temperature ethylene binding sites after 21 TPDs, even though the C 1s XPS and ISS results indicated significant carbon deposition. The DFT results indicate that once dehydrogenation has gone beyond ethylene, it should proceed to completion, depositing a pair of C atoms. To test this, we performed global optimization of Pt_4GeC_2/Al_2O_3 (Figure E.12), which revealed two pairs of structures. The isomers labeled $Split_1$ and $Split_2$ have similar structures with no CC bond, oriented differently on the support, and the $Intact_1$ and $Intact_2$ isomers have similar structures with a C_2 unit bridging between Pt atoms across the center of the cluster. The $Intact_1$ and $Intact_2$ are recognizable as relatives of LM' with an embedded C_2 unit. Since these would form by dehydrogenation of acetylene, the route to forming the Intact isomers is clear, but an obvious question is whether the barrier to C-C bond scission is large enough to prevent formation of the Split isomers. The computed barrier to C-C bond scission in Pt_4GeC_2 is 1.33 eV, which should inhibit Split isomer formation. Furthermore, the presence of adsorbates (ethane, ethylene, and acetylene) stabilizes the structures with the intact C_2 unit relative to those with the split C_2, making the $Intact_1$ structure the GM. Hence, under reaction conditions, where the clusters are saturated, DFT suggests that the $Intact_1$ structure (also shown in Figure 6.6A) should be thermodynamically and kinetically favored. Furthermore, we note that the two Intact isomers of Figure E.12 have near-identical reactivities with respect to ethane, ethylene, and acetylene. Finally, note that all these structures have carbon bound such that it does not physically block Pt sites, consistent with ISS observation of minimal Pt attenuation.

The presence of C_2 does, however, alter the electronic structure of the cluster. Generally, we see the C atoms adopting a negative charge when bound only to Pt atoms, (Figure E.12), though in the case of one isomer, we see that as the C binds to an oxygen in the Al_2O_3 support, in adopts a high positive charge, as might be expected. For the active structures, with the intact C_2 unit, we see that it acts as an oxidant (due to low-lying π states), adopting a net negative charge of either 0.29 $|e|$ or 0.42 $|e|$ on the lower-energy and higher-energy structures, respectively. The Ge in each isomer becomes more positively charged, at either +0.85 $|e|$ or +0.80 $|e|$. Despite their structural similarity, there are subtle differences in the charge distribution of the isomers of the active motif (see Bader charges in Figure E.12A). Ultimately, however, each isomer has one Pt atom which remains the active site, which has the same charge (-0.33 $|e|$) on each structure. The overall charge on the Pt_4 moiety remains negative, decreased slightly from the values typical for Pt_4Ge isomers, but is still higher than that for Pt_4/alumina (Figs. 6.2A and 6.6A). The interaction of C_2 with Pt_4Ge is strikingly different from its interaction with Pt_4, as shown in Fig. E.12.

To investigate the electronic structure differences between the Pt_4C_2 and Pt_4GeC_2 clusters in more detail we performed COHP local bonding analysis for the C-C bonds in Pt_4C_2 and Pt_4GeC_2 (Figure E.13). The main feature of these plots is the sharp stabilizing peak which lies above the Fermi level in Pt_4C_2 but immediately below it in Pt_4GeC_2. Combined with the evidence of Ge-C charge transfer, this indicates that the effect of adding Ge is to strengthen the C-C π-bonding in the partially coked cluster.

While Pt_4C_2 and Pt_4GeC_2 are structurally similar, have similar total amounts of electron transfer from the support, and feature the partially negatively charged C_2 unit, they differ in the source of electron transfer to C2: In Pt_4GeC_2, C_2 receives electrons largely from Ge, leaving Pt still quite anionic. In Pt_4C_2, C_2 draws electrons from Pt, leaving it closer to the charge neutral state. Thus, it appears that in Pt_4Ge/alumina, Ge and C_2 are in a synergistic electronic relationship that preserves the net negative charge on the Pt_4 moiety. Hence, Pt sites are neither blocked nor significantly changed electronically in Pt_4GeC_2/alumina

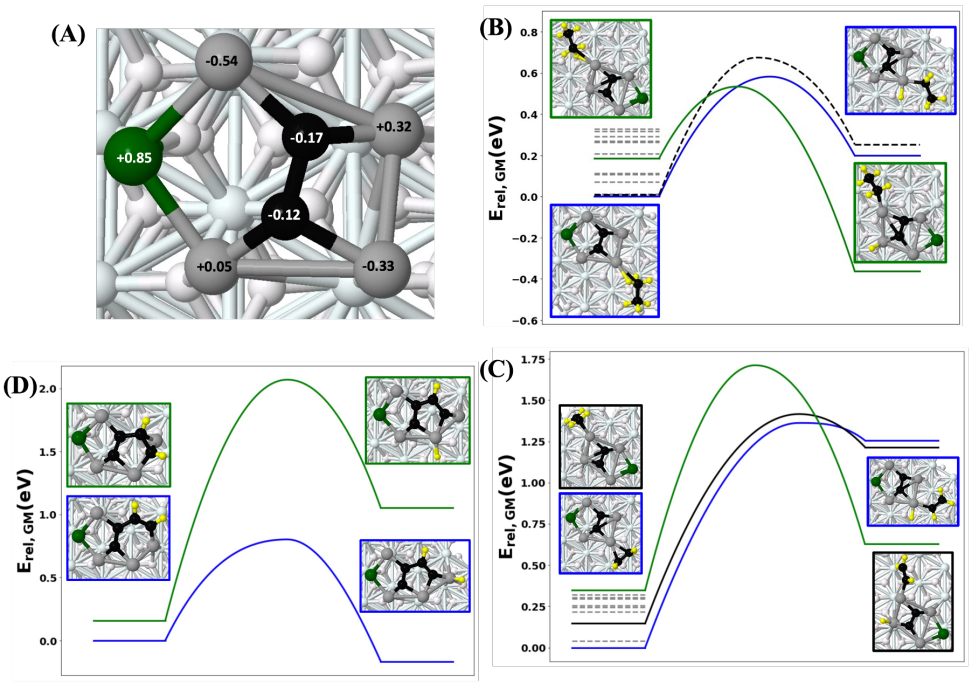

Figure 6.6: Representative ethane, ethylene, and acetylene C-H activation barriers on Pt_4GeC_2, the steady-state catalyst. (A) One dehydrogenation-active Pt_4GeC_2 isomer motif and representative C-H activation barriers for (B) ethane, (C) ethylene, and (D) acetylene, with certain key structures inset. Pt is shown in grey, Ge in green, C in black, H in yellow, Al in pale blue, and O in pale pink.

as compared to Pt_4Ge, and therefore, it is not surprising that Pt_4GeC_2 retains the strong C_2D_4 binding properties seen in the TPD. Hence, we expect the reactivity of the Pt sites in Pt_4GeC_2/alumina to be minimally affected by coking and remain comparable to that of Pt_4Ge/alumina.

The important remaining questions are whether Pt_4GeC_2/alumina is still active for ethane-to-ethylene dehydrogenation, and whether it is selective against additional carbon deposition, thereby resisting deactivation. Ethane sticks too weakly to any of these samples to allow the ethane-to-ethylene conversion process to be studied under our surface science conditions. We plan experiments at higher pressures (and with larger alkanes) to test the full alkane-to-alkene conversion process, but this will require a new major instrument that is not available presently. Therefore, ethane dehydrogenation on Pt_4GeC_2 is addressed by DFT in

Fig. 6.6B. Binding of ethane and ethylene on the Pt_4GeC_2 clusters in various geometries was sampled (Figs. E.14 and E.16), and then the barriers for C-H dissociation calculated (Figs. E.15, E.17). Again, adsorbates stabilize the isomers with the intact C_2 motif, which are active for ethane dehydrogenation, with lower C-H activation barriers than desorption energies. This suggests that Pt_4GeC_2 should still be active for ethane to ethylene dehydrogenation. We performed the same analysis of second C-H activation for the low-barrier C-H activation and found that while the second barrier is slightly higher than the first one, this should not prevent ethylene formation (Fig. E.6). In contrast, lowest energy Pt_4GeC_2 structure with a split C_2 unit (which we believe is inaccessible) did not chemisorb ethane. To be stable with respect to further carbon deposition, it is necessary that the resulting ethylene desorb instead of dehydrogenating further. For ethylene on Pt_4GeC_2/alumina (Figs. E.16, E.17 and 6.6C), some configurations were calculated to have highly endothermic (>1.2 eV) dehydrogenation, and in others, the activa-tion barriers were high (>2 eV). Some structures showed the possibility for dehydrogenation of ethylene, with barriers between 1.3-1.5 eV to access structures that are not highly endothermic, however, we note that these barriers are higher than those for the dehydrogenation of ethylene on the Pt_4Ge cluster, indicating that the Pt_4GeC_2 cluster is even more selective against ethylene dehydrogenation to form coke precursors than the initial Pt_4Ge catalyst. Acetylene dehydrogenation by Pt_4GeC_2 (Fig 6.6D, E.18) is possible, however due to the in-creased selectivity towards ethylene desorption, we consider the catalyst to remain an active catalyst with self-limiting coking. We note that the adsorption energies of acetylene to the cluster are quite high, (around $\sim$3 eV), so we may consider acetylene to act as coke itself, either dehydrogenated or not. This aligns with experi-ment, where no acetylene desorption is observed during TPD (Fig. E.11).

In order to assess possible coke formation via cracking on Pt_4GeC_2, we also computed the energetics of the C-C bond scission on relevant intermediates. A few of the pathways found are thermodynamically viable, however the kinetics render them unlikely compared to either C-H activation or desorption (Fig. E.19), with the exception of acetylene cracking,

where the barrier is ∼0.3 eV higher than the lowest barrier for C-H activation.

Ultimately, however, DFT calculations suggest that while coke formation on the Pt_4Ge system is not avoided, the cluster nonetheless retains its active and selective nature towards alkane dehydrogenation. Thus, the conclusion is that selectively-coked Pt_4GeC_2/alumina, generated under reaction conditions by a self-limiting coking process, is the actual stable, active, and selective catalytic species for alkane-to-alkene dehydrogenation.

It is interesting to compare the behavior of the Pt_4Ge system to Pt_nB_x and Pt_nSn_x, both of which were studied by similar methods.[12, 108, 206] For boron, saturated diborane exposures were used to borate size-selected Pt_n/alumina, and it was found that ethylene exclusively desorbed intact from the borated catalysts, i.e., car-bon deposition was suppressed. Unfortunately, however, the high temperature/strong ethylene binding sites were also completely blocked by boration, suggesting that coking was suppressed only because the ethylene all desorbed before the dehydrogenation onset temperature was reached.[108, 206] Because these strong binding sites are important for ethane-to-ethylene conversion, boration would, therefore, likely suppress this chemistry. In the case of Sn, a $SnCl_4/H_2$ treatment, similar to that used for Ge addition, was used to modify Pt_n clusters d-posited on both alumina[12] and silica.[10, 27] supports. The treatment yielded alloyed clusters with stoichiometries close to 1:1, for example Pt_4Sn3 when modifying Pt_4. The Pt_nSn_x clusters on either silica or alumina support were found to almost completely suppress ethylene dehydrogenation, in this case retaining some high temper-ature/strong ethylene binding sites, desirable for promoting ethane-to-ethylene conversion. The limitation for Sn alloying was that it resulted in a substantial reduction in the number of such sites compared to Pt_n (or Pt_nGe) which would tend to suppress ethane-to-ethylene activity. The advantage of Ge alloying is that small Ge:Pt ratios are sufficient to strongly modify the cluster electronic and catalytic properties, and let to the unique self-limiting coking effect. Another point of comparison is with a recent report from Zheng et al, selective CO poisoning was used to enhance catalytic hydrogenation reactions on alumina- and titania-supported Pd clusters/ [207]

6.3 Conclusion

In summary, from the TPD, XPS, and DFT results, we found that Pt_4Ge/alumina promotes intact desorption of ethylene in ethane dehydrogenation, largely, but not completely preventing carbon deposition. There is one minority isomer of Pt_4Ge/alumina (LM2, or LM') that acts as a gateway to carbon deposition on Pt_4Ge/alumina, gradually resulting in all the Pt_4Ge clusters becoming coked. However, contrary to expecta-tions, coking is not detrimental to catalytic activity, and instead preserves the desired catalytic properties while enhancing cluster catalyst stability. The coking is self-limiting: once Pt_4GeC_2/alumina forms, it decreases the further deposition of carbon by ethylene dehydrogenation through increased C-H activation barriers, eventually reaching a steady-state catalyst where no further changes in the ethylene binding sites or D_2 desorption are observed experimentally. Furthermore, Pt_4GeC_2/alumina still binds ethane strongly, with low activation barriers for ethane-to-ethylene conversion. Thus, the self-limiting coking of Pt_4Ge improves the selectivity of the catalyst without degrading the activity. The Ge atom in the cluster interacts with the carbon in the coked cluster, stabilizing the cluster, and preventing deactivation of the cluster via either physical blocking of sites, or dramatic change in electronic structure. This moderates the tendency of the cluster to coke, enabling the self-limiting behavior. The synergy between alloying and selective coking could be a way forward in creating ultra-stable sub-nano cluster catalysts for other reactions, solving the main limiting factor hampering wide-spread use of sub-nano clusters in catalysis.

6.4 Methods

Instrument design. Past publications detailed the instrument design and protocols used in this study.[10, 12, 108] Briefly, Pt_n^+ cluster ions were produced via laser ablation of a Pt target, collected by a series of quadrupole ion guides, mass selected by a quadruple mass filter, and then guided into the ultra-high vacuum system, where they were deposited on the

catalyst support. The support consisted of a thin alumina film grown on a Ta (110) single crystal, which was mounted via heater wires to a cryostat allowing temperature control in the 120 K to 1000 K range. For cleaning, the sample could be heated by electron bombardment; from behind the cryostat, a filament allowed bombardment of electrons to the single crystal, that could heat the crystal to over 2100 K. At that temperature, the alumina film and any deposited clusters desorb, and the sample was found to be clean by X-ray photoelectron spectroscopy (XPS).

Alumina film growth. A fresh alumina film was grown on the clean Ta (110) single crystal before each experiment, by evaporating Al in 5×10^{-6} Torr of O_2 at sample temperature of 970 K. These growth conditions produce alumina with a distorted hexagonal lattice that resembles both γ-alumina (111) or α-alumina (0001)/ [148, 208] Film thickness was monitored by XPS and was in the 4 to 6 nm range, which we previously found to give chemistry independent of film thickness. [149]

Pt_4/alumina sample preparation. Pt_n^+ clusters of the desired size, Pt_4 in this case, were deposited on the alumina film with deposition energy of ∼1 eV/atom and coverage equivalent to ∼0.1 monolayer (ML), corre-sponding to 1.5×10^{14} Pt atoms/cm^2. Just prior to deposition, the sample was flashed to 750 K to desorb any adventitious adsorbates, and then cluster deposition was carried out as the sample cooled, starting at 300 K.

Pt_4Ge/alumina sample preparation. The approach used to prepare alumina-supported Pt_nGe_m clusters was similar to that used in previous studies of Pt_nSn_m/alumina and Pt_nSn_m/SiO_2. [12, 27] In essence, the Pt clusters were used as seeds to obtain selective, self-limiting deposition by exposing the Pt_4/alumina sample to a 60 L dose of $GeCl_4$ vapor, then to 6000 L of H_2. The $GeCl_4$ preferentially binds to the Pt_n clusters, and the number of molecules that bind depends on the size of the cluster. When exposed to H_2, Cl reacts and desorbs as HCl, which can be detected mass spectrometrically. The final stage in the preparation was to heat the samples to 750K to desorb any remaining Cl atoms (as HCl) as well as to remove excess H atoms. The samples were characterized by X-ray photoelectron spectroscopy (XPS). The

Pt_n clusters were found to "seed" preferential Ge deposition on the clusters, resulting one Ge atom for every Pt_4 cluster deposited as discussed above. Note that if larger $GeCl_4$ exposures are used, the amount of Ge deposited does not change. Thus, Ge addition to the clusters is limited by the number of $GeCl_4$ precursor molecules than can adsorb per cluster, in this case 1 $GeCl_4/Pt_4$.

Some non-specific Ge deposition at defects in the alumina support film also occurs (as discussed in Appendix E section 6), but ethylene temperature programmed desorption indicates that these support-bound Ge atoms have little effect on the chemistry of Pt_4 deposited on the Ge-treated alumina. To show this, 0.1 ML Pt_4 clusters were deposited onto alumina supports that had been pre-treated with Ge, using the same protocol used in Ge addition to the clusters (60 L of GeCl4, 6000 L of H_2). C_2D_4 TPD on these samples gave results very similar to those for Pt_4 deposited on Ge-free alumina. Large dehydrogenation signals implying coking are seen, along with rapid deactivation in repeated TPD cycles, i.e., support-bound Ge does not suppress coking and sintering (see supporting information Fig. E.20, E.21). As shown in Fig. 6.3, Ge deposited on the clusters has very different results, strongly suppressing coking and stabilizing the clusters.

XPS quantification. XPS was used to characterize the ratio of Ge to Pt present in the samples, and to measure carbon deposition. Samples were analyzed via Al Kα XPS and the raw intensities were corrected to account for slight day-to-day changes in spectrometer sensitivity and X-ray intensity using the Al 2s intensities from the alumina support (details in Supplementary Information).

Temperature programmed desorption (TPD) experimental procedures. TPD was used to investigate C_2D_4 desorption and dehydrogenation/carbon deposition chemistry on the samples. To start each TPD cycle, the samples was held at 150 K and exposed to a 10 L dose of C_2D_4, which is sufficient to saturate all binding sites that are stable at 150 K. The sample was then heated at 3 K per second to 750 K, while monitoring desorption of species of interest (principally C_2D_4 and D_2) using a differentially pumped mass spectrometer that views

the sample through a 2.5 mm aperture on a skimmer cone, positioned ∼0.5 mm from the sample surface. The relationship between numbers of molecules desorbing from the sample and numbers of ions detected by the mass spectrometer was determined using a procedure described elsewhere,[12] calibrated by leaking C_2D_4 or D_2 into the main UHV chamber at measured pressures to create well defined fluxes of into the mass spectrometer.

C_2D_4 was used to minimize interference from mass spectrometer background from CO and H_2 which are al-ways present in UHV chambers. For C_2H_4, the intact desorption signal would have interference from CO (both mass 28) and the dehydrogenation signal would have background from H_2. For C_2D_4, detection of possible C_2D_2 product has interference from CO, and experiments were also done with C_2H_4, to verify absence of C_2H_2 desorption. There were no obvious deuteration effects on the ethylene desorption temperature dependence.

Computational Methods. Global optimization of the Pt_4Ge/alumina structures was performed with plane-wave density functional theory (PW-DFT) using the Vienna Ab-initio Simulation Package (VASP) [114–116] with projector augmented wave (PAW) potential,[118] using the PBE functional.[70] The kinetic energy cutoff for the plane wave basis sets was chosen as 400.0 eV, and Gaussian smearing with a width (σ) of 0.1 eV was used. The convergence criteria for electronic minimization and geometry optimization were 10^{-6} eV and 0.01 eV/Å, respectively. The D3 dispersion correction was used. [209] The model substrate used was an γ-alumina(0001) surface with cell parameters of a = 4.807 Åand c = 13.126 Å, previously found 20 to best match the experimental support. The lower layers of the slab were kept fixed during global optimization and subsequent adsorbate binding calculations. Only Γ-point sampling was used due to the larger supercell used in the study.

Our initial Pt_4Ge structure geometries were obtained using our in-house code PGOPT,[120] which uses a bond-length distribution (BLDA) algorithm in order to generate structure that are faster to optimize and less likely to result in errors during optimization. Once ∼200 Pt_4Ge structures had been generated, we took the thermally accessible structures within a cutoff of 0.4 eV, and generated a number of rough binding modes of C_2H_6, C_2H_4, and C_2H_2

using PGOPT, which we later refined with VASP local optimizations to obtain the final binding modes. The final ensemble of thermally-accessible catalyst states was computed for the initial cluster structures, and re-computed for every intermediate on the reaction profile, by weighting the optimized structures by the Boltzmann probability to be occupied at 700 K, based on DFT electronic energies.

The Pt_4GeC_2 structures were generated from the thermally accessible acetylene binding modes to Pt_4Ge by removing the hydrogens then optimizing the resulting structures with DFT. Bader charge analysis[121, 122, 124, 210] was performed to obtain the partial atomic charges. C-H activation barriers for low-lying and important binding modes were calculated using the climbing-image nudged elastic band (CI-NEB) method[210] and optimized until the force on all of the images was less than 0.02 eV/Å. For ethylene and acetylene, multiple non-equivalent C-H bond breaking events were attempted, focusing on the hydrogens closest to Pt atoms. For ethane, only the elongated activated C-H bonds were broken. Adsorption energies of ethane, ethylene, and acetylene to the Pt_4GeC_2 clusters were calculated with the equation $E_{ads} = E_{clust+ads} - E_{clust} - E_{gas}$, using the bare supported cluster which best matched the cluster core of the adsorbate-bound structure.

Local bonding analysis was performed using the LOBSTER program, version 4.1.0. [150, 151] The PBEvaspfit basis was used with 3s3p basis functions for Al, 2s2p for O and C, 5p5d6s for Pt, and 4s4p for Ge. All projections were converged with a charge spilling of less than 1.2 %.

CHAPTER 7

Promoter-poison partnership protects platinum performance in coked cluster catalysts

7.1 Introduction

The formation of coke, or carbonaceous deposits, is a persistent problem for dehydrogenation catalysts, as it results in their rapid deactivation. Deactivation is typically attributed to physical blocking of active sites on the catalyst. Coke formation on Pt-based alkane dehydrogenation catalysts originates from the lack of selectivity of the catalyst; side reactions for deeper dehydrogenation past alkenes and C-C cracking contribute to coke formation. Approaches to preventing coke formation include co-feeding H_2 [211], changing Pt nanoparticle size [212], and dopants or promoters such as Sn,[12, 27, 28] Ge,[13, 213] Si,[26] Ga,[214–216] Zn,[217] and B[9, 218, 219]. These approaches all favor desorption of the desired alkenes over deeper dehydrogenation or side- reactions.

Coke formation typically occurs in two stages; an initial fast coking regime, and a later regime where the buildup of further coke is much slower, [220, 221] which indicates that early coking stages change catalysts selectivity to limit further coking. This change in selectivity has been attributed to carbon blocking the most reactive and least selective sites, which can catalyze side-reactions leading to coke formation.[201, 202, 222–225] An additional explanation is that the presence of carbon can modify olefin adsorption strength on a surface, and increase the energy barrier for C-H activation. [221] Coke may therefore deactivate Pt catalysts via an electronic interaction, in addition to steric blocking.

The interaction between metal and coke influencing selectivity is reminiscent of dopants or promoters; the selectivity improvement from adding Sn or Ge to the Pt catalyst comes at the cost of activity, though not to the same extent as coking. Sn is the most widely-used dopant for Pt, though Ge has been found to produce similar improvements in stability against coking.[201, 202, 224, 225] XPS of subnano PtSn clusters shows a shift to lower binding energies, implying that Sn tends to donate electrons to Pt. [27] However, there have been reports that PtSn catalysts build up more coke than their pure Pt analogues,[226] suggesting that they are not simply resistant to the build-up of coke, but that their activity persists despite partial coking.

The contrast between the electronic and steric mechanisms of coking, and the role of doping are represented in Figure 7.1.

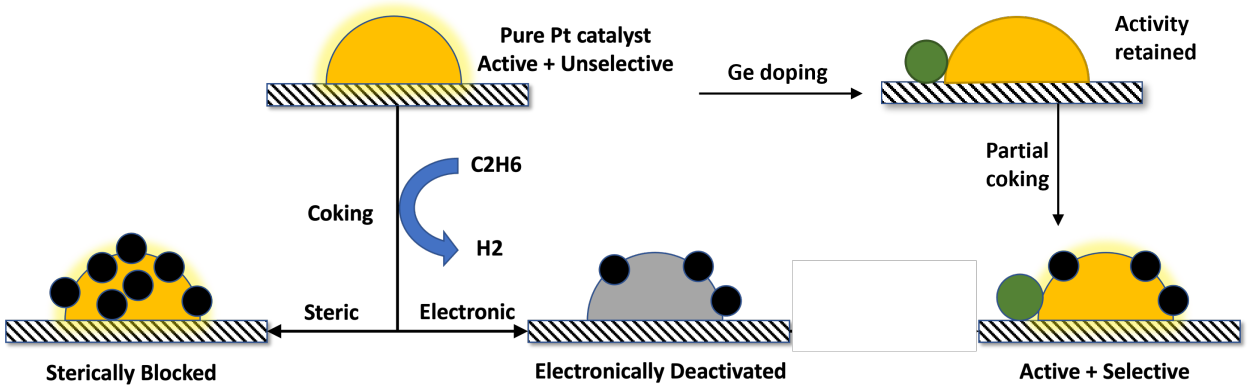

Figure 7.1: Schematic showing the steric and electronic deactivation mechanisms of coked platinum catalysts, and the activity-preserving effect of doping on partially coked catalysts.

Sub-nano clusters are promising catalysts due to their high atom utility, and ability to outperform bulk-like catalysts by breaking scaling relations.[227] Pure Pt clusters have been studied as alkane dehydrogenation catalysts,[19] as have various dopants to improve catalyst selectivity, including B,[9] Si, [26] Ge [13] Sn[12, 27, 28], and S[228]. Previous computational and experimental work investigating the role of dopants has spanned a number of supports;

PtSn clusters have been explored on both SiO_2 and Al_2O_3, [12, 27, 28] showing similar effects of doping on selectivity and stability, regardless of support. Additionally, PtB clusters have been investigated on MgO[218] and Al_2O_3,[9] also showing similar effects of the dopant independent of the support. The prediction of Ge as a superior dopant via DFT was based on MgO as the support, which was substantiated by experiment on Al_2O_3, also showing that the role of dopant can be generalized across support. [13, 229] Surface-supported clusters are fluxional, isomerizing rapidly under the high temperatures of real reactions such that metastable structures are thermally populated.[6] Higher-energy isomers often show greater catalytic activity than the global minimum isomer.[229–231] If the kinetic barriers for isomerisation are low, then the isomer populations will be determined by a Boltzmann distribution.[4] If a cluster were to have high isomerisation barriers then the ensemble would not thermally equilibrate, and macroscopic properties would be determined by the reduced set of accessible isomers, which could be useful if the prevalent isomers have superior activity.[7]

We recently predicted and observed that Ge-doped Pt_4 subnanoclusters, supported on Al_2O_3, display superior stability over pure Pt_4 due to the formation of a carbon-containing species Pt_4GeC_2, which is resistant to deactivation by coke and is predicted to be a catalyst for ethane dehydrogenation.[13, 229] This parallels the behavior of PtSn nanoparticles which remain active despite building up more coke than their pure Pt analogues[226]. Transforming a poisoning process into in-situ catalyst synthesis by doping, illustrated in the right-most part of Figure 7.1, is a key aspect of catalyst design that deserves greater attention. To apply this strategy to other reactions, we must first understand the fundamental chemistry behind the efficacy of Pt_4GeC_2.

In this paper we investigate the electronic synergy between Ge and coke in Pt_4 clusters in the context of ethane dehydrogenation with a combination of DFT calculations and experiment. For the DFT calculations, we focus on the "pristine" clusters Pt_4 and Pt_4Ge, and their partially coked counterparts Pt_4C_2, and Pt_4GeC_2. After obtaining the ensemble

of isomers, we perform transition state calculations to obtain barriers and determine the reactivities of these isomers towards ethane and ethylene dehydrogenation. Bonding analysis of the interaction between Ge and C_2 provides a chemical explanation of the stability trends. With supporting experimental evidence from ISS and TPD data, we observe that Ge mitigates the deactivating effect of C towards ethane dehydrogenation, and improves the selectivity towards ethylene desorption.

7.2 Results and discussion

7.2.1 Cluster Ensembles

In order to understand why Pt_4GeC_2 is a stable and selective catalyst, while Pt_4 continues to coke, we compute the geometries and C-H activation barriers of ethane, ethylene, and acetylene on Pt_4 and Pt_4C_2, and compare them to equivalent results for Pt_4Ge and Pt_4GeC_2. [229] The compositions Pt_4 and Pt_4Ge were chosen, as described in our previous work,[229] based on experimental compositions determined via XPS.

Figure 7.2 shows the full ensembles for Al_2O_3-supported (a) Pt_4, (b) Pt_4C_2, (c) Pt_4Ge, and (d) Pt_4GeC_2. Atomic Bader charges are shown on or near their corresponding atoms. Most Pt motifs are common to Pt_4 and Pt_4Ge, with Ge sitting on the edge of the Pt core. Addition of C_2 induces dramatic restructuring of both clusters, but the isomers for Pt_4C_2 and Pt_4GeC_2 are nonetheless very similar. Note the similarity between the Pt_4C_2 and Pt_4GeC_2 global minimum (GM) structures, as well as the similarity between the structures with the intact C_2 unit incorporated into the center of the cluster. The C atoms are mostly 3-coordinate and there are two motifs of carbon binding; either the C_2 unit has been split, or it remains intact. The Pt atoms are on the edges of the clusters, so incorporation of C into the Pt_4 cluster does not block Pt sites from interacting with gas-phase molecules. This contrasts with the conventional view of coke poisoning, which is that the Pt core retains its initial structure and active sites are blocked by a layer of carbon. Pt sites in these structures are

still exposed after coking, which suggests that coke alters the activity and selectivity of Pt subnanoclusters through electronic effects, rather than by steric blocking. This agrees with literature which suggests an electronic component to deactivation via coke formation.[220, 221] Thus, the particular stability of Pt_4GeC_2 must arise from a combination of electronic effects that work together to enhance selectivity without sacrificing activity.

The computed Bader charges are our first piece of evidence for the nature of these electronic effects. Ge always has a strong positive charge, as expected from electronegativities. In contrast, C atoms are negatively charged, which increases in magnitude in the presence of Ge. The average charge on Pt becomes increasingly negative upon addition of Ge, and becomes increasingly positive upon addition of C_2. However, the charges on individual Pt atoms depends strongly on the location of Pt relative to the Al_2O_3 surface. Pt atoms that are closer to the support adopt a positive charge, while Pt atoms that do not directly interact with the support adopt a negative charge. As C_2 and/or Ge are incorporated into the clusters, the Pt atoms closest to Ge become more negatively charged, while atoms closer to C become more positively charged.

So far we have described the isomeric ensembles of the 'bare' clusters, without adsorbates. Once we bind ethane, ethylene, and acetylene, the relative stabilities of the different Pt_4C_2 and Pt_4GeC_2 core structures change. For Pt_4C_2, binding ethylene and acetylene favors the isomer with the intact C_2 unit, to the point where the C_2H_2/Pt_4C_2 ensemble only contains Pt_4C_2 core structures with the intact C_2, and the C_2H_4/Pt_4C_2 ensemble only has the split isomer at higher energies (Fig F.1). For Pt_4GeC_2 the distinction between C-C bonded and split isomers is especially important because the latter do not contribute to catalysis. Binding energy calculations suggest that ethane will physisorb to the split isomer (Fig. F.3), but as there is no chemical bond between the ethane and the cluster, we can consider this isomer to be inactive. The C-C bonded isomer, which lies just 0.06 eV above the global minimum isomer in the absence of adsorbates, has ethane C-H activation barriers ranging from 0.42-0.50 eV, and so is catalytic. [229] Furthermore, once ethylene and acetylene bind

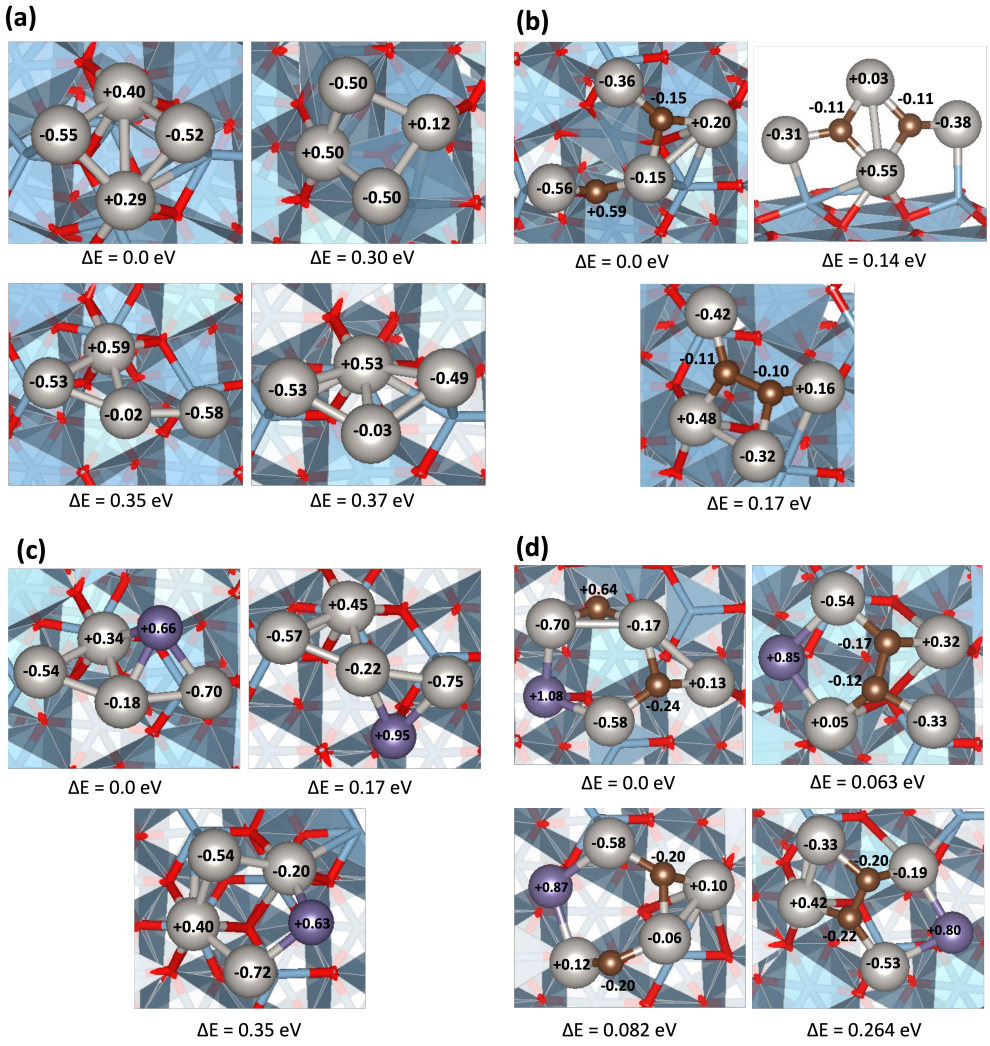

Figure 7.2: Thermally accessible structures obtained via global optimization for alumina–supported (a) Pt_4, (b) Pt_4C_2, (c) Pt_4Ge, and (d) Pt_4GeC_2. Bader charges are shown on or near each corresponding atom. Pt is shown in grey, C in brown, Ge in purple, Al in blue, and O in red.

to Pt_4GeC_2, the bonded isomer dominates the ensembles and the split isomer is pushed much higher in energy (Fig. F.3). For Pt_4C_2, the split isomer, while less reactive towards ethane (barriers ranging between 0.6-0.9 eV), is more reactive towards ethylene, with a C-H activation barrier 0f 0.80 eV (Fig F.2). The accessible binding modes for ethane and ethylene on Pt_4C_2 show a wider range of cluster cores than for Pt_4GeC_2 (as mentioned above, see SI for the structures), each of which with variable reactivity. We attribute this difference in activity of the split isomer in Pt_4C_2 compared to Pt_4GeC_2 to the fact that the Pt centers that bind ethane and ethylene in the split Pt_4C_2 isomer are bonded to Ge in Pt_4GeC_2 and therefore have very different electronic character. The relationship between isomerism and reactivity in Pt_4GeC_2 makes it important for us to establish the relative populations of the split and bonded isomers. The barrier to direct interconversion is 1.33eV (Fig. F.4), placing Pt_4GeC_2 in the unusual non-Boltzmann regime where the isomers do not thermally equilibrate. The populations will instead be determined by their formation rates, which are equivalent to the relative rates of dehydrogenation and C-C cracking on Pt_4Ge. We will discuss the kinetic data for these processes later.

7.2.2 Activity vs. Selectivity

To explore the balance of activity and selectivity of Pt_4, Pt_4C_2, Pt_4Ge, and Pt_4GeC_2, we plot the C-H activation barriers against the adsorption energies for ethane and ethylene, as shown in Figure 7.3 (a) and (b), respectively. The balance between adsorption energy and activation energy is a useful descriptor of reactivity because it captures the two main competing processes for an adsorbate bound to a catalyst. Each point represents an isomer and binding mode, so this representation accounts for the effect of cluster fluxionality. The corresponding ethane and ethylene isomer ensembles and C-H activation barriers can be found in the SI. The colored shapes reflect the isomer distributions of each cluster composition, and are intended only to highlight general trends in composition and catalytic properties. The dashed line represents the parity line, where the (first) C-H activation barrier is equal

in magnitude to the adsorption energy. Note that we use the first C-H activation barrier as the rate limiting step, as has been previously shown, [232] however to validate this, we calculated the second C-H activation barriers for ethane on the Pt_4, Pt_4C_2, Pt_4Ge, and Pt_4GeC_2 isomers with the lowest first C-H activation barriers. All the second C-H barriers are lower than the first one (Fig. F.5). The lower-left region of each graph in Figure 7.3 describes strong binding and low C-H activation barriers, which favors dehydrogenation, while the upper-right region describes weak binding and high barriers, which favors desorption. An

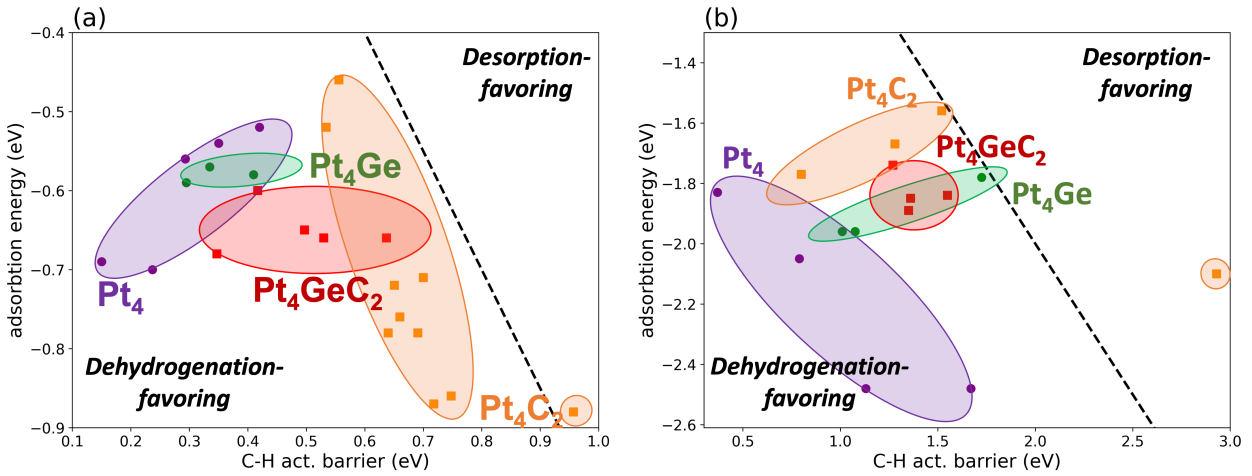

Figure 7.3: Comparison between adsorption energy and first C-H activation barrier per given isomer of Pt_4, Pt_4C_2, Pt_4Ge, and Pt_4GeC_2 for (a) ethane and (b) ethylene. The dashed line represents parity, where the adsorption energy is equal to that of the C-H activation barrier. The closer the given points are to the upper right corner, the more desorption-favoring that given adsorbate binding mode is; the closer to the bottom left, the more dehydrogenation–favoring the binding mode.

optimal selective catalyst will appear in the lower-left region of the ethane graph, as ethane dehydrogenation is the target reaction, and the upper-right region of the ethylene graph, as this is our desired product and dehydrogenation of ethylene will lead to coking. The adsorption energies are not corrected for the entropy of the adsorbate in the gas phase, to improve comparability between the adsorption and activation energies. This entropy correction is the same for all clusters on a graph, so it does not affect our conclusions about the effects of coking or doping on activity and selectivity. Furthermore, the precise entropy of ethylene in

the gas phase depends on the conversion of ethane to ethylene, which we cannot determine in a straightforward way from these calculations.

For ethane (Fig. 7.3(a)), we see that Pt_4 is the most active composition, as its points are furthest away from the parity line, i.e. the C-H activation barrier is lowest compared to the adsorption energy of ethane. Pt_4Ge overlaps with the Pt_4 distribution, indicating that the two have similar activities. Compared to Pt_4, Pt_4C_2 has a much wider spread of points that are closer to the parity line, showing that small coke deposits deactivate Pt for ethane dehydrogenation. Pt_4GeC_2 on the other hand does not shift so dramatically compared to Pt_4Ge, with adsorption energies and C-H activation barriers both increasing slightly when carbon is added. The Pt_4GeC_2 points remain clustered quite close to Pt_4 and Pt_4Ge, indicating that a small amount of coke does not significantly deactivate Pt_4Ge for ethane dehydrogenation.

For activity towards ethylene (Fig. 7.3(b)), we see a different trend with composition. The Pt_4 points are much farther from the parity line than all other cluster compositions, highlighting the tendency for Pt_4 to dehydrogenate ethylene and coke. All other cluster compositions, with dopant and/or poison, are located much closer to the parity line, indicating increased preference for desorption of ethylene over dehydrogenation. The GM $C_2H_{4/}Pt_4C_2$ isomer is an outlier, binding ethylene strongly but having a very large activation barrier, while the higher-energy isomers are grouped in a region with weak binding and surmountable barriers. In contrast, the Pt_4Ge and Pt_4GeC_2 regions in Figure 7.3a are clustered close to the parity line, indicating superior selectivity for ethylene desorption to Pt_4.

One aspect that Figure 7.3 does not capture is the tendency for side-reactions, such as cleavage of the C-C bond preferentially over the C-H bond, to compete. This is known to be a coke-promoting side reaction on Pt catalysts, [220–223] and that the addition of dopants limits their occurrence. [217, 224, 233–235] In order to assess the preference for C-C vs. C-H cleavage of Pt_4, Pt_4C_2, Pt_4Ge, and Pt_4GeC_2, we computed C-C bond breaking barriers for isomers where we already had the barriers for C-H activation. These results are summarized in Table F.1 and Figure F.6. Ultimately, we find for Pt_4, once acetylene forms, the barrier for

C-C bond breaking is lower than that of C-H activation (0.76 eV compared to 0.97 eV). Prior to acetylene formation, however, C-H activation is preferential. This agrees with literature. [220–222] This also holds for Pt_4C_2; only for acetylene does C-C cleavage have a lower barrier than C-H activation. However, in the presence of coke, all barriers are greater, reflecting the general deactivation of the catalyst. Thus, for the Pt_4C_2 ensemble, it is possible to access the split C_2 isomer via splitting of acetylene, prior to dehydrogenation. This enables the full Pt_4C_2 ensemble to be kinetically accessible. In contrast, Pt_4Ge always favors C-H activation over C-C cleavage, regardless of the adsorbate. Not only does this prevent a coke-forming side-reaction, but this also kinetically traps the ensemble into structures with the intact C_2 unit, which, as mentioned above, is in fact the active isomer for ethane activation.

7.2.3 Bonding Analysis

The next question is, 'How do Ge and C_2 interact to produce a coke-resistant cluster catalyst?'. To answer this question we calculate integrated crystal orbital Hamilton populations (ICOHPs)[236] for C-C bonds in Pt_4C_2 and Pt_4GeC_2, and the species formed when each of these binds an ethylene molecule, C_2H_4/Pt_4C_2 and C_2H_4/Pt_4GeC_2. This analysis is done for isomers which contain carbon in the form of C-C dimers, rather than separated C atoms, due to their greater activity and accessibility as Pt_4GeC_2. These isomers are the most catalytically important (Fig F.3), and the structural similarities between the doped and undoped clusters allow us to draw conclusions about the electronic effects of doping. The results are shown in Figure 7.4, where the ICOHPs are shown (blue annotations) alongside the respective C-C bonds. Comparing Pt_4C_2 to Pt_4GeC_2 we find that doping with Ge increases the C-C ICOHP from -11.5 eV to -12.8 eV; added Ge enhances the C-C bond strength. Molecular orbitals (Fig. F.8), density of states, and COHPs (Fig. F.9) show that this is due to Ge donating electrons into a C-C π-bonding orbital. The bond strength comparison explains energetic differences in the isomer distributions of Pt_4C_2 and Pt_4GeC_2 in Figure 7.2 - in Pt_4C_2 the isomer with the C-C bond is 0.17 eV above the global minimum, in which the

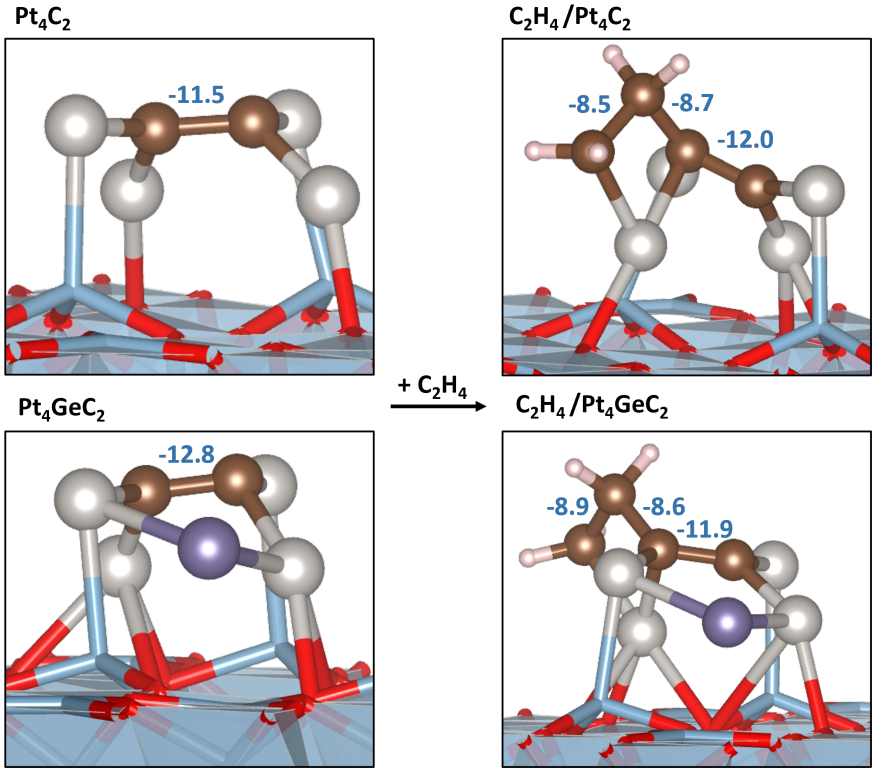

Figure 7.4: C-C ICOHPs (blue numbers, units of eV) for Pt_4C_2 (upper left), Pt_4GeC_2 (lower left), C_2H_4/Pt_4C_2 (upper right), and C_2H_4/Pt_4GeC_2 (lower right). Pt is shown in grey, C in brown, Ge in purple, H in white, Al in blue, and O in red.

C atoms are separated, while the energy gap between equivalent isomers of Pt_4GeC_2 is only 0.06 eV. Next, we compare Pt_4C_2 and Pt_4GeC_2 isomers with ethylene bound to both Pt and to the C_2 unit. When binding a C_2H_4 molecule, the intra-cluster C-C bond in Pt_4C_2 is strengthened (ICOHP rises from -11.5 eV to -12.0 eV), while the equivalent bond inPt_4GeC_2 is weakened (ICOHP falls from -12.8 eV to -11.9 eV). This implies that Ge weakens the binding of ethylene to Pt_4GeC_2 because the internal C-C bond must be partially broken, while the initially weaker bond in Pt_4C_2 is strengthened by binding ethylene. Pt_4GeC_2 is therefore resistant to coking relative to Pt_4C_2. This is reflected in the ethylene binding energies, which are -2.10 eV for Pt_4C_2 and -1.85 eV for Pt_4GeC_2.

7.2.4 Role of Ge Content in C-C interactions

We have determined that doping with Ge strengthens the C-C bond in Pt_4GeC_2, so we wish to know whether this behavior is general. Since the bond strength maps onto the relative energies of isomers with C atoms bonded or separated, we can screen isomers and categorise them by the numbers of C-C and Pt-C bonds, which is more efficient than bonding analysis with ICOHP. We performed global optimizations of $Pt_4Ge_xC_2$ (x = 0-2) and in Figure 7.5 we plot the numbers of C-C (orange) and Pt-C (blue) bonds in each isomer vs isomer energy. The orange points show the number of C-C bonds, defined as a C-C distance of less than

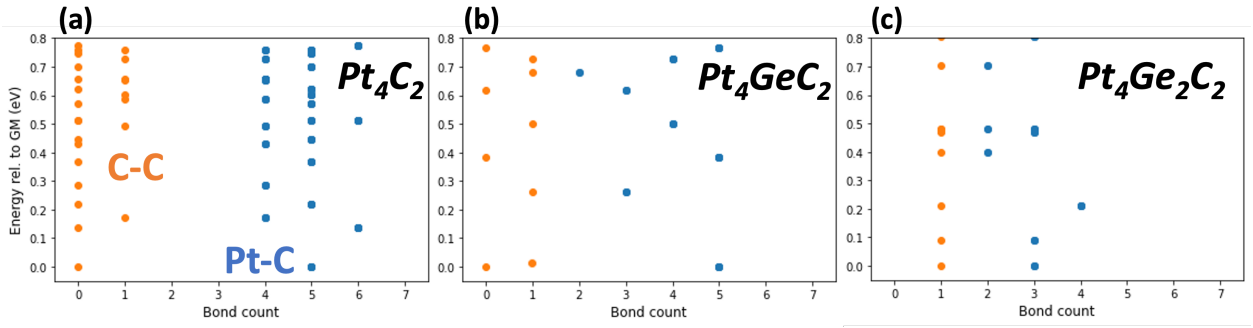

Figure 7.5: Plots showing number of C-C and Pt-C bonds agains the energy of a given isomer relative to the GM structure for (a) Pt_4C_2, (b) Pt_4GeC_2, and (c) $Pt_4Ge_2C_2$, showing the dependence of number of C-C bonds with Ge content for $Pt_4Ge_xC_2$ clusters.

1.75 Å, which can only be 0 or 1 here. In Pt_4C_2 most of the low-energy isomers have no C-C bond, while Pt_4GeC_2 shows a more even distribution of C-C separated and bonded isomers, and $Pt_4Ge_2C_2$ features only C-C bonded isomers. The blue points show the number of Pt-C bonds in each isomer, defined by a 2.25 Å cutoff length. The number of Pt-C bonds falls as the amount of Ge in the cluster increases, from 4-6 in Pt_4C_2 to 2-4 in $Pt_4Ge_2C_2$. It therefore appears that strengthening C-C bonds by Ge doping causes clusters to adopt structures with more C-C bonds at the expense of Pt-C bonds. The phenomenon of Ge doping strengthening C-C bonding appears to be general across a range of Ge concentrations, and we anticipate that this could be extended to other Pt_n cluster sizes.

7.2.5 Experimental Support

We previously reported a study of desorption, decomposition, and carbon deposition on Pt_4 and Pt_4Ge supported on alumina thin films, measured by temperature programmed desorption (TPD) experiments. [229] For the readers convenience, the experimental methodology is briefly summarized in the SI. The Pt ISS intensities and the numbers of C_2D_4 molecules adsorbed during the low temperature C_2D_4 dose prior to TPD runs are quantified in Figure 7.6 in a way that facilitates comparison to the DFT results presented here. Results

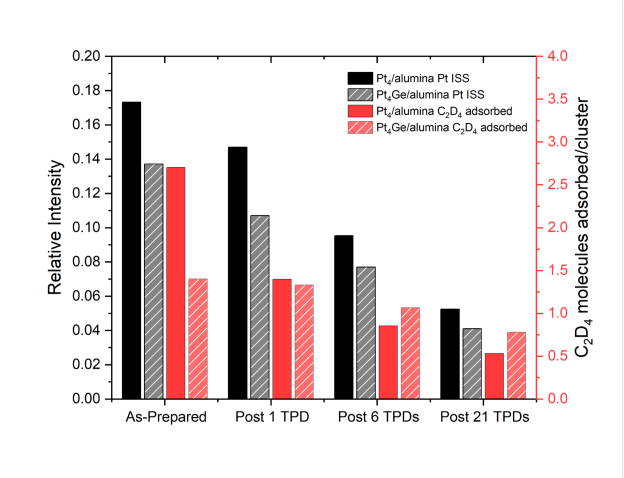

Figure 7.6: Pt relative intensities from He^+ ion scattering spectroscopy of Pt_4/alumina (black) and Pt_4Ge/alumina (hatched grey). The secondary axis highlights the number of C_2D_4 molecules adsorbed to Pt sites on Pt_4/alumina (red) and Pt_4Ge/alumina (hatched light red) per cluster.

are given for as-prepared Pt_4/alumina and Pt_4Ge/alumina, i.e., ISS intensities measured for as-prepared samples, and C_2D_4 molecules adsorbed extracted from analysis of the first TPD runs on fresh, separately prepared samples. Results are also summarized for the Pt ISS intensities and C_2D_4 molecules adsorbing for samples prepared and then subjected to 1 TPD run, 6 TPD runs, and 21 TPD runs, all obtained with separately prepared samples to avoid sample damage from ISS. The numbers of C_2D_4 molecules adsorbed on the samples are indicative of the number of ethylene binding sites available at different stages of reaction/deactivation, and the Pt ISS intensities are proportional to the fraction of the

deposited Pt atoms (identical in all samples) that are He^+ accessible in the topmost sample layer. Both the numbers of C_2D_4 molecules adsorbing, and the fraction of exposed Pt atoms are adversely affected by the carbon deposition and/or Pt sintering that occurs during ethylene TPD, particular for the Pt_4/alumina samples. It is clear, however, that TPD has quite different effects on the two measurements. We see that, while both the number of Pt sites and the number of C_2D_4 molecules desorbing attenuate, they do not attenuate to the same extent for either Pt_4 or Pt_4Ge. Pt sites remain even when the total number of C_2D_4 sites, measured by number of molecules adsorbed, have decreased. This suggests both that the deactivation via coke formation is electronic in nature, rather than physical blocking of sites, and that coke induces restructuring of the Pt clusters, where Pt sites remain accessible. For Pt_4Ge, we see that the overall attenuation is less for both Pt sites, and C_2D_4 molecules adsorbed, and that the number of molecules adsorbed decreases less relative to attenuation of Pt sites compared to Pt_4.

7.3 Conclusions

We have studied the electronic behavior of four dehydrogenation catalysts, Pt_4, Pt_4C_2, Pt_4Ge, and Pt_4GeC_2, all supported on α-Al_2O_3, to explore the role that Ge plays in mitigating deactivation via coke formation. Pt_4 is predicted to be a potent ethane dehydrogenation catalyst, but suffers from poor selectivity, driving deep dehydrogenation that leads to carbon deposition and catalyst deactivation. This deactivation is attributed to electronic effects, as coke formation does not primarily block sites, but changes the electronic properties of the cluster, with the C_2 unit withdrawing electron density from Pt while triggering restructuring.

Comparison between calculated adsorption energies and C-H activation barriers show that Pt_4Ge is more selective than Pt_4, and the partially coked Pt_4GeC_2 is even more selective. In Pt_4GeC_2, Ge donates electrons to C, preventing the depletion of electron density

on Pt, allowing it to retain activity despite some coke formation. Additionally, Ge strengthens the C-C bond in Pt_4GeC_2 and disfavors further binding of coke to the C_2 unit. Thus, Pt_4GeC_2 is an active dehydrogenation catalyst despite carbon deposition, with desirable selectivity arising from the interaction between Ge and C_2. We additional see that, by varying Ge content of Pt_4C_2 clusters between 0 and 2, that added Ge favors the formation of C-C bonds in the cluster ensembles. The *ab initio* results are substantiated by experimental results, which demonstrate that the loss of accessible ethylene binding sites during coking is insufficient to explain loss of activity, reflecting that the effect observed for both Pt_4 and Pt_4Ge is electronic rather than steric. The cooperative interaction between Ge and C_2 invites us to see the two species as co-dopants for Pt_4, where Ge as a promoter prevents the poisoning effect of C_2 alone. We believe that the observations reported here help to explain the behavior of other coke-resistant catalysts, and should be applicable to other compositions and reactions.

7.4 Methods

7.4.1 Computational Methods

Calculations on surface-supported clusters were performed using plane-wave DFT in VASP[237], using the PBE exchange-correlation functional[238], PAW pseudopotentials[239], DFT-D3 dispersion correction, [209] and a plane-wave cut-off of 500 eV. Unit cells were constructed from a 5-layer 3x3 supercell of α-Al_2O_3 with a 15 Å vacuum gap, which was previously optimized. [19] Transition states were calculated using the climbing-image nudged elastic band (CI-NEB) method implemented in VTST.[240, 241] QTAIM analysis was performed using the Bader code developed by the Henkelman group.[242, 243]

Global optimizations were performed with a BLDA approach [244] to generating chemically-reasonable initial structures, both for cluster structure sampling, and adsorbate binding sampling. For the adsorbate binding, we explored C-H activation without additional coverage

of H_2, in order to best match the surface science conditions of the experiment, where D_2 is observed to readily desorb from the clusters during TPD cyclrs. [229] The in-house codes PGOPT and GOCIA were used to run the global optimizations.

Local-basis projections for bonding analysis were performed with LOBSTER,[150] using the PBEVaspFit basis set and a projection basis of $5p5d6s$ for Pt, $4s4p$ for Ge, $3s3p$ for Al, and $2s2p$ for C and O.[236, 245] All projections reported less than 1.2% charge spilling.

DFT calculations on gas-phase models were performed with the Amsterdam Density Functional (ADF) package[246], version 2019.304, using the PBE functional.[238] Slater-type basis sets of triple-ζ + polarization quality were used on all atoms, with orbitals up to 4d (Pt), 3d (Ge) and 1s (C) included in the frozen core.[247]

7.4.2 Experimental Methods

The relative intensities in He^+ ion scattering spectroscopy (ISS) was summarized from the series of ISS previous results for Pt_4/alumina and Pt_4Ge/alumina [229]. The relative intensities are calculated by taking the average Pt ISS signals of the first 3 data points of the corresponding series of ISS, of which the ISS signals are calculated by integrating the background subtracted Pt integrated intensities normalized to the total integrated ISS signals for the full ion scattering spectrum that remain relatively invariant to compensate for the fluctuation of He^+ ions scattered. The Pt ISS signals for the as deposited samples are extrapolated, to reveal what the initial Pt ISS signals would be at, from the gradual leveled curve rising from the ISS intensities after some exposure of the samples under He + ions; the extrapolated numbers are close to their corresponding Pt ISS signals post 750 K heat treatment, thus indicating the presence of adventitious adsorbates or H and Cl atoms present on the sample surfaces as well as that the clusters do not sinter much after a single heat treatment on the sample surface.

The C_2D_4 adsorbed molecules per cluster are calculated from the sum of the high temperature C_2D_4 desorption peaks (attributed to C_2D_4 binding to Pt) and half of the D_2 desorbed

molecules (as each C_2D_4 produces 2 D_2 molecules) in the temperature programmed desorption from our previous work [229].

APPENDIX A

Supplementary information for CO_2 Hydrogenation to Formate and Formic Acid by Bimetallic Palladium-Copper Hydride Clusters

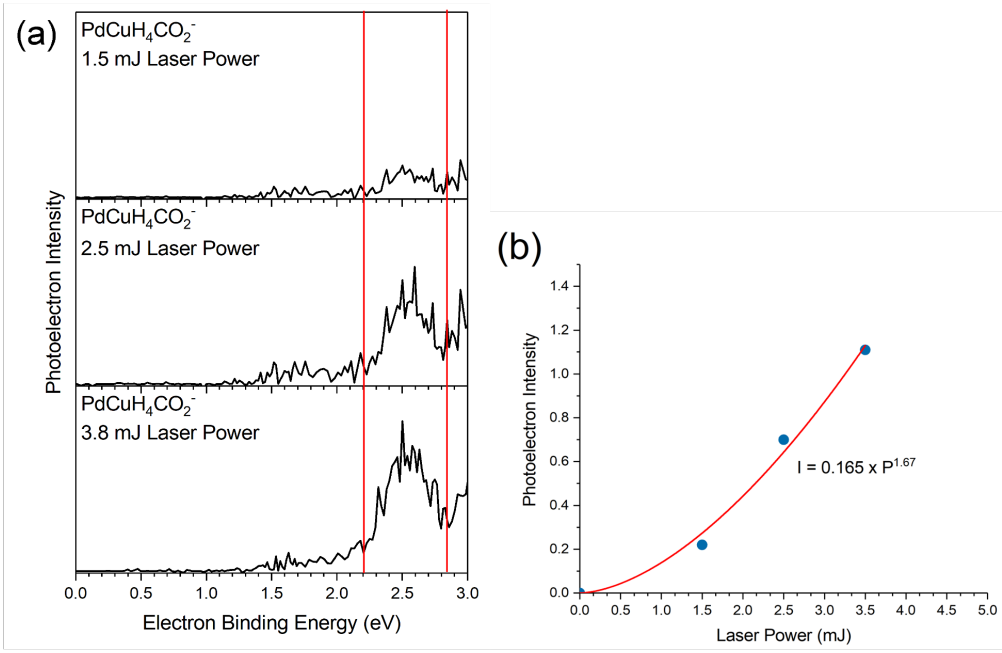

Figure A.1: (a) The photoelectron spectra of $PdCuH_4CO_2^-$ taken with different laser power while maintaining other collection conditions unchanged. The total photoelectron intensity is obtained by integrating the area between 2.2 and 2.8 eV. (b) The relationship between the integrated photoelectron intensity and the laser power showing a near-quadratic power dependence of the intensity.

Table A.1: $PdCuH_4^-$ Structure A

Pd	-0.992891	-0.032683	0.000232
Cu	1.622275	0.010286	-0.000109
H	-2.372982	0.781278	0.448798
H	-2.370836	0.779828	-0.454592
H	0.367342	-1.060402	-0.003102
H	3.003471	0.704410	0.001362

Table A.2: $PdCuH_4^-$ Structure B

Pd	0.000000	0.000000	0.000000
Cu	0.000000	0.000000	2.577226
H	1.087728	0.000000	1.114403
H	-1.123286	-0.003254	1.329942
H	1.098208	0.001418	-1.206535
H	0.685280	0.001519	3.961415

Table A.3: $PdCuH_4^-$ Structure C

C	-3.142312	0.641552	-0.065717
O	-2.429792	-0.429212	0.120290
Cu	-0.567932	-0.614621	-0.025250
Pd	1.858292	0.186738	0.003279
O	-4.370691	0.721932	0.032206
H	2.938388	1.417216	-0.307489
H	2.970900	1.285078	0.581391
H	0.892435	-1.218641	-0.179411
H	-2.555374	1.559356	-0.338731

Table A.4: $PdCuH_4^-$ Structure D

C	-2.644209	-0.138181	0.012066
O	-2.157665	1.036407	0.014986
Pd	-0.218888	-0.003385	-0.016279
Cu	2.391423	-0.052320	0.012476
O	-3.787716	-0.583745	0.025255
H	0.979214	-1.047506	-0.038128
H	1.031072	0.999229	-0.022800
H	-1.799290	-1.013707	-0.006271
H	3.934914	-0.057221	0.059914

Table A.5: $PdCuH_4^-$ Structure E

C	2.074167	0.337914	0.008990
O	3.047442	-0.076366	0.615654
Pd	0.263515	-0.567544	-0.128968
Cu	-2.155473	0.317657	0.125870
O	1.924473	1.706170	-0.198591
H	-1.209145	-0.953097	0.633328
H	-3.309676	1.305074	-0.134938
H	1.668674	-0.323010	-1.042684
H	1.016854	1.800094	-0.563874

Table A.6: $PdCuH_4^-$ Structure F

Cu	1.502264	-0.000113	-0.000036
Pd	-1.016030	-0.016576	0.000006
H	0.152497	1.075049	0.000178
H	3.019241	-0.309266	0.000605

APPENDIX B

Supporting information for Ensemble of Metastable States Can Accelerate Sintering of Size-Selected Cluster Catalysts via Ostwald Ripening

B.1 More Detailed Discussion Regarding the MC simulation:

1. A full DFT-based PES sampling was done on Pt_n /TiO_2 (n = 1–8) and relevant isomers were chosen based on their Boltzmann populations at 700 K. 2. MC simulation of the problem based on the obtained local minima structures was done as following: a) Interconversion of local minima for a given cluster: The probability of this step is calculated based on the energy difference of the initial and final structure. Again we should emphasize that a more quantitative approach would involve calculating reaction barriers which is not feasible given the numerous pathways for each cluster. Moreover, by BEP relationships, processes that are more uphill also have higher barriers, and vice versa, so we expect a qualitatively reliable picture from thermodynamics defining the probability of atom transitions from one cluster to another. In addition, the initial cluster distribution was based on the Boltzmann population at 700 K. Note that the interconversion is done when an atom leaves the cluster or a new atom joins the cluster (and the new cluster shape is chosen based on the energy of available isomers). b) Emission of a Pt atom from a local minimum of a given cluster onto the support or onto another nearby cluster. c) Migration of a Pt atom over the support. d) Attachment of a Pt atom to a cluster. Important parameters used in MC simulation: Total number of MC steps: 100,000; Temperature: 700

K; Number of initial clusters: 100; size of the support: $\sim$ 158Å$\times\sim$72 Å, or (24$\times$24) unit cells of TiO_2 (110); step size of monomer displacement: a random number between 0 and 4 Å.

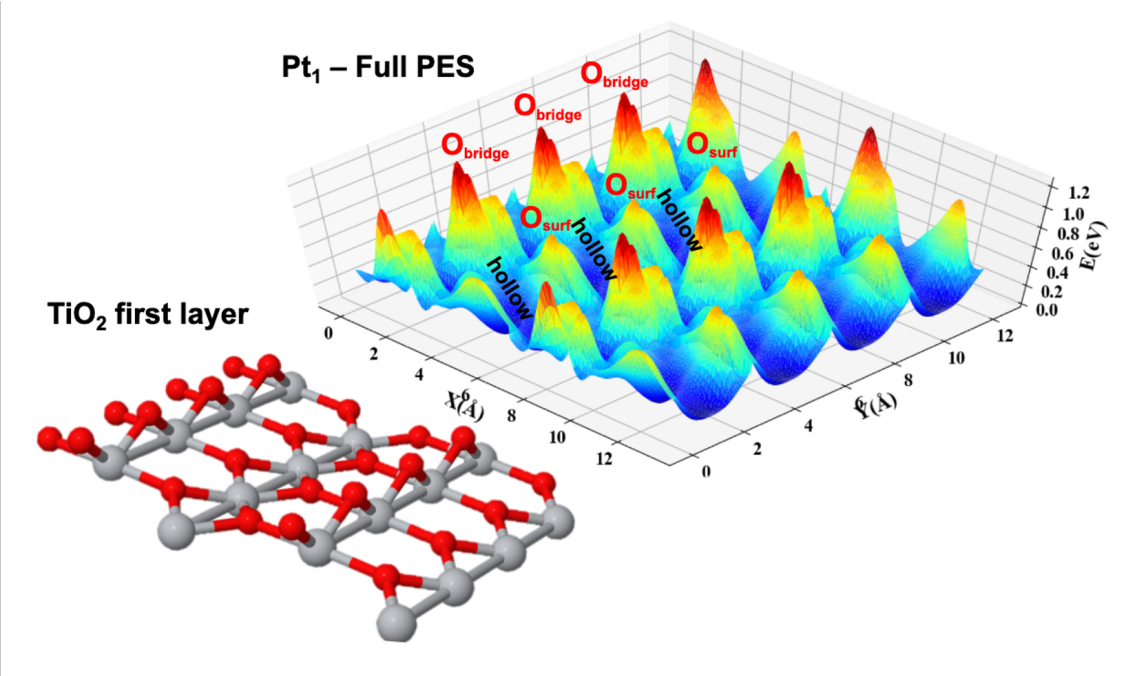

Figure B.1: Full PES of Pt_1 /TiO_2 (110) along with the first layer of the model obtained from DFT calculations.

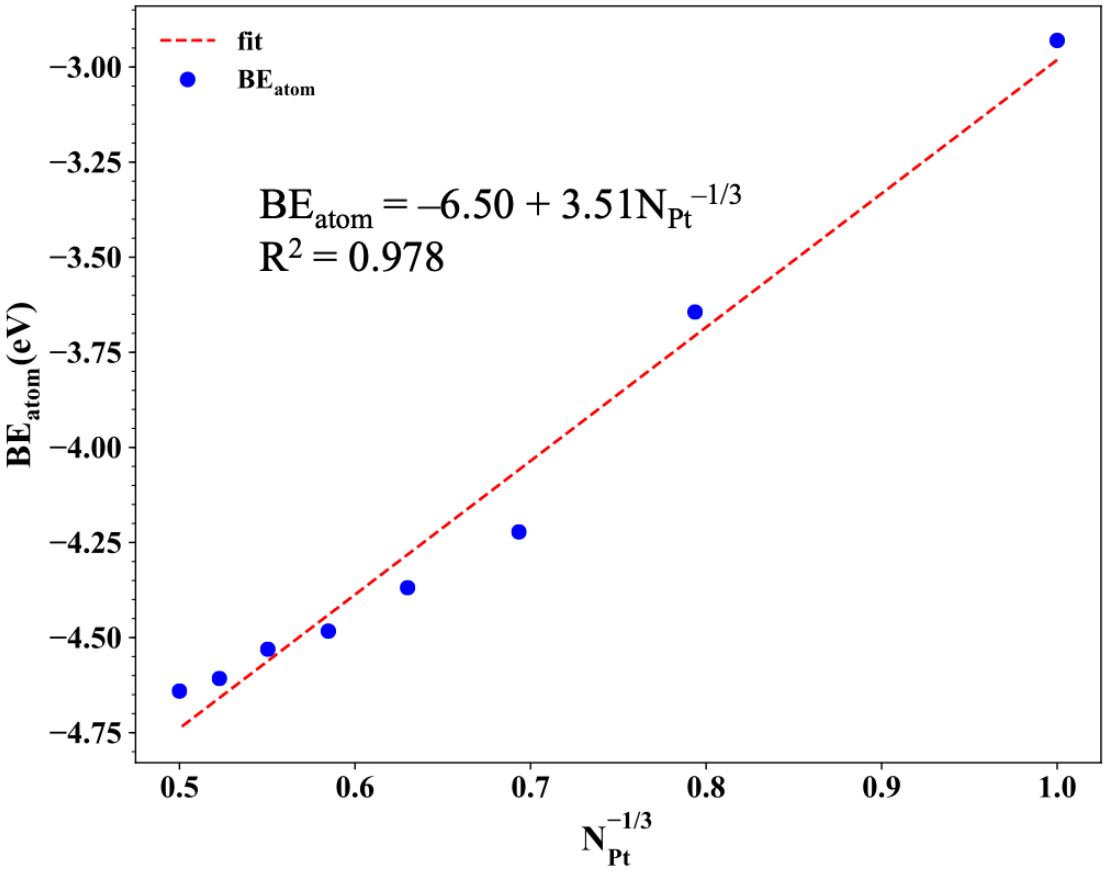

Figure B.2: Binding energies of Pt_n/TiO_2 (110) (n = 2–8) (divided by the number of atoms in the cluster) as function of number of Pt atoms in the cluster

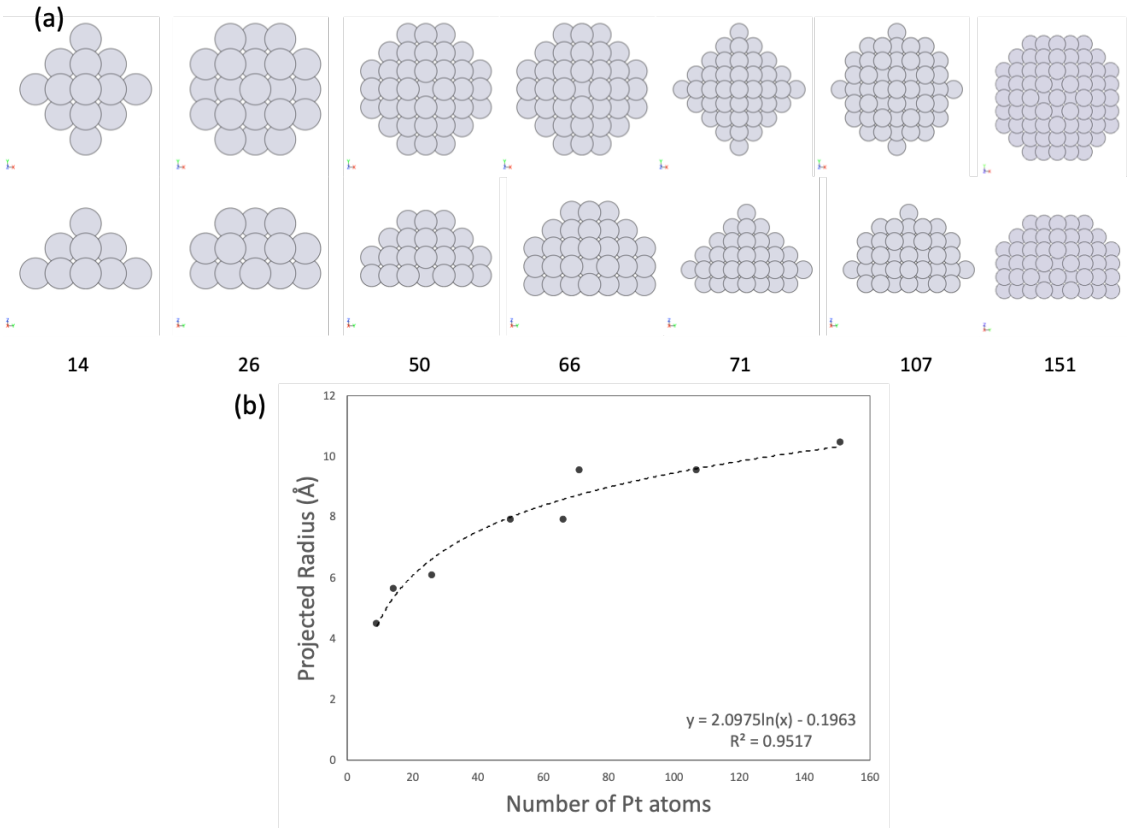

Figure B.3: (a) Winterbottom constructs of Pt on a surface, used to estimate the radius growth of biggamers forPt_{9+} . (b) the plot that gives the function for the growth of the Pt biggamers

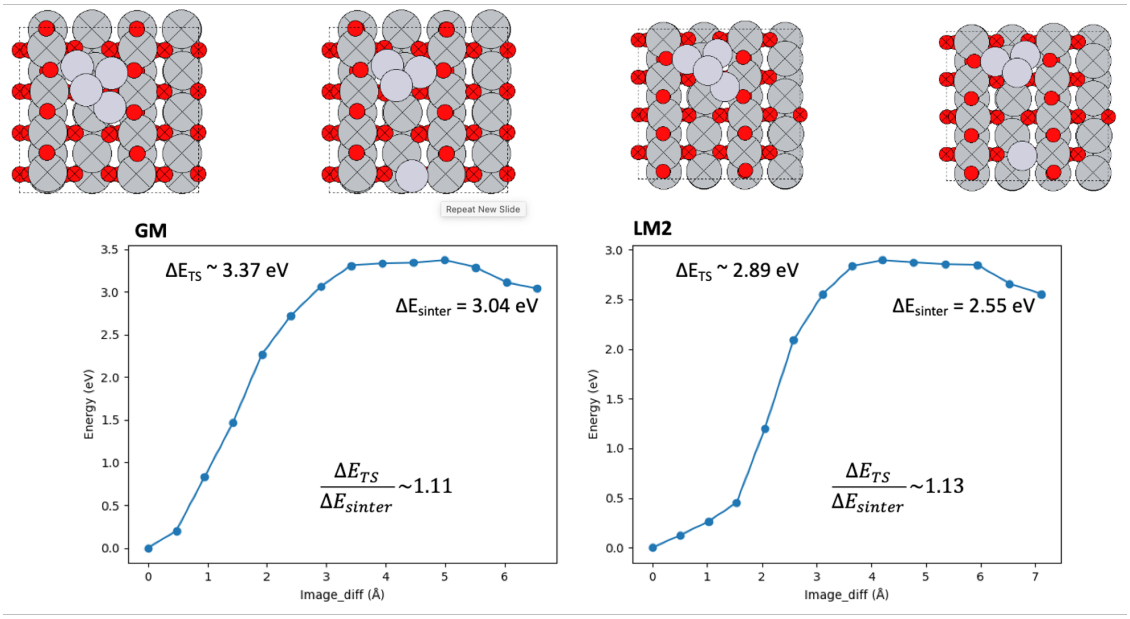

Figure B.4: Reaction barriers calculated using NEB for Pt_4 dissociation to Pt_3 and Pt for the global minimum and second local minimum structures.

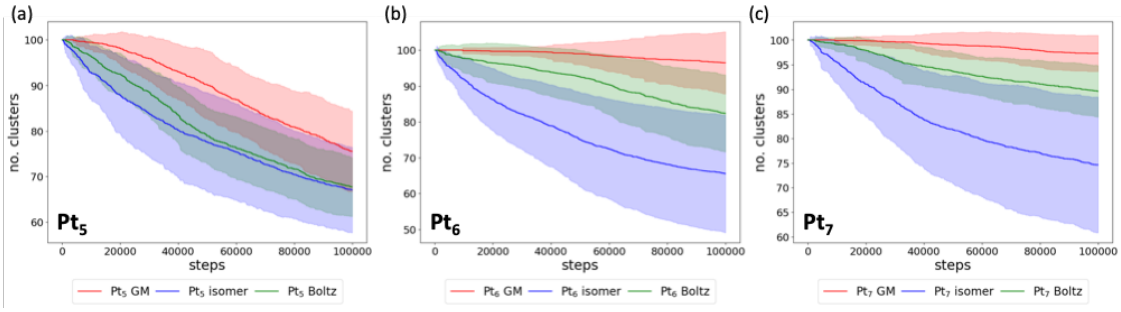

Figure B.5: Plots showing the standard deviation for the three different runs for the cluster sizes not depicted in the main text. (a) is Pt_5 , (b) is Pt_6 , and (c) is Pt_7. Red: GM run, blue: isomer run, green: Boltzmann run.

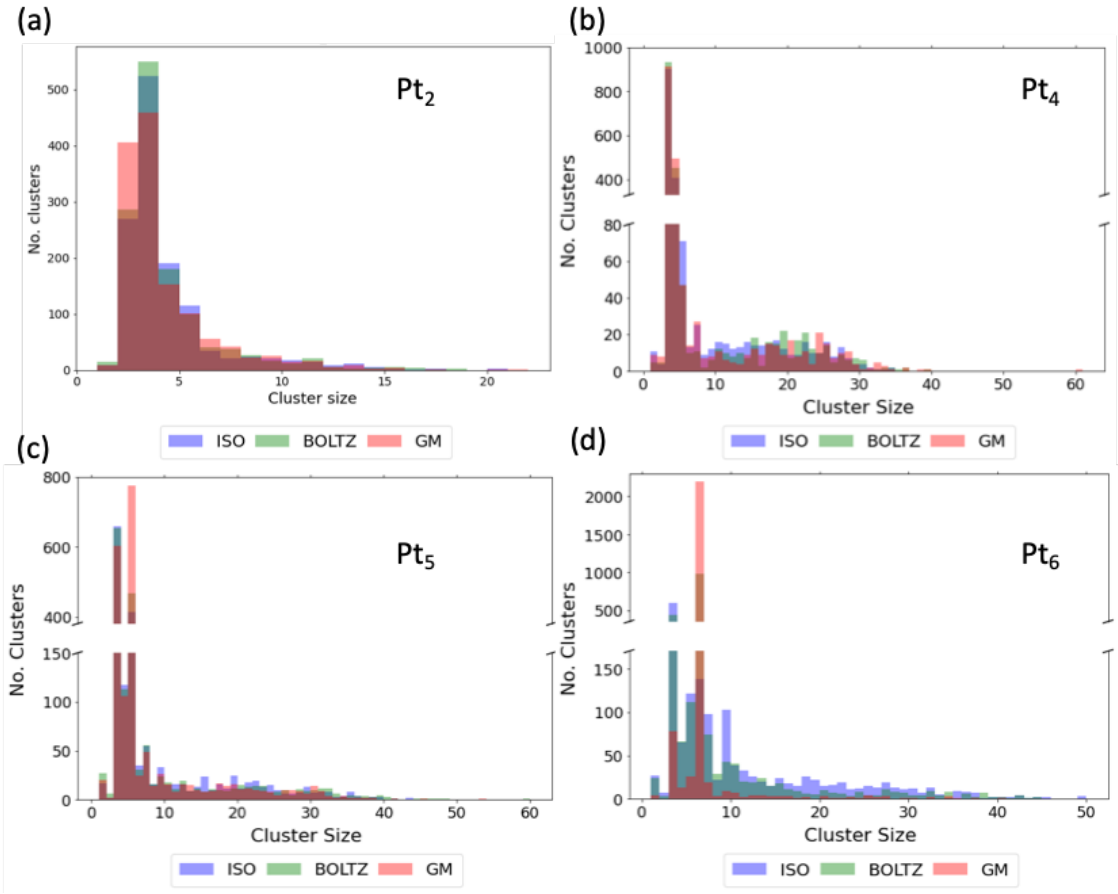

Figure B.6: Cluster size distribution in the final MC step of the simulation of GM-only, Boltzmann, and isomer simulations for monodisperse Pt_n/TiO_2 (110) (n = 2, 3, 5, 6)

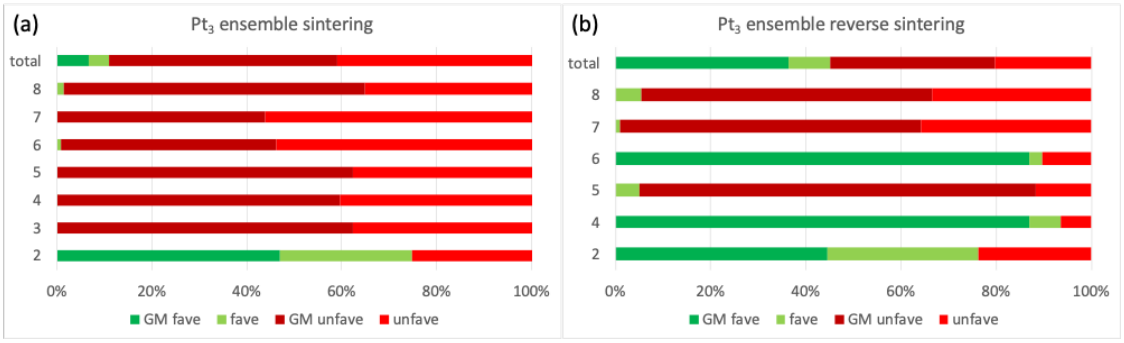

Figure B.7: Favorability (in %) of (a) sintering and (b) reverse sintering of Pt_3 in the presence of Pt_n (n = 2–8) cluster (bottom to top row in each panel). Green and red indicate the proportion of thermodynamically favorable and unfavorable pathways respectively. The amount each possible pathway contributes to either case is scaled by the Boltzmann probability of the combination of isomers in the sintering process occurring together. The dark green or dark red indicates the GM contribution to favorable or unfavorable sintering, respectively. Note that this Figure is not based on sintering simulations, but directly on the computed energetics of all possible sintering and reverse sintering pathways.

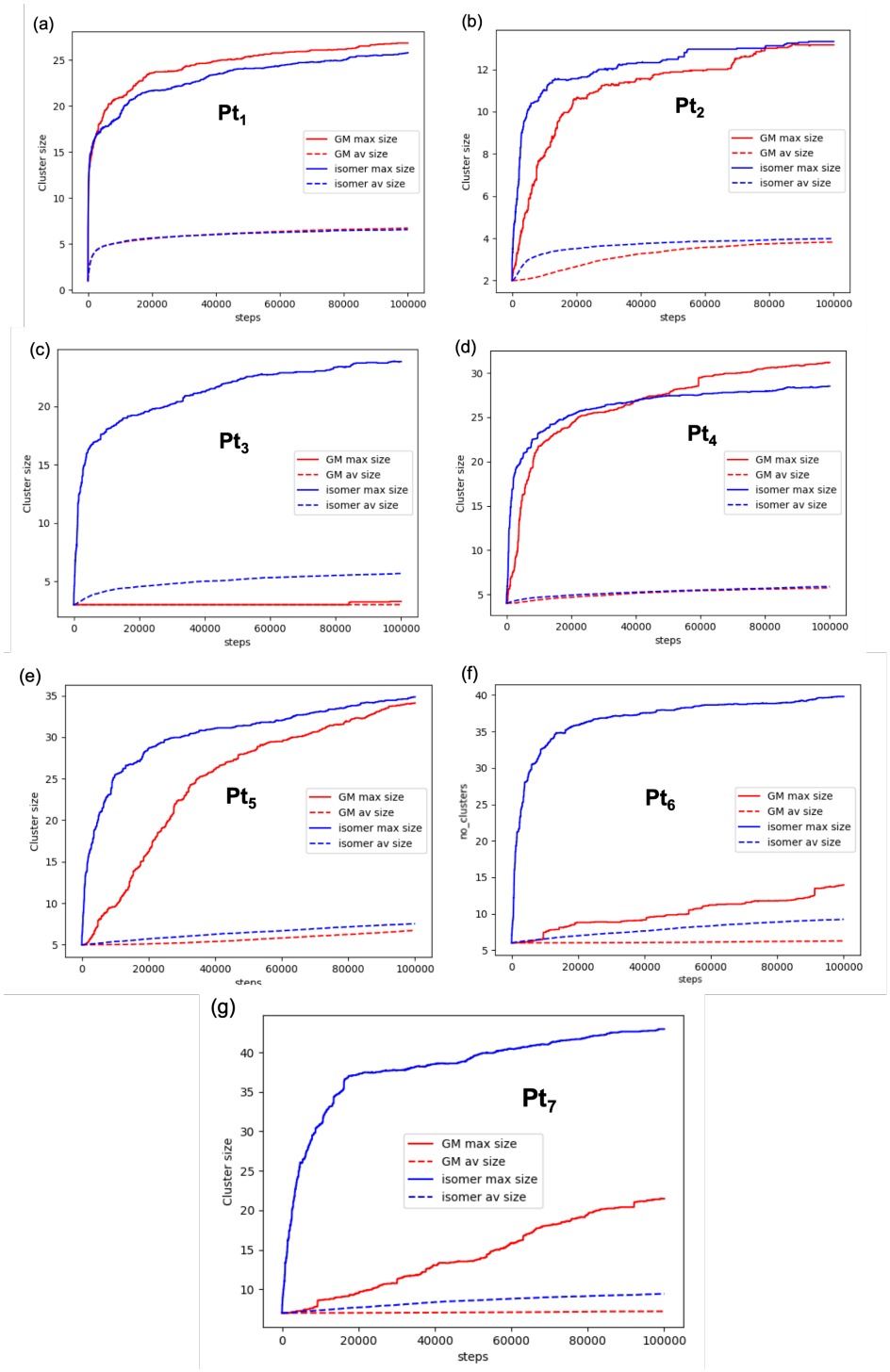

Figure B.8: Maximum (solid curves) and average (dashed curves) cluster size for GM (red) and isomer (blue) runs for Pt_n/TiO_2 (110) (n = 2–7) at every MC step.

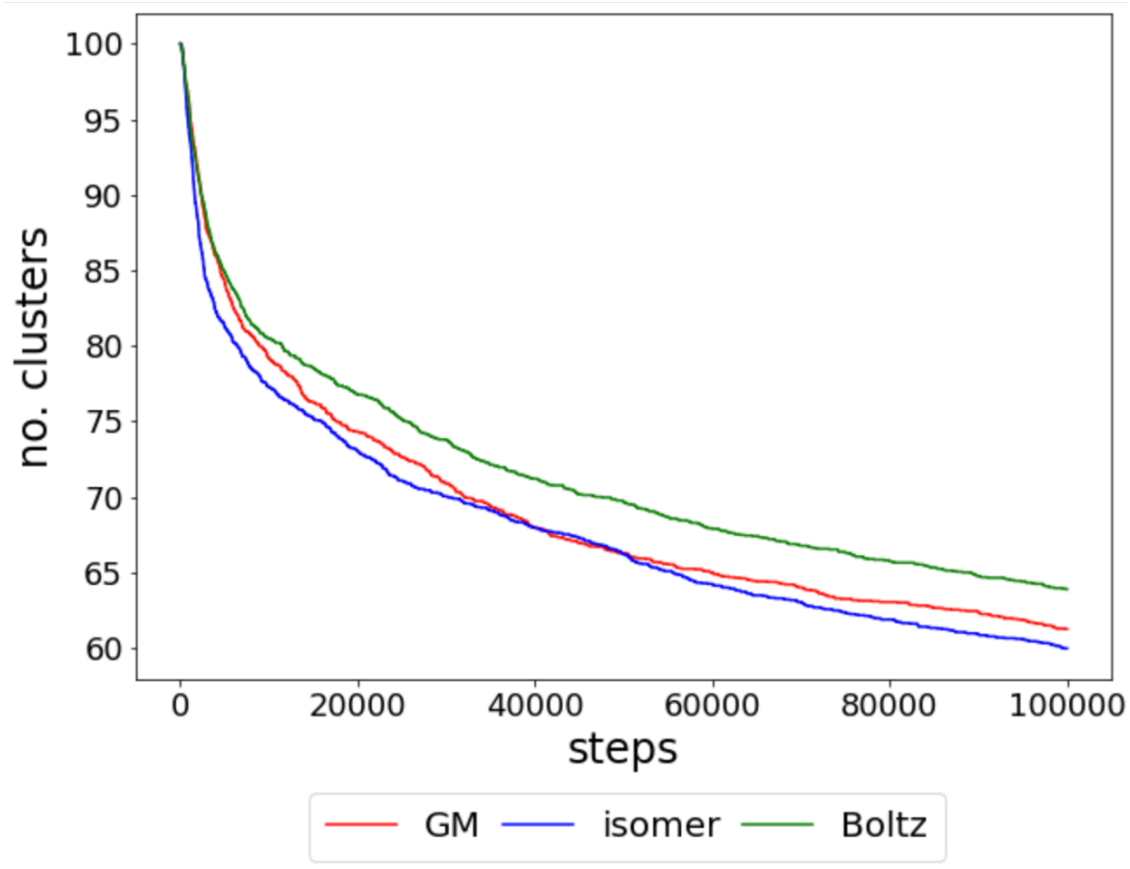

Figure B.9: Sintering of polydisperse $Pt_{2\text{-}7}$ cluster systems. GM, Boltzmann, and isomer setups are shown in red, green and blue, respectively.

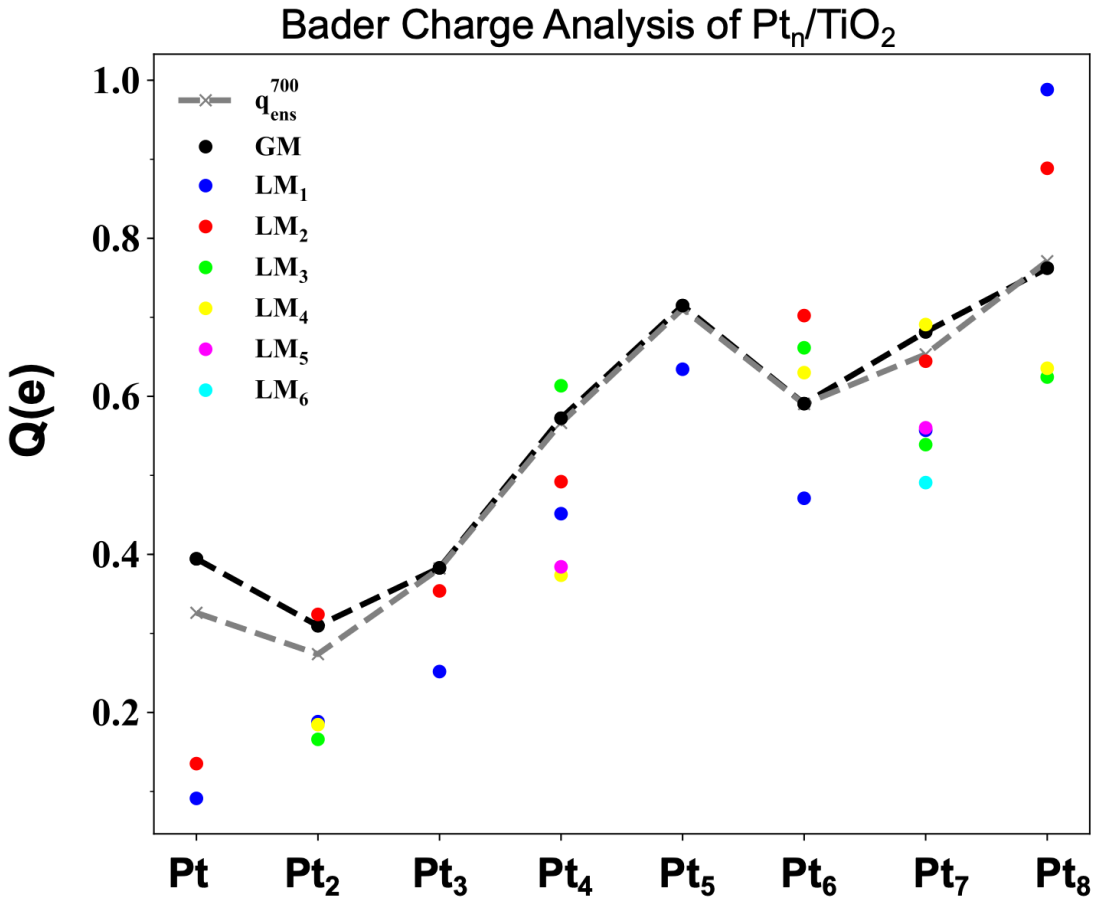

Figure B.10: Bader charge analysis of all thermally accessible isomers of Pt_n/TiO_2 (110) (n = 1– 8) at 700 K. Note that the gray dashed line shows the ensemble average charge of the cluster obtained using the Boltzmann population calculated at 700 K. GM: global minimum, LM_i : i-th local minimum structure.

Cluster	Q_{atom1}(e)	Q_{atom2}(e)	Q_{atom3}(e)	Q_{atom4}(e)	Q_{atom5}(e)	Q_{atom6}(e)	Q_{atom7}(e)	Q_{atom8}(e)
Pt	0.394							
Pt_2	0.188	0.122						
Pt_3	0.177	–0.118	0.324					
Pt_4	0.226	–0.074	0.105	0.314				
Pt_5	0.140	–0.069	0.213	0.219	0.212			
Pt_6	0.332	0.042	0.024	–0.110	0.220	0.083		
Pt_7	–0.103	0.324	0.140	0.–0.16	0.208	0.267	–0.138	
Pt_8	–0.114	–0.020	0.292	0.175	–0.102	0.225	0.225	0.181

Table B.1: Bader charges of every atom in Pt_n/TiO_2 global minima structures. A charge separation is found in Pt_3, Pt_7, and Pt_8.

APPENDIX C

Supplementary Information: "Magic" Sinter-Resistant Cluster Sizes of Pt_n Supported on Alumina

C.1 Computational Methods

C.1.1 Monte Carlo Simulations Details

Information for Pt+ cluster:

For Pt_9 and above, their radii and energies were calculated based on the following two formulas which are the fitting functions using the GM radii and energy from Pt1-8.

$$\text{Energy For } Pt_n = (-5.187 \times n - 1963)/27.2114 + 73.66723149, \text{ for } n \leq \tag{C.1}$$

$$\text{Radius For } Pt_n = 1.290 * \log(n) + 1.750, \text{ for } n \leq 9 \tag{C.2}$$

Placed and Varied method:

To keep the cluster edge-to-edge distance between different cluster and fix the total number of clusters (100 clusters) inside the system, we shrink or increase the number of primitive cells that are using accordingly but also keep the shape of super cells the same, which is done during the placed and varied method. The placed and varied method is firstly put the given 100 global minimum (GM) clusters hexagonal close packed with approximately 5 Angstrom edge-to-edge distance (which is the approximate distance that one monomer can

move) and found the smallest number of primitive cells that contains these hexagonal close packed clusters. Then, each cluster was able to move randomly in a smaller radius around the original assigned center to vary. We check the Radius Density Function of each system to make sure that the system is surely random enough and preserve the edge-to-edge distance approximately 5 Angstrom.

The algorithm for finding the new center is below:

Input:

$(x_1, y_1), (x_2, y_2)$: the coordinates of two overlapped clusters

type1, type2: the numbers of atoms in these two overlapped clusters

allLocations: will store the list of all possible locations

Output:

(new_X, new_Y): the coordinate assigned to the new cluster

Algorithm:

t = type1 / (type1 + type2);

proposedX = x_2 + t × ($x_1 - x_2$);

proposedY = y_2 + t × ($y_1 - y_2$);

shortestDistance = distance between (x_1, y_1) and (proposedX, proposedY);

new_X = x_1;

new_Y = y_1;

foreach *coordination* ***in*** *allLocations* **do**

  if *distance between coordination and (proposedX, proposedY) < shortestDistance* **then**

    shortestDistance = distance between coordination and (proposedX, proposedY) ;

    (new_X, new_Y) = coordination;

  end

end

Algorithm 1: New Coordinate Assignment Algorithm

C.1.2 Overlap Checking Details

In a 2-D system without periodic boundary conditions, the process of checking whether two clusters in the system are overlapped is easy. We can simply compare the Euclidean distance between two clusters with the sum of the radii. But, when periodic boundary condition is applied to the system, the Euclidean metric in $\mathbb{R}^2$ no longer preserves the correct distance between two clusters. Since periodic boundary condition on quadrangle which identifies the opposite boundary as the same is homeomorphic to the torus, one way to solve this problem is to try to figure out a correct metric for the torus. But, there is no canonical way to find a metric that preserves the property of Euclidean distance as well as follows the periodic boundary condition. Instead of finding the metric for the torus, we propose to translate the clusters to create images of the original clusters with newly assigned coordinates according to periodic boundary conditions and then use the euclidean distance to check overlap directly. But it is not wise to copy and translate eight times for all repeated information which will increase the computation time and memory significantly. Thus, we first select the clusters that have the potential to overlap and only copy and translate those potential clusters to reduce computation time and memory cost.

We divided the selection of potential clusters into two cases. One is the boundary overlap case which deals with the periodic boundary images from left, right, up, and down. The other is the corner boundary overlap case which deals with the periodic boundary images from upper-left, upper-right, down-left, and down-right. The core of these two algorithms is to obtain the Largest Cluster Radius (LCR) in the system. In the boundary overlap case, once we obtain the LCR in the system, we can determine whether one cluster has the potential to overlap due to periodic boundary conditions by checking how close the cluster is to the boundary of the system. If the distance between the cluster and the boundary minus the radius of the cluster is smaller than LCR, then this cluster has the potential to overlap on that specific boundary (either left, right, up or down). The next step is to find a list of clusters that might overlap with the selected cluster and translate

all clusters in that list to their periodic images. Here is the algorithm for this process:

Input:

selectedCluster: selected cluster.

allClusterList: will store the list of all cluster in the system

Output:

newClusterList: will store the list of potential clusters for overlap checking.

Algorithm:

delta = Distance between cluster and the boundary - The radius of cluster - LCR;

foreach *cluster* ***in*** *allClusterList* **do**

  if *cluster == selectedCluster* **then**

    Continue;

  end

  if *Distance between cluster and the opposite of the boundary <= delta* **then**

    Shift this cluster to its periodic boundary image;

    Add this image to newClusterList;

  end

end

Algorithm 2: Boundary Overlap Algorithm

In the corner overlap case, we do similar things by checking whether the selected cluster is too close to two of the adjacent boundaries by comparing its distance with LCR. We rationally assume that the supercells that are used is big enough so that it is impossible for one cluster to be close to three or all four boundaries.

C.2 Analytic Methods

C.2.1 Computation Methods for Competing Pathways

The favor energy sum for Pt_x is all the possible combinations of the above equation times their Boltzmann probability. Then the energy is normalized by the total number of atoms in the system, so in this case it will be normalized by x+y. For reverse driving force of Pt_x where x can be varied from 2-7, energy will be calculate by all the possible combination of $Pt_x + Pt_y \longrightarrow Pt_z + Pt_w$ where y can be varied from 2 to 7 and z and w depends on the value of x and y. If $x \geq y$, then z = x - 1 and w = y + 1. If $x < y$, then z = x + 1 and w = y - 1 to make sure that we always build smaller cluster sizes.

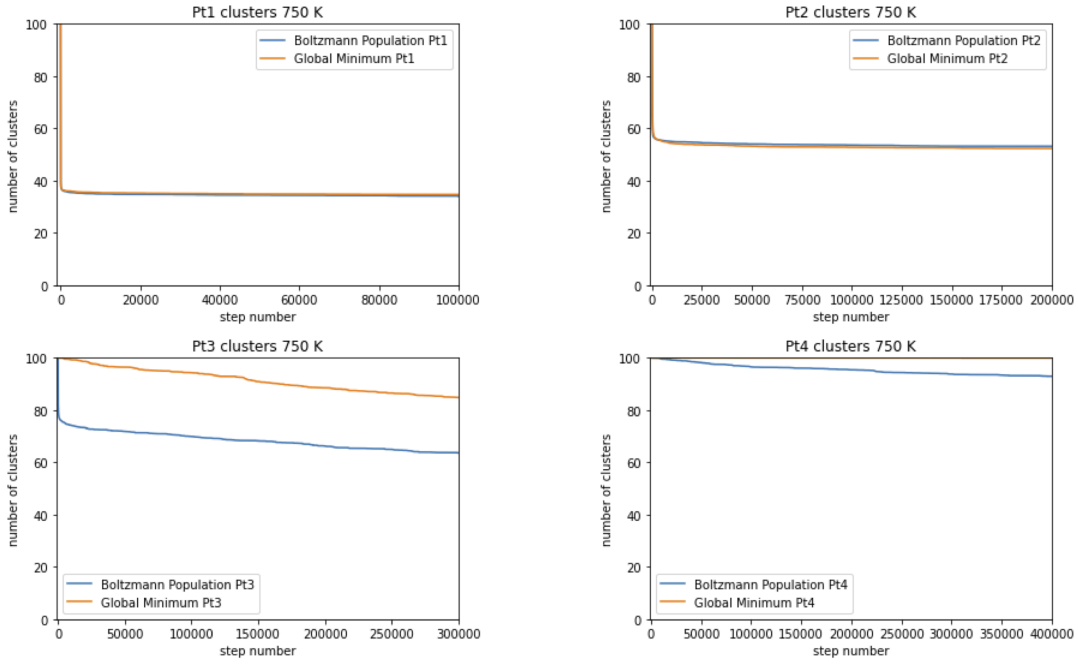

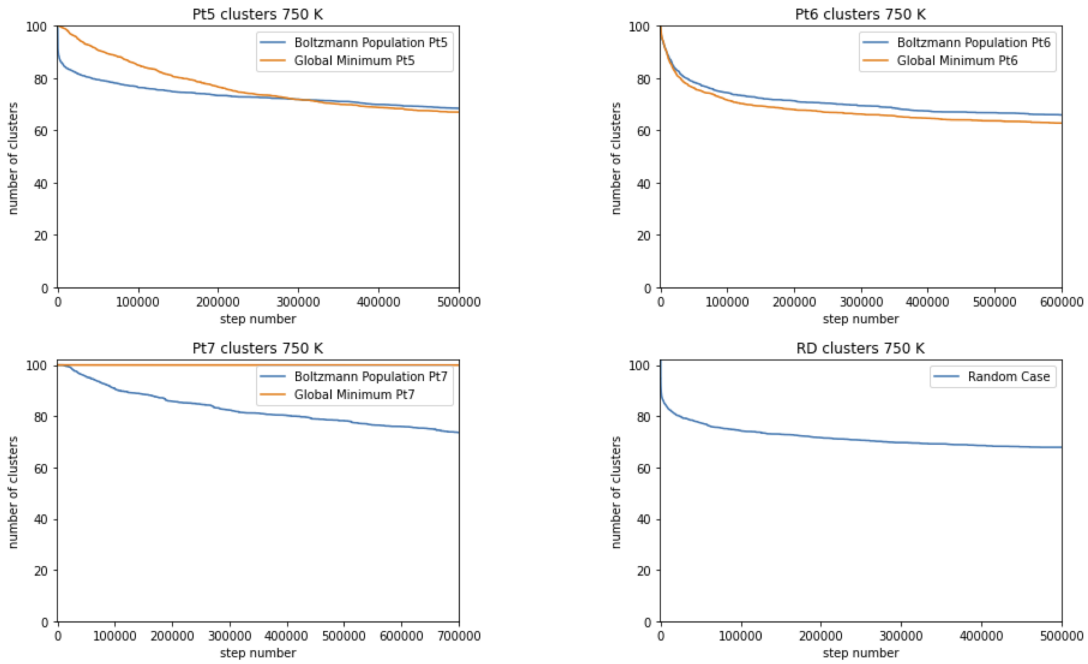

Figure C.1: Sintering Step Plots for Pt_1 to Pt_7 comparing the steps between Boltzmann population case and global minimum case. The final plot is for random case.

Figure C.2: Favoribility (in percent) of reverse sintering and ensemble sintering for Pt_2 to Pt_7.

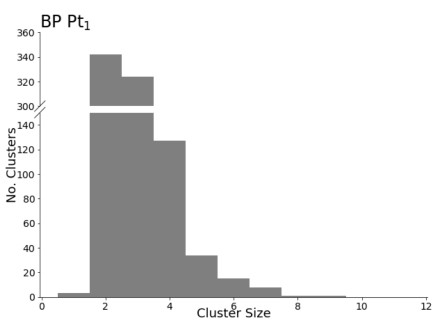
BP Pt$_1$
No. Clusters
Cluster Size

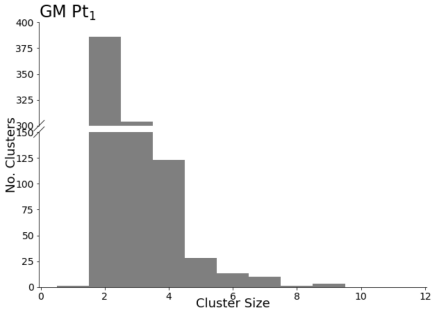
GM Pt$_1$
No. Clusters
Cluster Size

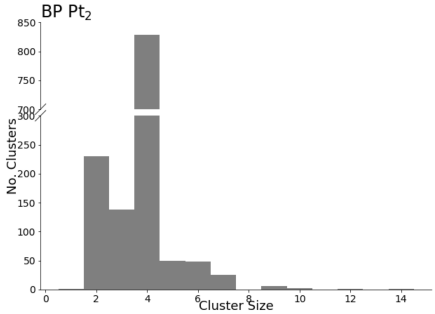
BP Pt$_2$
No. Clusters
Cluster Size

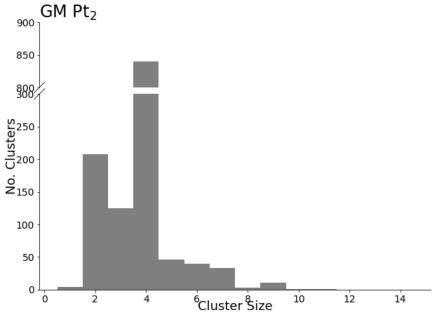
GM Pt$_2$
No. Clusters
Cluster Size

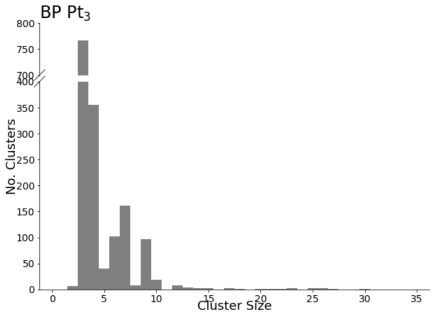
BP Pt$_3$
No. Clusters
Cluster Size

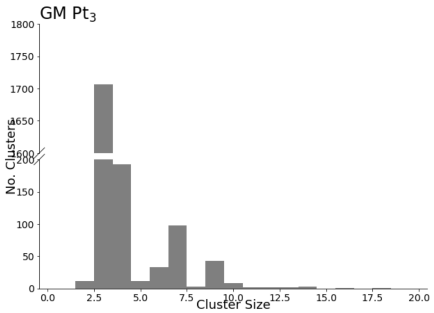
GM Pt$_3$
No. Clusters
Cluster Size

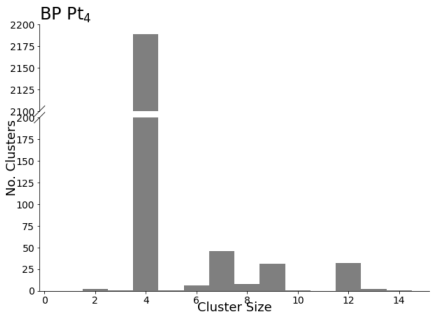
BP Pt$_4$
No. Clusters
Cluster Size

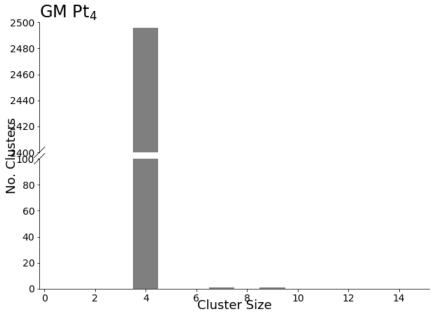
GM Pt$_4$
No. Clusters
Cluster Size

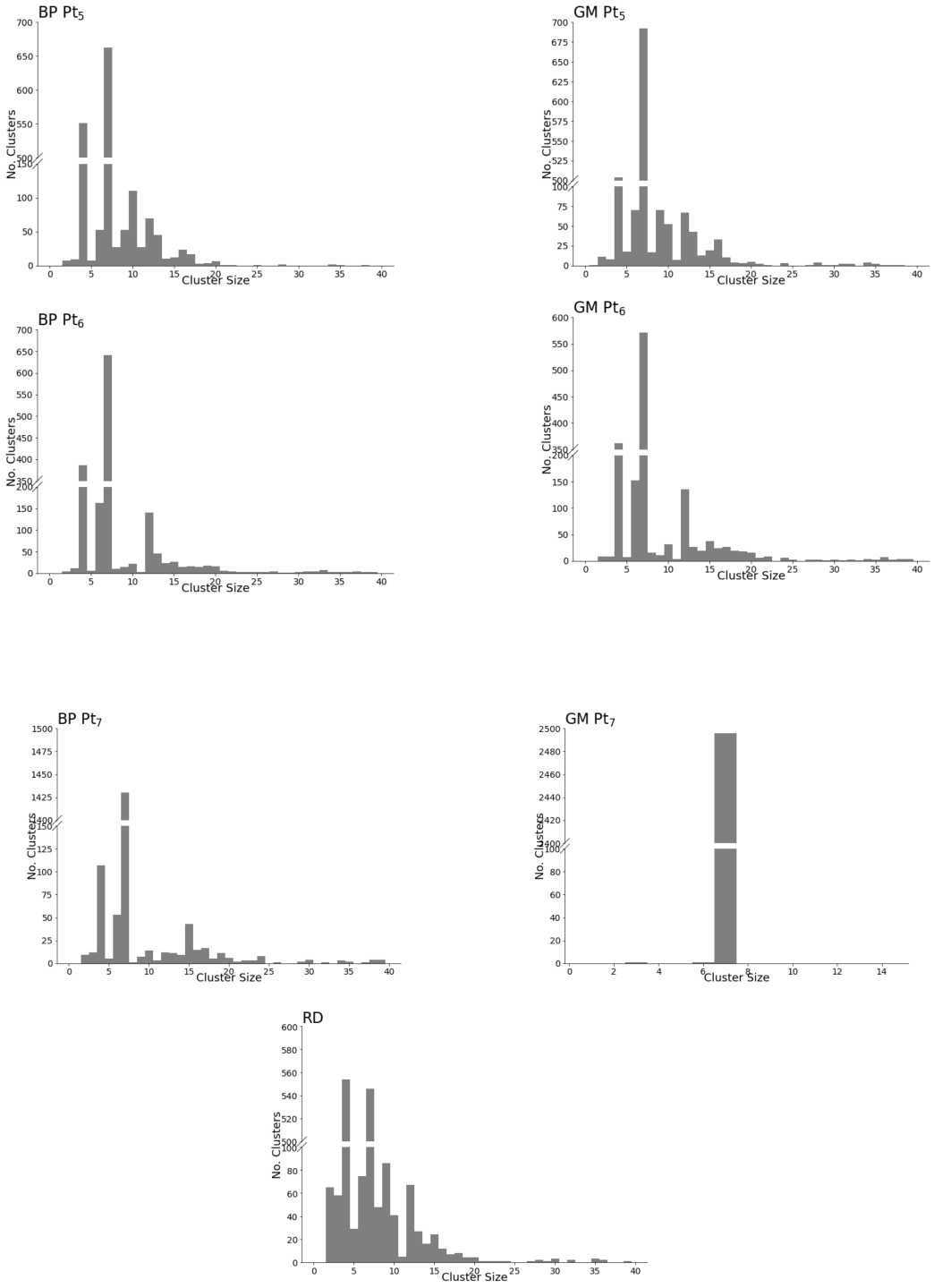

Figure C.3: Final Histograms for both Boltzmann population case and global minimum case from Pt_1 to Pt_7. And the final histogram for random case.

Pt3 GM

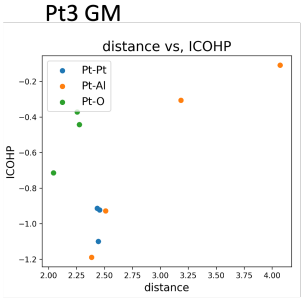

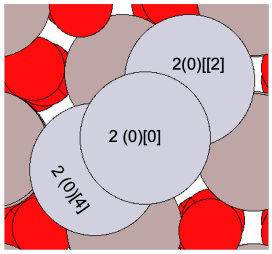

Pt3 LM1

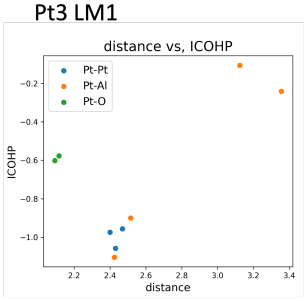

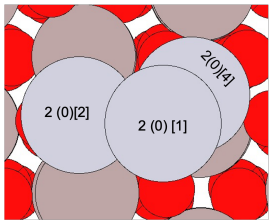

Pt4 GM

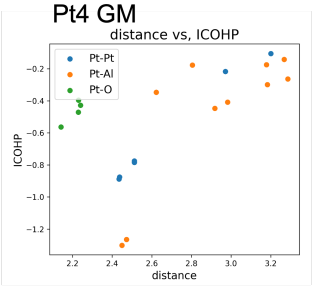

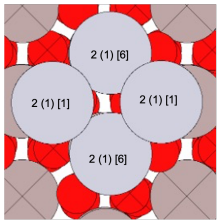

Pt4 LM1

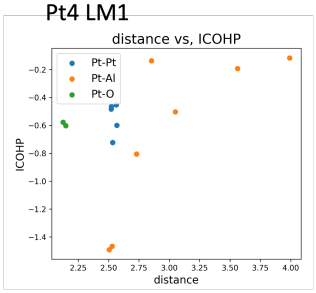

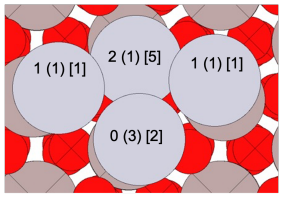

Pt5 GM

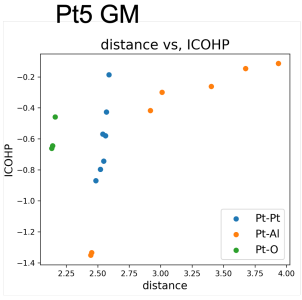

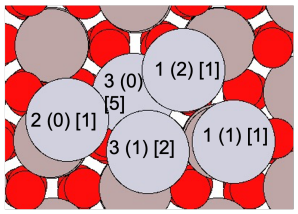

Pt5 LM1

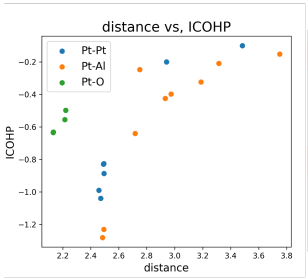

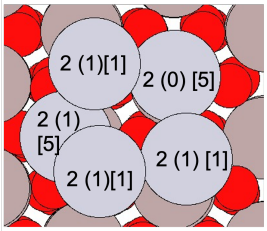

Pt5 LM2

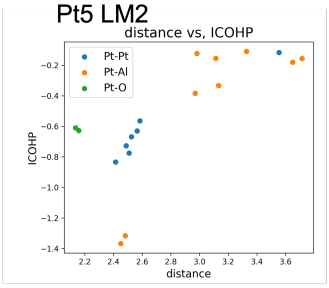

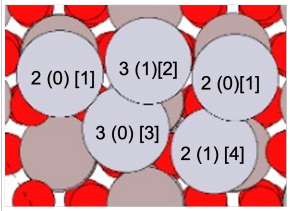

Pt5 LM3

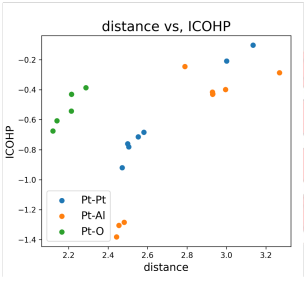

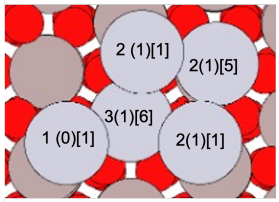

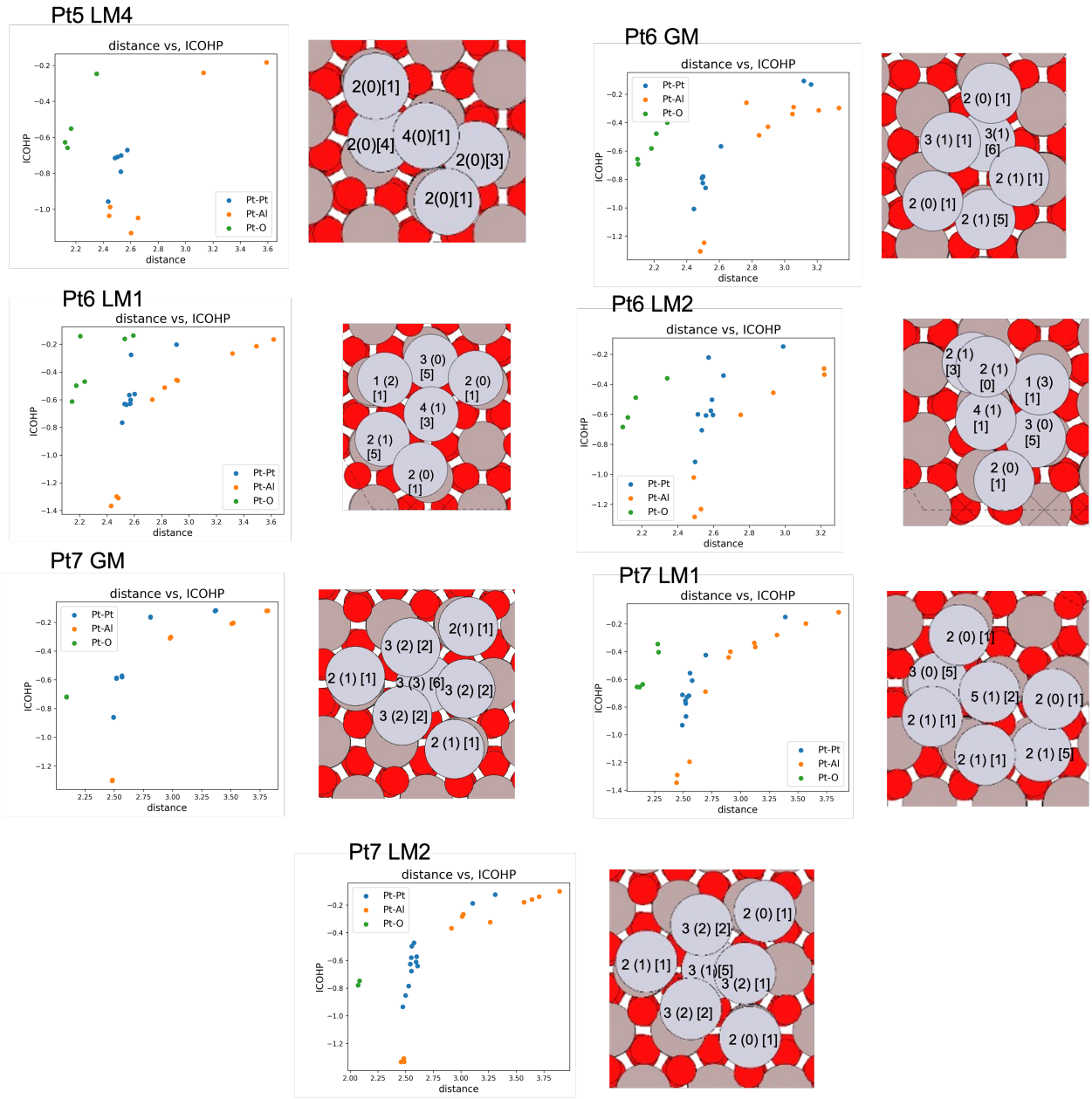

Figure C.4: ICOHP plotted against bond distance for relevant isomers of Pt_3 - Pt_7. The given cluster is shown with the number of strong and weak Pt bonds, as well as Pt-support bonds overlaid on the appropriate atoms in the format "strong, (weak) [support]" bonds.

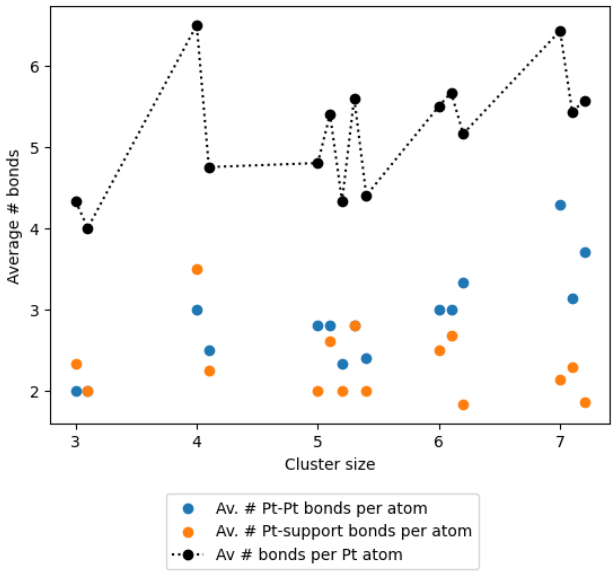

Figure C.5: Plot of the average number of bonds per Pt atom with each cluster size and isomer, broken down into the total number of bonds, as well as the Pt-Pt bonds and Pt–support bonds. Note the peaks at Pt_4 and Pt_7 GM structures, indicating that they have generally better-coordinated Pt atoms than other cluster sizes and isomers.

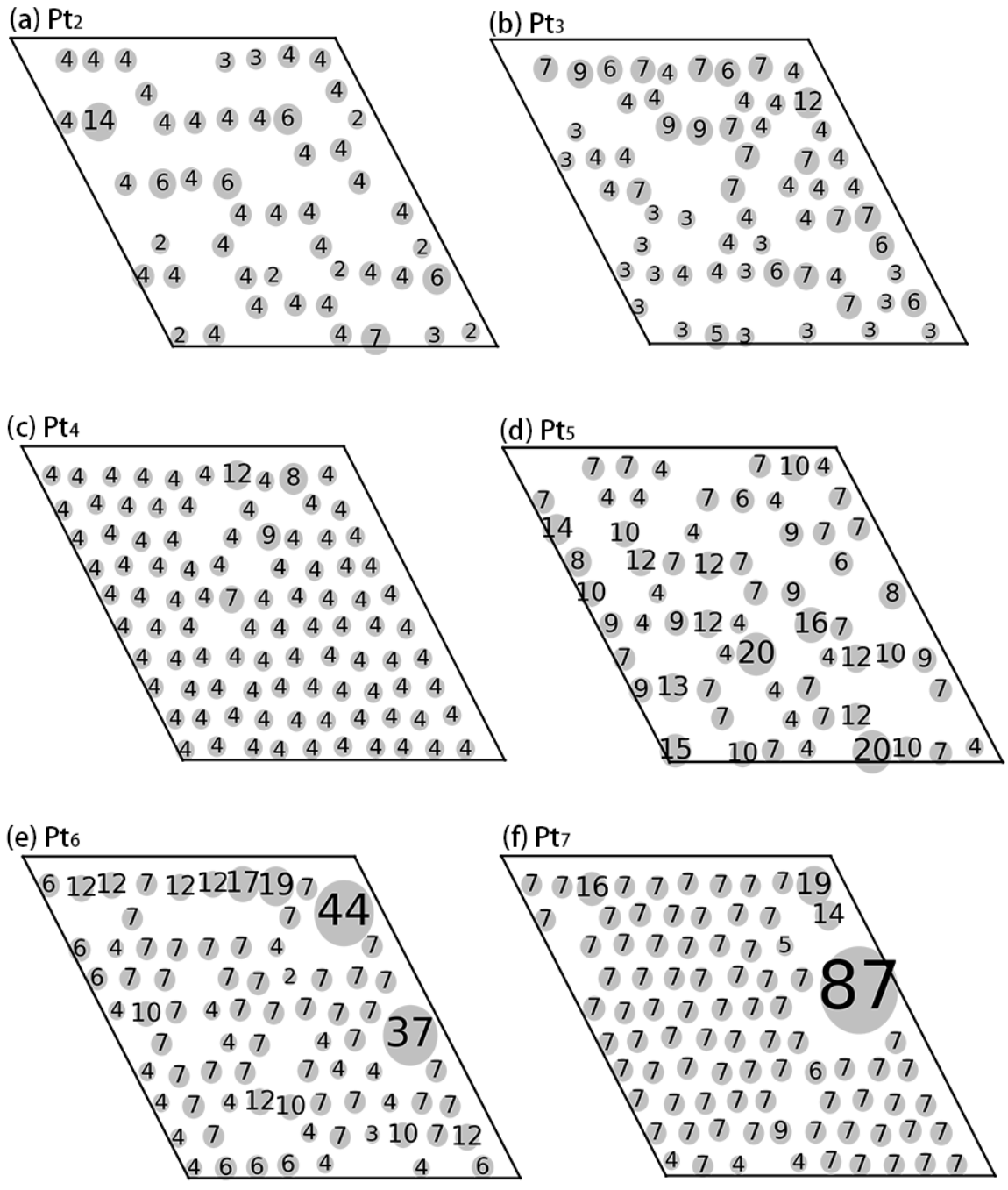

Figure C.6: Example endpoints of sintering simulations representing different spatial regimes.

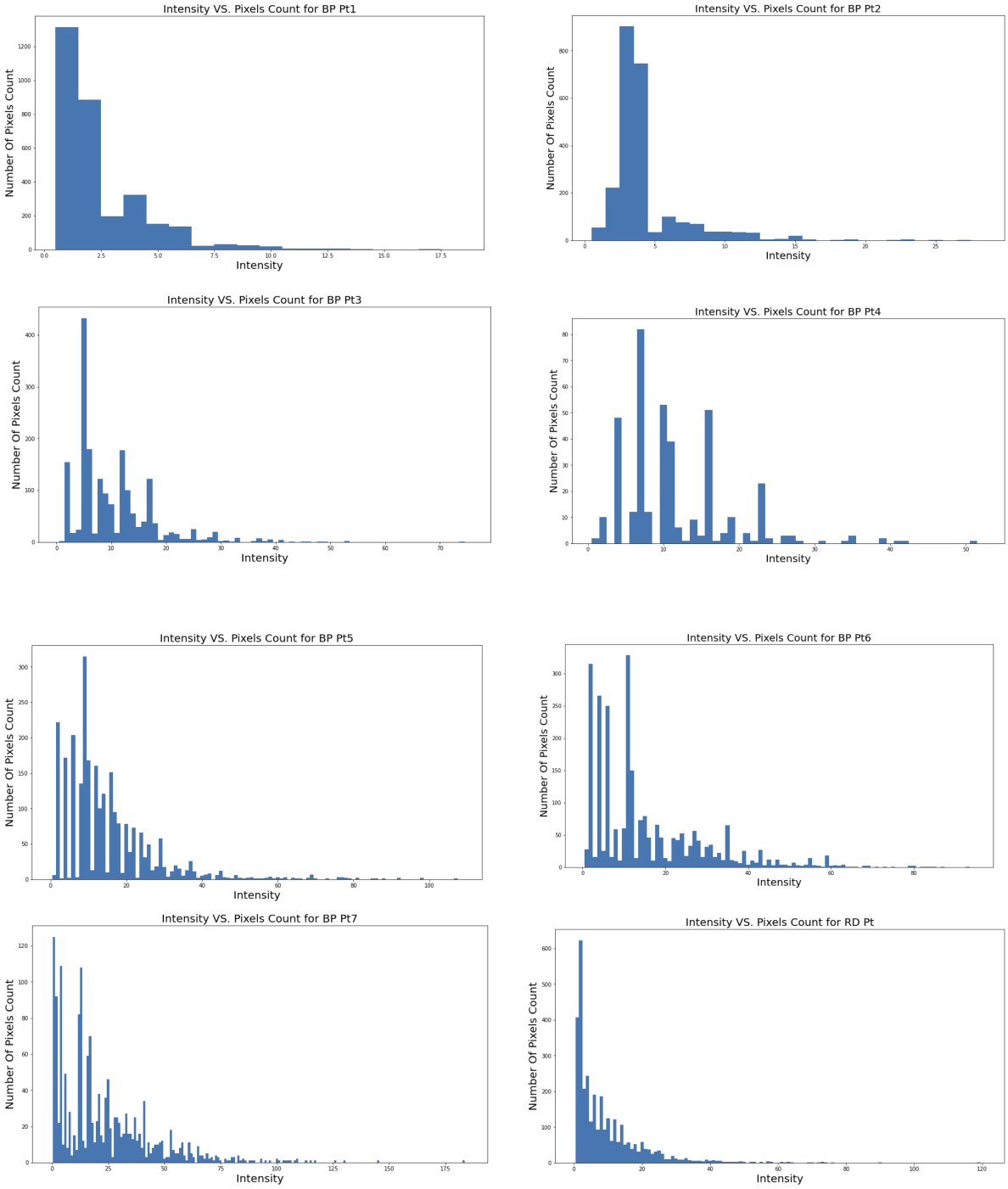

Figure C.7: Heatmaps Intensity Plots from Pt_1 to Pt_7 for Boltzmann population case and random case. The intensity is calculated by partitioning the supercell into 30×30 regions called pixel and the intensity is the number of sintering even in that pixel. Number of pixels count is counting how many such region or pixel has that particular intensity.

APPENDIX D

Supplementary information: Interpreting *operando* XANES of Supported Cu and CuPd in Conditions of Oxidative Deydrogenation of Propane: Dynamic Changes in Composition and Size

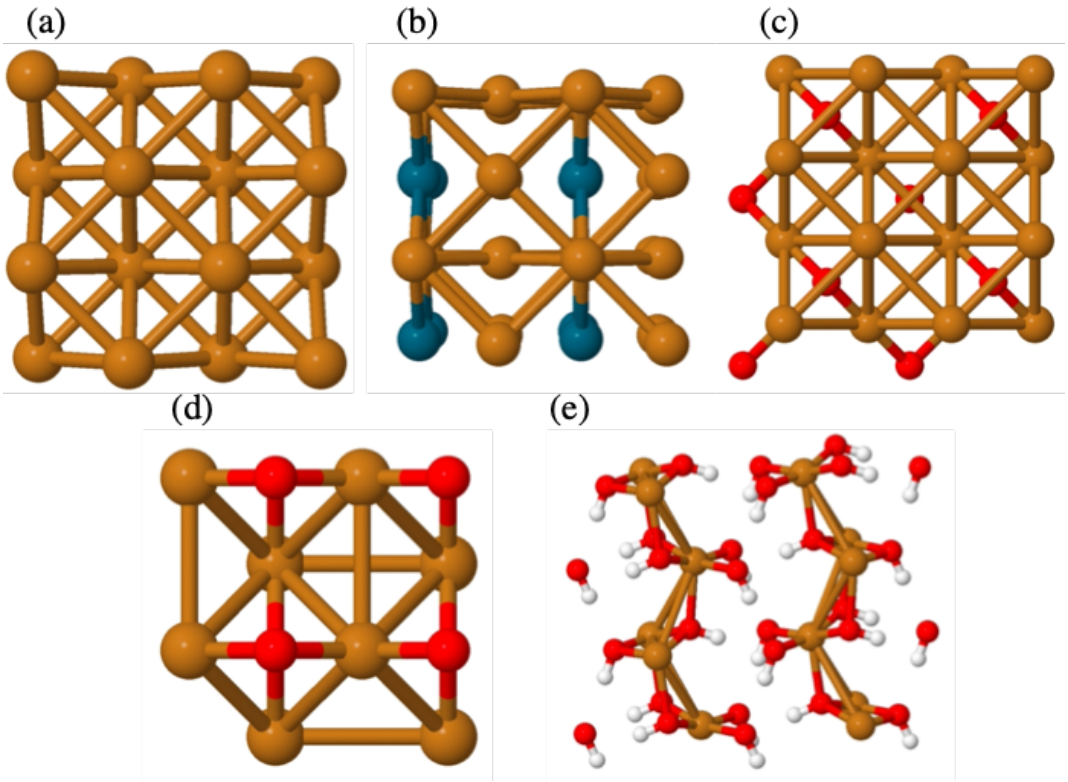

Figure D.1: The bulk structures used for the FDMNES calculations of the XANES used as the bulk standards. (a) bulk Cu, (b) bulk Cu_3Pd, (c) bulk Cu_2O, (d) bulk CuO, (e) bulk $Cu(OH)_2$. Structures taken from the materials project database.

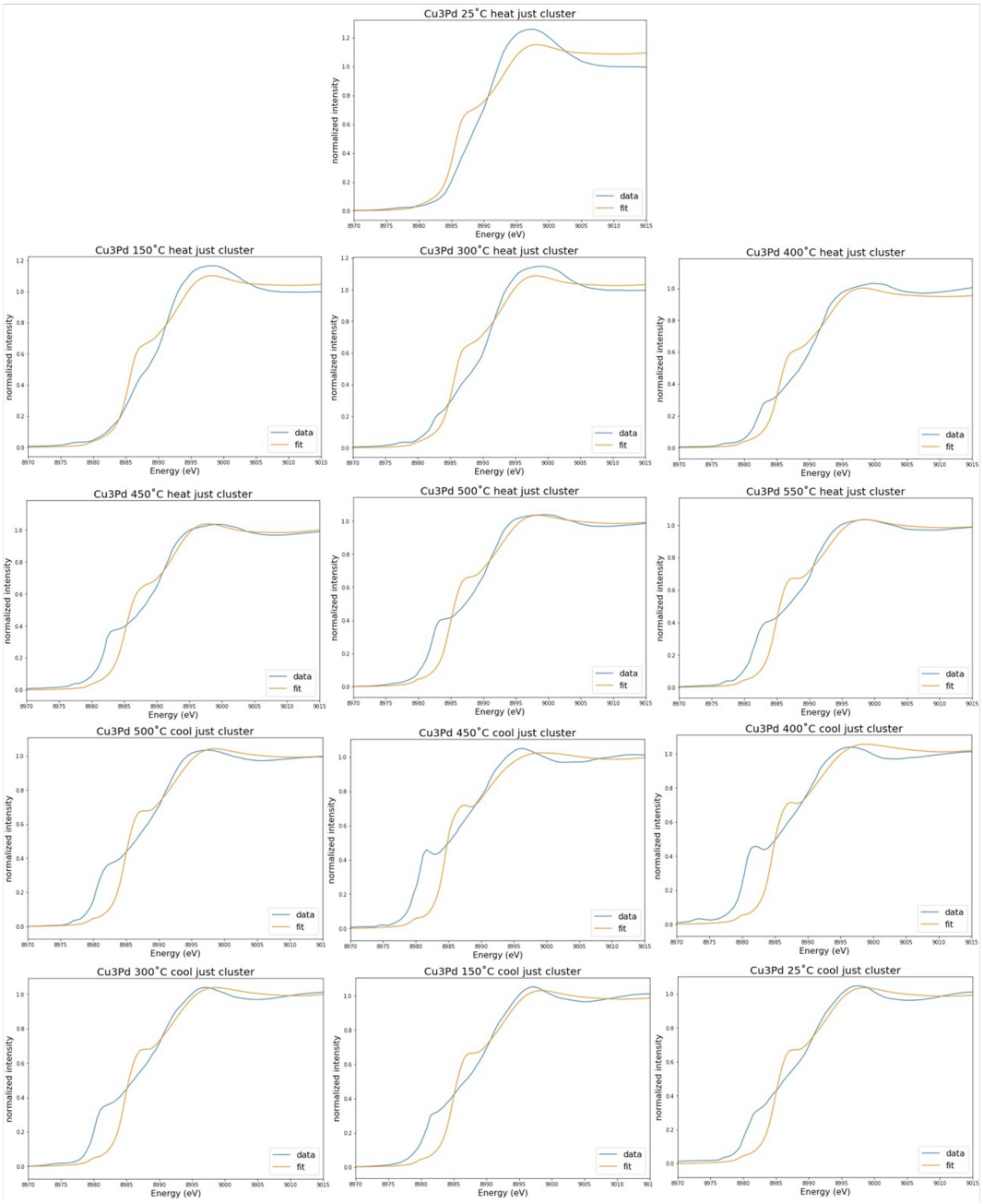

Figure D.2: Cluster-only fits for Cu_3PdO_x *operando* XANES, showing an inadequate ability for the cluster-only approach to capture the shift in the rising-edge energy as the temperature changes.

	25	150	300	400	450	500	550
R-factor heating	0.0359976	0.0224910	0.0250985	0.0227043	0.0295045	0.0295668	0.0348260
R-factor cooling	0.0334549	0.0331863	0.0451353	0.0680008	0.0628864	0.0410360	–

Table D.1: Tabulated R-factor values for the cluster-only fits for Cu_3PdO_x.

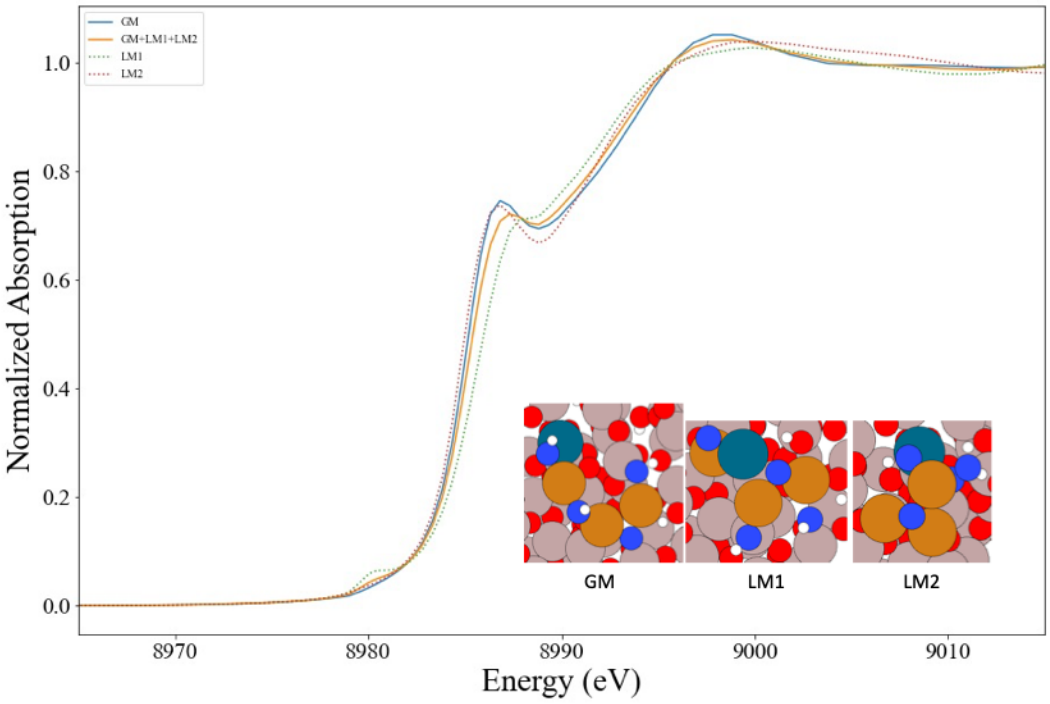

Figure D.3: Shows the minor changes dues to the Boltzmann-averaged spectrum of $Cu_3PdO_2(OH)_2$, with the relevant structures inset.

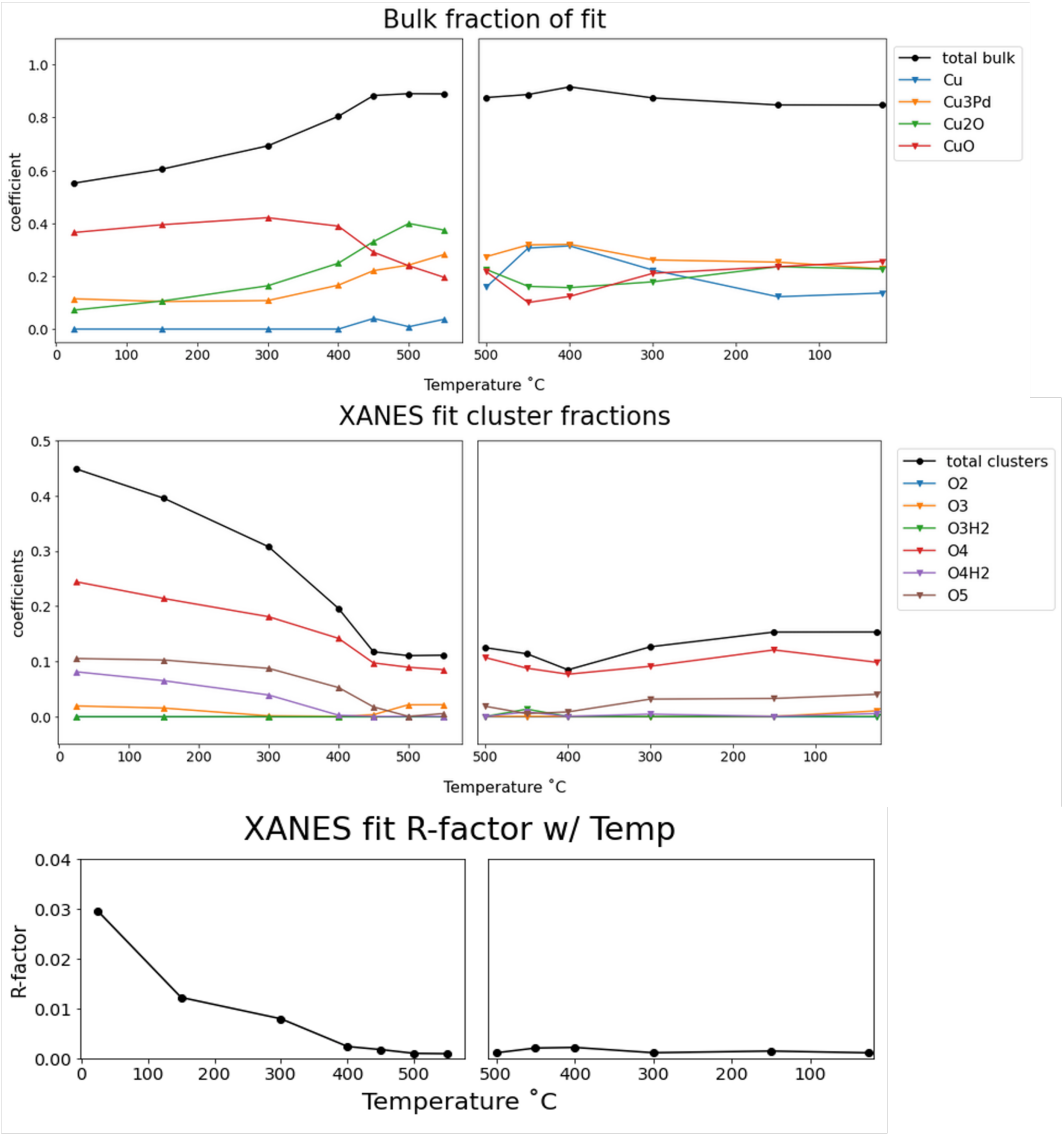

Figure D.4: Plot of XANES coefficients with a Boltzmann-averaged spectrum for $Cu_3PdO_4H_2$, to account for the presence of thermally accessible higher-lying isomers. Note that there are virtually no differences to the spectra seen in Figure 5c-h.

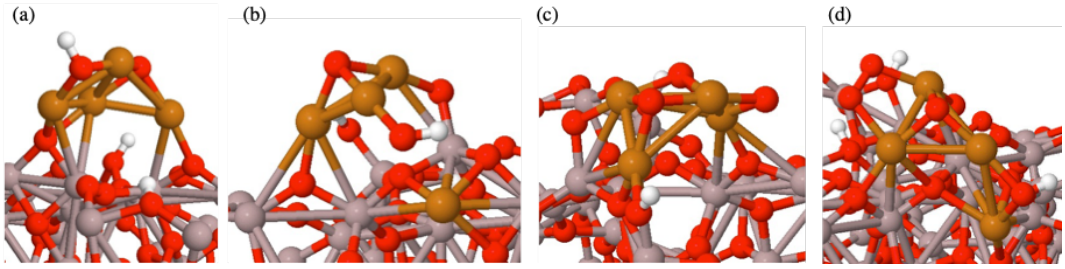

Figure D.5: Global minimum Cu_4Ox/α-Al_2O_3 structures for each oxygen content taken from (ref). (a) Cu_4O_2 (b) Cu_4O_3 (c) Cu_4O_5 (d) Cu_4O_5.These are the structures used as standards for the linear combination fitting of the Cu_4O_x experimental *operando* XANES.

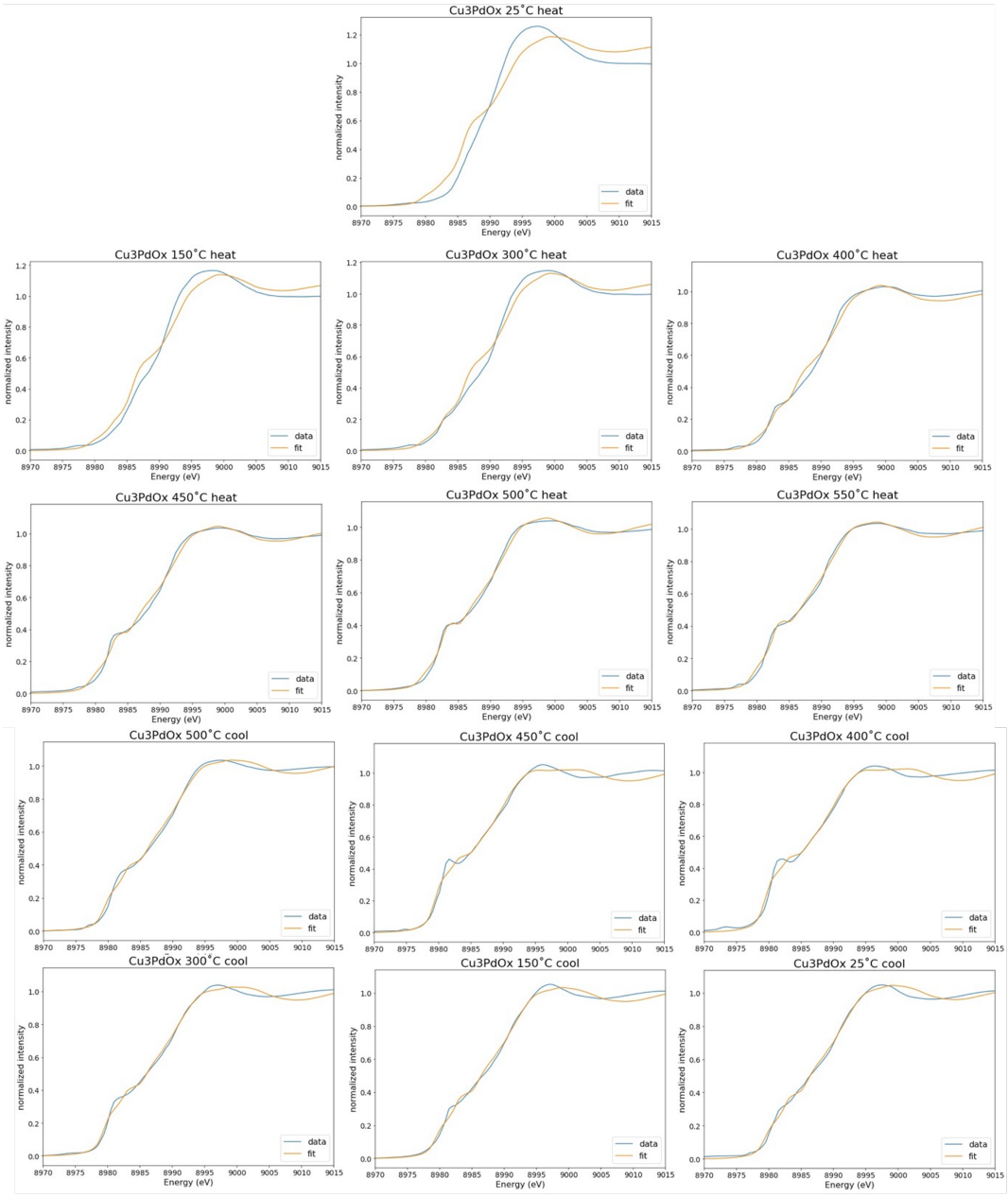

Figure D.6: The data + fit from the LCF process for Cu_3Pd with both bulk and cluster standards for all temperatures measured with the *operando* XANES, both heating and cooling. Note that during the cooling, while the rising edge is pretty much nailed, the sharpness of the shoulder peak is not reproduced by the fit. Compare to the cluster-only fit and note the improvement in capturing the rising edge energy.

	25	150	300	400	450	500	550
R-factor heating	0.0290865	0.0119796	0.0075351	0.002773	0.0020200	0.0010778	0.000982
R-factor cooling	0.0011668	0.0015472	0.0011924	0.0022733	0.0021478	0.0013456	–

Table D.2: Tabulated R-factor values for the cluster + bulk fits.

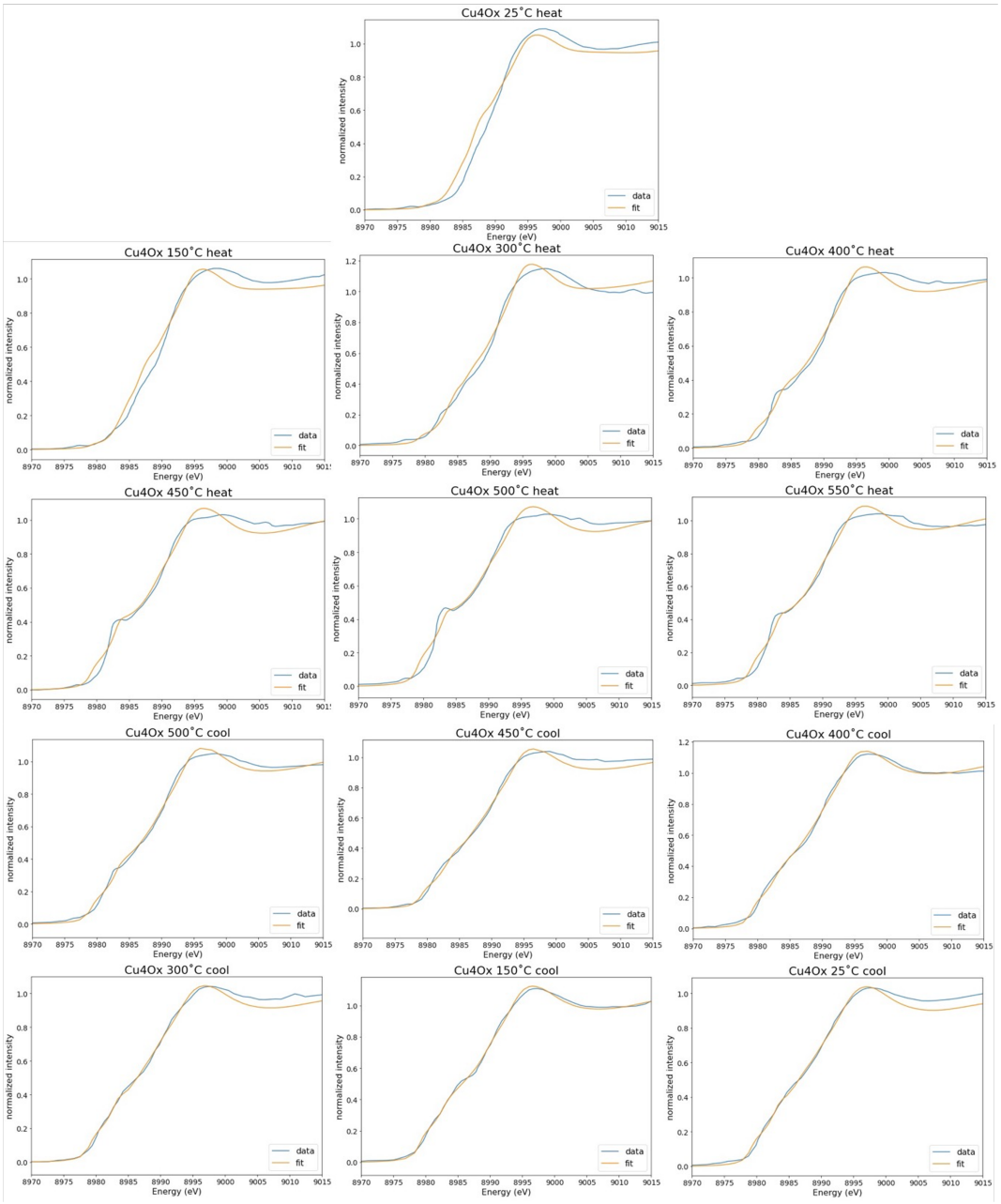

Figure D.7: The fit + data for each *operando* XANES measurement for Cu_4O_x during the heating/cooling cycle. Note that we can tell that the bulk is being overestimated in the fits initially because the fit is much more sharply peaked than the fit, which is a feature of the bulk Cu- compare the standards to each other to see the difference, and note that the rise in intensity starting 9010/9015 eV is characteristic of a bulk oxide, rather than a copper oxide cluster.

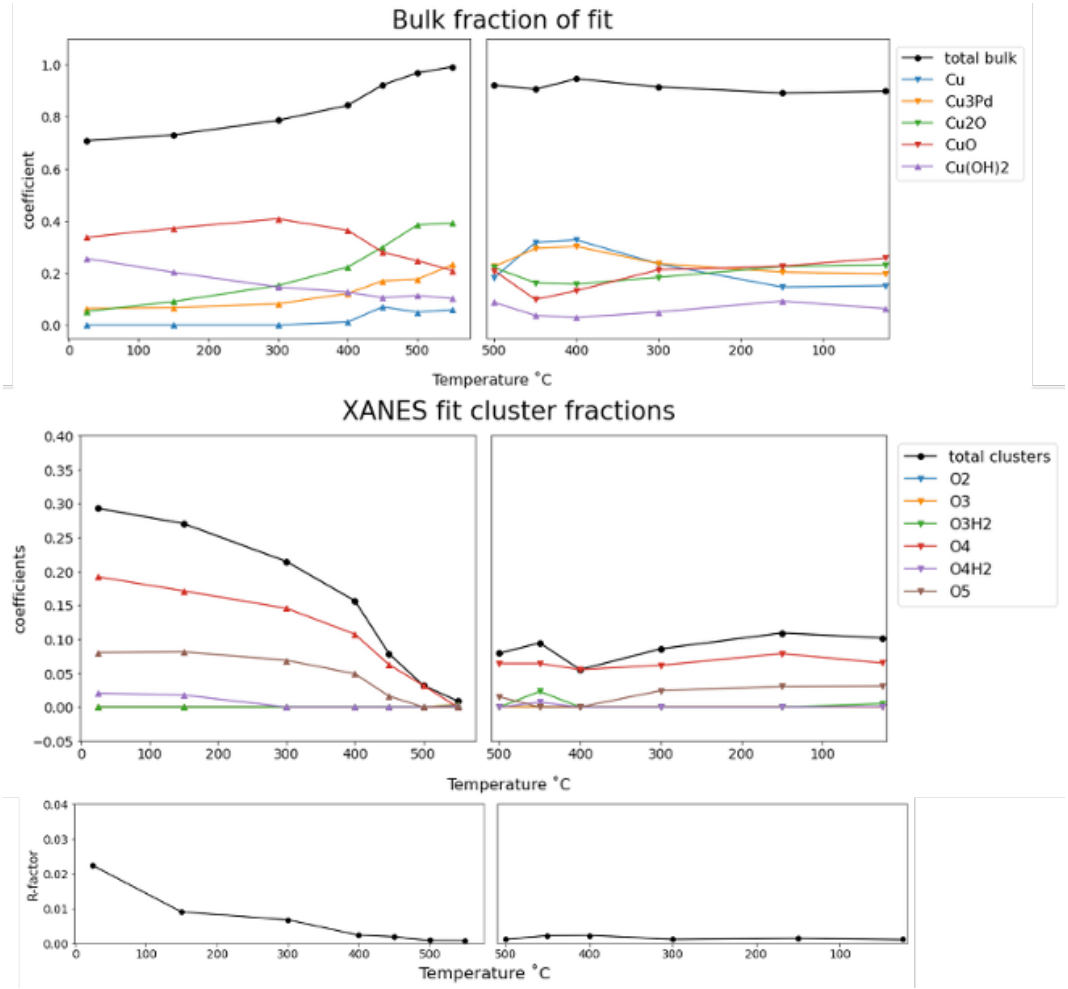

Figure D.8: Cu_3Pd fits with $Cu(OH)_2$ as part of the basis set with temperature that show strange fluctuations which were previously seen for less complete fits done prior to this attempt. These unphysical fluctuations are why we ultimately excluded $Cu(OH)_2$ from the final fit for the Cu_3Pd clusters.

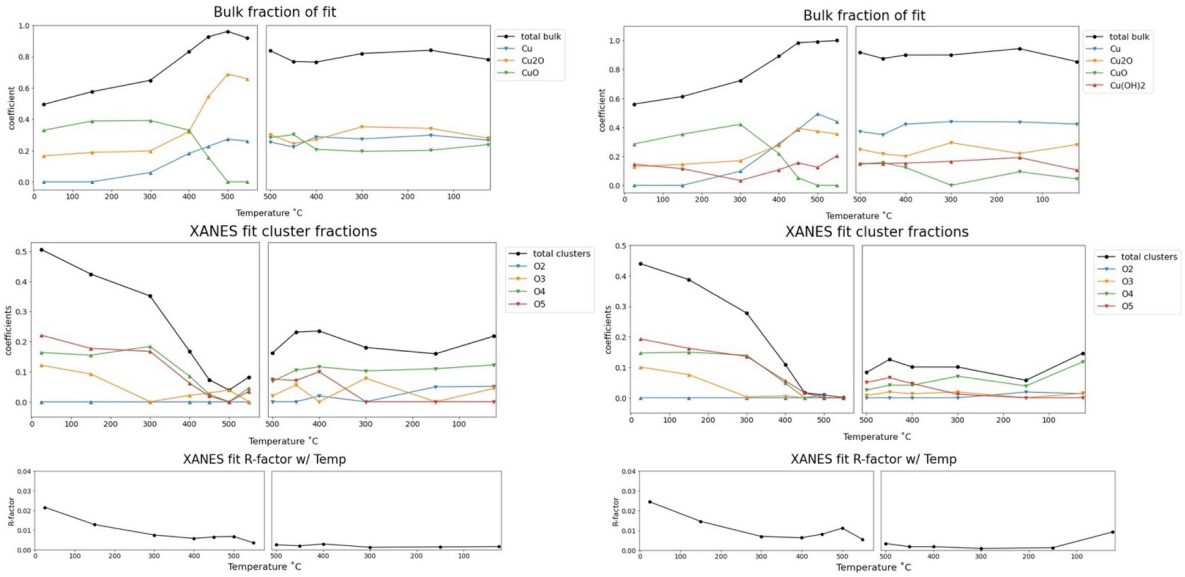

Figure D.9: Shows the difference between the Cu_4O_x fit without and with $Cu(OH)_2$ bulk included- despite the marginally better R-factor, we don't use the version that excludes $Cu(OH)_2$, because of the significant fluctuations in composition and total cluster/bulk fraction as the temperature peaks then decreases, making the results seem less physical- there is a strange discontinuity with the Cu2O fraction from 550°C to 500°C as it's cooled which doesn't make sense. However, whenc $Cu(OH)_2$ is included in the fit, we find that that strange Cu_2O peak is no longer present, and many of the strange fluctuations present in the fit without are smoothed out, yielding a much more reasonable physical result. We emphasize, however, that when including $Cu(OH)_2$, looking at how the R-factor changes on the graph, we see that there is a fairly small change compared to without, which one would assume implies that the $Cu(OH)_2$ fraction is fairly small, which is in fact not the case. There is also the fact that including the $Cu(OH)_2$ does lead to some changes in the overall bulk composition (the cluster composition distribution doesn't change much, only the overall fraction is reduced somewhat). This highlights the fact that when doing LCF, especially when considering it for subnano clusters, it is important to have a thorough basis set, and to do a variety of fit tests that take into account any variations in the basis set, and the impact that might play on the physical reasonability of the results.

	25	150	300	400	450	500	550
w/ $Cu(OH)_2$ R-factor heating	0.0244926	0.0146618	0.0070381	0.006408	0.0081514	0.011209	0.0055531
w/ $Cu(OH)_2$ R-factor cooling	0.009254	0.0013398	0.0009637	0.0018807	0.0018665	0.0034625	–
w/ out $Cu(OH)_2$ R-factor heating	0.0215978	0.0128344	0.0075387	0.0058171	0.0065956	0.0068294	0.0035345
w/out $Cu(OH)_2$ R-factor cooling	0.0016524	0.0014955	0.0013135	0.0029989	0.0020279	0.0025945	–

Table D.3: Comparison of R-factors with and without $Cu(OH)_2$ in the basis set for the Cu_4 fits shown above in Figure S11.

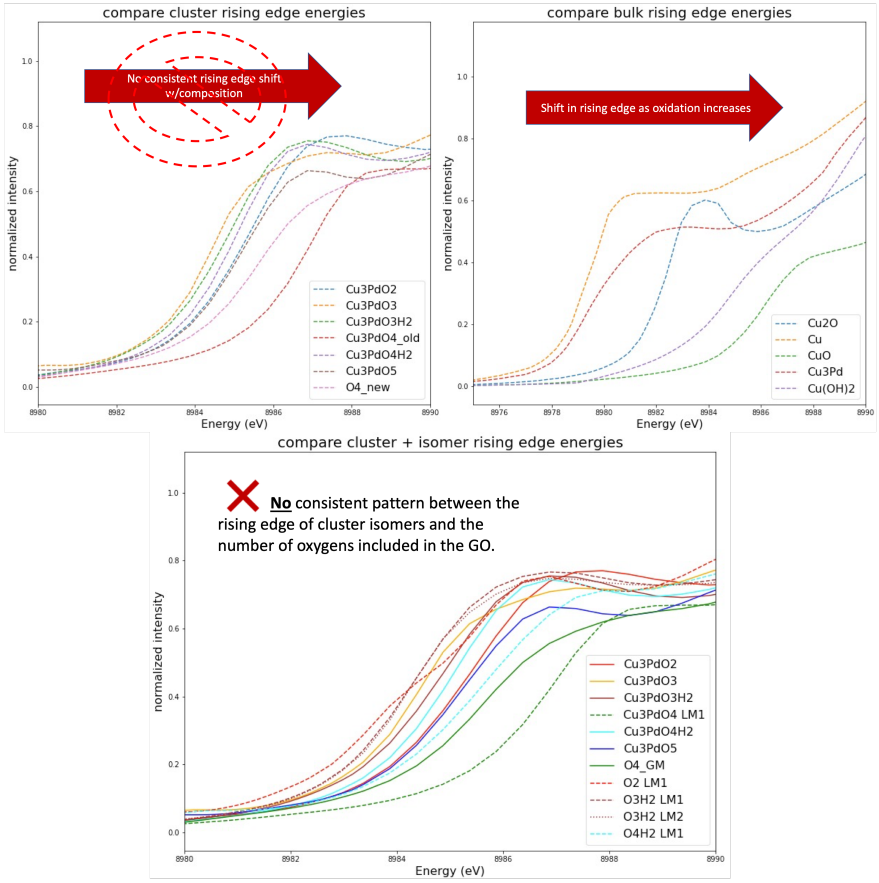

Figure D.10: Further demonstrating the lack of correlation between the oxygen content of the Cu_3Pd clusters and the rising edge energies, in direct contrast to bulk systems.

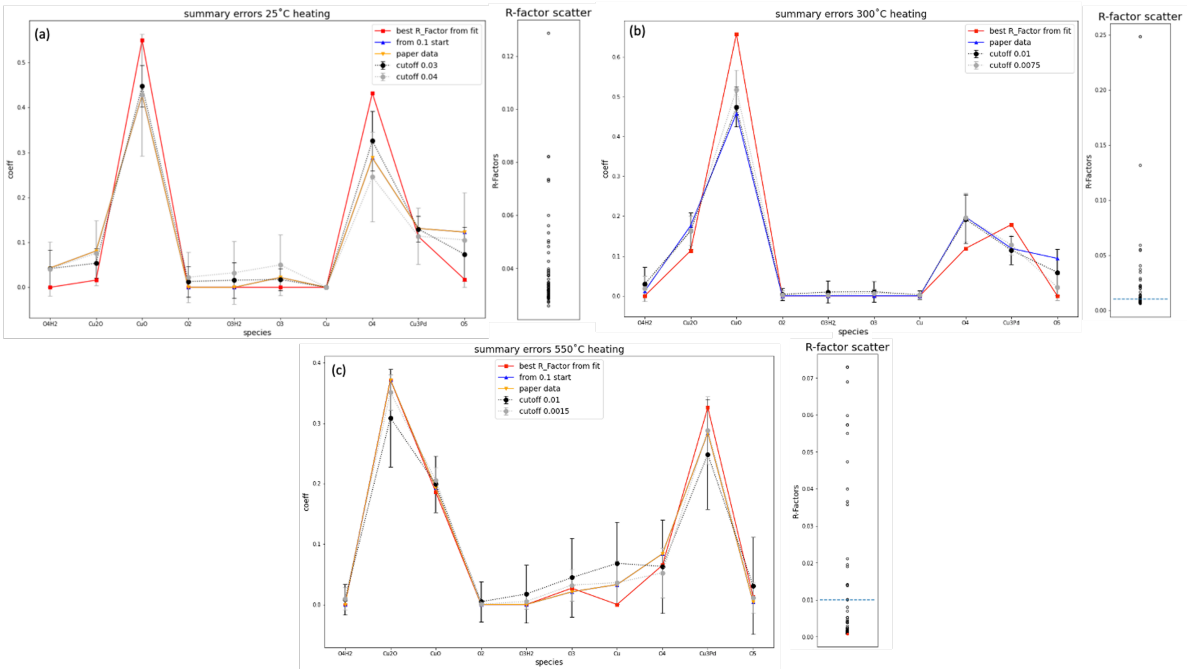

Figure D.11: Analysis of the stability of Athena's fitting procedure for three temperatures, spanning the range of R-factors obtained in the original fits. (a) 25°C, (b) 300°C, and (c) 550°C. The stability of the with was tested by randomizing the initial coefficients of the standards for the fit, and then performing the fit with Athena as usual. This was done 75 times, and the results plotted above. The different lines represent different cutoffs for R-factors to exclude, some of which which were artificially high due to the randomly chosen initial coefficients. Also shown are the averages with standard deviations for the larger and smaller R-factor cutoffs to show that the closer to the minimum R-factor, generally the smaller the uncertainty becomes, indicating that the closer the results are to the minimum R-factor, the more likely they are to be similar, indicating stability of fit. Also noteworthy is that as the minimum R-factor decreases, the overall uncertainty of the fits decreases, from $25 \rightarrow 300 \rightarrow 550$ °C, indicating that as the R-factor improves, the more stable the overall fit is (as one would expect). Based on these results, we believe that the stability of our fits is sufficient to support our claims of the general trends observed as temperature changes. Furthermore, this suggests that doing multiple fits with Athena for each spectrum, starting from more varied standard coefficients, is important to get an idea of the stability of the fits, especially when using a larger number of standards, which can lead to a less stable solution.

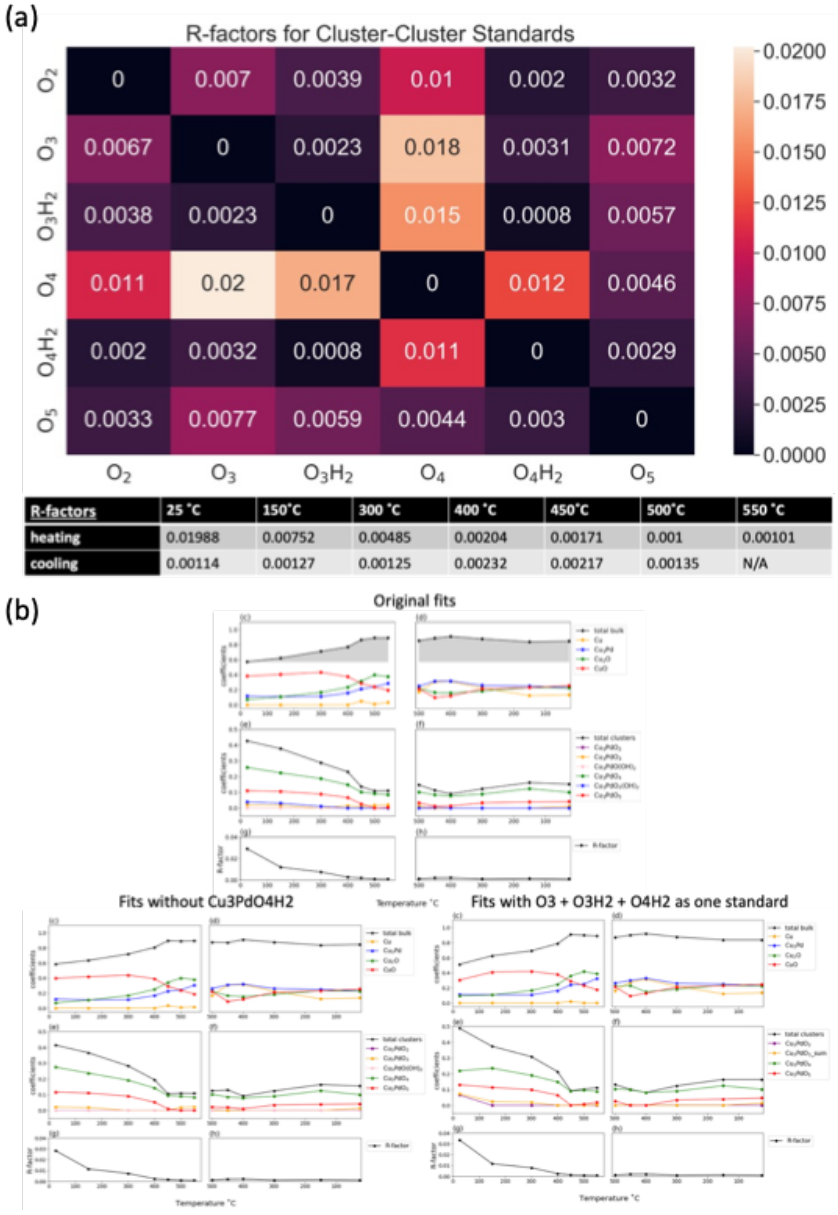

R-factors	25 °C	150°C	300 °C	400 °C	450°C	500°C	550 °C
heating	0.01988	0.00752	0.00485	0.00204	0.00171	0.001	0.00101
cooling	0.00114	0.00127	0.00125	0.00232	0.00217	0.00135	N/A

Figure D.12: (a) R-Factor comparison between all cluster standards, compared to the R–factors of each fit (shown in the table). Note that most of the differences are more than the well-behaved fits, indicating that the fits are good enough to discriminate between even these quite similar fits. (b) Different fit results with different standards, encompassing the original fits, and compared to fits where the $Cu_3PdO_4H_2$ standard is neglected due to similarity to the $Cu_3PdO_3H_4$ standard spectrum, and where the $Cu_3PdO_xH_2$ standards are folded into the Cu_3PdO_3 standard, emphasizing that these changes to the set of standards have minimal impact on the results, and does not change any conclusions drawn from the fits.

D.1 Supplementary Notes: different attempts for quality of fit

- Cluster only- see the earlier SI figure with all the fits.

• Breaking each cluster XANES into each individual Cu atom contributions and then performing the fits with this expanded basis set to see if we could track any significant changes in the types active sites from that- some of the fits were vaguely better than the full cluster only, however not significantly

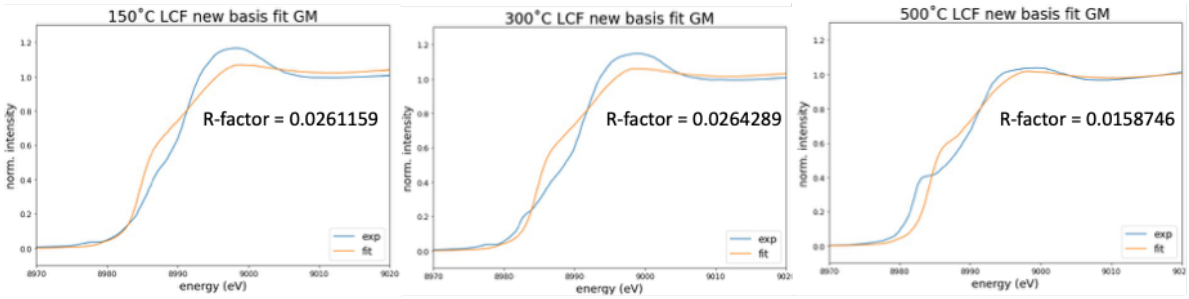

Figure D.13: Shows the expanded (active site) basis set fits, demonstrating somewhat of an improvement over the full cluster fits, but only minorly.

• Cluster+bulk- significant improvement in the R factors

o First attempt didn't include bulk Cu_3Pd, and there was a lot of fluctuation and oscillation with temperature that looked unphysical

o Once bulk Cu_3Pd was added, the smoothness of the coefficients was much better, emphasizing the importance of a good basis set for a good + physical result

o Note that when fitting with the LM1 and LM2 isomer spectra, the fit was not as high-quality

o Note also that when I was fitting with the LM1 and LM2s, the fit wasn't as good- it appeared the bigger the basis set the worse the fit- it would get caught in a minimum where there was a small amount of something (e.g. coefficient ¡= 0.03 or so) that was not important to the fit, but going back and systematically attempting to eliminate any too small coefficients artificially reduces the size of the basis basis set, because the amount of

one standard in the fit does depend somewhat on the mere presence of another apparently. Basically this just exposes the fact that the least squares minimization is unstable and does not lead to a unique solution, and basis set choice must be chosen quite carefully.

• There is also the fact that the bulk-only fits give results that are very similar (and slightly better in R-factor) to the bulk + cluster fits, however based on all of our other experiences we feel that the difference is minor enough that we cannot say that the bulk-only fits truly are better based solely on the magnitude of the R-factor. As we see interesting effects of the growth of the bulk fraction when including both cluster and bulk standards, that is what we decided to focus this paper on.

• Ultimately, the question is what is the best basis set to choose to get the most physical reasonable results rather than perhaps simply the best R-factor. It is possible to get similar R-factors for changes in coefficients with temperature that fluctuate quite strangely- as in the case when Cu_3Pd was excluded- indicating that there is something crucial missing from the fit. This can somewhat be seen even in the last Cu_4 fit that includes $Cu(OH)_2$, but it has the most physical coefficient evolution with temperature of all the other fits.

APPENDIX E

Supplementary Information for Got Coke? Self-Limiting Poisoning Makes an Ultra Stable and Selective Sub-nano Cluster Catalyst

E.1 TEM images of Pt_4 clusters

Scanning TEM in high angle annular dark field mode was used to image several sizes of Pt_n clusters deposited on Au supported ultra-thin carbon films, as shown in Fig. E.1. For the XPS, ISS, and TPD experiments in the manuscript, it is desirable to have a cluster spot with well-defined size, and high enough coverage to allow XPS measurements, and for those experiments, deposition was done with the alumina deposition substrates positioned *LESS THAN OR EQUAL TO** 0.5 mm behind a 2 mm diameter deposition mask. For imaging, the quad-TEM-grid holder did not allow the grids to be positioned very close behind the deposition mask, and because the cluster beam diverges rapidly as it is decelerated to the 1 eV/atom deposition energy, the deposited cluster spot was much larger than the exposed region of the TEM grid. By comparing the deposition currents for grid holder positions with, and without TEM grids, we estimate that only 0.85% of the cluster current impacted on the exposed central region of the grids.

Fig. E.1A shows an image of Pt10 clusters on an ultra-thin carbon film, and Fig. E.1B shows the ImageJ analysis, which counted 133 cluster spots, with mean diameter of 0.82 nm. The analysis has significant uncertainty due to the substantial contrast variation from the carbon grid; nonetheless, the spot density is nearly identical to the density predicted from

the estimated coverage (131 clusters in the analysis area). Furthermore, the cluster spots were found to be stable in both position and contrast in repeated images. Both the spot stability under the e-beam and the spot density, suggest that the Pt10 clusters were stable with respect to diffusion, agglomeration, and ripening, even for a carbon support, where metal-support binding tends to be relatively weak. Fig. E.1C shows a higher magnification image of Pt10¬ clusters deposited on a 31 nm thick oxidized aluminum film, which should better represent the behavior on the alumina/Ta (110) substrate used in the XPS, ISS, and TPD experiments. Here too, the spots were present with density close to that predicted from the estimated deposition density, and were stable under the e-beam, suggesting that Pt10¬/alumina is reasonably stable with respect to sintering.

The final image in Fig. E.1D is for Pt_4 deposited on an ultrathin carbon film at 0.01 ML-equivalent coverage. As expected, the cluster spots were smaller, with lower contrast compared to Pt10/carbon, and again were stable under the e-beam, however, in this case the number of clearly identifiable spots was more than an order of magnitude smaller than expected from the estimated deposition density. We attribute the discrepancy to the difficulty of distinguishing the faint spots associated with 4 atom clusters, from contrast variations in the carbon film. Alternatively, the low spot density might be taken as evidence that the Pt_4 clusters were sintering to produce a smaller number of larger clusters, however, in that scenario, the average sintered Pt_n cluster would contain more than 40 atoms, and therefore would appear brighter and/or larger than the Pt10 clusters in Fig. E.1A. We conclude from the absence of large, high contrast spots, that the Pt_4/carbon clusters are also stable, but were simply lost within the contrast variation of the carbon film. In this context, we note that attempts to image Pt1/carbon TEM grids showed no features distinguishable from the grid contrast variations. We would not expect to observe single atoms with our non-aberration-corrected STEM, but again, the absence of observable features is consistent with isolated atoms also being stable with respect to sintering to clusters large enough to see.

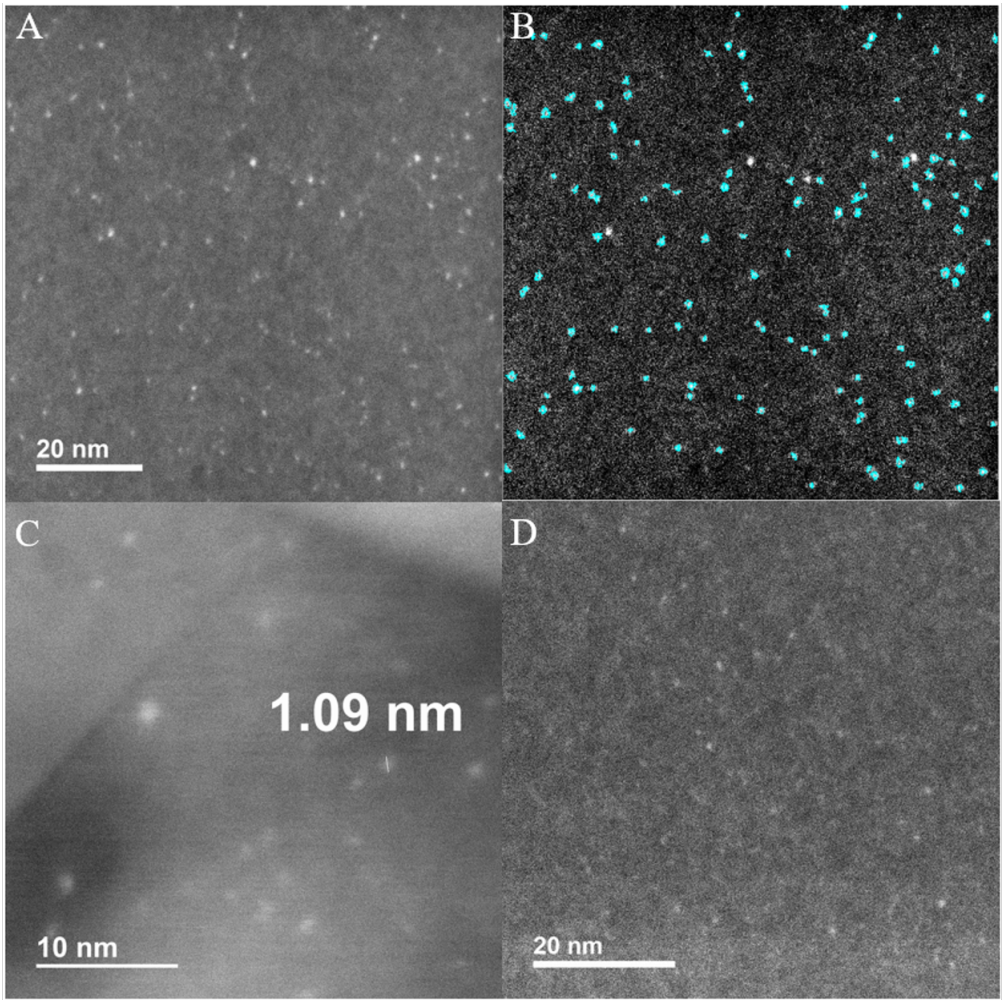

Figure E.1: (A) S/TEM HAADF Image of 0.01 ML equivalent of Pt10 clusters deposited on an ultra-thin carbon film. (B) ImageJ analysis of the cluster coverage of (A). (C) Image of 0.01ML Pt10 deposited on a 31 nm thick, oxidized aluminum film grid, the cluster diameter was found to be 1.09 nm. (D) Image of 0.01 ML Pt_4 deposited an ultra-thin carbon film grid, showing the absence of any high contrast features that might have formed by sintering.

E.2 Desorption during the first heating of Pt_4Ge/alumina: Removing HCl and absence of C_2D_4 binding to the clusters

The Pt_4Ge/alumina samples as prepared, prior to any heating, still had some Cl atoms on the surface, and the clusters were saturated with hydrogen. Therefore, the final step in the preparation process was to heat the samples to drive off Cl and H, and the desorption

behavior is shown in Fig. E.2. The sample was cooled to 150 K and exposed to 10 L of C_2D_4, which we added as probe of exposed cluster binding sites. The sample was then heated at 3 K/sec to 750 K while monitoring C_2D_4, D2, H35Cl, and 35Cl2 desorption. Cl2 desorption was not observed, so data are shown only for C_2D_4, D2, H35Cl. A small amount of C_2D_4 desorbed at low temperatures, where C_2D_4 desorption from the alumina support is expected, with no desorption observed at the higher temperatures characteristic of Pt binding sites. The conclusion is that, because the Pt clusters were saturated with Cl and H, C_2D_4 adsorbed only on the support, and as expected, no D_2 desorption (or carbon deposition) was observed – further evidence (cf. Fig. 2) that C¬2D4 does not dehydrogenate on the Ge/alumina support. The major desorption was of HCl, which began as soon as the sample was heated above the 300 K temperature used for the GeCl4 and H2 doses in the Ge deposition treatment. As shown, no further HCl desorption occurred in the 2nd and 3rd heatings (5 were tested), indicating that no Cl remained on the surface after the first heating. H2 presumably also desorbed during the first heating, however, because the UHV background is high at mass 2, we did not attempt to measure the small amount of H2 that would be desorbed from the 0.1 ML coverage of Pt.

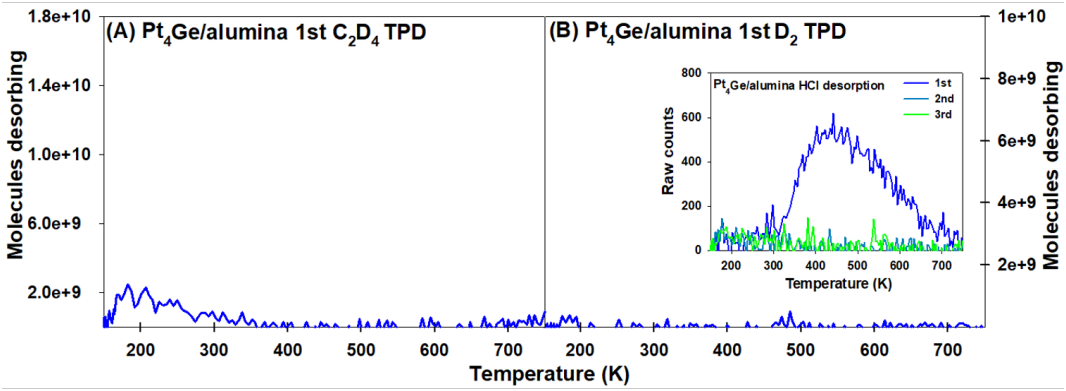

Figure E.2: TPD measured during the first heating of the Pt_4Ge/alumina sample, under conditions identical to the TPDs shown in Fig. 2 of the main paper. (A) C_2D_4 desorption. (B) D_2

E.3 TPD quantification

As described above, we calibrated the relationship between the number of molecules desorbing from the surface and the ion counts measured by the mass spectrometer during TPD. The data shown in Fig. 2 of the main paper have been corrected to molecules desorbing using the calibration process, and the TPD curves were then integrated to obtain the total numbers of molecules desorbing in each TPD cycle. The integrated numbers of molecules desorbing are shown in Tables E.1 and E.2, for the first 6 TPD cycles on Pt_4/alumina and Pt_4Ge/alumina. In later cycles the signals for D_2 are small enough that uncertainties due to correction for mass spectrometer background makes them unreliable. It should be noted that there are also uncertainties relating to how the (unknown) desorption angular distributions affect detection efficiencies, and how the detection efficiency of the mass spectrometer varies with the distance of the desorption site from axis of the mass spectrometer. It is difficult to quantify either of these uncertainties, and we, therefore, assign a rather large ±50% uncertainty to the values in the tables.

Integrated desorption values are given in terms of numbers of C_2D_4 or D_2 molecules desorbing per Pt atom on the surface, and in terms of molecules/cluster. This is possible because we know quite precisely how many clusters were deposited in the analysis area. For Pt_4 clusters, the 0.1 ML equivalent coverage translates to 1.18×10^12 clusters or 4.71×10^12 atoms in the cluster spot, all of which are visible to the TPD mass spectrometer. Some molecules also desorb from the Pt-free alumina and Ge/alumina supports, and those integrated values are given in the "alumina" and "Ge/alumina" lines in the table. To allow direct comparison with the results for the cluster-containing samples, they also have been normalized to the numbers of Pt atoms or clusters are present in the cluster-containing samples. The desorbing molecule values for the cluster-containing samples have been corrected by subtracting the alumina and Ge/alumina values. The total number of C_2D_4 molecules adsorbed during the 150 K dose starting each TPD cycle was estimated assuming that only carbon was left on the surface at 750 K. In that case, total C_2D_4 adsorbed = C_2D_4 desorbing

+ 0.5*D_2 desorbing.

E.4 XPS quantification

The Ge:Pt coverage ratio prepared by the $GeCl_4/H_2$/heating process used to prepare Pt_4Ge/alumina was estimated from the ratio of Ge 2p and Pt 4d XPS intensities. Because the deposition currents are monitored and the cluster spot is defined by a mask, we know the coverage of Pt atoms on the cluster-containing samples quite accurately (1.5 x 10^14 Pt atoms/cm^2). Furthermore, all the Pt and Ge atoms are in the surface layer, where attenuation of the photoelectrons should be negligible, therefore the Pt 4d intensity can be used to put the Pt and Ge coverages on an absolute basis. The ratio of background-subtracted, integrated Ge and Pt XPS intensities (IGe/IPt) is related to the coverage ratio XGe/XPt as follows:

$$X_{Ge}/X_{Pt} = (I_{Ge}/\sigma_{Ge})/(I_{Pt}/\sigma_{Pt})$$

where σ_{Ge} and σ_{Pt} are the Ge 2p and Pt 4d sub-level photoemission cross sections, taken from Yeh and Lindau.[204] The cross section ratio was checked against and agrees well with a ratio derived from the empirical atomic sensitivity factors for our instrument configuration corrected by the ratio of the effective attenuation lengths [248].

It was found that the total amount of Ge deposited for by the $GeCl_4/H_2$/heating treatment on a Pt_4/alumina sample was 9.7 x 10^13 Ge atoms/cm^2. For a Pt-free alumina sample exposed to the same $GeCl_4/H_2$/heating treatment, the Ge coverage deposited on the alumina support was found to be 5.7 $\times$ 10^13 Ge atoms/cm^2. Because the Pt_4 coverage on Pt_4/alumina was small, it is reasonable to assume that the non-selected Ge deposition on the alumina support was similar in the Pt_4/alumina and alumina samples, and therefore we can estimate the coverage of Ge deposited in association with the Pt_4 clusters to be 4.0 $\times$ 10^13 Ge/cm^2. This is comparable to the density of Pt_4 clusters deposited on the sample,

thus the stoichiometry of the clusters is estimated to be $Pt_4Ge1.07$, which is within the uncertainty of Pt_4Ge_1.

The XPS data in these experiments was taken on different days, and has been corrected for variations in the X-ray source intensity or spectrometer sensitivity, using the Al 2s intensity from the alumina support films as a reference. Because the alumina film thicknesses varied slightly between samples, the intensities were also corrected for the alumina thicknesses (determined from the Al 2s: Ta 4d ratio also measured in each spectrum), using the EALs calculated for Al 2s electrons in alumina.[248] Note that this thickness correction was quite small. For example, for typical alumina support film thickness (e.g. 4.7 nm vs. 4.6 nm), the effect of thickness on the Al 2s intensities should be only 0.9%.

E.5 Sampling protocol

In the case of sampling for supported bare Pt_4Ge and Pt_4GeC_2, initially 200 minima were identified, of which we 124 (respectively 126 for Pt_4GeC_2) minima were unique, and 76 (respectively 74) were duplicates. Of these structures, for Pt_4Ge, there were only 16 within 1.4 eV of the GM, and only 4 for Pt_4GeC_2. For adsorbate sampling, we used 3 lowest-energy bare isomers, and sampled the adsorbate binding to each of them. We used 150 additional initial configurations for ethane on each minimum of the bare cluster (or a total of 450 structures); 50 – for ethylene (i.e. total of 150); and 40 (i.e. total of 120) – for acetylene, chosen based on the rate of duplicate appearance. For ethane binding, the number of formal duplicates was 10-20 per cluster core, however when visually filtering out structures that were minimally different, but with slight rotations and minimal C-H activation differenced (i.e. likely the structures that would relax to the lowest energy structure), the number of duplicated was closer to 100. For ethylene, the number of duplicates was 20-25 (given some ambiguity in structural identity). For acetylene, the number of duplicates was 25-30 for each Pt_4GeC_2 isomer sampled. For Pt_4GeC_2, we sampled a total of 600 ethane binding modes,

200 ethylene binding modes, and 160 binding modes for acetylene."

E.6 Evidence suggesting that Pt_n clusters do not diffuse significantly as deposited on alumina or Ge-alumina supports.

Alumina grown on Ta (110) single crystals will have defects and grain-boundaries that could bind the Pt clusters differently than terrace sites, possibly modifying the cluster electronic and chemical properties. One piece of evidence that the clusters are stable with respect to diffusion is the TEM results presented above, which show that the clusters do not diffuse on the surface even under the influence of the TEM beam.

In addition, the TPD data also are consistent with the clusters not diffusing significantly as deposited. This evidence comes from two observations, the first of which shows that when the $GeCl_4/H_2$ treatment is done to the alumina support (with no Pt clusters present), the small amount of non-specific Ge deposition tends to occur at the defects in the alumina film. Consider the CO TPD results for the blank alumina surface (black trace) in Fig E.14, following CO exposure at 95 K. The amount of CO desorbing from the clean alumina surface corresponds to 5.6×1013 CO molecules per cm2, i.e., just a few percent of a CO monolayer. This value is almost identical to the 5.7 x 1013 Ge atoms that are observed by XPS to deposit when Pt-free alumina substrates are given the $GeCl_4/H_2$ treatment. Clearly Ge deposits on only a small fraction of the alumina sites, which appear to be defects.

The red trace labeled Ge/alumina shows CO desorption from an alumina film that was given the normal $GeCl_4/H_2$ treatment, then heated to 750 K to drive off HCl and H2, then saturated with CO at 95 K. The amount of CO desorbing decreased by 40%, indicating that Ge deposition on the alumina blocked or modified 40% of the alumina defect sites such that they no longer adsorbed CO at 95 K. It should be noted that there may be additional Ge that deposited at alumina defect sites that do not bind CO (with or without Ge) at 95 K, but clearly there is propensity for Ge to deposit at defects, resulting in a small coverage

of Ge atoms on the Ge/alumina surface.

The second observation is that when Pt_4 is deposited on the Ge/alumina surface, and then probed by C_2D_4 TPD (Fig. E.13), the result is quite similar to that for Pt_4/alumina, with a large high temperature C_2D_4 desorption peak and substantial D_2 desorption during the 1st TPD, both gradually diminishing in subsequent TPD runs due to coke deposition on the clusters. If Pt_4 clusters had significant propensity to diffuse to defects on the support, a substantial fraction of the clusters would be associated with defect-bound Ge on the Ge/alumina support, and we would expect the TPD behavior to resemble the behavior for Pt_4Ge/alumina, i.e., little D_2 desorption even in the first TPD run, and persistent high temperature C_2D_4 desorption in repeated TPD runs. In the first TPD run in Fig. E.13, the C_2D_4 and D_2 quantification indicates that 41% of the total amount of C_2D_4 that adsorbed, dehydrogenated to generate D2. This fraction is quite similar to 44% fraction that is observed for Pt_4/alumina, i.e., it appears that at least 90% of the Pt_4 clusters deposited on the Ge/alumina surface are chemically identical to Pt_4 deposited on Ge-free alumina. The remaining ¡10% fraction is not unexpected, because random deposition on a surface with a few percent of Ge site should result in a small fraction landing at Ge sites.

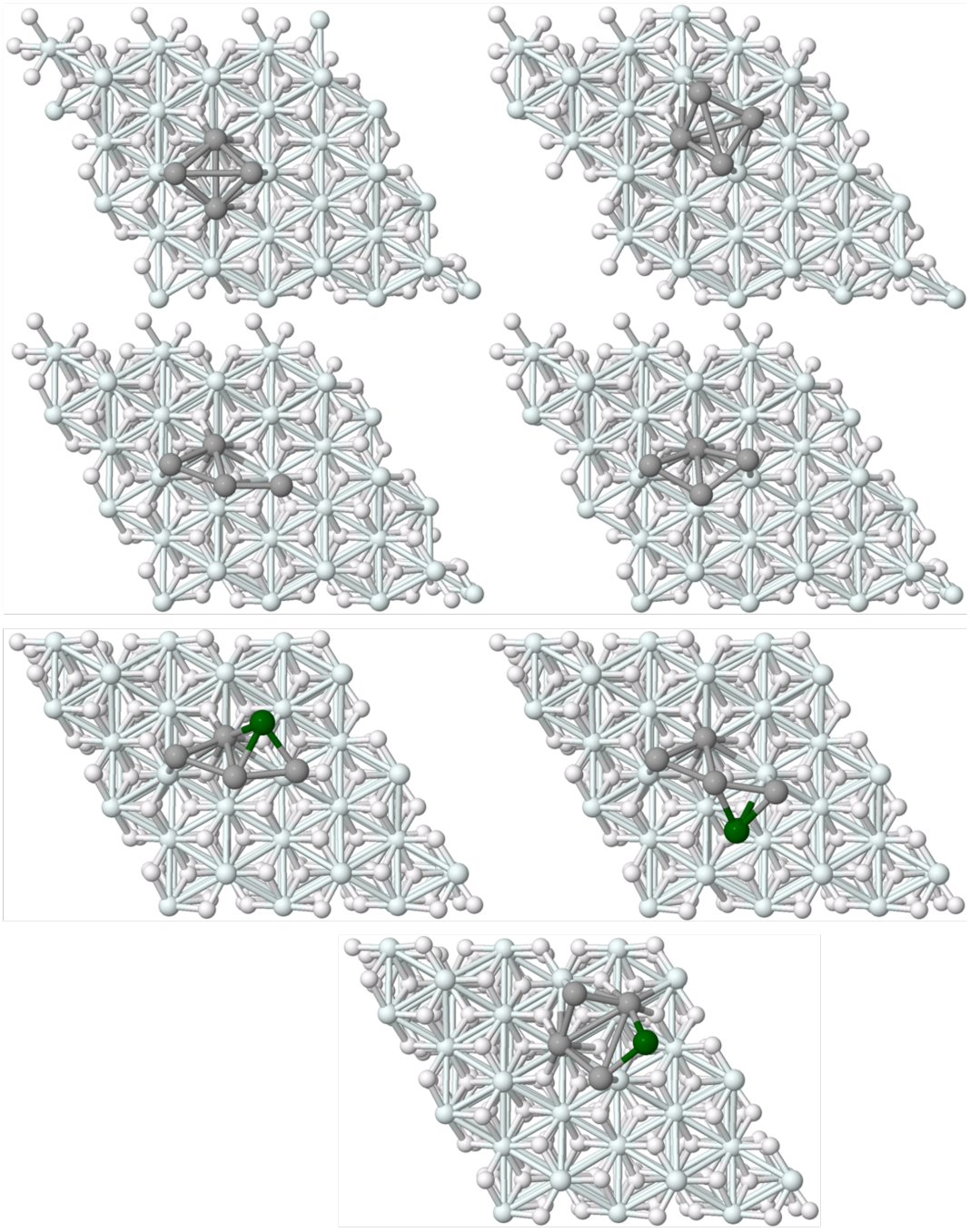

Figure E.3: Pt4 and Pt_4Ge alumina structures shown on entire Al_2O_3 support.

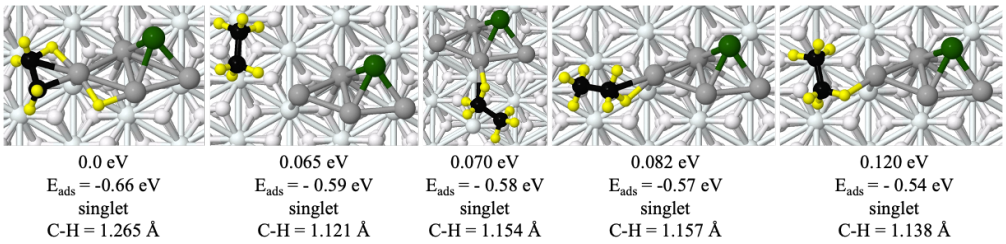

Figure E.4: Key low energy binding geometries for ethane on Pt_4Ge/alumina.

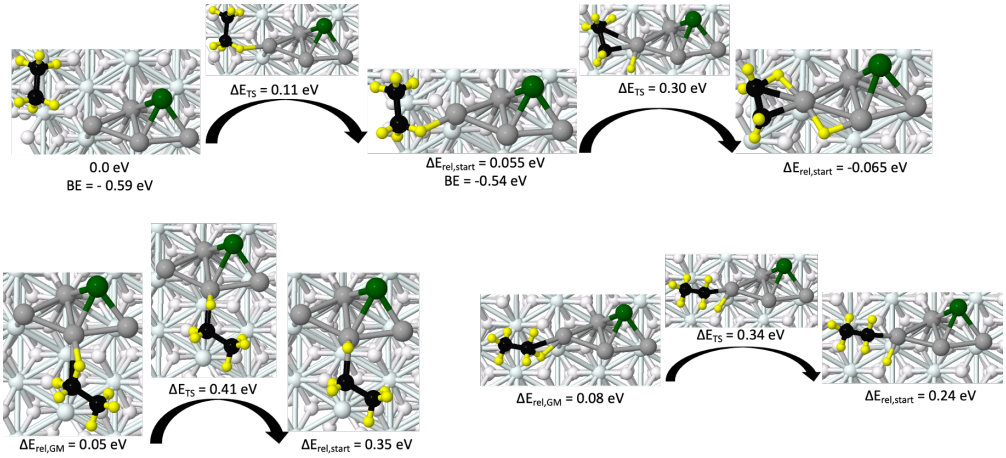

Figure E.5: Pt_4Ge/alumina ethane C-H activation barrier endpoints and TS structures for barriers shown in Figure 5b.

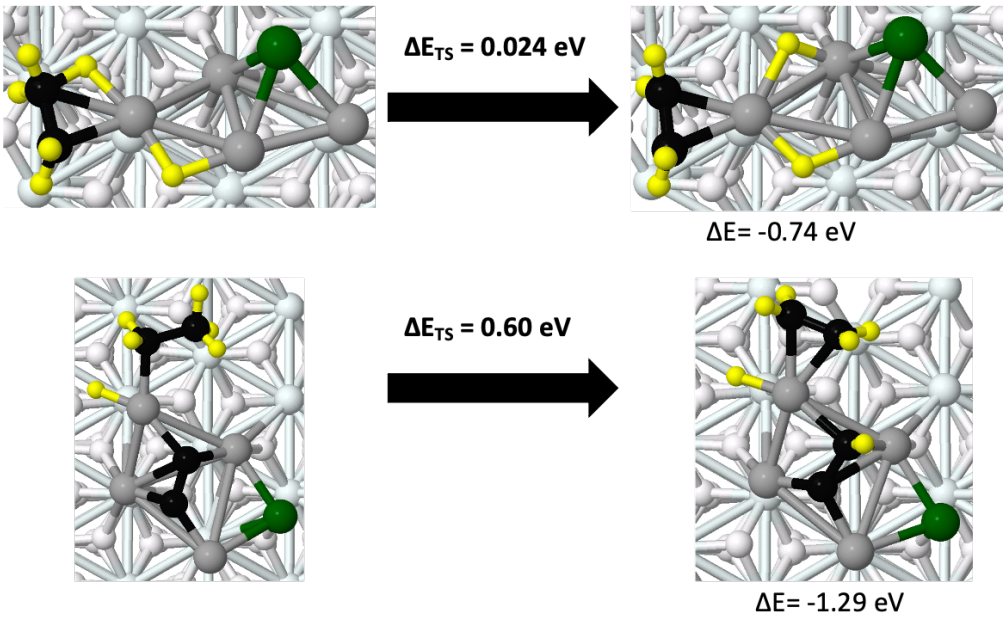

Figure E.6: Second ethane C-H activation barriers and endpoints for chosen Pt_4Ge Pt_4Ge/alumina and Pt_4GeC_2 Pt_4Ge/alumina isomers.

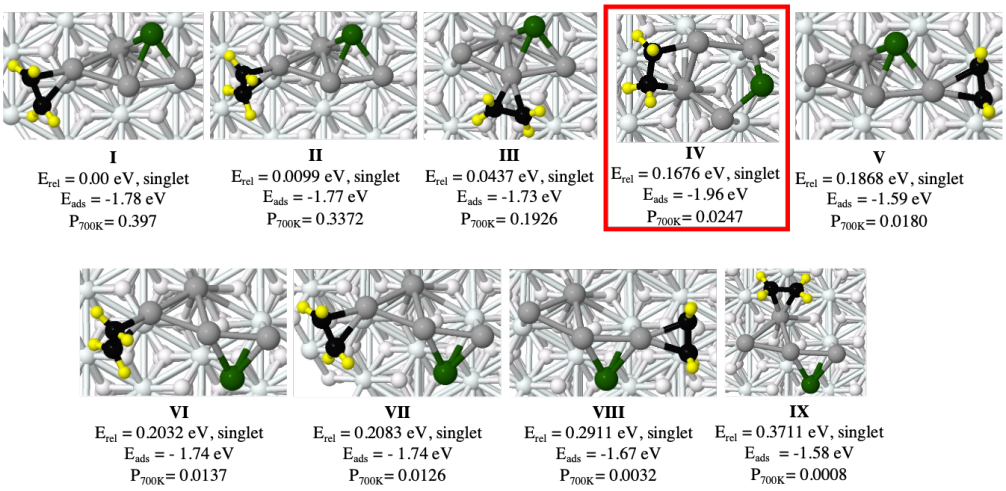

Figure E.7: All thermally accessible binding geometries for ethylene on Pt_4Ge/alumina

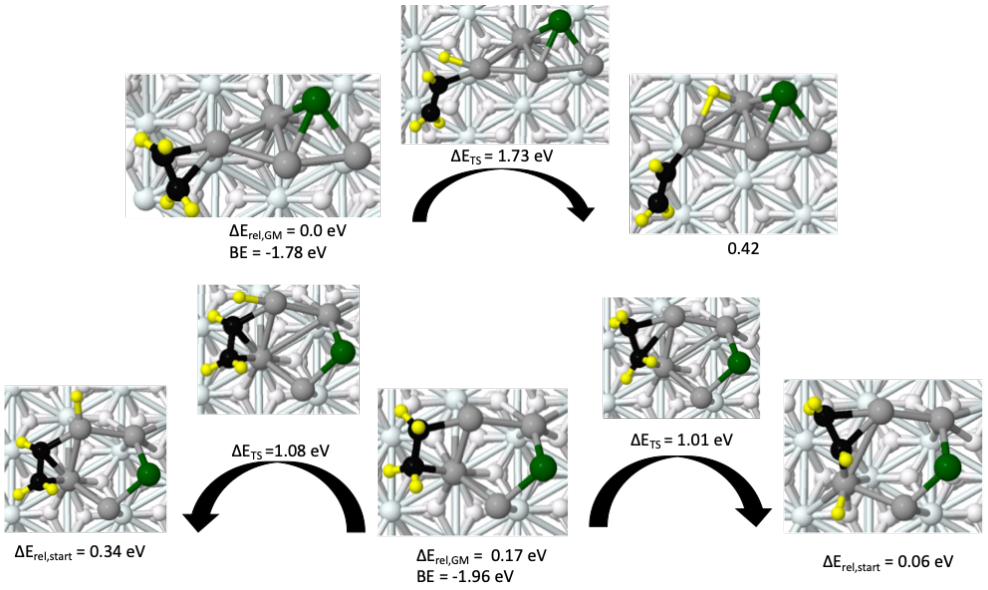

Figure E.8: Pt_4Ge/alumina ethylene C-H activation barrier endpoints and TS structures for barriers shown in Figure 5b.

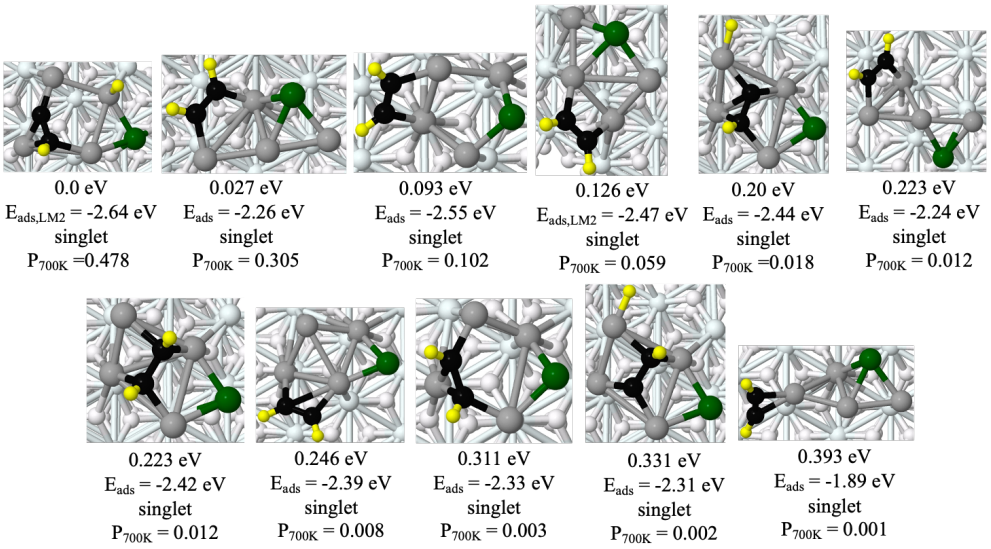

Figure E.9: All thermally accessible low energy binding geometries for acetylene on Pt_4Ge/alumina.

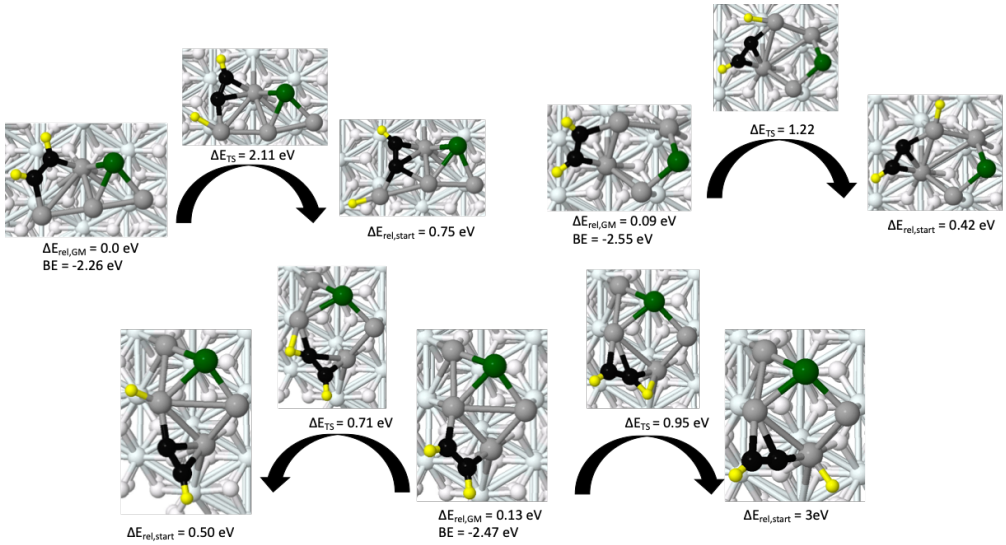

Figure E.10: Pt_4Ge/alumina acetylene C-H activation barrier endpoints and TS structures for barriers shown in Figure 5c.

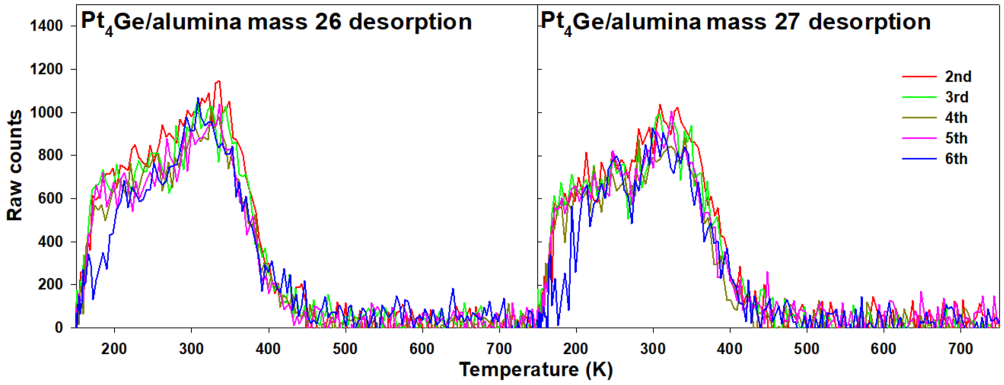

Figure E.11: Mass 26 and 27 from consecutive C_2H_4TPD experiments of Pt_4Ge/alumina samples. The samples were created and dosed with C_2H_4exactly the same way as the C_2D_4 TPD experiments in the methods section. $C_2H_4$was dosed instead of C_2D_4 due to C_2D_2 mass being 28, which is also the mass of CO. CO has a high background and would greatly interfere with C_2D_2 desorption. Although CO would also interfere with C_2H_4desorption, fragmentation of C_2H_4(assuming mass 28 gives 100% signals) from our mass spectrometer results in 67 % mass 26 and 61 % mass 27, hence observing these two mass is adequate for evidence of C_2H_4 desorption. If C_2H_2 desorbs, the majority of the detected mass would be mass 26 and should show up in the mass 26 during TPD experiments; the mass 26 and mass 27 TPD results here are almost identical. With no obvious peaks in mass 26 that distinguish from mass 27, we can conclude no C_2H_2 desorbed off from C_2H_4 dosed Pt_4Ge/alumina samples during TPD experiments.

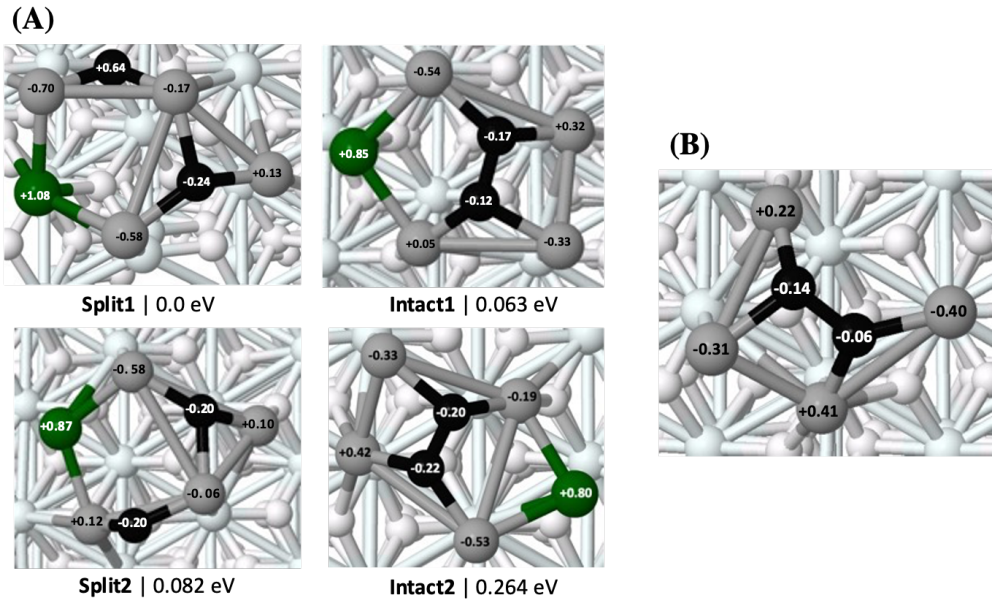

Figure E.12: (A) The ensemble of Pt_4GeC_2/alumina structures, obtained from global optimization and acetylene dehydrogenation. (B) The structure of Pt_4C_2, comparable to the two active Pt_4GeC_2 isomers. All structures have Bader charges shown superimposed on their respective atoms.

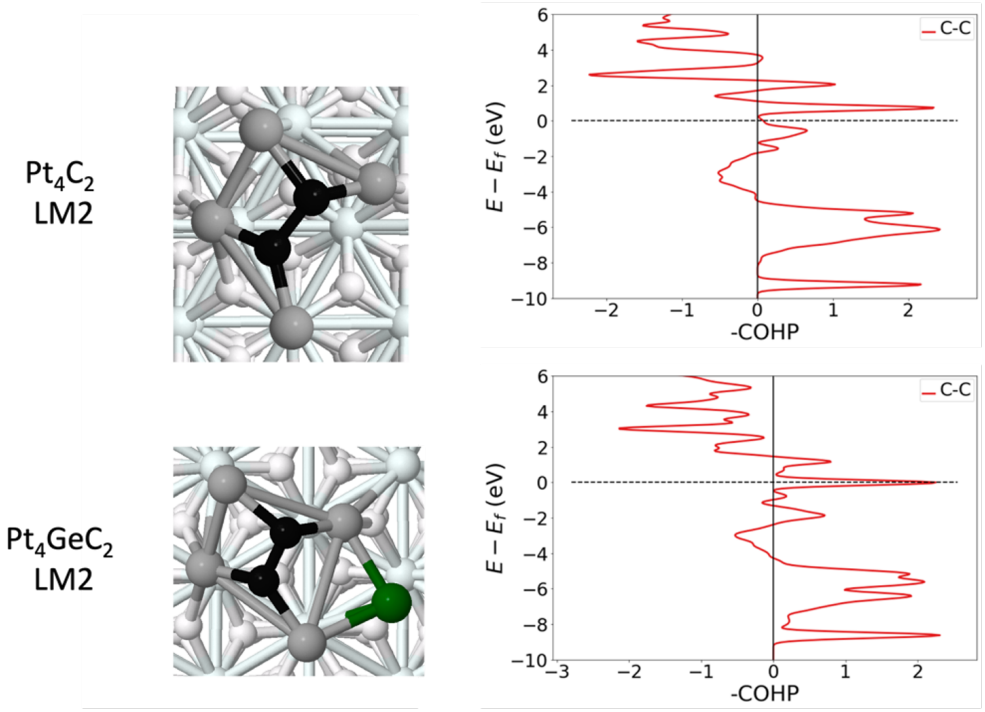

Figure E.13: C-C COHP plots for isomers of Pt_4C_2 and Pt_4GeC_2, containing bonded C_2 units

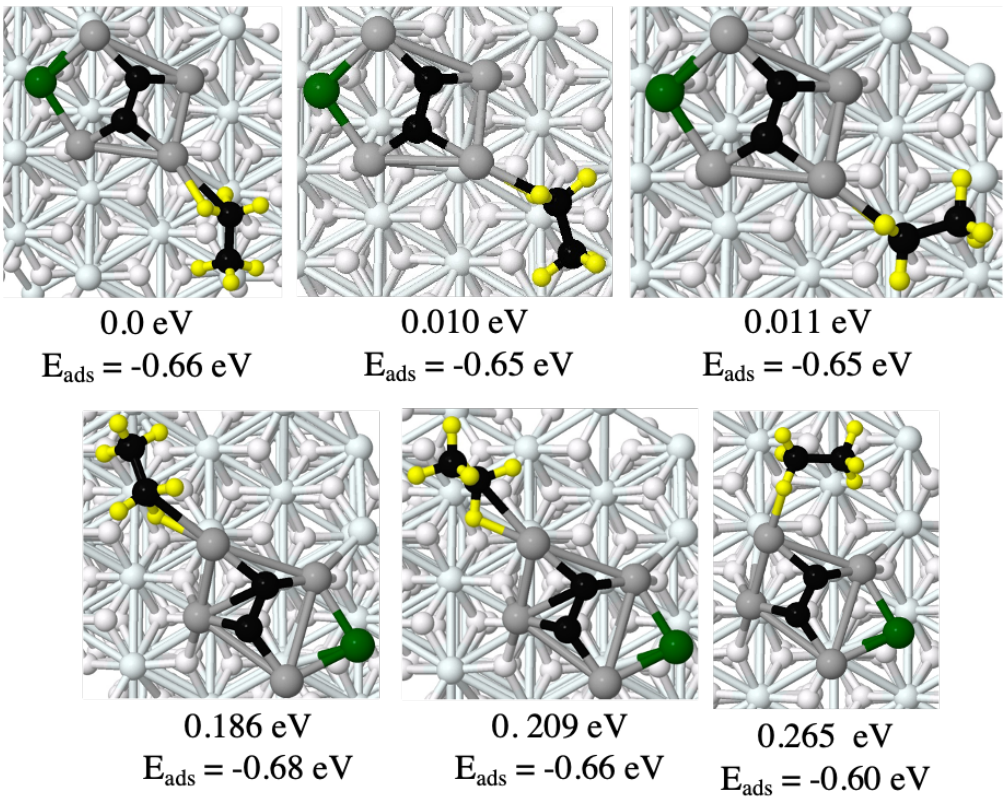

Figure E.14: Typical low energy binding geometries on the active isomers for ethane on Pt_4GeC_2/alumina.

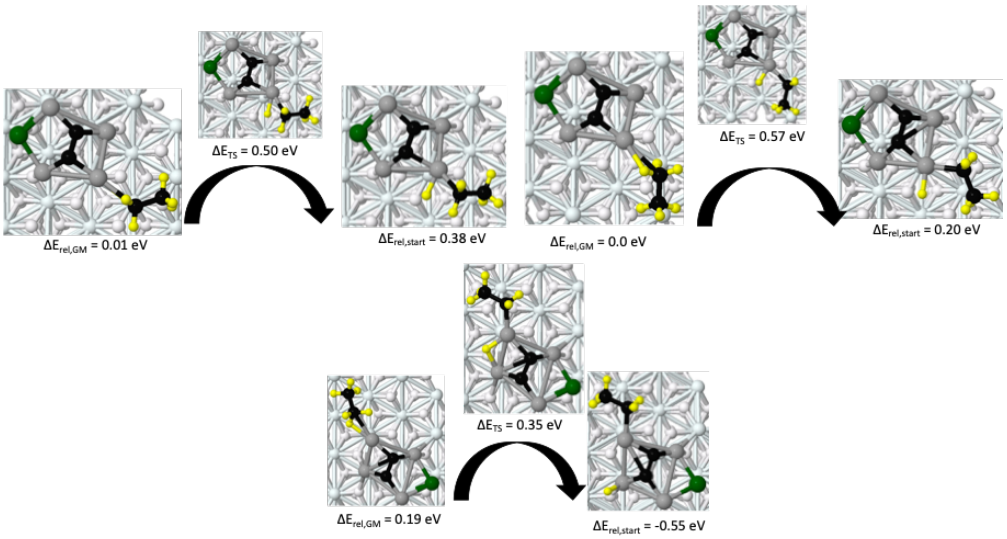

Figure E.15: Pt_4GeC_2/alumina ethane C-H activation barrier endpoints and TS structures from Figure 6b.

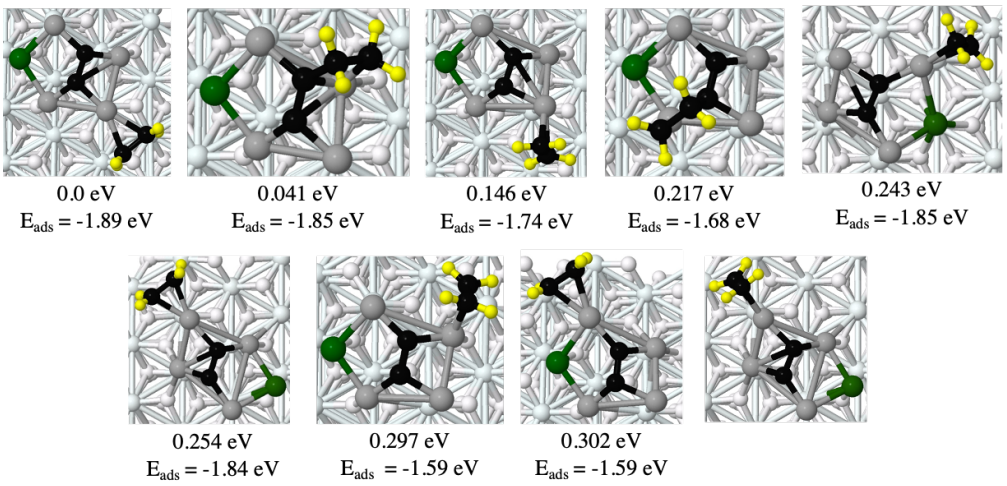

Figure E.16: Representative accessible ethylene binding modes for Pt_4GeC_2/alumina of the active isomers.

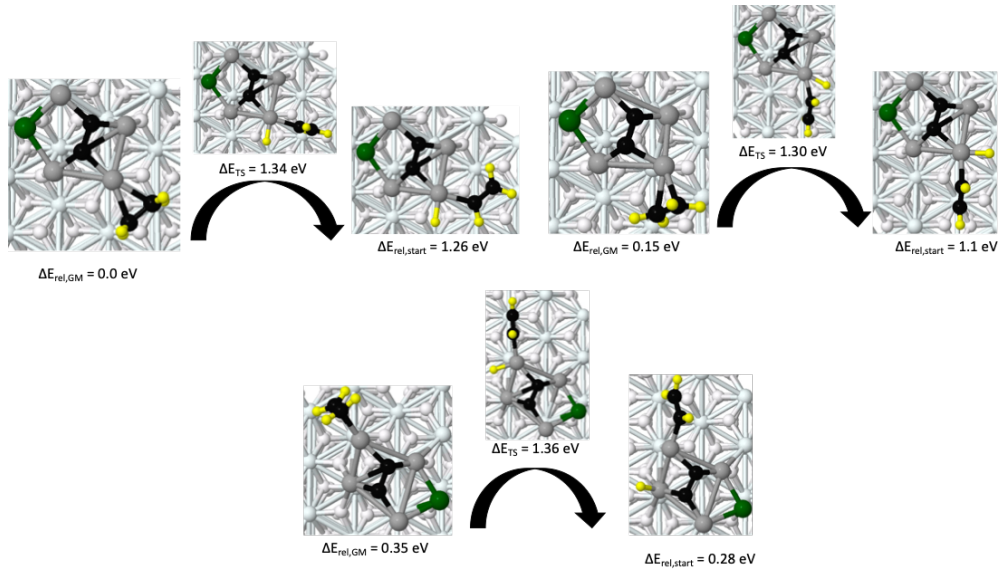

Figure E.17: Pt_4GeC_2/alumina ethylene C-H activation endpoints and TS structures for barriers in Figure 6c.

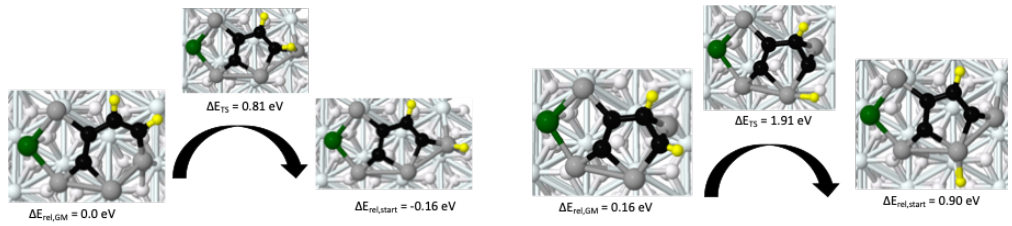

Figure E.18: Pt_4GeC_2/alumina acetylene C-H activation endpoints (only acetylene structures in the ensemble) and TS structures for barriers in Figure 6d.

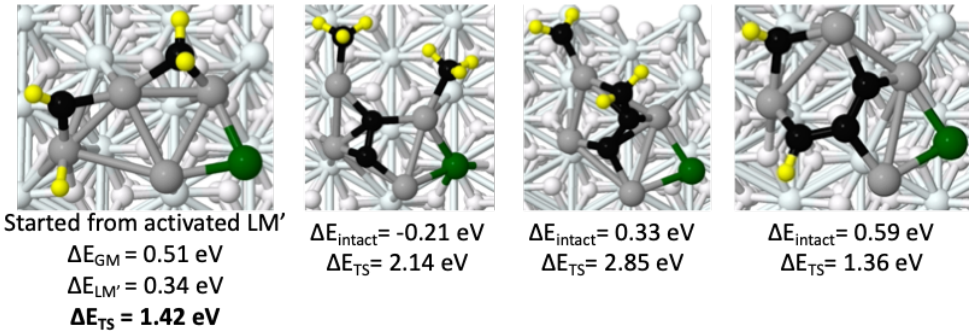

Figure E.19: Energetically accessible C-C cracking endpoints, with relative energies and reported barriers.

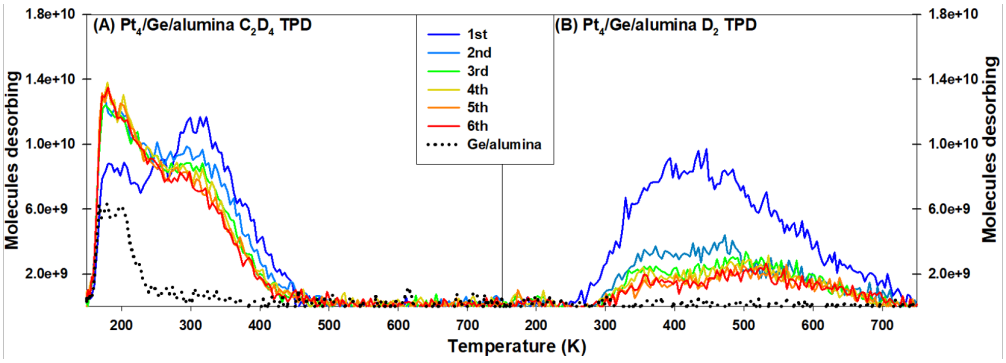

Figure E.20: TPD results showing (A) C_2D_4 and (B) D_2 desorption from Pt_4 deposited on Ge dosed alumina support.

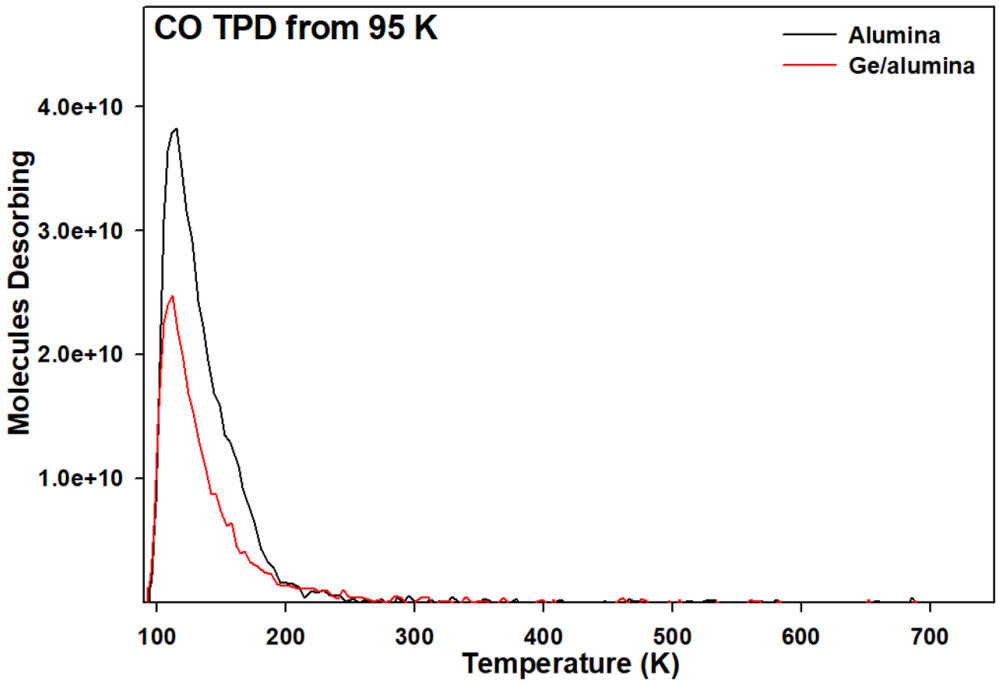

Figure E.21: TPD results of CO desorption from blank alumina and Ge/alumina samples.

Pt4 average	C2D4 /cluster	D2 /cluster	Total C_2D_4/cluster	Accumulated C atoms
1st	1.63	2.54	2.90	2.54
2nd	1.45	0.98	1.94	3.52
3rd	1.27	0.72	1.63	4.24
4th	1.18	0.58	1.47	4.82
5th	1.07	0.50	1.32	5.32
6th	1.01	0.43	1.23	5.75
Alumina	0.4			

Table E.1: Desorbing molecule numbers during first 6 TPDs from Pt_4/alumina.

Pt4Ge average	C2D4 /cluster	D2 /cluster	Total C_2D_4/cluster	Accumulated C atoms
1st	N/A	N/A	N/A	N/A
2nd	1.47	0.49	1.71	0.49
3rd	1.47	0.40	1.67	0.89
4th	1.41	0.33	1.57	1.22
5th	1.34	0.30	1.48	1.52
6th	1.32	0.28	1.46	1.79
Alumina	0.38			

Table E.2: Desorbing molecule numbers during first 6 TPDs from Pt_4Ge/alumina.

APPENDIX F

Supplementary information: Promoter-poison partnership protects platinum performance in coked cluster catalysts

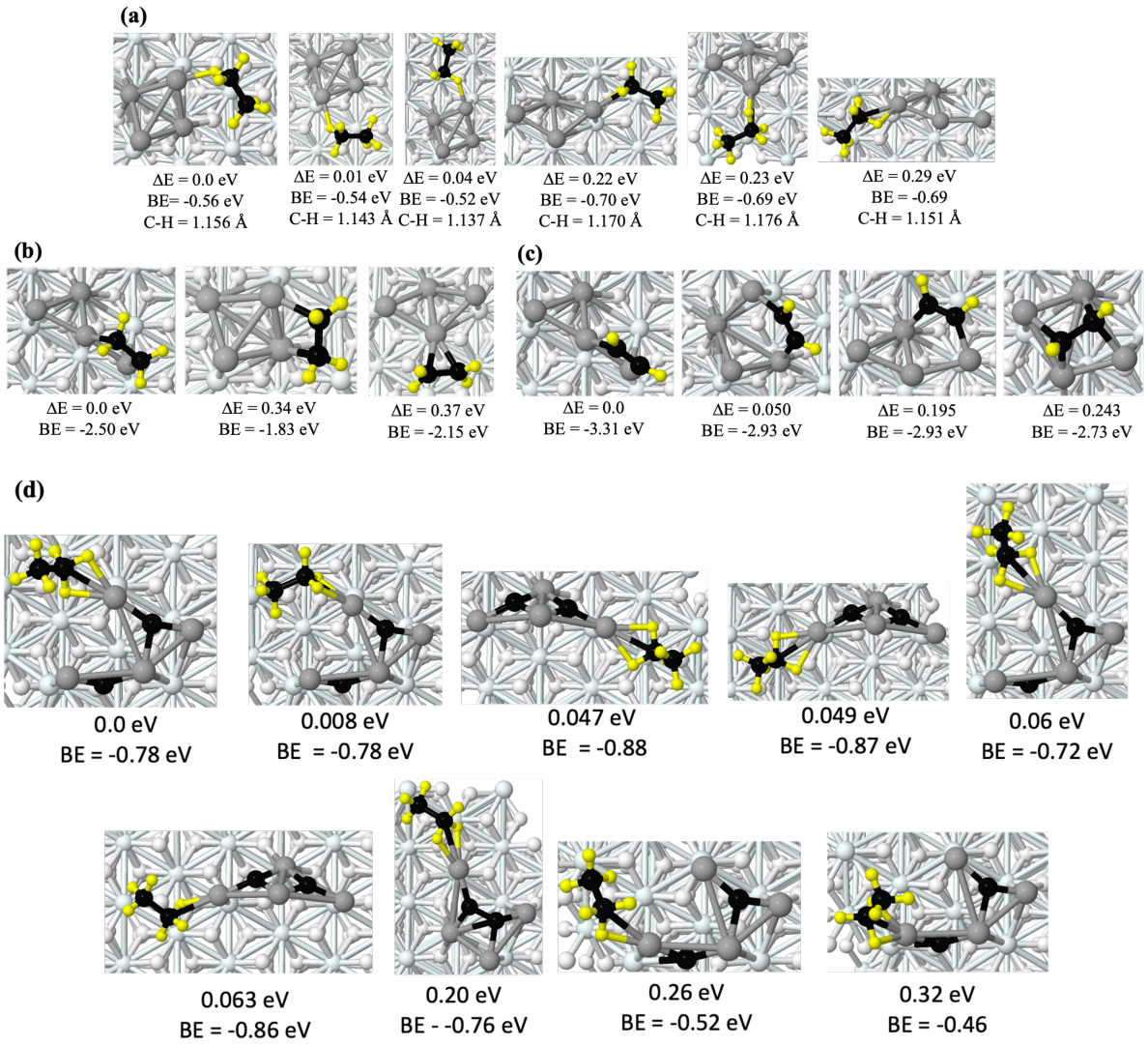
(a)
ΔE = 0.0 eV
BE= -0.56 eV
C-H = 1.156 Å
ΔE = 0.01 eV
BE = -0.54 eV
C-H = 1.143 Å
ΔE = 0.04 eV
BE = -0.52 eV
C-H = 1.137 Å
ΔE = 0.22 eV
BE = -0.70 eV
C-H = 1.170 Å
ΔE = 0.23 eV
BE = -0.69 eV
C-H = 1.176 Å
ΔE = 0.29 eV
BE = -0.69
C-H = 1.151 Å
(b)
ΔE = 0.0 eV
BE = -2.50 eV
ΔE = 0.34 eV
BE = -1.83 eV
ΔE = 0.37 eV
BE = -2.15 eV
(c)
ΔE = 0.0
BE = -3.31 eV
ΔE = 0.050
BE = -2.93 eV
ΔE = 0.195
BE = -2.93 eV
ΔE = 0.243
BE = -2.73 eV
(d)
0.0 eV
BE = -0.78 eV
0.008 eV
BE = -0.78 eV
0.047 eV
BE = -0.88
0.049 eV
BE = -0.87 eV
0.06 eV
BE = -0.72 eV
0.063 eV
BE = -0.86 eV
0.20 eV
BE - -0.76 eV
0.26 eV
BE = -0.52 eV
0.32 eV
BE = -0.46

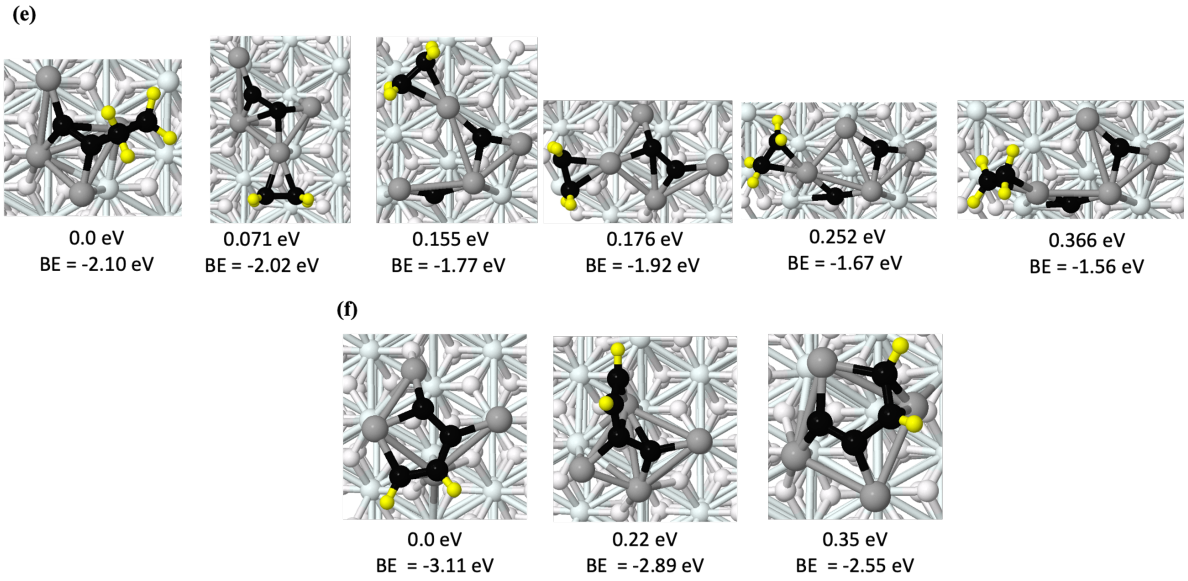

Figure F.1: Accessible binding modes of (a) ethane/Pt_4, (b) ethylene/Pt_4, (c) acetylene/Pt_4, (d) ethane/Pt_4C_2, (e) ethylene/Pt_4C_2, and (f) acetylene/Pt_4C_2.

Pt_4 + ethane

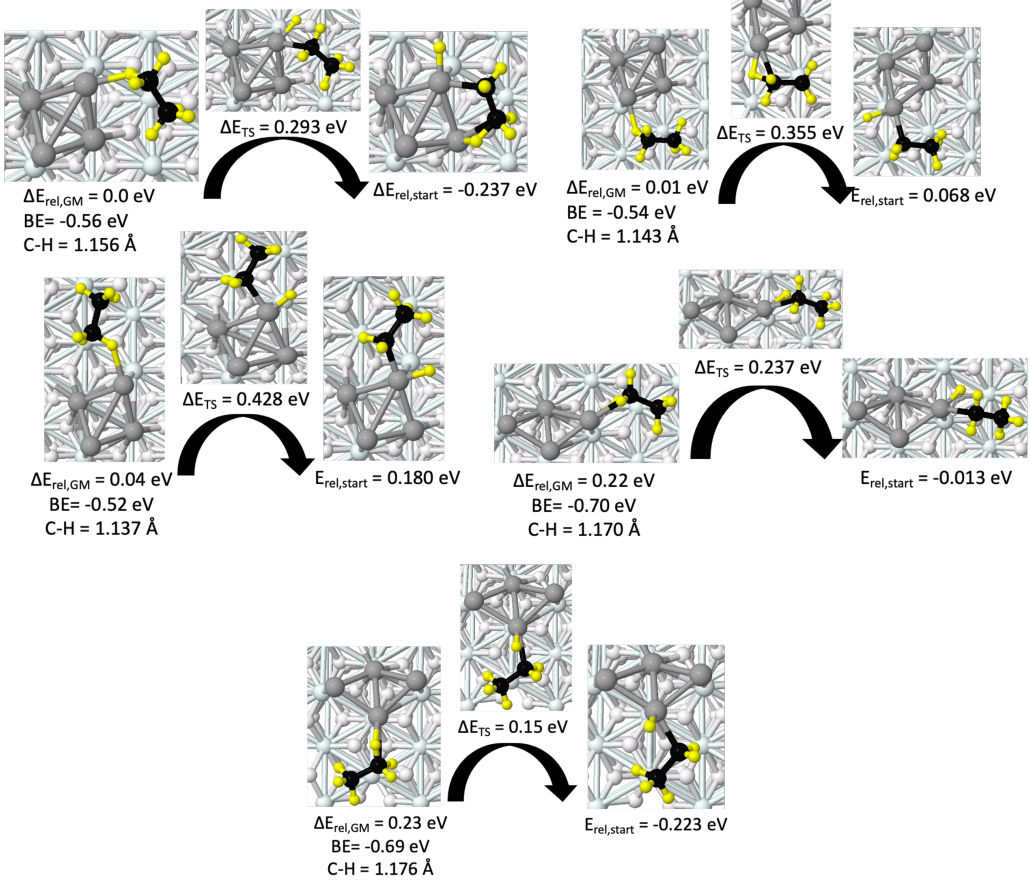

Pt_4 + ethylene

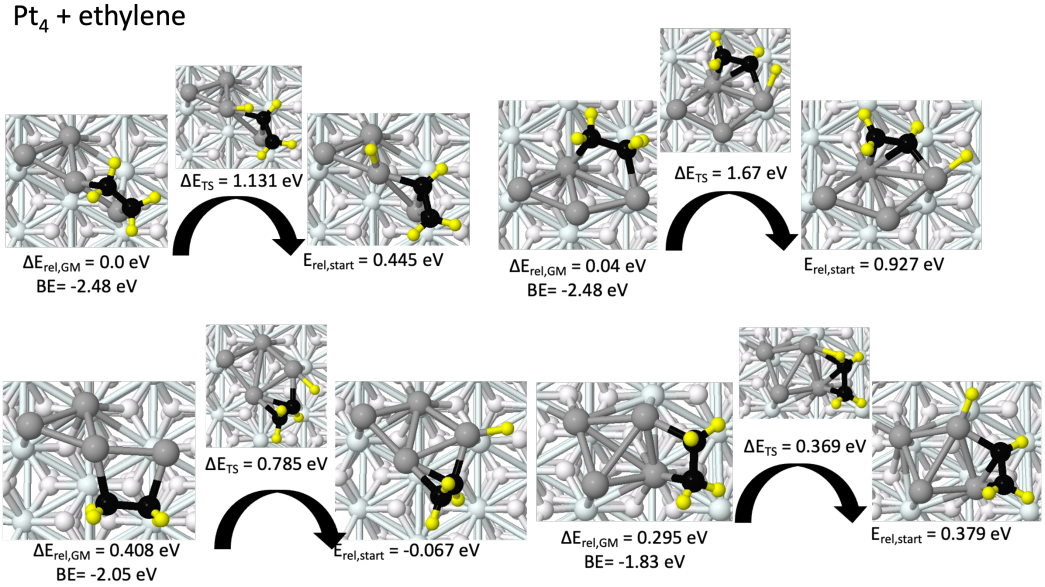

Pt_4 + acetylene

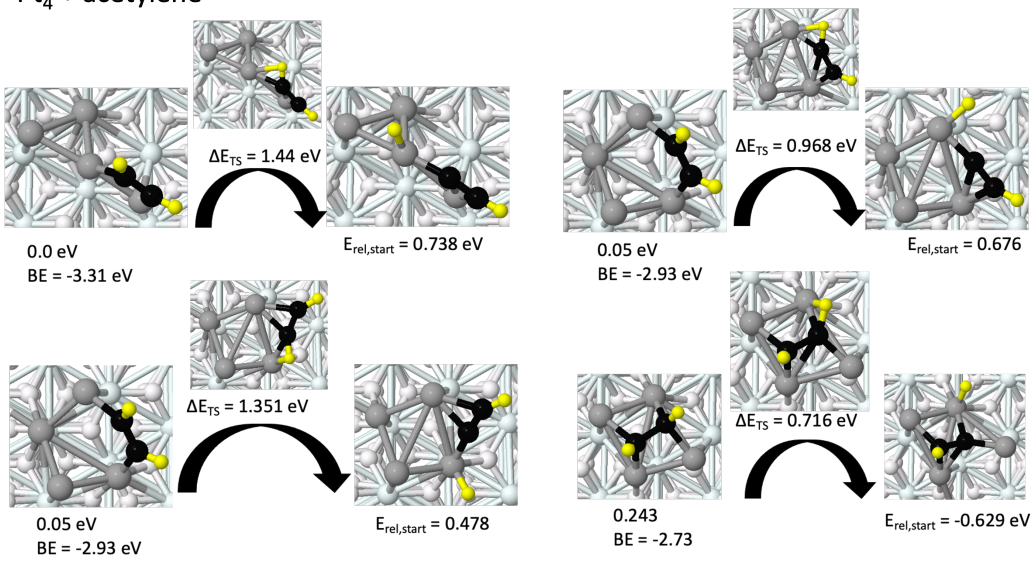

Pt_4C_2 + ethane

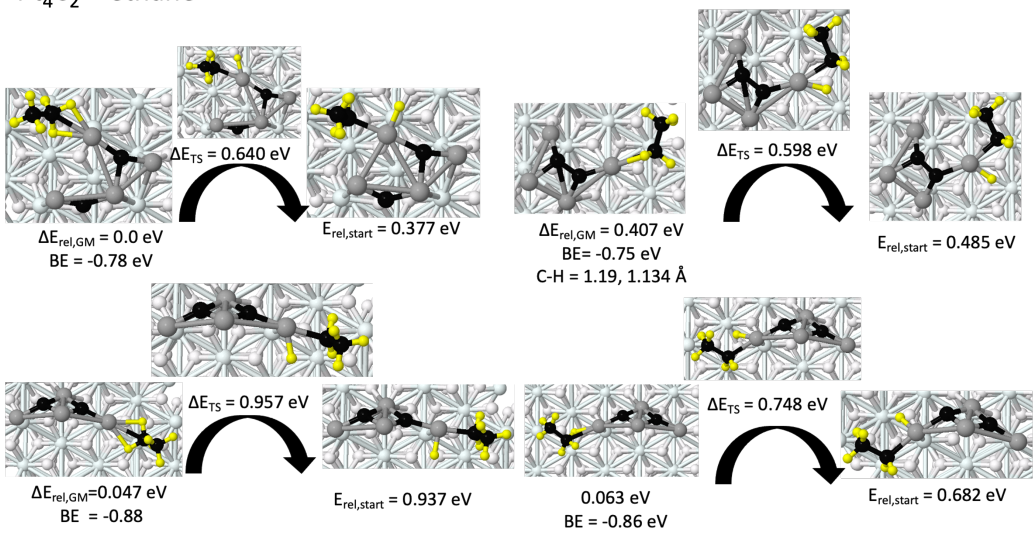

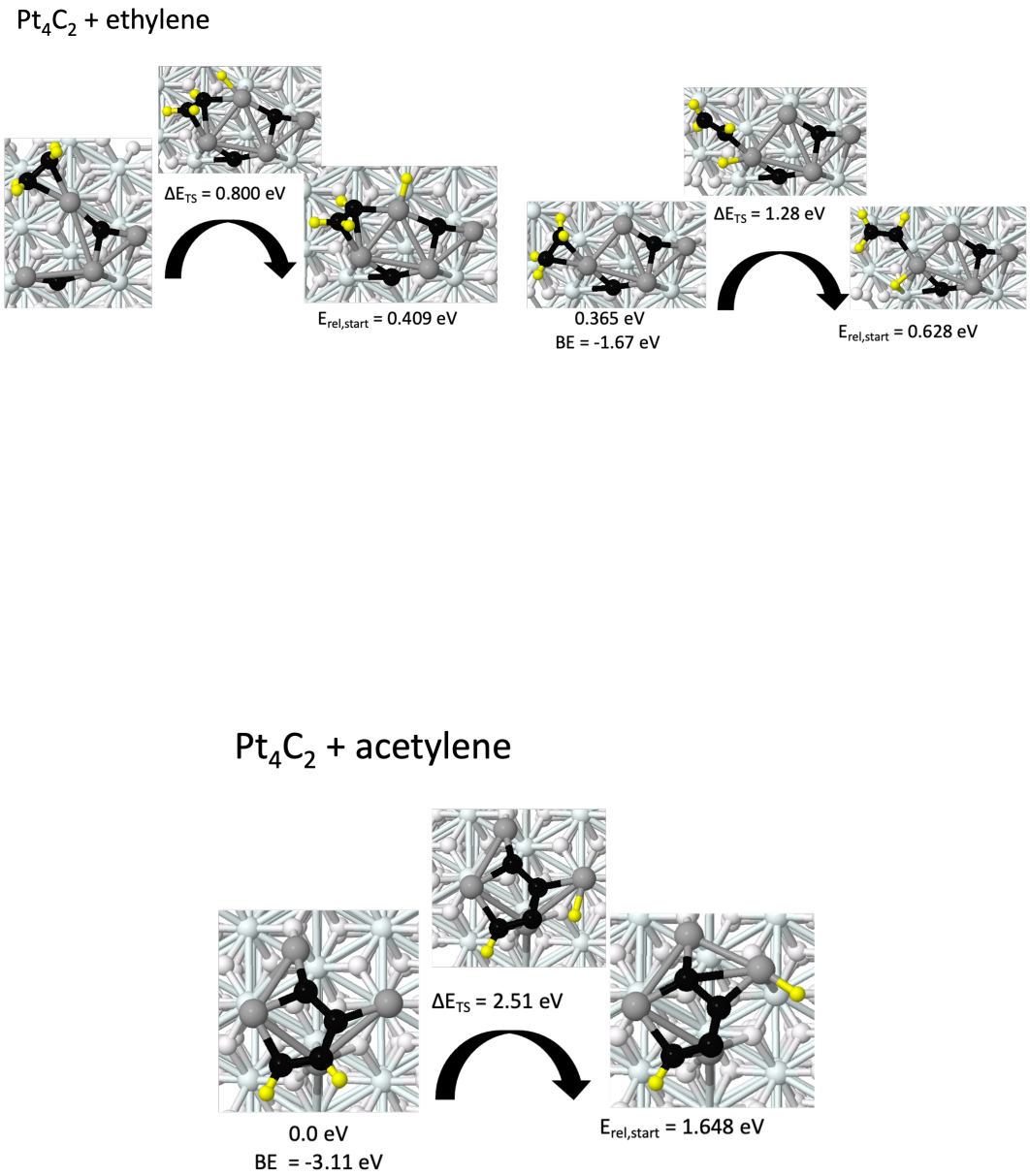

Figure F.2: C-H activation barriers for ethane, ethylene, and acetylene for Pt_4 and Pt_4C_2.

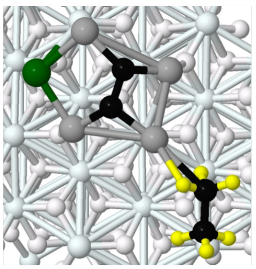

0.0 eV
BE = -0.66 eV
C-H = 1.123 Å

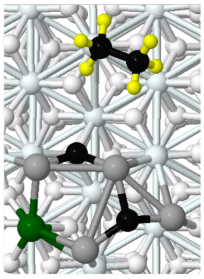

0.01 eV
BE = -0.60 eV
No C-H

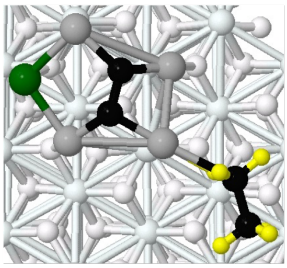

0.010 eV
BE = -0.65 eV
C-H = 1.132 Å

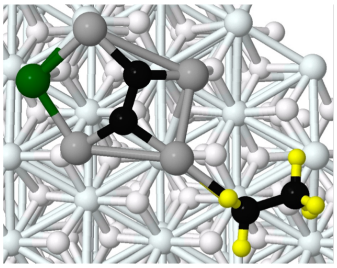

0.011 eV
BE = -0.65 eV
C-H = 1.130 Å

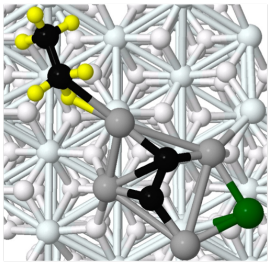

0.186 eV
BE = -0.68

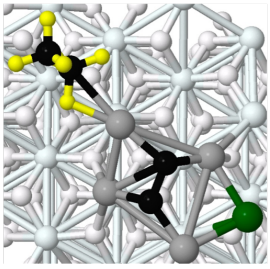

0. 209 eV
BE = -0.66 eV

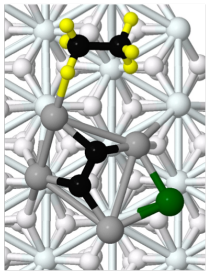

0.265 eV
BE = -0.60 eV

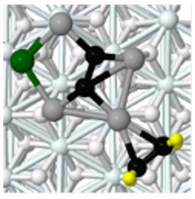

0.0 eV
E_{ads} = -1.89 eV

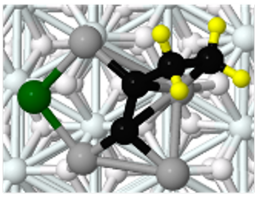

0.041 eV
E_{ads} = -1.85 eV

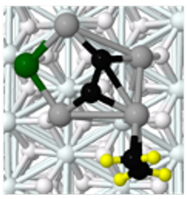

0.146 eV
E_{ads} = -1.74 eV

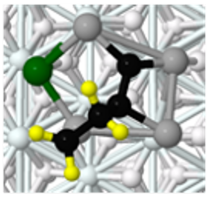

0.217 eV
E_{ads} = -1.68 eV

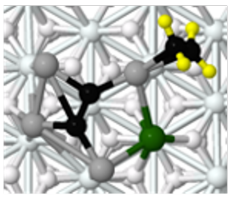

0.243 eV
E_{ads} = -1.85 eV

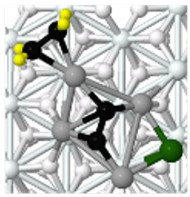

0.254 eV
E_{ads} = -1.84 eV

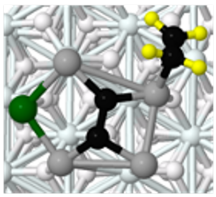

0.297 eV
E_{ads} = -1.59 eV

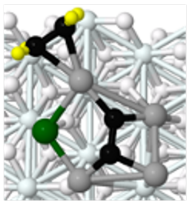

0.302 eV
E_{ads} = -1.59 eV

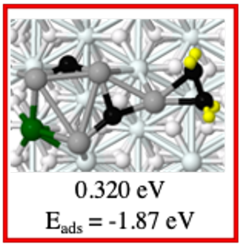

0.320 eV
E_{ads} = -1.87 eV

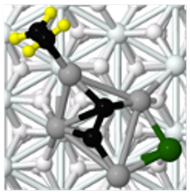

0.349 eV
E_{ads} = -1.74 eV

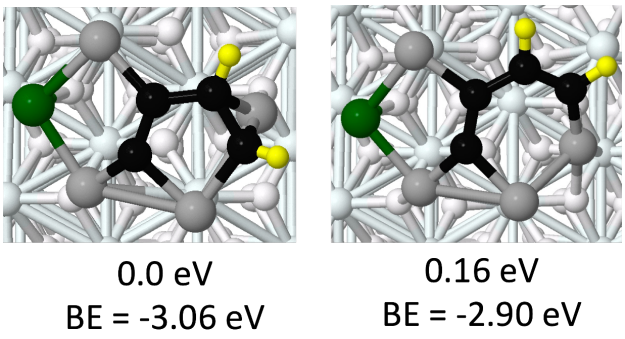

Figure F.3: Relevant binding modes of (a) ethane/ Pt_4GeC_2 (b) ethylene/ Pt_4GeC_2 and (c) acetylene/Pt_4GeC_2.

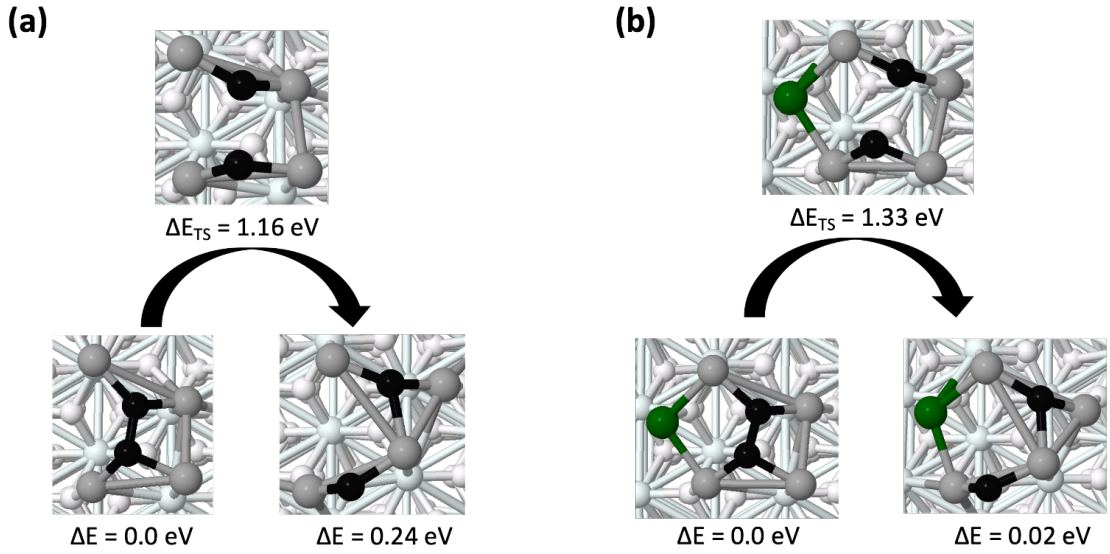

Figure F.4: C-C bond breaking NEBs for Pt_4C_2 and Pt_4GeC_2.

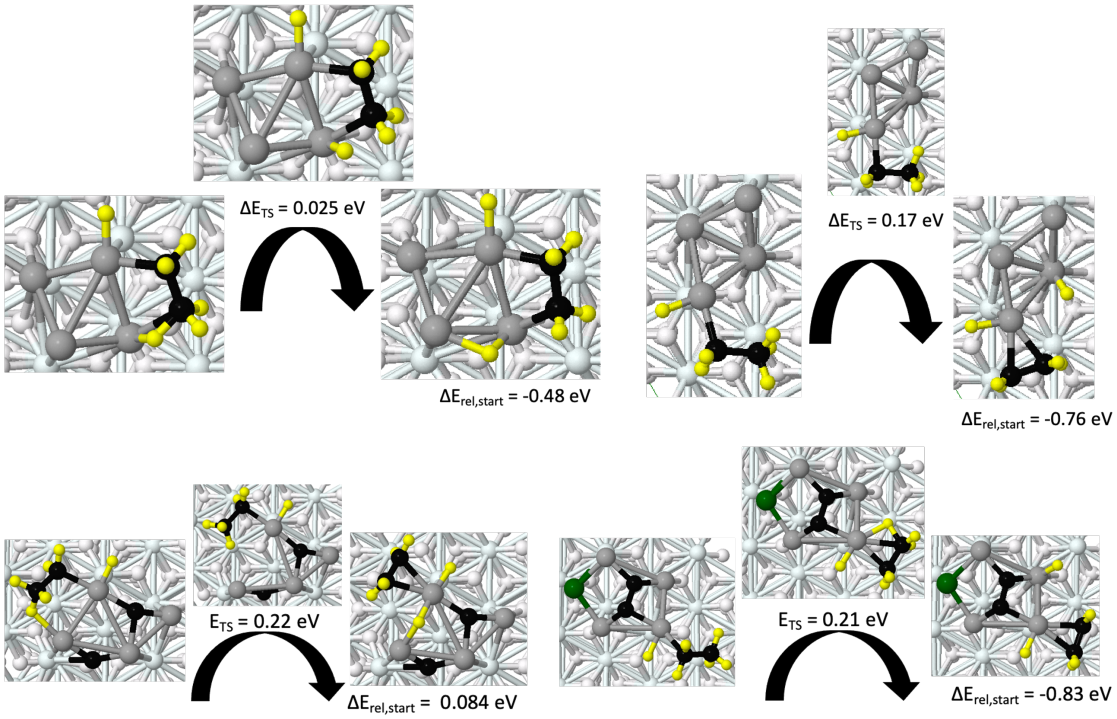

Figure F.5: Second C-H activation barriers for relevant adsorbate binding modes of Pt_4, Pt_4C2, and Pt_4GeC_2. Additional barriers for $Pt_4Ge(C2)$ can be found in ref [229].

	C-H barrier	C-C barrier		C-H barrier	C-C barrier
	0.15 eV	1.28 eV		0.41 eV	*0.62 eV
$Pt_4 + C_2H_6$	0.24 eV	1.03 eV	Pt4Ge + C_2H_6	0.29 eV	*1.10 eV
	0.44 eV	1.41 eV			
$Pt_4 + C_2H_4$	0.40 eV	1.46 eV	$Pt_4Ge + C_2H_4$	1.01 eV	1.81 eV
Pt_4 + C2H2	0.97 eV	0.76 eV	Pt4Ge + C2H2	1.22 eV	1.55 eV
	0.71 eV	1.24 eV		2.11 eV	1.92 eV
Pt_4C_2	–	1.16 eV	Pt_4GeC_2	–	1.33 eV
$Pt_4C_2 + C_2H_6$	0.60 eV	1.40 eV	$Pt_4GeC_2 + C_2H_6$	0.42 eV	1.74 eV
	0.32 eV	1.21 eV			
$Pt_4C_2 + C_2H_4$	1.39 eV	3.11 eV	$Pt_4GeC_2 + C_2H_4$	1.36 eV	2.85 eV
	2.23 eV	*2.10 eV			
$Pt_4C_2 + C_2H_2$	2.33 eV	1.85 eV	$Pt_4GeC_2 + C_2H_2$	0.81 eV	1.36 eV

Table F.1: Comparison between C-H activation barriers and C-C cracking barriers for various isomers of Pt_4, Pt_4C_2 and Pt_4Ge and Pt_4GeC_2. Both different adsorbate binding modes and alternate cluster core configurations are represented. See Figure F.6 below for structures associated with the barriers.

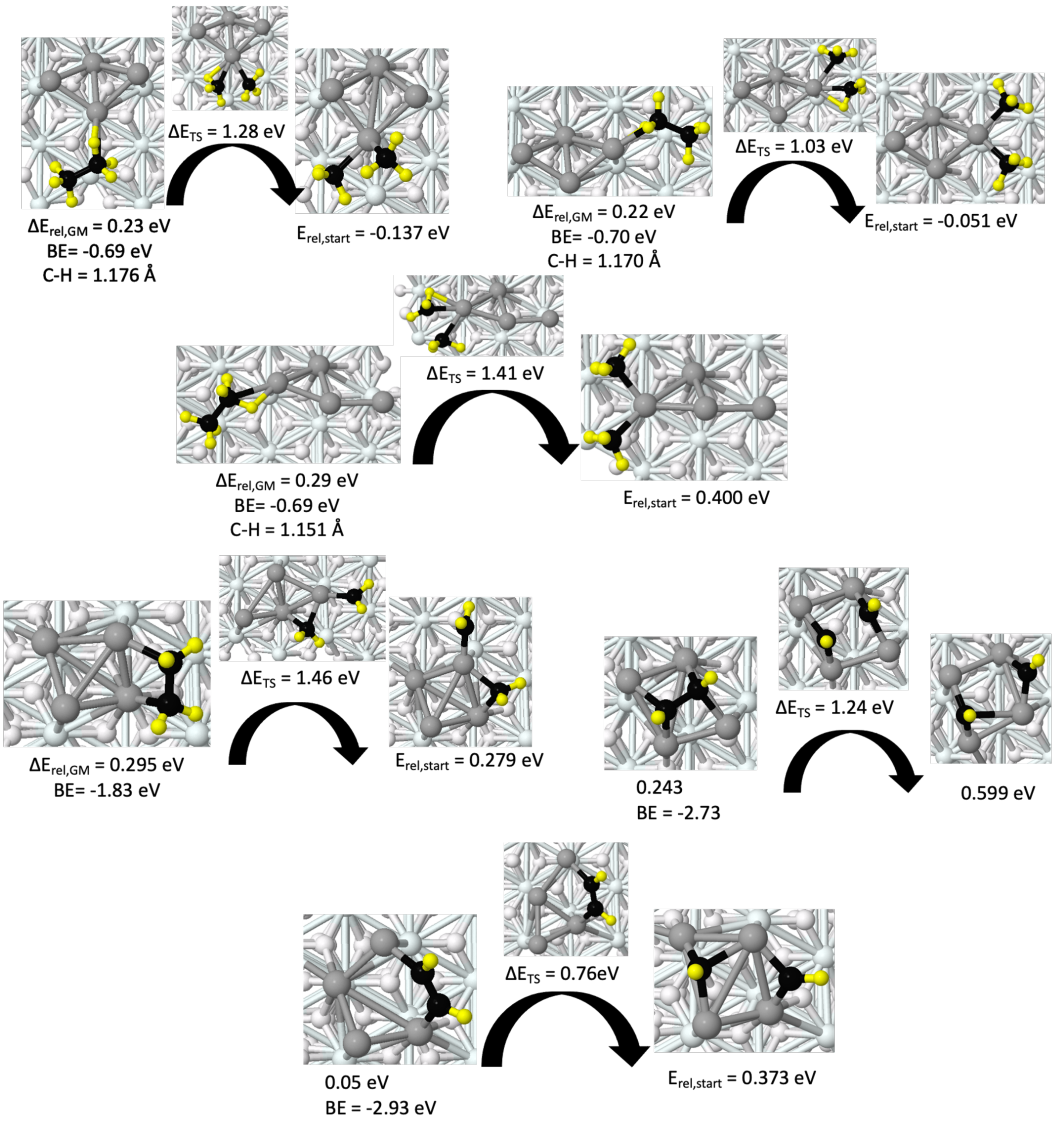
ΔE_TS = 1.28 eV
ΔE_rel,GM = 0.23 eV
BE= -0.69 eV
C-H = 1.176 Å
E_rel,start = -0.137 eV
ΔE_rel,GM = 0.22 eV
BE= -0.70 eV
C-H = 1.170 Å
ΔE_TS = 1.03 eV
E_rel,start = -0.051 eV
ΔE_TS = 1.41 eV
ΔE_rel,GM = 0.29 eV
BE= -0.69 eV
C-H = 1.151 Å
E_rel,start = 0.400 eV
ΔE_TS = 1.46 eV
ΔE_rel,GM = 0.295 eV
BE= -1.83 eV
E_rel,start = 0.279 eV
ΔE_TS = 1.24 eV
0.243
BE = -2.73
0.599 eV
ΔE_TS = 0.76eV
0.05 eV
BE = -2.93 eV
E_rel,start = 0.373 eV

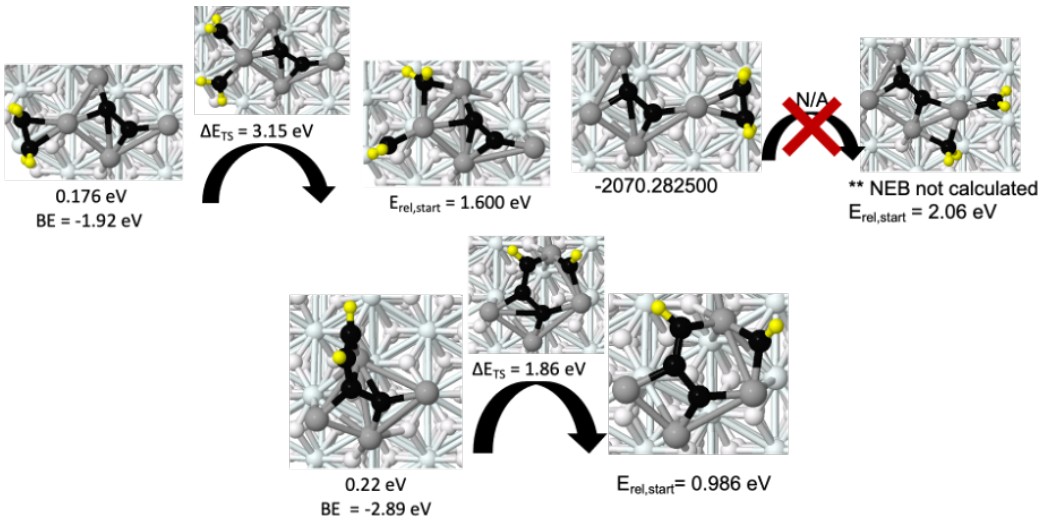

Figure F.6: C-C bond breaking barriers for relevant structures of Pt_4 and Pt_4C_2. See ref [229] for corresponding Pt_4Ge and Pt_4GeC_2 structures. One barrier was not calculated due to the energy of the endpoint being higher than the comparable barrier for C-H activation.

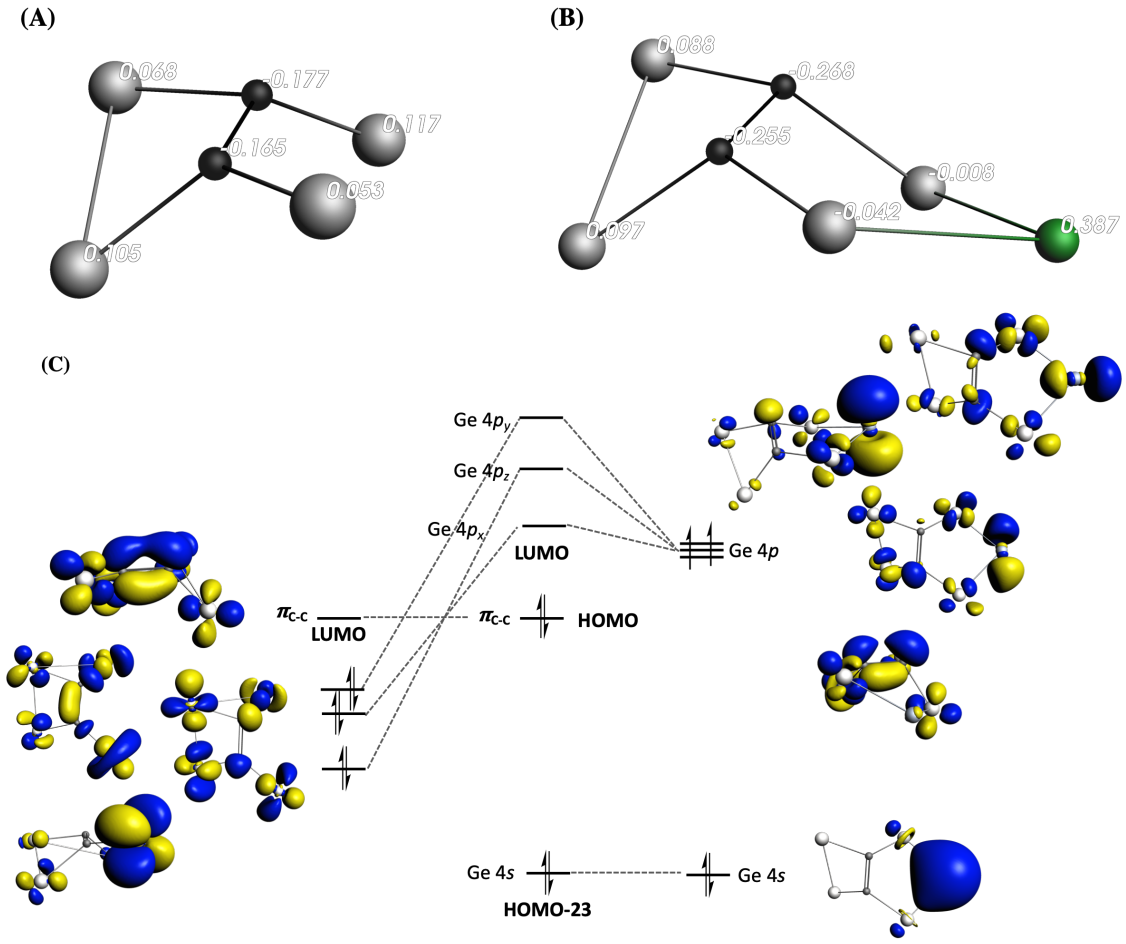

Figure F.7: The structures of gas-phase models of (A) Pt_4C_2 and (B) Pt_4GeC_2 with Bader charges annotated over their respective atoms. (C) The Frontier molecular orbital (MO) diagram showing the interaction of Pt_4C_2 with Ge in Pt_4GeC_2. Orbitals plotted with an isovalue of 0.06.

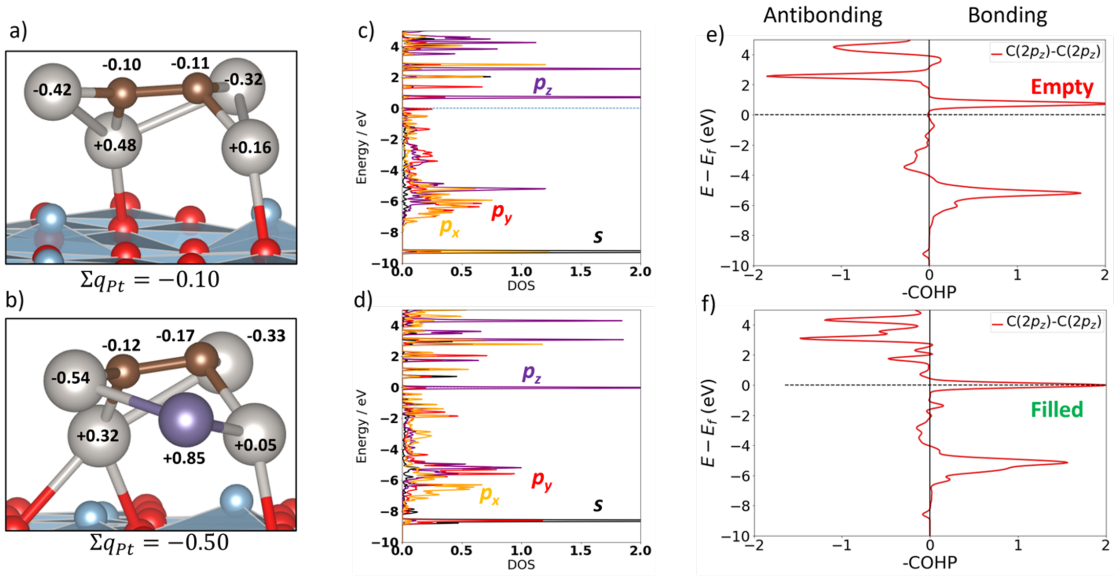

Figure F.8: Electronic structure and bonding properties of active isomers of Pt_4C_2 and Pt_4GeC_2. (a,b) Structures of Pt_4C_2 and Pt_4GeC_2 on Al_2O_3 with Pt shown in grey, C in brown, and Ge in purple, Al in blue, and O in red. Each atom is labelled with its computed QTAIM charge, and $\sum_{q,Pt}$ denotes the sum of the Pt charges. (c,d) Projected density of states (PDOS) plots for the 2s,p orbitals of carbon annotated with pz Mulliken populations. The 2s PDOS is in black, px in orange, py in red, and pz in purple. (e,f) ICOHP plots for the C 2pz- C 2pz interaction, annotated with the C-C atomic ICOBI.

F.1 Supplementary Note- Experimental Analysis

Each TPD cycle involves first saturating the catalysts with C2D4 at 150 K, then heating to drive desorption of either intact C_2D_4 or of D_2, the latter indicating carbon deposition. The raw TPD data is from our previous work and explored more in detail there [19]. The as-prepared Pt_4 catalyst has a high T desorption peak for ethylene around 310 K for the first 2 TPD cycles, but rapidly decreases, indicating rapid loss of strong ethylene binding sites. D_2 desorption also rapidly decreases in successive TPD runs. For Pt_4Ge, in contrast, the high-T ethylene and D_2 desorption features are stable over repeated runs, with much less D_2 desorption compared to Pt_4. This reflects higher stability and selectivity against coking of the Pt_4Ge clusters. ISS allows us to track changes induced by TPD cycles in in the surface layer of the catalysts, which can be compared to the estimated total number of strong ethylene binding sites per clusters, estimated prior to each TPD cycle. For Pt_4/Al_2O_3, the "as-prepared" Pt ISS intensity reflects a catalyst where essentially all the Pt atoms are in the He^+-accessible surface layer. The Pt intensities were attenuated, relative to those for the as-prepared catalyst, by factors of 15%, 45%, and 70%, respectively, after 1, 6, and 21 TPD runs, reflecting shadowing/blocking of He^+ scattering by bound C atoms. Note, however, that after 6 TPD runs, 6 to 8 C atoms per Pt_4 cluster were estimated to be present,[229] but more than half of the Pt atoms remained He^+-accessible, whereas saturating the Pt clusters with CO molecules resulted in much larger (80%) attenuation of Pt ISS signals.[19] This supports our results showing restructuring of Pt_4 upon the addition of C_2, which has also been seen experimentally on the surfaces of larger NPs. [249] The number of ethylene molecules adsorbed in strong binding sites decreases more rapidly after each TPD run, by factors of 48%, 68% and 80%, respectively, after 1, 6 and 21 runs. The decline in strong ethylene binding sites is partly offset by an increase in weak binding sites. [229] Thus, the combination of ISS and TPD suggests that while there is some steric site blocking by carbon deposition, the larger effect on ethylene binding is electronic, decreasing the binding energies such that few strong binding sites remain. Because these strong binding sites are responsible

for the dehydrogenation activity, the catalyst deactivates. For Pt_4Ge the as-prepared ISS intensity was 21% lower than for as-prepared Pt_4, attributed to Ge atoms partially shadowing or blocking He+ scattering from Pt. The attenuations of the Pt ISS signal, relative to as-prepared Pt_4Ge, were 22%, 44%, and 70% after 1, 6, and 21 TPD runs respectively, similar to Pt_4. In contrast, the loss of strong of ethylene binding sites per Pt_4Ge was much smaller than for Pt_4, at 5%, 24%, and 44%, respectively. Pt_4Ge clusters were estimated to have a total of ca. 2 C atoms present per cluster after 6 TPDs – just one third of the number deposited per Pt_4. Thus, experiment shows that there is less, but still significant coking on Pt_4Ge, that similar fractions of the initial Pt atoms remain in the surface layer, and that the loss of strong ethylene binding sites is inhibited by Ge. This, too, supports our conclusions that Pt_4Ge restructures upon the addition of C_2, and that the improved stability of Pt_4GeC_2 arises from electronic effects due to the interaction between the Ge, Pt, and C.

Bibliography

(1) Billinge, S. J. L.; Levin, I. *Science* **2007**, *316*, 561–565.

(2) Bergmann, A.; Cuenya, B. R. *ACS Catalysis* **2019**, *9*, 10020–10043.

(3) Zandkarimi, B.; Alexandrova, A. N. *The Journal of Physical Chemistry Letters* **2019**, *10*, 460–467.

(4) Zhang, Z.; Zandkarimi, B.; Alexandrova, A. N. *Accounts of Chemical Research* **2020**, *53*, Publisher: American Chemical Society, 447–458.

(5) Zhai, H.; Alexandrova, A. N. *ACS Catalysis* **2017**, *7*, Publisher: American Chemical Society, 1905–1911.

(6) Zhai, H.; Alexandrova, A. N. *The Journal of Physical Chemistry Letters* **2018**, *9*, 1696–1702.

(7) Lavroff, R. H.; Morgan, H. W. T.; Zhang, Z.; Poths, P.; Alexandrova, A. N. *Chemical Science* **2022**, *13*, 8003–8016.

(8) Poths, P.; Alexandrova, A. N. *The Journal of Physical Chemistry Letters* **2022**, *13*, 4321–4334.

(9) Ha, M.-A.; Baxter, E. T.; Cass, A. C.; Anderson, S. L.; Alexandrova, A. N. *J. Am. Chem. Soc.* **2017**, 8.

(10) Gorey, T.; Zandkarimi, B.; Li, G.; Baxter, E.; Alexandrova Anastassia; Anderson, S. *ACS Catalysis* **2020**, *10*, 4543–4558.

(11) Zandkarimi, B.; Gorey, T. J.; Li, G.; Munarriz, J.; Anderson, S. L.; Alexandrova, A. N. *Chemistry of Materials* **2020**, *32*, doi: 10.1021/acs.chemmater.0c02926, 8595–8605.

(12) Li, G.; Zandkarimi, B.; Cass, A. C.; Gorey, T. J.; Allen, B. J.; Alexandrova, A. N.; Anderson, S. L. *The Journal of Chemical Physics* **2020**, *152*, 024702.

(13) Jimenez-Izal, E.; Liu, J.-Y.; Alexandrova, A. N. *Journal of Catalysis* **2019**, *374*, 93–100.

(14) Gorey, T. J.; Zandkarimi, B.; Li, G.; Baxter, E. T.; Alexandrova, A. N.; Anderson, S. L. *The Journal of Physical Chemistry C* **2019**, *123*, 16194–16209.

(15) Oliver-Meseguer, J.; Cabrero-Antonino, J. R.; Domınguez, I.; Leyva-Pérez, A.; Corma, A. *Science* **2012**, *338*, 1452–1455.

(16) Hansen, T. W.; DeLaRiva, A. T.; Challa, S. R.; Datye, A. K. *Accounts of Chemical Research* **2013**, *46*, 1720–1730.

(17) Parkinson, G. S.; Novotny, Z.; Argentero, G.; Schmid, M.; Pavelec, J.; Kosak, R.; Blaha, P.; Diebold, U. *Nature Materials* **2013**, *12*, 724–728.

(18) Lei, Y.; Mehmood, F.; Lee, S.; Greeley, J.; Lee, B.; Seifert, S.; Winans, R. E.; Elam, J. W.; Meyer, R. J.; Redfern, P. C.; Teschner, D.; Schlögl, R.; Pellin, M. J.; Curtiss, L. A.; Vajda, S. *Science* **2010**, *328*, 224–228.

(19) Baxter, E. T.; Ha, M.-A.; Cass, A. C.; Alexandrova, A. N.; Anderson, S. L. *ACS Catalysis* **2017**, *7*, 3322–3335.

(20) Campbell, C. T. *Surface Science Reports* **1997**, *27*, 1–111.

(21) Bartholomew, C. H. *Applied Catalysis A: General* **2001**, *212*, 17–60.

(22) Argyle, M.; Bartholomew, C. *Catalysts* **2015**, *5*, 145–269.

(23) Goodman, E. D.; Schwalbe, J. A.; Cargnello, M. *ACS Catalysis* **2017**, *7*, 7156–7173.

(24) Fukamori, Y.; König, M.; Yoon, B.; Wang, B.; Esch, F.; Heiz, U.; Landman, U. *ChemCatChem* **2013**, *5*, 3330–3341.

(25) Wettergren, K.; Schweinberger, F. F.; Deiana, D.; Ridge, C. J.; Crampton, A. S.; Rötzer, M. D.; Hansen, T. W.; Zhdanov, V. P.; Heiz, U.; Langhammer, C. *Nano Letters* **2014**, *14*, 5803–5809.

(26) Jimenez-Izal, E.; Zhai, H.; Liu, J.-Y.; Alexandrova, A. N. *ACS Catalysis* **2018**, *8*, 8346–8356.

(27) Gorey, T. J.; Zandkarimi, B.; Li, G.; Baxter, E. T.; Alexandrova, A. N.; Anderson, S. L. *The Journal of Physical Chemistry C* **2019**, *123*, 16194–16209.

(28) Zandkarimi, B.; Gorey, T. J.; Li, G.; Munarriz, J.; Anderson, S. L.; Alexandrova, A. N. *Chemistry of Materials* **2020**, *32*, 8595–8605.

(29) Gilroy, K. D.; Ruditskiy, A.; Peng, H.-C.; Qin, D.; Xia, Y. *Chemical Reviews* **2016**, *116*, 10414–10472.

(30) Kim, D.; Xie, C.; Becknell, N.; Yu, Y.; Karamad, M.; Chan, K.; Crumlin, E. J.; Nørskov, J. K.; Yang, P. *Journal of the American Chemical Society* **2017**, *139*, 8329–8336.

(31) Mori, K.; Sano, T.; Kobayashi, H.; Yamashita, H. *Journal of the American Chemical Society* **2018**, *140*, 8902–8909.

(32) Vasileff, A.; Xu, C.; Jiao, Y.; Zheng, Y.; Qiao, S.-Z. *Chem* **2018**, *4*, 1809–1831.

(33) Tang, Q.; Lee, Y.; Li, D.-Y.; Choi, W.; Liu, C. W.; Lee, D.; Jiang, D.-e. *Journal of the American Chemical Society* **2017**, *139*, 9728–9736.

(34) Zhu, S.; Jiang, B.; Cai, W.-B.; Shao, M. *Journal of the American Chemical Society* **2017**, *139*, 15664–15667.

(35) Kato, S.; Matam, S. K.; Kerger, P.; Bernard, L.; Battaglia, C.; Vogel, D.; Rohwerder, M.; Züttel, A. *Angewandte Chemie International Edition* **2016**, *55*, 6028–6032.

(36) Wang, W.-H.; Himeda, Y.; Muckerman, J. T.; Manbeck, G. F.; Fujita, E. *Chemical Reviews* **2015**, *115*, 12936–12973.

(37) Green, A. E.; Justen, J.; Schöllkopf, W.; Gentleman, A. S.; Fielicke, A.; Mackenzie, S. R. *Angewandte Chemie International Edition* **2018**, *57*, 14822–14826.

(38) Liu, G.; Ciborowski, S. M.; Zhu, Z.; Chen, Y.; Zhang, X.; Bowen, K. H. *Physical Chemistry Chemical Physics* **2019**, *21*, 10955–10960.

(39) Dodson, L. G.; Thompson, M. C.; Weber, J. M. *Annual Review of Physical Chemistry* **2018**, *69*, 231–252.

(40) Thompson, M. C.; Ramsay, J.; Weber, J. M. *Angewandte Chemie International Edition* **2016**, *55*, 15171–15174.

(41) Tang, S.-Y.; Rijs, N. J.; Li, J.; Schlangen, M.; Schwarz, H. *Chemistry - A European Journal* **2015**, *21*, 8483–8490.

(42) Zhang, X.; Liu, G.; Meiwes-Broer, K.-H.; Ganteför, G.; Bowen, K. *Angewandte Chemie International Edition* **2016**, *55*, 9644–9647.

(43) Jiang, L.-X.; Zhao, C.; Li, X.-N.; Chen, H.; He, S.-G. *Angewandte Chemie International Edition* **2017**, *56*, 4187–4191.

(44) Liu, Y.-Z.; Jiang, L.-X.; Li, X.-N.; Wang, L.-N.; Chen, J.-J.; He, S.-G. *The Journal of Physical Chemistry C* **2018**, *122*, 19379–19384.

(45) Pascher, T. F.; Ončák, M.; van der Linde, C.; Beyer, M. K. *ChemPhysChem* **2019**, DOI: 10.1002/cphc.201900095.

(46) Ma, S.; Sadakiyo, M.; Heima, M.; Luo, R.; Haasch, R. T.; Gold, J. I.; Yamauchi, M.; Kenis, P. J. A. *Journal of the American Chemical Society* **2016**, *139*, 47–50.

(47) Gao, D.; Zhou, H.; Cai, F.; Wang, J.; Wang, G.; Bao, X. *ACS Catalysis* **2018**, *8*, 1510–1519.

(48) Kyriakou, G.; Boucher, M. B.; Jewell, A. D.; Lewis, E. A.; Lawton, T. J.; Baber, A. E.; Tierney, H. L.; Flytzani-Stephanopoulos, M.; Sykes, E. C. H. *Science* **2012**, *335*, 1209–1212.

(49) Long, R.; Li, Y.; Liu, Y.; Chen, S.; Zheng, X.; Gao, C.; He, C.; Chen, N.; Qi, Z.; Song, L.; Jiang, J.; Zhu, J.; Xiong, Y. *Journal of the American Chemical Society* **2017**, *139*, 4486–4492.

(50) Bai, S.; Shao, Q.; Wang, P.; Dai, Q.; Wang, X.; Huang, X. *Journal of the American Chemical Society* **2017**, *139*, 6827–6830.

(51) Zhai, H.; Alexandrova, A. N. *ACS Catalysis* **2017**, *7*, 1905–1911.

(52) Zandkarimi, B.; Alexandrova, A. N. *WIREs Computational Molecular Science* **2019**, *9*, DOI: 10.1002/wcms.1420.

(53) Sun, G.; Sautet, P. *Journal of the American Chemical Society* **2018**, *140*, 2812–2820.

(54) Zhai, H.; Alexandrova, A. N. *The Journal of Physical Chemistry Letters* **2018**, *9*, 1696–1702.

(55) Jimenez-Izal, E.; Alexandrova, A. N. *Annual Review of Physical Chemistry* **2018**, *69*, 377–400.

(56) Baxter, E. T.; Ha, M.-A.; Cass, A. C.; Alexandrova, A. N.; Anderson, S. L. *ACS Catalysis* **2017**, *7*, 3322–3335.

(57) Ha, M.-A.; Baxter, E. T.; Cass, A. C.; Anderson, S. L.; Alexandrova, A. N. *Journal of the American Chemical Society* **2017**, *139*, 11568–11575.

(58) Li, X.; Grubisic, A.; Stokes, S. T.; Cordes, J.; Ganteför, G. F.; Bowen, K. H.; Kiran, B.; Willis, M.; Jena, P.; Burgert, R.; Schnöckel, H. *Science* **2007**, *315*, 356–358.

(59) Zhang, X.; Liu, G.; Ganteför, G.; Bowen, K. H.; Alexandrova, A. N. *The Journal of Physical Chemistry Letters* **2014**, *5*, 1596–1601.

(60) Liu, G.; Ciborowski, S. M.; Bowen, K. H. *The Journal of Physical Chemistry A* **2017**, *121*, 5817–5822.

(61) Liu, G.; Zhu, Z.; Ciborowski, S. M.; Ariyarathna, I. R.; Miliordos, E.; Bowen, K. H. *Angewandte Chemie International Edition* **2019**, *58*, 7773–7777.

(62) Buendıa, F.; Beltrán, M. R.; Zhang, X.; Liu, G.; Buytendyk, A.; Bowen, K. *Physical Chemistry Chemical Physics* **2015**, *17*, 28219–28227.

(63) Lang, S. M.; Bernhardt, T. M.; Chernyy, V.; Bakker, J. M.; Barnett, R. N.; Landman, U. *Angewandte Chemie International Edition* **2017**, *56*, 13406–13410.

(64) Jewell, L.; Davis, B. *Applied Catalysis A: General* **2006**, *310*, 1–15.

(65) Gerhards, M.; Thomas, O. C.; Nilles, J. M.; Zheng, W.-J.; Bowen, K. H. *The Journal of Chemical Physics* **2002**, *116*, 10247–10252.

(66) Zhang, X.; Wang, Y.; Wang, H.; Lim, A.; Gantefoer, G.; Bowen, K. H.; Reveles, J. U.; Khanna, S. N. *Journal of the American Chemical Society* **2013**, *135*, 4856–4861.

(67) Robinson, P. J.; Ganteför, G.; Alexandrova, A.; Bowen, K. H. *The Journal of Chemical Physics* **2015**, *143*, 094307.

(68) Wang, H.; Zhang, X.; Ko, Y. J.; Gantefoer, G.; Bowen, K. H.; Li, X.; Kiran, B.; Kandalam, A. K. *The Journal of Chemical Physics* **2014**, *140*, 164317.

(69) Graham, J. D.; Buytendyk, A. M.; Zhang, X.; Collins, E. L.; Kiran, B.; Gantefoer, G.; Eichhorn, B. W.; Gutsev, G. L.; Behera, S.; Jena, P.; Bowen, K. H. *The Journal of Physical Chemistry A* **2014**, *118*, 8158–8162.

(70) Perdew, J. P.; Burke, K.; Ernzerhof, M. *Physical Review Letters* **1996**, *77*, 3865–3868.

(71) Frisch, M. J. et al. Gaussian˜16 Revision C.01, Gaussian Inc. Wallingford CT, 2016.

(72) Hay, P. J.; Wadt, W. R. *The Journal of Chemical Physics* **1985**, *82*, 270–283.

(73) Wadt, W. R.; Hay, P. J. *The Journal of Chemical Physics* **1985**, *82*, 284–298.

(74) Hay, P. J.; Wadt, W. R. *The Journal of Chemical Physics* **1985**, *82*, 299–310.

(75) Peterson, K. A.; Puzzarini, C. *Theoretical Chemistry Accounts* **2005**, *114*, 283–296.

(76) Čížek, J. In *Advances in Chemical Physics*, _eprint: https://onlinelibrary.wiley.com/doi/pdf/10.1002 John Wiley & Sons, Ltd: 1969, pp 35–89.

(77) Purvis, G. D.; Bartlett, R. J. *The Journal of Chemical Physics* **1982**, *76*, 1910–1918.

(78) Scuseria, G. E.; Janssen, C. L.; Schaefer, H. F. *The Journal of Chemical Physics* **1988**, *89*, 7382–7387.

(79) Scuseria, G. E.; Schaefer, H. F. *The Journal of Chemical Physics* **1989**, *90*, 3700–3703.

(80) Hegarty, D.; Robb, M. A. *Molecular Physics* **1979**, *38*, 1795–1812.

(81) Eade, R. H.; Robb, M. A. *Chemical Physics Letters* **1981**, *83*, 362–368.

(82) Schlegel, H.; Robb, M. A. *Chemical Physics Letters* **1982**, *93*, 43–46.

(83) Bernardi, F.; Bottoni, A.; McDouall, J. J. W.; Robb, M. A.; Schlegel, H. B. *Faraday Symposia of the Chemical Society* **1984**, *19*, 137.

(84) Frisch, M.; Ragazos, I. N.; Robb, M. A.; Schlegel, H. B. *Chemical Physics Letters* **1992**, *189*, 524–528.

(85) Yamamoto, N.; Vreven, T.; Robb, M. A.; Frisch, M. J.; Schlegel, H. B. *Chemical Physics Letters* **1996**, *250*, 373–378.

(86) Siegbahn, P. E. *Chemical Physics Letters* **1984**, *109*, 417–423.

(87) Robb, M. A.; Niazi, U. *Reports in Molecular Theory* **1990**, *1*, 23–55.

(88) Klene, M.; Robb, M. A.; Frisch, M. J.; Celani, P. *The Journal of Chemical Physics* **2000**, *113*, 5653–5665.

(89) Reed, A. E.; Weinstock, R. B.; Weinhold, F. *The Journal of Chemical Physics* **1985**, *83*, 735–746.

(90) Hansen, T. W.; DeLaRiva, A. T.; Challa, S. R.; Datye, A. K. *Accounts of Chemical Research* **2013**, *46*, doi: 10.1021/ar3002427, 1720–1730.

(91) Parkinson, G. S.; Novotny, Z.; Argentero, G.; Schmid, M.; Pavelec, J.; Kosak, R.; Blaha, P.; Diebold, U. *Nature Materials* **2013**, *12*, 724–728.

(92) Lei, Y.; Mehmood, F.; Lee, S.; Greeley, J.; Lee, B.; Seifert, S.; Winans, R. E.; Elam, J. W.; Meyer, R. J.; Redfern, P. C.; Teschner, D.; Schlögl, R.; Pellin, M. J.; Curtiss, L. A.; Vajda, S. *Science* **2010**, *328*, 224–228.

(93) Campbell, C. T. *Surface Science Reports* **1997**, *27*, 1–111.

(94) Bartholomew, C. H. *Applied Catalysis A: General* **2001**, *212*, 17–60.

(95) Argyle, M. D.; Bartholomew, C. H. *Catalysts* **2015**, *5*, 145–269.

(96) Goodman, E. D.; Schwalbe, J. A.; Cargnello, M. *ACS Catalysis* **2017**, *7*, 7156–7173.

(97) Fukamori, Y.; König, M.; Yoon, B.; Wang, B.; Esch, F.; Heiz, U.; Landman, U. *ChemCatChem* **2013**, *5*, doi: 10.1002/cctc.201300250, 3330–3341.

(98) Bartholomew, C. H. In *Catalyst Deactivation 1994*, Delmon, B., Froment, G. F. B. T. .-. S. i. S. S., Catalysis, Eds.; Elsevier: 1994; Vol. 88, pp 1–18.

(99) Bartholomew, C. H. *Applied Catalysis A: General* **1993**, *107*, 1–57.

(100) Campbell, C. T.; Parker, S. C.; Starr, D. E. *Science* **2002**, *298*, 811 LP –814.

(101) Campbell, C. T. *Accounts of Chemical Research* **2013**, *46*, doi: 10.1021/ar3003514, 1712–1719.

(102) Bartholomew, C. H. In *Catalyst Deactivation*, Bartholomew, C. H., Fuentes, G. A. B. T. .-. S. i. S. S., Catalysis, Eds.; Elsevier: 1997; Vol. 111, pp 585–592.

(103) Wynblatt, P.; Gjostein, N. A. *Acta Metallurgica* **1976**, *24*, 1165–1174.

(104) Houk, L. R.; Challa, S. R.; Grayson, B.; Fanson, P.; Datye, A. K. *Langmuir* **2009**, *25*, 11225–11227.

(105) Parker, S. C.; Campbell, C. T. *Physical Review B* **2007**, *75*, 35430–35444.

(106) Ha, M. A.; Dadras, J.; Alexandrova, A. *ACS Catalysis* **2014**, *4*, 3570–3580.

(107) Graham, G. W.; Jen, H.-W.; Ezekoye, O.; Kudla, R. J.; Chun, W.; Pan, X. Q.; McCabe, R. W. *Catalysis Letters* **2007**, *116*, 1–8.

(108) Ha, M. A.; Baxter, E. T.; Cass, A. C.; Anderson, S. L.; Alexandrova, A. N. *Journal of the American Chemical Society* **2017**, *139*, 11568–11575.

(109) Dadras, J.; Jimenez-Izal, E.; Alexandrova, A. N. *ACS Catalysis* **2015**, *5*, 5719–5727.

(110) Wichner, N. M.; Beckers, J.; Rothenberg, G.; Koller, H. *Journal of Materials Chemistry* **2010**, *20*, 3840–3847.

(111) Zhang, Z.; Zandkarimi, B.; Alexandrova, A. N. *Accounts of Chemical Research* **2020**, *53*, 447–458.

(112) Jimenez-Izal, E.; Alexandrova, A. N. *Annual Review of Physical Chemistry* **2018**, *69*, 377–400.

(113) Alloyeau, D.; Prévot, G.; Le Bouar, Y.; Oikawa, T.; Langlois, C.; Loiseau, A.; Ricolleau, C. *Physical Review Letters* **2010**, *105*, 1–4.

(114) Kresse, G.; Furthmüller, J. *Computational Materials Science* **1996**, *6*, 15–50.

(115) Kresse, G.; Furthmüller, J. *Physical Review B* **1996**, *54*, 11169–11186.

(116) Kresse, G.; Hafner, J. *Physical Review B* **1993**, *47*, 558–561.

(117) Kresse, G.; Furthmüller, J. *Physical Review B* **1994**, *40*, 14251–14271.

(118) Kresse, G.; Joubert, D. *Physical Review B* **1999**, *59*, 1758–1775.

(119) Zhang, J.; Alexandrova, A. N. *The Journal of chemical physics* **2011**, *135*, 174702–174711.

(120) Zhai, H.; Alexandrova, A. N. *Journal of Chemical Theory and Computation* **2016**, *12*, 6213–6226.

(121) Tang, W.; Sanville, E.; Henkelman, G. *Journal of Physics Condensed Matter* **2009**, *21*, 084204–084210.

(122) Sanville, E.; Kenny, S. D.; Smith, R.; Henkelman, G. *Journal of Computational Chemistry* **2007**, *28*, 899–908.

(123) Henkelman, G.; Arnaldsson, A.; Jónsson, H. *Computational Materials Science* **2006**, *36*, 354–360.

(124) Yu, M.; Trinkle, D. R. *Journal of Chemical Physics* **2011**, *134*, 064111–064118.

(125) Guangjing, L.; Zandkarimi, B.; Cass, A. C.; Gorey, T. J.; Allen, B. J.; Alexandrova, A. N.; Anderson, S. L. *J. Chem. Phys.* **2020**, *152*, 024702–024713.

(126) Dadras, J.; Shen, L.; Alexandrova, A. *Journal of Physical Chemistry C* **2015**, *119*, 6047–6055.

(127) Rahm, J.; Erhart, P. *Journal of Open Source Software* **2020**, *5*, 1944–1946.

(128) Reuter, K. In Wiley: 2011, pp 71–111.

(129) Andersen, M.; Panosetti, C.; Reuter, K. *Frontiers in Chemistry* **2019**, *7*, 202.

(130) Reuter, K.; Scheffler, M. *Physical Review B* **2006**, *73*, 45433.

(131) Bronsted, J. N. *Chemical Reviews* **1928**, *5*, doi: 10.1021/cr60019a001, 231–338.

(132) Evans, M. G.; Polanyi, M. *Transactions of the Faraday Society* **1938**, *34*, 11–24.

(133) Koizumi, K.; Nobusada, K.; Boero, M. *Chemistry - A European Journal* **2017**, *23*, 1531–1538.

(134) Mao, Q.; Luo, K. H. *Journal of Statistical Physics* **2015**, *160*, 1696–1708.

(135) Song, P.; Wen, D. *Journal of Nanoparticle Research* **2010**, *12*, 823–829.

(136) Beniya, A.; Higashi, S.; Ohba, N.; Jinnouchi, R.; Hirata, H.; Watanabe, Y. *Nature Communications* **2020**, *11*, 1888.

(137) Allian, A. D.; Takanabe, K.; Fujdala, K. L.; Hao, X.; Truex, T. J.; Cai, J.; Buda, C.; Neurock, M.; Iglesia, E. *Journal of the American Chemical Society* **2011**, *133*, doi: 10.1021/ja110073u, 4498–4517.

(138) Vajda, S.; Pellin, M. J.; Greeley, J. P.; Marshall, C. L.; Curtiss, L. A.; Ballentine, G. A.; Elam, J. W.; Catillon-Mucherie, S.; Redfern, P. C.; Mehmood, F.; Zapol, P. *Nature Materials* **2009**, *8*, 213–216.

(139) Kaden, W. E.; Wu, T.; Kunkel, W. A.; Anderson, S. L. *Science* **2009**, *326*, 826–829.

(140) Hansen, T. W.; DeLaRiva, A. T.; Challa, S. R.; Datye, A. K. *Accounts of Chemical Research* **2013**, *46*, Publisher: American Chemical Society, 1720–1730.

(141) Alloyeau, D.; Prévot, G.; Bouar, Y. L.; Oikawa, T.; Langlois, C.; Loiseau, A.; Ricolleau, C. *Physical Review Letters* **2010**, *105*, DOI: 10.1103/physrevlett.105.255901.

(142) Ha, M.-A.; Dadras, J.; Alexandrova, A. *ACS Catalysis* **2014**, *4*, 3570–3580.

(143) Dadras, J.; Shen, L.; Alexandrova, A. *The Journal of Physical Chemistry C* **2015**, *119*, 6047–6055.

(144) Zandkarimi, B.; Alexandrova, A. N. *WIREs Computational Molecular Science* **2019**, *9*, e1420.

(145) Jimenez-Izal, E.; Alexandrova, A. N. *Annual Review of Physical Chemistry* **2018**, *69*, PMID: 29490204, 377–400.

(146) Zandkarimi, B.; Poths, P.; Alexandrova, A. N. *Angewandte Chemie International Edition* **2021**, *60*, 11973–11982.

(147) Chen, P. J.; Goodman, D. W. *Surface Science* **1994**, *312*.

(148) Madey, T. E. In *Chemisorption and Reactivity on Supported Clusters and Thin Films: Towards an Understanding of Microscopic Processes in Catalysis*, Lambert, R. M., Pacchioni, G., Eds.; Springer Netherlands: Dordrecht, 1997, pp 105–116.

(149) Kane, M. D.; Roberts, F. S.; Anderson, S. L. *The Journal of Physical Chemistry C* **2015**, *119*, 1359–1375.

(150) Maintz, S.; Deringer, V. L.; Tchougréeff, A. L.; Dronskowski, R. *Journal of Computational Chemistry* **2016**, *37*, 1030–1035.

(151) Dronskowski, R.; Bloechl, P. E. *The Journal of Physical Chemistry* **1993**, *97*, 8617–8624.

(152) Müller, P. C.; Ertural, C.; Hempelmann, J.; Dronskowski, R. *The Journal of Physical Chemistry C* **2021**, *125*, 7959–7970.

(153) *Current topics in ion chemistry and physics: Low energy ion-surface interactions low energy ion-surface interactions v. 3*; Rabalais, J. W., Ed.; Wiley Series In Ion Chemistry and Physics; John Wiley & Sons: Chichester, England, 1994.

(154) Kumar, R.; Mintz, M. H.; Schultz, J.; Rabalais, J. *Surface Science* **1983**, *130*, L311–L316.

(155) Rabalais, J. W., *Principles and applications of ion scattering spectrometry*; Wiley Series on Mass Spectrometry; John Wiley & Sons: Nashville, TN, 2002.

(156) Roberts, F. S.; Kane, M. D.; Baxter, E. T.; Anderson, S. L. *Phys. Chem. Chem. Phys.* **2014**, *16*, 26443–26457.

(157) Zlotea, C.; Oumellal, Y.; Provost, K.; Morfin, F.; Piccolo, L. *Applied Catalysis B: Environmental* **2018**, *237*, 1059–1065.

(158) Guda, A. A.; Guda, S. A.; Lomachenko, K. A.; Soldatov, M. A.; Pankin, I. A.; Soldatov, A. V.; Braglia, L.; Bugaev, A. L.; Martini, A.; Signorile, M.; Groppo, E.; Piovano, A.; Borfecchia, E.; Lamberti, C. *Catalysis Today* **2019**, *336*, 3–21.

(159) Nayak, C.; Jain, P.; Vinod, C. P.; Jha, S. N.; Bhattacharyya, D. *Journal of Synchrotron Radiation* **2019**, *26*, 137–144.

(160) Frenkel, A. I.; Rodriguez, J. A.; Chen, J. G. *ACS Catalysis* **2012**, *2*, 2269–2280.

(161) Benfatto, M.; Meneghini, C. In *Synchrotron Radiation*; Springer Berlin Heidelberg: 2014, pp 213–240.

(162) Timoshenko, J.; Cuenya, B. R. *Chemical Reviews* **2020**, *121*, 882–961.

(163) Bordiga, S.; Groppo, E.; Agostini, G.; van Bokhoven, J. A.; Lamberti, C. *Chemical Reviews* **2013**, *113*, 1736–1850.

(164) Zhou, Y.; Doronkin, D. E.; Zhao, Z.; Plessow, P. N.; Jelic, J.; Detlefs, B.; Pruessmann, T.; Studt, F.; Grunwaldt, J.-D. *ACS Catalysis* **2018**, *8*, 11398–11406.

(165) Matos, J.; Ono, L. K.; Behafarid, F.; Croy, J. R.; Mostafa, S.; DeLaRiva, A. T.; Datye, A. K.; Frenkel, A. I.; Cuenya, B. R. *Physical Chemistry Chemical Physics* **2012**, *14*, 11457.

(166) Timoshenko, J.; Halder, A.; Yang, B.; Seifert, S.; Pellin, M. J.; Vajda, S.; Frenkel, A. I. *The Journal of Physical Chemistry C* **2018**, *122*, 21686–21693.

(167) Yao, S. et al. *ACS Catalysis* **2014**, *4*, 1650–1661.

(168) Lamberti, C.; Bordiga, S.; Bonino, F.; Prestipino, C.; Berlier, G.; Capello, L.; D'Acapito, F.; i Xamena, F. X. L.; Zecchina, A. *Phys. Chem. Chem. Phys.* **2003**, *5*, 4502–4509.

(169) Liu, Y.; Marcella, N.; Timoshenko, J.; Halder, A.; Yang, B.; Kolipaka, L.; Pellin, M. J.; Seifert, S.; Vajda, S.; Liu, P.; Frenkel, A. I. *The Journal of Chemical Physics* **2019**, *151*, 164201.

(170) Timoshenko, J.; Lu, D.; Lin, Y.; Frenkel, A. I. *The Journal of Physical Chemistry Letters* **2017**, *8*, 5091–5098.

(171) Zandkarimi, B.; Sun, G.; Halder, A.; Seifert, S.; Vajda, S.; Sautet, P.; Alexandrova, A. N. *The Journal of Physical Chemistry C* **2020**, *124*, 10057–10066.

(172) Yang, B.; Liu, C.; Halder, A.; Tyo, E. C.; Martinson, A. B. F.; Seifert, S.; Zapol, P.; Curtiss, L. A.; Vajda, S. *The Journal of Physical Chemistry C* **2017**, *121*, 10406–10412.

(173) Halder, A.; Ha, M.-A.; Zhai, H.; Yang, B.; Pellin, M. J.; Seifert, S.; Alexandrova, A. N.; Vajda, S. *ChemCatChem* **2020**, *12*, 1307–1315.

(174) Reske, R.; Mistry, H.; Behafarid, F.; Cuenya, B. R.; Strasser, P. *Journal of the American Chemical Society* **2014**, *136*, 6978–6986.

(175) Liu, Y.; Halder, A.; Seifert, S.; Marcella, N.; Vajda, S.; Frenkel, A. I. *ACS Applied Materials &amp Interfaces* **2021**, *13*, 53363–53374.

(176) Kresse, G.; Hafner, J. *Physical Review B* **1994**, *49*, 14251–14269.

(177) Dudarev, S. L.; Botton, G. A.; Savrasov, S. Y.; Humphreys, C. J.; Sutton, A. P. *Physical Review B* **1998**, *57*, 1505–1509.

(178) Sun, G.; Alexandrova, A. N.; Sautet, P. *ACS Catalysis* **2020**, *10*, 5309–5317.

(179) Cheng, L.; Yin, C.; Mehmood, F.; Liu, B.; Greeley, J.; Lee, S.; Lee, B.; Seifert., S.; Winans, R. E.; Teschner, D.; Schlögl, R.; Vajda, S.; Curtiss, L. A. *ACS Catalysis* **2013**, *4*, 32–39.

(180) Joly, Y. *Physical Review B* **2001**, *63*, DOI: 10.1103/physrevb.63.125120.

(181) Joly, Y.; Bunău, O.; Lorenzo, J. E.; Galéra, R. M.; Grenier, S.; Thompson, B. *Journal of Physics: Conference Series* **2009**, *190*, 012007.

(182) Jain, A.; Ong, S. P.; Hautier, G.; Chen, W.; Richards, W. D.; Dacek, S.; Cholia, S.; Gunter, D.; Skinner, D.; Ceder, G.; Persson, K. A. *APL Materials* **2013**, *1*, 011002.

(183) Ravel, B.; Newville, M. *Journal of Synchrotron Radiation* **2005**, *12*, 537–541.

(184) Gaur, A.; Shrivastava, B. D.; Joshi, S. K. *Journal of Physics: Conference Series* **2009**, *190*, 012084.

(185) Zhang, N.; Wang, W.; Brugger, J.; Zhang, G.; Zeng, D. *Journal of Molecular Liquids* **2017**, *230*, 200–208.

(186) Yang, J. et al. *Journal of the American Chemical Society* **2021**, *143*, 14530–14539.

(187) Brugger, J.; Etschmann, B.; Liu, W.; Testemale, D.; Hazemann, J.; Emerich, H.; van Beek, W.; Proux, O. *Geochimica et Cosmochimica Acta* **2007**, *71*, 4920–4941.

(188) Wang, C.; Chen, D. P.; Sang, X.; Unocic, R. R.; Skrabalak, S. E. *ACS Nano* **2016**, *10*, 6345–6353.

(189) Chen, W.-T.; Hsu, C.-W.; Lee, J.-F.; Pao, C.-W.; Hsu, I.-J. *ACS Omega* **2020**, *5*, 4991–5000.

(190) Pankin, I. A.; Martini, A.; Lomachenko, K. A.; Soldatov, A. V.; Bordiga, S.; Borfecchia, E. *Catalysis Today* **2020**, *345*, 125–135.

(191) Joo, S. H.; Park, J. Y.; Tsung, C.-K.; Yamada, Y.; Yang, P.; Somorjai, G. A. *Nature Materials* **2008**, *8*, 126–131.

(192) Bhasin, M.; McCain, J.; Vora, B.; Imai, T.; Pujadó, P. *Applied Catalysis A: General* **2001**, *221*, 397–419.

(193) Nie, L.; Meng, A.; Yu, J.; Jaroniec, M. *Scientific Reports* **2013**, *3*, DOI: 10.1038/srep03215.

(194) Yang, D.; Fu, S.; Huang, S.; Deng, W.; Wang, Y.; Guo, L.; Ishihara, T. *Microporous and Mesoporous Materials* **2020**, *296*, 109802.

(195) Musselwhite, N.; Na, K.; Sabyrov, K.; Alayoglu, S.; Somorjai, G. A. *Journal of the American Chemical Society* **2015**, *137*, 10231–10237.

(196) Lu, J.; Elam, J. W.; Stair, P. C. *Accounts of Chemical Research* **2013**, *46*, 1806–1815.

(197) Lu, J.; Fu, B.; Kung, M. C.; Xiao, G.; Elam, J. W.; Kung, H. H.; Stair, P. C. *Science* **2012**, *335*, 1205–1208.

(198) Gorey, T. J.; Dai, Y.; Anderson, S. L.; Lee, S.; Lee, S.; Seifert, S.; Winans, R. E. *Surface Science* **2020**, *691*, 121485.

(199) Pham, H. N.; Sattler, J. J. H. B.; Weckhuysen, B. M.; Datye, A. K. *ACS Catalysis* **2016**, *6*, 2257–2264.

(200) Iglesias-Juez, A.; Beale, A. M.; Maaijen, K.; Weng, T. C.; Glatzel, P.; Weckhuysen, B. M. *Journal of Catalysis* **2010**, *276*, 268–279.

(201) Mariscal, R.; Fierro, J. L.; Yori, J. C.; Parera, J. M.; Grau, J. M. *Applied Catalysis A: General* **2007**, *327*, 123–131.

(202) Ballarini, A. D.; de Miguel, S.; Castro, A.; Scelza, O. *Catalysis in Industry* **2013**, *5*, 283–296.

(203) Redhead, P. *Vacuum* **1962**, *12*, 203–211.

(204) Yeh, J.; Lindau, I. *Atomic Data and Nuclear Data Tables* **1985**, *32*, 1–155.

(205) Dai, Y.; Gorey, T. J.; Anderson, S. L.; Lee, S.; Lee, S.; Seifert, S.; Winans, R. E. *The Journal of Physical Chemistry C* **2016**, *121*, 361–374.

(206) Baxter, E. T.; Ha, M.-A.; Cass, A. C.; Zhai, H.; Alexandrova, A. N.; Anderson, S. L. *The Journal of Physical Chemistry C* **2018**, *122*, 1631–1644.

(207) Qin, R.; Wang, P.; Liu, P.; Mo, S.; Gong, Y.; Ren, L.; Xu, C.; Liu, K.; Gu, L.; Fu, G.; Zheng, N. *Research* **2020**, *2020*, DOI: 10.34133/2020/4172794.

(208) Chen, P.; Goodman, D. *Surface Science* **1994**, *312*, L767–L773.

(209) Grimme, S.; Antony, J.; Ehrlich, S.; Krieg, H. *The Journal of Chemical Physics* **2010**, *132*, 154104.

(210) Henkelman, G.; Uberuaga, B. P.; Jónsson, H. *The Journal of Chemical Physics* **2000**, *113*, 9901–9904.

(211) Sattler, J. J. H. B.; Beale, A. M.; Weckhuysen, B. M. *Physical Chemistry Chemical Physics* **2013**, *15*, 12095.

(212) Zhang, W.; Wang, H.; Jiang, J.; Sui, Z.; Zhu, Y.; Chen, D.; Zhou, X. *ACS Catalysis* **2020**, *10*, 12932–12942.

(213) Huang, Z.; Fryer, J. R.; Park, C.; Stirling, D.; Webb, G. *Journal of Catalysis* **1998**, *175*, 226–235.

(214) Sattler, J. J. H. B.; Gonzalez-Jimenez, I. D.; Luo, L.; Stears, B. A.; Malek, A.; Barton, D. G.; Kilos, B. A.; Kaminsky, M. P.; Verhoeven, T. W. G. M.; Koers, E. J.; Baldus, M.; Weckhuysen, B. M. *Angewandte Chemie International Edition* **2014**, *53*, 9251–9256.

(215) Payard, P.-A.; Rochlitz, L.; Searles, K.; Foppa, L.; Leuthold, B.; Safonova, O. V.; Comas-Vives, A.; Copéret, C. *JACS Au* **2021**, *1*, 1445–1458.

(216) Raman, N.; Wolf, M.; Heller, M.; Heene-Würl, N.; Taccardi, N.; Haumann, M.; Felfer, P.; Wasserscheid, P. *ACS Catalysis* **2021**, *11*, 13423–13433.

(217) Cybulskis, V. J.; Bukowski, B. C.; Tseng, H.-T.; Gallagher, J. R.; Wu, Z.; Wegener, E.; Kropf, A. J.; Ravel, B.; Ribeiro, F. H.; Greeley, J.; Miller, J. T. *ACS Catalysis* **2017**, *7*, 4173–4181.

(218) Dadras, J.; Jimenez-Izal, E.; Alexandrova, A. N. *ACS Catalysis* **2015**, *5*, 5719–5727.

(219) Aly, M.; Fornero, E. L.; Leon-Garzon, A. R.; Galvita, V. V.; Saeys, M. *ACS Catalysis* **2020**, *10*, 5208–5216.

(220) Lian, Z.; Ali, S.; Liu, T.; Si, C.; Li, B.; Su, D. S. *ACS Catalysis* **2018**, *8*, 4694–4704.

(221) Lian, Z.; Si, C.; Jan, F.; Zhi, S.; Li, B. *ACS Catalysis* **2021**, *11*, 9279–9292.

(222) Nykänen, L.; Honkala, K. *ACS Catalysis* **2013**, *3*, 3026–3030.

(223) Yang, M.-L.; Zhu, Y.-A.; Zhou, X.-G.; Sui, Z.-J.; Chen, D. *ACS Catalysis* **2012**, *2*, 1247–1258.

(224) Hook, A.; Celik, F. E. *The Journal of Physical Chemistry C* **2017**, *121*, 17882–17892.

(225) Borgna, A.; Garetto, T.; Apesteguia, C. *Applied Catalysis A: General* **2000**, *197*, 11–21.

(226) Kumar, M. S.; Chen, D.; Holmen, A.; Walmsley, J. C. *Catalysis Today* **2009**, *142*, 17–23.

(227) Zandkarimi, B.; Alexandrova, A. N. *Journal of Physical Chemistry Letters* **2019**, *10*, 460–467.

(228) Jo, Y.; Kim, T. W.; Oh, J.; Kim, D.; Suh, Y.-W. *Journal of Catalysis* **2022**, *413*, 127–137.

(229) Poths, P.; Li, G.; Masubuchi, T.; Morgan, H. W. T.; Zhang, Z.; Alexandrova, A. N.; Anderson, S. L. *ACS Catalysis* **2023**, *13*, 1533–1544.

(230) Liu, G. X.; Poths, P.; Zhang, X. X.; Zhu, Z. G.; Marshall, M.; Blankenhorn, M.; Alexandrova, A. N.; Bowen, K. H. *Journal of the American Chemical Society* **2020**, *142*, 7930–7936.

(231) Halder, A.; Ha, M. A.; Zhai, H. C.; Yang, B.; Pellin, M. J.; Seifert, S.; Alexandrova, A. N.; Vajda, S. *Chemcatchem* **2020**, *12*, 1307–1315.

(232) Hauser, A. W.; Gomes, J.; Bajdich, M.; Head-Gordon, M.; Bell, A. T. *Physical Chemistry Chemical Physics* **2013**, *15*, 20727.

(233) Hook, A.; Massa, J. D.; Celik, F. E. *The Journal of Physical Chemistry C* **2016**, *120*, 27307–27318.

(234) Wang, Z.; Chen, Y.; Mao, S.; Wu, K.; Zhang, K.; Li, Q.; Wang, Y. *Advanced Sustainable Systems* **2020**, *4*, 2000092.

(235) Furukawa, S.; Tamura, A.; Ozawa, K.; Komatsu, T. *Applied Catalysis A: General* **2014**, *469*, 300–305.

(236) Dronskowski, R.; Blochl, P. E. *Journal of Physical Chemistry* **1993**, *97*, 8617–8624.

(237) Kresse, G.; Furthmuller, J. *Physical Review B* **1996**, *54*, 11169–11186.

(238) Perdew, J. P.; Burke, K.; Ernzerhof, M. *Physical Review Letters* **1996**, *77*, 3865–3868.

(239) Blochl, P. E. *Physical Review B* **1994**, *50*, 17953–17979.

(240) Sheppard, D.; Xiao, P. H.; Chemelewski, W.; Johnson, D. D.; Henkelman, G. *Journal of Chemical Physics* **2012**, *136*, 8.

(241) Henkelman, G.; Uberuaga, B. P.; Jonsson, H. *Journal of Chemical Physics* **2000**, *113*, 9901–9904.

(242) Bader, R. F. W. *Chemical Reviews* **1991**, *91*, 893–928.

(243) Tang, W.; Sanville, E.; Henkelman, G. *Journal of Physics-Condensed Matter* **2009**, *21*, DOI: 10.1088/0953-8984/21/8/084204.

(244) Zhai, H.; Alexandrova, A. N. *Journal of Chemical Theory and Computation* **2016**, *12*, 6213–6226.

(245) Deringer, V. L.; Tchougreeff, A. L.; Dronskowski, R. *Journal of Physical Chemistry A* **2011**, *115*, 5461–5466.

(246) Te Velde, G.; Bickelhaupt, F. M.; Baerends, E. J.; Guerra, C. F.; Van Gisbergen, S. J. A.; Snijders, J. G.; Ziegler, T. *Journal of Computational Chemistry* **2001**, *22*, 931–967.

(247) Van Lenthe, E.; Baerends, E. J. *Journal of Computational Chemistry* **2003**, *24*, 1142–1156.

(248) Powell, C.; Jablonski, A. *Journal of Surface Analysis* **2002**, *9*, 322–325.

(249) Wu, J.; Helveg, S.; Ullmann, S.; Peng, Z.; Bell, A. T. *Journal of Catalysis* **2016**, *338*, 295–304.